SOCIETY FOR MAGNETIC RESONANCE IMAGING

FIFTH ANNUAL MEETING

28 FEBRUARY – 4 MARCH 1987

San Antonio Convention Center
San Antonio, Texas

PROGRAM AND ABSTRACTS

Guest Editors
David D. Stark, M.D.
Val M. Runge, M.D.

Pergamon Press
New York • Oxford • Beijing • Frankfurt • São Paulo • Sydney • Tokyo • Toronto

SIEMENS

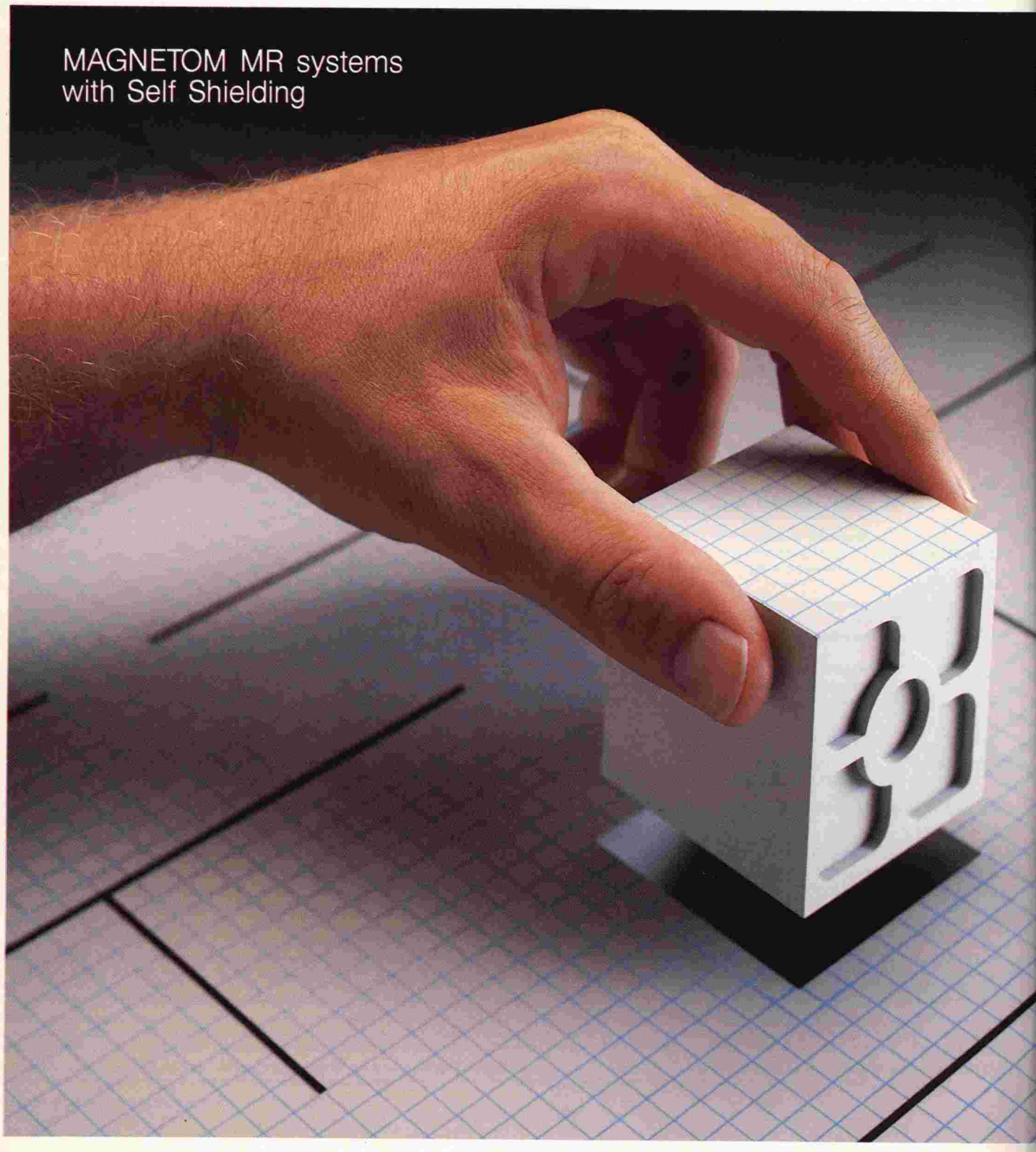

MAGNETIC RESONANCE IMAGING

VOLUME 5, SUPPLEMENT I 1987

CONTENTS

Special Issue: Fifth Annual Meeting—Program and Abstracts

INDEXED IN CABS, BIOSIS Database, Excerpta Medica, Electron, & Commun. Abstr., Chemical Abstr., INSPEC Database, Index Medicus, MEDLINE, Index of European Radiological Journals.

ISSN 0730-725X
(687)

What happens when your cryogens don't arrive on time?

You quickly lose your piece of mind.

Everything has to stop while your multi-million dollar MRI investment just sits there waiting for the cryogen delivery. You lose patient revenue. Your staff sits idle.

But that doesn't have to happen.

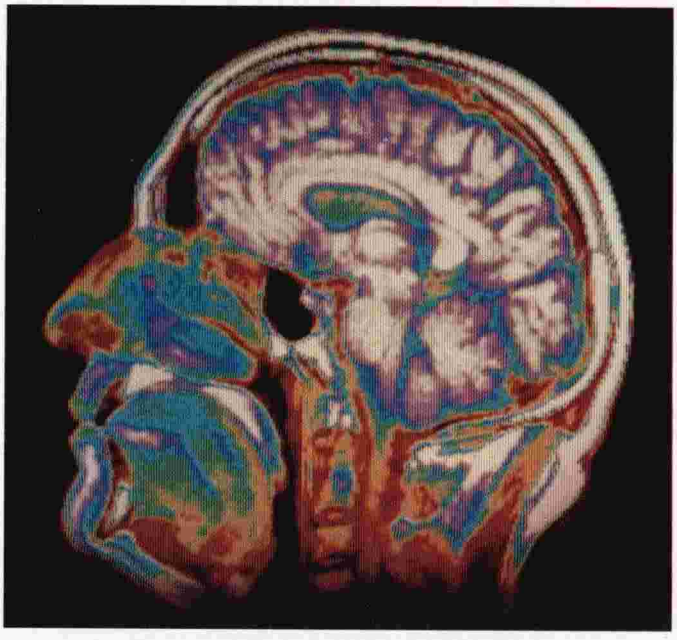

Choose your cryogen supplier carefully

If you've chosen your cryogen supplier carefully, as you have your MRI supplier, your cryogens will be routinely delivered on time.

That's why more MRI owners have depended on cryogens produced by Linde than produced by any other cryogen supplier.

Even our competitors have depended on us. After all, we are a very secure source.

Buy directly from the source

The fact is that Linde not only has invested in more crude helium reserves than any other MRI cryogen supplier, but also is the world's largest commercial producer of refined liquid helium.

We own and operate three of the six commercial helium plants located in the United States.

The benefit to you is obvious — you are assured of a reliable, long-term source of rare liquid helium.

In addition, Linde is also one of the world's largest producers of liquid nitrogen.

Our commitment to develop our own resources and production facilities enables us to provide you with the best service possible. We don't have to rely on the resources of other suppliers.

When you buy CRYOSCAN™ liquid helium and liquid nitrogen from Linde, you buy cryogens produced by Linde — direct from the source.

Look for a commitment of resources that meets your needs

With Linde as your supplier, you have the benefit of the largest cryogen delivery network in the United States, in fact, in the world.

It includes liquid transfill stations in every strategic part of the country, with more being built. The nation's largest owned and operated, commercial trailer and local truck fleet to ensure that your cryogen delivery arrives on time. And non-magnetic, "super insulated" dewars that are designed and made specifically for the MRI environment.

As a Linde customer, you are provided with service and support based on more than 75 years of experience and investment in cryogen production, distribution and use.

We built the nation's first liquid nitrogen production facility in 1907 and the world's first liquid helium production facility in 1917.

Demand local service

Only Linde has over 600 local distributor locations staffed with experienced people who will meet with you and discuss your needs, face to face.

It's a personalized service that starts with working out a delivery schedule that meets your needs and a site survey to determine the best and safest way to deliver your cryogens to your facility or mobile system.

Your local Linde representative will also work with you on how to reduce your liquid helium losses and provide your staff with safety information and literature to aid

you in the proper handling of your CRYOSCAN™ products.

As you can see, we provide more than just an impersonal "800" number for ordering and support, a number that may be located thousands of miles away, in another time zone.

We provide you with local contacts who offer you round-the-clock service, versus a round-the-clock telephone number.

Expect products and people dedicated to MRI

Your CRYOSCAN™ liquid helium and liquid nitrogen are delivered in dewars specifically designed for medical MRI. Combined with our unique dewar filling procedures and our rapid delivery, you are assured of receiving the most liquid cryogen possible.

Only Linde provides your gaseous helium in unique aluminum cylinders designed to assure you of a safe source of pressure for transfilling, along with CRYOSCAN™ non-magnetic regulators made specifically for the MRI environment.

We at Linde understand your MRI needs. Our MRI cryogens manager is a former Chief Technologist who has spent his entire business career working with diagnostic imaging professionals like yourself.

Our personnel at your local Linde distributor locations are experts dedicated to delivering your CRYOSCAN™ cryogens to you safely and on time.

Keep in mind the bottom line of your MRI investment

The continued MRI performance, patient throughput and profitability that you require start with the performance of your cryogen supplier.

There is no substitute for routine on-time delivery.

For more information on CRYOSCAN™ products, call your local Linde Distributor. Or call ***1-800-445-4633,*** *in New Jersey 201-271-4535*

LINDE UNION CARBIDE MEDICAL GASES

Your partner in health care for over 75 years

Acclaimed Best Seller

ONCOLOGIC IMAGING

Editors:
David G. Bragg, M.D.
University of Utah School of Medicine
Philip Rubin, M.D.
University of Rochester Cancer Center
James E. Youker, M.D.
Medical College of Wisconsin

And the Reviewers Tell Us Why

"This is the first comprehensive textbook of diagnostic imaging of malignant tumors. . . . It is without question, a major, new addition to the library of any department of oncology, surgery, medicine or radiotherapy."

James D. Cox, M.D.
Professor and Chairman, Department of Radiation Oncology, Columbia-Presbyterian Medical Center, New York, New York

"This textbook provides a major reference on imaging patients with oncologic disease and I strongly recommend it for all departments of radiology that participate in the evaluation of a significant number of these patients."

Paul M. Silverman, M.D.
Duke University Medical Center, Durham, North Carolina in *Investigative Radiology*, July 1986

"This book is a must for any radiologist who attends tumor board or has frequent contact with oncologists. It bridges the gap that occurs when clinicians try to extract staging information from imaging specialists."

Linda K. Olson
UCSD Medical Center, San Diego, California in *American Journal of Roentgenology*, June 1986

CONTENTS

1985 664 pp. 850 illustrations ISBN 0 08 033653 1 Hardcover US$140.00

PERGAMON BOOKS

US: Maxwell House, Fairview Park, Elmsford, NY 10523 UK: Headington Hill Hall, Oxford OX3 OBW, England

PTS
FREQUENCY SYNTHESIZERS

HIGH-PERFORMANCE DIRECT SYNTHESIZERS
Accurate, stable, quiet frequencies on command, fast. For NMR, imaging, SATCOM, surveillance, ATE. Sources adapting to your needs with options. High demonstrated reliability. Thousands in use.

PTS 040

Range: 0.1-40MHz
Resolution: 0.1Hz-100KHz (opt.)
Switching: 5-20μs
Output: +3 to +13dBm: 50 ohm
Spurious Outputs: −75dB

Phase Noise: −75dBc, (0-15KHz)
Freq. St'd: Oven, TCXO, Ext.
Interface: BCD par. or GPIB
Size: 19″W, 5¼″H, 18″D
Price: $4,400.00*

Other Options:
Progr. Attenuator, 0-90db
(or 0-99dB with GPIB)
nx10MHz output 20-140MHz
or any 10MHz line (20-140)

PTS 120

Range: 90-120MHz
Resolution: 0.1Hz-100KHz (opt.)
Switching: 5-20μs
Output: +3 to +10dBm: 50 ohm
Spurious Outputs: −75dBc

Phase Noise: −75dBc, (0.5Hz-15KHz)
Freq. St'd: Oven, TCXO, Ext.
Interface: BCD par. or GPIB
Size: 19″W, 5¼″H, 18″D
Price: $4,400.00*

Other Options:
Progr. Attenuator, 0-90dB
(or 0-99dB with GPIB)
nx10MHz output 20-140MHz
or any 10 MHz line (20-140)

PTS 160

Range: 0.1-160MHz
Resolution: 0.1Hz-100KHz (opt.)
Switching: 5-20μs
Output: +3 to +13dBm: 50 ohm
Spurious Outputs: −75dB

Phase Noise: −63dBc, (0-15KHz)
Freq. St'd: Oven, TCXO, Ext.
Interface: BCD par. or GPIB
Size: 19″W, 5¼″H, 18″D
Price: $5,600.00*

Other Options:
Progr. Attenuator, 0-90dB
(or 0-99dB with GPIB)
nx10MHz output 20-140MHz
or any 10 MHz line (20-140)

PTS 250

Range: 1-250MHz
Resolution: 0.1Hz-100KHz (opt.)
Switching: 5-20μs
Output: +3 to +13dBm: 50 ohm
Spurious Outputs: −70dB

Phase Noise: −63dBc, (0-15KHz)
Freq. St'd: Oven, TCXO, Ext.
Interface: BCD par. or GPIB
Size: 19″W, 5¼″H, 18″D
Price: $6,400.00*

Other Options:
Progr. Attenuator, 0-90dB
(or 0-99dB with GPIB)
nx10MHz output 20-140MHz
or any 10 MHz line (20-140)

PTS 500

Range: 1-500MHz
Resolution: 0.1Hz-100KHz (opt.)
Switching: 5-20μs
Output: +3 to +13dBm: 50 ohm
Spurious Outputs: −70dB

Phase Noise: −63dBc, (0-15KHz)
Freq. St'd: Oven, TCXO, Ext.
Interface: BCD par. or GPIB
Size: 19″W, 5¼″H, 18″D
Price: $7,500.00*

Other Options:
Progr. Attenuator, 0-90dB
(or 0-99dB with GPIB)
nx10MHz output 20-140MHz
or any 10 MHz line (20-140)

*Prices are US only, manual & remote, (BCD), 1 Hz res. with oven std.

2 UNITS FOR THE PRICE OF ONE!
0.1-160 or 250 MHz
+ 0.1-3 MHz, TLU, 1 Hz
ALL IN ONE PACKAGE
ΔCOST-$600
PTS 160/250 DELTA

***NEW:* Choice of table-look-up resolution with steady-phase switching.**

PROGRAMMED TEST SOURCES, INC.
P.O. Box 517, 9 Beaver Brook Rd., Littleton, MA 01460 617-486-3008

GRADIENT WAVEFORM RESEARCH SPURS EXPANDING CLINICAL UTILITY.

Motion Artifact Suppression Technique (MAST™)

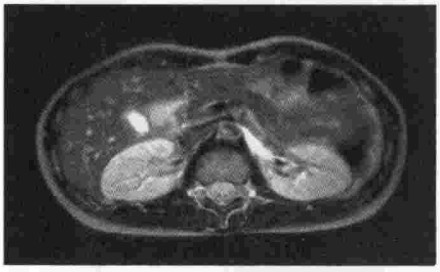

Ungated multiecho study of the normal liver: TE=26, 100ms, TR=2000ms. (a) The first echo, pre-MAST; (b) the second, MAST.

MAST suppresses artifacts arising from in-view motion, offering dramatic improvements in image quality without sacrificing scan time. MAST minimizes cardiac and respiratory motion artifacts and suppresses additional unwanted motion such as involuntary orbit movement, peristalsis and CSF and blood flow.

HYBRID™ Fast Scan Imaging

HYBRID Q=4: Glioma of splenium corpus callosum, 4.26 minutes.

Using a unique approach to data acquisition that enables coverage of more than one standard view in a single HYBRID view, this technique reduces acquisition time by a factor of two or four for a substantial throughput increase. HYBRID maintains clinical resolution and contrast, and may increase S/N in the region of interest.

Contrast Enhanced FAST™ (CE-FAST™)

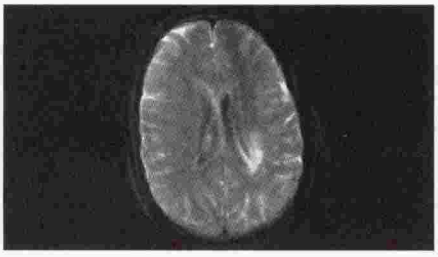

Non-excised, irradiated portion of glioma, 40 sec.

CE-FAST, a major fast scan breakthrough, reduces data collection time from the current average of 10 minutes to ≈40 seconds while maintaining maximum T_2 contrast. As a result, it dramatically increases throughput, reduces motion and chemical shift artifacts, and heightens image quality.

Direct Oblique Imaging

Gated, oblique image of the normal heart with the scanning plane oriented towards the aortic arch.

Direct Oblique Imaging, the ability to image the body in any non-orthogonal plane (as opposed to simple tilts), enables increased anatomical visualization and thereby improves diagnostic evaluation. It greatly enhances the imaging of organs and structures not in the center of the body, particularly the heart.

Additional Technique Development Includes . . .

- Short Tau Inversion Recovery (STIR™)
- Centrally Ordered Phase Encoding (COPE™)
- STimulated Echo Progressive (STEP™) Imaging
- Quadrature-design coils
- Contiguous slice profiles
- Further advances in MR cardiology, angiology and spectroscopy

Some features of Picker's VISTA® MR systems are classified as investigational devices and limited by federal law to investigational use. As such, they cannot be made available until necessary government approvals have been granted.

QUICK STEP™

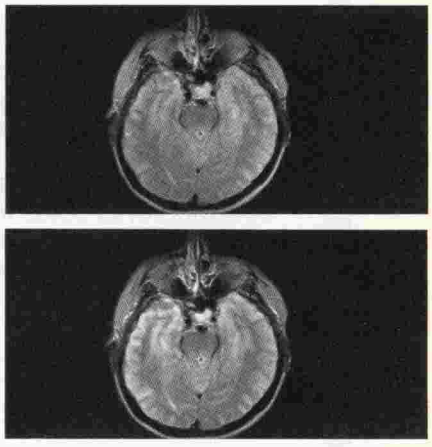

Intrasellar lesion: (a) standard 2DFT, 17.1 minutes; (b) QUICK STEP, 8.5 minutes.

Employing a new approach to phase encoding, QUICK STEP provides contrast and resolution equal to a T_2-weighted SE sequence while offering time savings of two, four or greater. QUICK STEP markedly augments patient throughput and improves patient comfort and acceptance.

Blood Flow Analysis

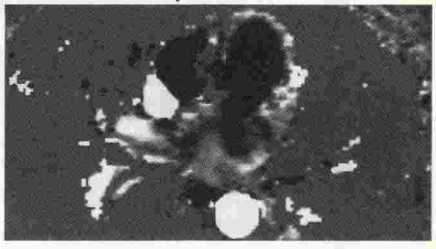

Transverse phase map of the heart showing ascending and descending aorta.

MRI flow studies allow non-invasive assessment of inaccessible and deep blood vessels. Our research indicates that high velocity flow in the coronary artery may soon be precisely quantified. Further software development should establish MRI as a viable alternative to many angiographic procedures.

PICKER

THE IMAGE OF EXCELLENCE

SEE THESE INNOVATIONS AND MORE AT RSNA '86!

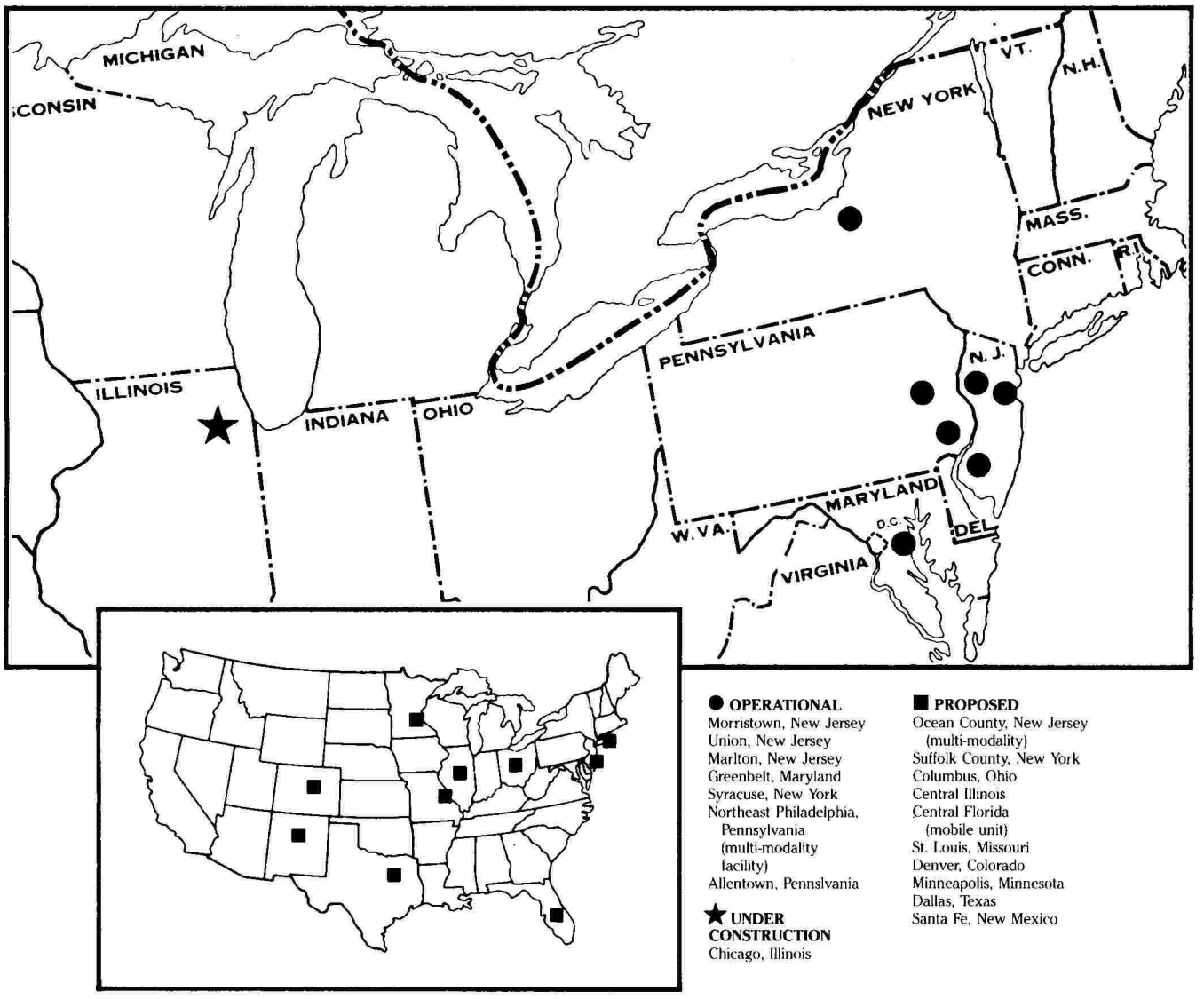

● **OPERATIONAL**
Morristown, New Jersey
Union, New Jersey
Marlton, New Jersey
Greenbelt, Maryland
Syracuse, New York
Northeast Philadelphia, Pennsylvania (multi-modality facility)
Allentown, Pennsylvania

★ **UNDER CONSTRUCTION**
Chicago, Illinois

■ **PROPOSED**
Ocean County, New Jersey (multi-modality)
Suffolk County, New York
Columbus, Ohio
Central Illinois
Central Florida (mobile unit)
St. Louis, Missouri
Denver, Colorado
Minneapolis, Minnesota
Dallas, Texas
Santa Fe, New Mexico

LEADING THE NATION IN MRI CENTER DEVELOPMENT

Why have more physicians and hospitals selected NMR of America to fully develop their plans for free-standing MRI centers?

■ **Freedom of Choice**
Only NMR of America offers a full range of investment opportunities to meet the financial needs and interests of its co-developers.

■ **Freedom from Detail**
From site selection through staffing and operations, NMR of America offers co-developers a full range of financial, medical, technical and marketing services.

■ **Freedom from Unnecessary Costs**
NMR of America's national presence means cost-saving contracts on equipment and supplies from all major MRI vendors.

■ **Freedom from Worry**
NMR of America can offer physicians and hospitals complete turn-key projects while preserving investors' total management prerogatives.

To discover how NMR of America can meet your local needs with local solutions, call or write Connie Ortisi, project coordinator.

NMR of America, Inc.

355 Madison Avenue • Morristown, New Jersey 07960 • 201-539-1082

NOTES:

Session designations are as follows --

Mam sessions are on **Monday morning**
Mpm sessions are on **Monday afternoon**
Tam sessions are on **Tuesday morning**
Tpm sessions are on **Tuesday afternoon**
Wam sessions are on **Wednesday morning**
Wpm sessions are on **Wednesday afternoon**

Rooms are assigned as follows --

Symposia **"Symp"** and Proffered oral abstract **"A"** sessions are in the **River Room**
"B" sessions are in **Room C-107**
"C" sessions are in **Room C-101**
"D" sessions are in **Room C-102**
"E" sessions are in **Room C-108**

Sunday and Monday nights, 5:15 - 7:15 pm, the **Evening Tutorial Program** is in **Rooms 109, 110, 111**

EDUCATIONAL PROGRAM

	SATURDAY	SUNDAY
8:15 am	Opening Remarks	
8:30 am	Basic Physics	New Techniques
		9 am – 7:30 pm
		Exhibits Open
10 am	Break	Break
10:30 am	CNS (Brain)	Body
	Noon – 5	
	Exhibits Open	
Noon	Lunch	Lunch
1 pm	CNS (Spine, Head & Neck)	Spectroscopy
3 pm	Break	Break
3:30 pm	Body	Socioeconomics
		5:15 – 7:15 pm
		Evening Tutorials

SCIENTIFIC PROGRAM

	MONDAY	TUESDAY	WEDNESDAY
	Opening Remarks		
	(Mam-Symp) Symposium: Neuroradiology	(Tam-Symp) Symposium: Motion Artifacts	(Wam-Symp) Symposium Spectroscopy
	9 am – 7:30 pm	9 am – 5 pm	9 am – Noon
	Exhibits	Exhibits	Exhibits
	Break	Break	Break
10:20 am	Proffered Papers	Proffered Papers	Proffered Papers
	(Mam-A) Neuro-Clinical	(Tam-A) Body-Artifacts	(Wam-A) Spectroscopy
	(Mam-B) Cardiovascular	(Tam-B) Chest-Vascular	(Wam-B) Body - Contrast Agents
	(Mam-C) Musculoskeletal	(Tam-C) Neuro-Techniques	(Wam-C) Cardiovascular
	(Mam-D) Spectroscopy - Multinuclear	(Tam-D) Relaxometry	(Wam-D) Technical Developments
	(Mam-E) Works-in-Prog.	(Tam-E) Works-in-Prog.	(Wam-E) Works-in-Prog.
Noon	Lunch	Lunch	Lunch
	Poster Session	Poster Session	
	(Mpm-Symp) Symposium: Vascular Imaging & Flow Imaging	(Tpm-Symp) Symposium: Contrast Agents	(Wpm-Symp) Symposium: Body Imaging
	Break	Break	Break
3:20 pm	Proffered Papers	Proffered Papers	Proffered Papers
	(Mpm-A) Vascular Flow	(Tpm-A) Contrast Agents	(Wpm-A) Abdomen-Pelvis
	(Mpm-B) Neuro-Clinical	(Tpm-B) Technical Developments	(Wpm-B) Musculoskeletal
	(Mpm-C) Technical Developments	(Tpm-C) Surface Coils	(Wpm-C) Head & Neck
	(Mpm-D) Relaxometry	(Tpm-D) Neuro-Clinical	(Wpm-D) Safety, Image Processing
	5:15 – 7:15 pm	Time TBA	5 pm – ADJOURN 1987
	Evening Tutorials	Dinner – Mexican Fiesta	SMRI MEETING

PROGRAM: FIFTH ANNUAL SMRI MEETING

FRIDAY, 27 FEBRUARY

REGISTRATION FOR EDUCATIONAL PROGRAM PARTICIPANTS
5 – 9 pm
Location to be posted at Hilton Palacio del Rio Hotel

SATURDAY, 28 FEBRUARY
RIVER ROOM
8:15 am – 5:30 pm

EDUCATIONAL PROGRAM

8:15 am	OPENING REMARKS	W. Bradley
8:30 – 10 am	BASICS	
	Physics	G. Fullerton
	Spatial Characteristics	P. Sprawls
	Contrast Mechanisms	F. Wehrli
10 – 10:30 am	MORNING BREAK – River Room Foyer	
10:30 am – Noon	CNS (BRAIN)	
	Adult/Neoplastic	M. Brant-Zawadski
	Adult/Nonneoplastic	W. Bradley
	Brain Iron and Spectroscopy	B. Drayer
Noon – 1 pm	LUNCH	
Noon – 5 pm	MANUFACTURERS' EXHIBITS OPEN – MISSION ROOM	
1 – 3 pm	CNS (SPINE, HEAD & NECK)	
	Pediatric CNS	B. Flannigan
	Adult/Intrinsic Cord	K. Maravilla
	Adult/Disc Disease	M. Modic
	Head and Neck	R. Lufkin
3 – 3:30 pm	AFTERNOON BREAK – EXHIBIT HALL – MISSION ROOM	
3:30 – 5:30 pm	BODY I	
	Blood Flow	R. Peshock
	Musculoskeletal/TMJ/Knee	S. Harms
	STIR	F. Smith
	Site Planning	M. Bronskill

SUNDAY, 1 MARCH
RIVER ROOM
8:30 am – 5:30 pm

8:30 – 10 am	NEW TECHNIQUES	
	Fast Scanning	E. Hendrick
	Contrast Agents (Principles)	V. Runge
	Contrast Agents (Clinical)	G. Wolf
	Chemical Shift Imaging	L. Axel
9 am – 7:30 pm	**MANUFACTURERS' EXHIBITS – MISSION ROOM**	
10 – 10:30 am	MORNING BREAK – EXHIBIT HALL – MISSION ROOM	
10:30 am – Noon	BODY II	
	Cardiac	C. Higgins
	Abdomen	D. Stark
	Pelvis	J. Weinreb
	Pediatric Body	R. Dietrich
Noon – 1 pm	LUNCH	
1 – 3 pm	SPECTROSCOPY	
	Spectroscopy/Basics	J. Gore
	Localization Techniques	P. Bottomley
	Cardiac Spectroscopy	R. Nunnally
	Spectroscopy, Clinical Application	M. Weiner
3 – 3:30 pm	AFTERNOON BREAK – EXHIBIT HALL – MISSION ROOM	
3:30 – 5 pm	SOCIOECONOMICS	
	Economic Issues	L. Muroff
	Medicolegal Issues	D. Holmquest
	Technology Diffusion	B. Hillman
	Practicing MRI in the Changing Economic Environment	S. Young
5 – 5:15 pm	CLOSING REMARKS	W. Bradley

SUNDAY EVENING PROGRAM FOLLOWS

REGISTRATION FOR EDUCATIONAL PROGRAM PARTICIPANTS
5 – 9 pm
Location to be posted at the Hilton Palacio del Rio Hotel

Rooms 109, 110, 111
5:15 – 7:15 pm

EVENING TUTORIAL PROGRAM

Clinical Case Review Sessions

These will offer fundamental instruction on MR image interpretation, analysis of interesting clinical cases and image artifacts. Jeffrey Weinreb has invited a distinguished panel of MRI Physicians and Physicists to discuss their own special cases. Attendees at the SMRI are encouraged to participate in these Case Review Sessions and are requested to bring their own unusual, interesting, or difficult clinical cases and artifacts. These sessions will be organized into small groups, and it will be an excellent opportunity for participants to see how the experts approach clinical MRI cases, to ask questions, and to work out problems.

List of Participants

Ernesto Blanco
Michael Bronskill
R. Nick Bryan
Rosalind Dietrich
Ronald Peshock
Jonathan Rubin
Val Runge
James Stewart
Jeffrey Weinreb
Michael Wood

Physics Tutorial

Chandra Chatterjee has organized a review of basic magnetic resonance physics. The behavior of tissue magnetization, imaging techniques, MR software and hardware will be discussed in an interactive format designed for the beginner.

– NOTES –

MONDAY, 2 MARCH

FIFTH ANNUAL MEETING – SOCIETY FOR MAGNETIC RESONANCE IMAGING

RIVER ROOM
8:15 am

OPENING REMARKS — G. D. Fullerton

SCIENTIFIC PROGRAM: MAGNETIC RESONANCE IMAGING

RIVER ROOM
8:30 – 10 am

(Mam-Symp) SYMPOSIUM: NEURORADIOLOGY — CLINICAL REVIEW

Presiding: R. N. Bryan

Techniques	R. N. Bryan
White Matter Disease	D. Chakeres
Neoplasms	M. Gado
Ischemia	A. N. Hasso
Spine	K. R. Maravilla

9 am – 7:30 pm — MANUFACTURERS' EXHIBITS – MISSION ROOM

10 – 10:20 am — MORNING BREAK – EXHIBIT HALL – MISSION ROOM

MONDAY MORNING PROGRAM, continued

MONDAY, 2 MARCH, continued
RIVER ROOM
10:20 am

(Mam-A) PROFFERED PAPER SESSION: NEURO-CLINICAL

Presiding: A. E. James & R. B. Lufkin

Parallel sessions A - D will consist of presentations twelve (12) minutes in length, the first beginning promptly at 10:20 am. The abstracts to be presented in each session have been numbered to correspond with the session designations.

ROOM C-107
10:20 am

(Mam-B) PROFFERED PAPER SESSION: CARDIOVASCULAR

Presiding: R. M. Peshock & M. L. Winkler

ROOM C-101
10:20 am

(Mam-C) PROFFERED PAPER SESSION: MUSCULOSKELETAL

Presiding: S. Harms & F. Shellock

ROOM C-102
10:20 am

(Mam-D) PROFFERED PAPER SESSION: SPECTROSCOPY - MULTINUCLEAR

Presiding: C. L. Partain & R. Nunnally

ROOM C-108
10:20 am

(Mam-E) WORKS-IN-PROGRESS I

The Program for the Works-in-Progress sessions will be available upon your arrival in San Antonio.

Noon - 1 pm LUNCH

MISSION ROOM
1 - 1:30 pm

(P) POSTER SESSION

Abstracts numbered P-1 through P-18 will be available for viewing during ALL Exhibit Hours. Authors are requested to be present at their poster from 1 - 1:30 pm Monday & Tuesday, March 2 & 3.

MONDAY AFTERNOON PROFFERED PAPER SESSIONS FOLLOW

MONDAY, 2 MARCH, continued
RIVER ROOM
1:30 – 3 pm

(Mpm–Symp) SYMPOSIUM: VASCULAR IMAGING AND FLOW MEASUREMENT

Presiding: W. G. Bradley

Overview	W. G. Bradley
Angiography	D. Nishimura
Cardiac Applications	J. Utz
Cerebrospinal Fluid	J. B. Rubin
Quantitation	P. M. Pattany

3 – 3:20 pm AFTERNOON BREAK – EXHIBIT HALL – MISSION ROOM

RIVER ROOM
3:20 pm

(Mpm–A) PROFFERED PAPER SESSION: VASCULAR FLOW

Presiding: I. R. Young & J. Frahm

Parallel sessions A – D will consist of presentations twelve (12) minutes in length, the first beginning promptly at 3:20 pm. The abstracts to be presented in each session have been numbered to correspond with the session designations.

ROOM C–107
3:20 pm

(Mpm–B) PROFFERED PAPER SESSION: NEURO–CLINICAL

Presiding: V. Runge & D. Spigos

ROOM C–101
3:20 pm

(Mpm–C) PROFFERED PAPER SESSION: TECHNICAL DEVELOPMENTS

Presiding: P. Sprawls & S. Wall

ROOM C–102
3:20 pm

(Mpm–D) PROFFERED PAPER SESSION: RELAXOMETRY

Presiding: S. McCarthy & N. Matwiyoff

MONDAY EVENING PROGRAM FOLLOWS

MONDAY, 2 MARCH, continued
Rooms 109, 110, 111
5:15 – 7:15 pm

EVENING TUTORIAL PROGRAM

Clinical Case Review Sessions

These will offer fundamental instruction on MR image interpretation, analysis of interesting clinical cases and image artifacts. Jeffrey Weinreb has invited a distinguished panel of MRI Physicians and Physicists to discuss their own special cases. Attendees at the SMRI are encouraged to participate in these Case Review Sessions and are requested to bring their own unusual, interesting, or difficult clinical cases and artifacts. These sessions will be organized into small groups, and it will be an excellent opportunity for participants to see how the experts approach clinical MRI cases, to ask questions, and to work out problems.

List of Participants

Ernesto Blanco
Michael Bronskill
R. Nick Bryan
Rosalind Dietrich
Ronald Peshock
Jonathan Rubin
Val Runge
James Stewart
Jeffrey Weinreb
Michael Wood

Physics Tutorial

Chandra Chatterjee has organized a review of basic magnetic resonance physics. The behavior of tissue magnetization, imaging techniques, MR software and hardware will be discussed in an interactive format designed for the beginner.

-NOTES-

(Tam–Symp) SYMPOSIUM: MOTION ARTIFACTS

Presiding: E. M. Haacke

Characteristics of Motion Artifacts	M. L. Wood
Methods of Suppression of Motion Artifacts	G. H. Glover
Clinical Examples	I. R. Young
Summary & Future Directions	E. M. Haacke

9 am – 5 pm MANUFACTURERS' EXHIBITS – MISSION ROOM

10 – 10:20 am MORNING BREAK – EXHIBIT HALL – MISSION ROOM

RIVER ROOM
10:20 am

(Tam–A) PROFFERED PAPER SESSION: BODY – ARTIFACTS

Presiding: P. Joseph & S. Thomas

Parallel sessions A – D will consist of presentations twelve (12) minutes in length, the first beginning promptly at 10:20 am. The abstracts to be presented in each session have been numbered to correspond with the session designations.

ROOM C–107
10:20 am

(Tam–B) PROFFERED PAPER SESSION: CHEST – VASCULAR

Presiding: R. Pettigrew & M. Bronskill

ROOM C–101
10:20 am

(Tam–C) PROFFERED PAPER SESSION: NEURO–TECHNIQUES

Presiding: K. Davis & H. Stein

ROOM C–102
10:20 am

(Tam–D) PROFFERED PAPER SESSION: RELAXOMETRY

Presiding: G. Fullerton & R. Dietrich

ROOM C–108
10:20 am

(Tam–E) WORKS–IN–PROGRESS II

The Program for the Works–in–Progress sessions will be available upon your arrival in San Antonio.

TUESDAY AFTERNOON PROGRAM FOLLOWS

TUESDAY, 3 MARCH, continued

Noon – 1 pm LUNCH

MISSION ROOM
1 – 1:30 pm

(P) POSTER SESSION

Abstracts numbered P-1 through P-18 will be available for viewing during ALL Exhibit Hours. Authors are requested to be present at their poster from 1 – 1:30 pm Monday & Tuesday, March 2 & 3.

RIVER ROOM
1:30 – 3 pm

(Tpm-Symp) SYMPOSIUM: CONTRAST AGENTS

Presiding: G. L. Wolf

Physics of MR Image Contrast Enhancement	R. E. Hendrick
Status of Paramagnetic Contrast Agents	V. M. Runge
MR Contrast Agents as Indicators for Tissue Perfusion and Function	G. L. Wolf

3 – 3:20 pm AFTERNOON BREAK – EXHIBIT HALL – MISSION ROOM

RIVER ROOM
3:20 pm

(Tpm-A) PROFFERED PAPER SESSION: CONTRAST AGENTS

Presiding: B. Englestad & H. P. Niendorf

Parallel sessions A – D will consist of presentations twelve (12) minutes in length, the first beginning promptly at 3:20 pm. The abstracts to be presented in each session have been numbered to correspond with the session designations.

ROOM C-107
3:20 pm

(Tpm-B) PROFFERED PAPER SESSION: TECHNICAL DEVELOPMENTS

Presiding: R. E. Hendrick & J. Heiken

ROOM C-101
3:20 pm

(Tpm-C) PROFFERED PAPER SESSION: SURFACE COILS

Presiding: B. Kneeland & S. Saini

ROOM C-102
3:20 pm

(Tpm-D) PROFFERED PAPER SESSION: NEURO-CLINICAL

Presiding: B. Flannigan & G. Sze

DINNER

MEXICAN FIESTA-STYLE PARTY

Exact Time & Place To Be Posted

In keeping with San Antonio's festive atmosphere, this party including dinner, will be held on Tuesday evening in the Convention Center. This is included in the Registration Fee (except for one-day registrants) and additional guests are welcome ($20.00 each).

Several Mexican culinary delights will be provided:

-- hand-patted tortillas
-- ceviche de Mexico
-- chili con queso
-- fajitas
-- and more...

Also:

-- Beer, Margaritas and milder fare

Entertainment:

-- Trio of mariachis

RIVER ROOM
8:30 – 10 am

(Wam–Symp) SYMPOSIUM: SPECTROSCOPY

Presiding: J. C. Gore

Overview	J. C. Gore
Techniques for Clinical In Vivo Spectroscopy	P. Bottomley
In Vivo NMR Spectroscopy in Humans: Brain and Tumors	R. Nunnally
Applications of NMR Spectroscopy for Clinical Diagnosis	M. Weiner

9 am – Noon MANUFACTURERS' EXHIBITS – MISSION ROOM

10 – 10:20 am MORNING BREAK – EXHIBIT HALL – MISSION ROOM

RIVER ROOM
10:20 am

(Wam–A) PROFFERED PAPER SESSION: SPECTROSCOPY

Presiding: M. Barany & F. Wehrli

Parallel sessions A – D will consist of presentations twelve (12) minutes in length, the first beginning promptly at 10:20 am. The abstracts to be presented in each session have been numbered to correspond with the session designations.

ROOM C–107
10:20 am

(Wam–B) PROFFERED PAPER SESSION: BODY – CONTRAST AGENTS

Presiding: A. Lupetin & P. Hahn

ROOM C–101
10:20 am

(Wam–C) PROFFERED PAPER SESSION: CARDIOVASCULAR

Presiding: D. Hahn & L. Axel

ROOM C–102
10:20 am

(Wam–D) PROFFERED PAPER SESSION: TECHNICAL DEVELOPMENTS

Presiding: K. Ohtomo & M. L. Wood

ROOM C–108
10:20 am

(Wam–E) WORKS–IN–PROGRESS III

The Program for the Works–in–Progress sessions will be available upon your arrival in San Antonio.

WEDNESDAY AFTERNOON PROGRAM FOLLOWS

WEDNESDAY, 4 MARCH, continued

Noon – 1 pm LUNCH

RIVER ROOM
1:30 – 3 pm

(Wpm–Symp) SYMPOSIUM: BODY IMAGING

Presiding: C. B. Higgins & J. T. Ferrucci, Jr.

Cardiovascular	C. B. Higgins
Abdomen and Pelvis	J. T. Ferrucci, Jr.
Musculoskeletal	J. Beltran

3 – 3:20 pm AFTERNOON BREAK – RIVER ROOM FOYER

RIVER ROOM
3:20 pm

(Wpm–A) PROFFERED PAPER SESSION: ABDOMEN–PELVIS

Presiding: J. Weinreb & D. Kushner

Parallel sessions A – D will consist of presentations twelve (12) minutes in length, the first beginning promptly at 3:20 pm. The abstracts to be presented in each session have been numbered to correspond with the session designations.

ROOM C–107
3:20 pm

(Wpm–B) PROFFERED PAPER SESSION: MUSCULOSKELETAL

Presiding: E. Kanal & D. Kopp

ROOM C–101
3:20 pm

(Wpm–C) PROFFERED PAPER SESSION: HEAD & NECK

Presiding: F. W. Smith & J. Clanton

ROOM C–102
3:20 pm

(Wpm–D) PROFFERED PAPER SESSION: SAFETY, IMAGE PROCESSING

Presiding: R. Ehman & R. Price

THIS CONCLUDES THE 5TH ANNUAL MEETING OF THE SOCIETY FOR MAGNETIC RESONANCE IMAGING

(P) POSTER ABSTRACTS

(P) POSTER SESSION

AVAILABLE FOR VIEWING DURING ALL EXHIBIT HOURS

AUTHORS PRESENT 1 - 1:30 pm

MONDAY AND TUESDAY, MARCH 2 & 3

MISSION ROOM

P-1
NMR RELAXATION TIMES OF MUSCLES REFLECT MODIFICATIONS IN EXPRESSION OF DYSTROPHIC GENE

L. K. Misra, T. F. Egan, D. R. Courtney, Chen Lin, D. W. Bearden, C. F. Hazlewood

Dept. of Internal Medicine (Hematology/Oncology Div.), University of Texas Health Science Center at Houston, 6431 Fannin, Houston, TX 77030
Dept. of Physiology, Baylor College of Medicine, Houston, Texas

Muscular dystrophy is transmitted by a single autosomal gene. The expression of this gene, however, is affected by other genes, and, therefore, conventional genetic selection techniques have been successfully used to alter the pathologic events in animal models of the disease. Our objective was to study the effects of selection-induced changes in the expression of dystrophic gene on the proton NMR relaxation times of muscles.

Four week-old New Hampshire chicken of lines 412, 413, and 307 were used in this study. All these three chicken lines were developed from the F_2 generation of a cross between the original dystrophic line 304 and normal New Hampshire chicken. Because of common origin, line 412 chickens provide genetically-related normal controls to the dystrophic chicken of lines 413 and 307. In development of line 413, intense selection pressure for persistant muscle fiber hypertrophy and low fat deposition was applied in the breeding program. In contrast, line 307 chickens were selected for rapid, progressive muscle fiber atrophy and high lipid content. The muscle function of all chicks was evaluated by the exhaustion score (E.S.) method. The proton T_1 and T_2 relaxation times of the most severely affected pectoralis major muscles were measured by the inversion recovery and Carr-Purcell-Meiboom-Gill methods, respectively, on Bruker SXP NMR spectrometer at 30 MHz.

The E.S. of normal chicks (line 412) was 22±2. Dystrophic chicks of both lines (413 and 307) had an E.S. of 0 indicating a marked impairement in their muscle function. This muscle damage was reflected in a significant increase in the NMR relaxation times. Multiexponential behavior was present in both relaxation times, but results of the longer relaxing fractions of T_1 and T_2 will be summarized. The T_1 values for normal muscles were 784±56 ms which were significantly shorter than those of dystrophic muscles. The changes in the T_1 values were sensitive enough to distinguish the atrophic and hypertrophic lesions. The atrophic muscles of line 307 chicks had significantly longer T_1 values (1170±102 ms) than the hypertrophic muscles of chicks from line 413 (1005±18 ms). Although the T_2 values of dystrophic muscles were longer than the normal muscles (99±25 ms), there was no significant difference between the hypertrophic (219±20 ms) and atrophic (228±20 ms) muscles. This study suggests that changes in the NMR relaxation times may be useful in detecting different pathologic lesions which result due to modification in the expression of dystrophic genes in related genotypes.

(Supported by Department of Health and Human Services Grant R01 AM38741-01).

P-2
CORRELATION OF BIOCHEMICAL AND HISTOLOGICAL ANALYSES OF MAGNETIC RESONANCE IMAGING OF NORMAL AND DISEASED

(infarcts, tumors) HUMAN BRAIN FIXED IN FORMALIN.

WIESLAWA M. ANDRZEJEWSKA ,M.D., DONALD CHAKERES,M.D., ALLAN YATES,M.D.,Ph.D., CAROL BOESEL, M.D., JEAN BLANDEAU MS

Department of Geriatrics/Neuropathology; Department of Radiology (MRI); Department of Neuropathology

College of Medicine, The Ohio State University, Columbus, Ohio.

The histologic and biochemical basis for the signal changes seen in pathology with magnetic resonance imaging (MRI) are still unclear. The goal of our study was to determine the chemical and morphological changes with direct correlation to MRI. The material studied consisted of postmortem brains. This technique allows for exact correlation of MRI and quantitative analysis of human brain tissue. We have already completed studies which have shown that chemical composition of normal tissues does not change following our fixation technique so that the chemical data measured is similar to in vivo data.

We examined six normal and seven abnormal brains with infarctions. The human brains were removed at autopsy andfixed in 10% buffered formalin. After fixation for one week the brain was washed in buffered water with the same composition except without formalin. Buffered water was used to rinse the brain and prevent drying during sectioning. The buffered solution had osmolality of 308 mosm/kg corresponding to a normal osmolality of cerebro spinal fluid (CSF) of 288 mosm/kg. Immediately after washing MRI was completed using a General Electric Signal 1.5 Tesla unit. Spin echo TR 2500 and TE 20.75 ms , and partial saturation TR 600 TE 20 ms images were made in the axial plane. The signal for pathologic regions of the brains were compared to normal areas and recorded as to wether the signal was higher or lower for correlation of the chemical and histologic data. The following day gross sections of the brain were made in a similar plane to the MRI. The brain slices were keep in buffered water and sample were taken from various regions of interest for chemical and histologic analysis. The chemical studies included analysis of % weght of water, nonlipid residue (NLR), total lipid extract (TLE), cholesterol,phospholipids, and galactolipids, and the ratio of total lipids and the nonlipid residue (TLE/NLR). Gross and histologic grading of the pathology based degree, chronicity, location,, demyelination and type of pathology was correlated to the MRI signal of the identical regions.

The mean values for the chemical data were % water white matter 71.6, gray matter 81.9, TLE white matter 15.6, gray matter 5.9, NLR white matter 8.7, gray matter 9.5, TLE/NLR white matter 1.7, gray matter .62, % of TLE for cholesterol white matter 27.5, gray matter 22.0, phospholipids white matter 45.9, gray matter 69.5, galactolipids white matter 26.4, gray matter 7.3. The average mean water % for white matter infarcts for the center, edge, and adjacent regions were respectively 89.4, 86.1, and 81.5. The average TLE/NLR ratios for the same white matter regions within the infarcts were .9, 1.05and1.13.The average water content of the gray matter infarcts was 82.6%, TLE/NLR 0.9%, NLR 5%. , TLE 4.5%. The spin echo TR 2500 and TE 75 ms images had similar gray scale contrast for the normal tissues as seen with in vivo imaging. The shorter TR studies were similar in image contrast to the longer TR studies which is different than seen in vivo. The areas of white matter pathology were all seen a high signal regions on all pulse sequence techniques. The known regions of gray matter infarcts were not as alearly seen.

We conclude that there is a high correlation between the chemical composition, histology and the MRI signal of brain tissue fixed in this fashion. The changes in the chemistri reflect histologic abnormalities which are in turn displayed by MRI. These results give insights into in vivo imaging since the chemistry data and the long TR spin echo images are similar to in vivo studies. The results of our study suggest that in clinical setting the knowledge of better understanding of cerebrovascular disorders is essential.

P-3
MAGNETIC RESONANCE IMAGING OF CEREBRAL VASCULITIS

David J. Rippe, M.D., Mary Edwards, M.D.

Department of Radiology, Indiana University School of Medicine, Indianapolis, IN 46223

MRI continues to demonstrate efficacy in the evaluation of cerebral vascular disease. Five patients with cerebral vasculitis were evaluated using both low (0.15 tesla) and high (1.5 tesla) field MR units. The results were correlated with conventional neuroradiologic studies including computed tomography and angiography. Findings on MRI included diffuse cortical atrophy, infarction, attenuation of cerebral vasculature, and evidence of extensive collateralization (moyamoya). MRI was found to be more sensitive in demonstrating the ischemic manifestations of cerebral vasculitis than CT. We conclude that MRI offers an effective noninvasive method for evaluating cerebral vasculitis and its consequences.

P-4
MR EVALUATION OF FOCAL AND DIFFUSE THYROID DISORDERS

Warren B. Gefter, M.D., Charles E. Spritzer, M.D., Brian Eisenberg, M.D., Herbert Y. Kressel, M.D., Leon Axel, M.D., Ph.D., Michael Velchik, M.D., Abass Alavi, M.D., John Schenck, M.D., Ph.D.

Departments of Radiology and Pathology, Hospital of the University of Pennsylvania, Philadelphia, PA, and the General Electric Corp. Research & Development Center, Schenectady, NY

The increased signal-to-noise which can be obtained with high-field MR systems in combination with local (surface) receiver coils can support images with submillimeter pixel sizes. The thyroid gland, being a midline superficial structure, is well-suited to evaluation by MR using local coils. Such a technique combines high spatial resolution with the superb soft tissue contrast of MR. This exhibit presents results of our initial study of the normal and abnormal thyroid in more than 50 patients using high-field surface coil MR imaging.

Fifty-five patients were examined using a 1.5 Tesla system. Diagnoses included 19 normals, 10 benign nodules, 3 carcinomas, 12 multinodular glands, 3 Hashimoto's thyroiditis, 2 Graves' disease, 1 thyroglossal duct cyst, and 3 patients status post subtotal thyroidectomy. Two studies were nondiagnostic due to motion. A 16 x 9 cm mask-shaped local receiver coil was used. Multislice axial (with selected coronal and sagittal) images of 5 mm slice thickness and 0-2.5 mm gap were acquired with a 256 x 128 matrix. Using a 16 cm field-of-view, corresponding pixel sizes were .6 x 1.25 mm. Spin echo pulse sequences with short TR/TE (400/600 msec/20-25 msec) and long TR/TE (2000-2500/35-80 msec) were employed, using 2-4 excitations. I^{123} radionuclide scans were obtained in 30 cases.

The normal thyroid gland is nearly homogeneous with intensity similar or slightly greater than muscle on the short TR/TE images. The gland becomes relatively brighter with long TR/TE. Surrounding structures including trachea, carotid and jugular vessels, cartilages, and neck musculature are well-depicted.

Follicular adenomas are round, well-circumscribed heterogeneous nodules which increase significantly in intensity on the long TR/TE images. Two of 3 showed central high signal areas due to hemorrhage, one having a peripheral low signal hemosiderin ring. Colloid and hemorrhagic cysts are sharply marginated, homogeneous lesions with high signal on both short and long TR/TE sequences. A functioning nodule on radionuclide scan was virtually isointense with normal gland on both short and long TR/TE images. Two of 3 carcinomas appeared as nonfocal lesions (irregular or nodular areas) having relatively higher signal with long TR/TE. Associated cervical lymphadenopathy in these cases was clearly depicted by increased intensity on the long TR/TE images. A follicular adenoma containing microscopic papillary carcinoma in the periphery appeared similar to other follicular adenomas.

Multinodular goiters are enlarged glands with multiple high signal nodular areas best identified on long TR/TE scans. Multiple very high signal foci probably representing cystic areas of hemorrhage and/or colloid may be present on the short TR/TE images. Tracheal displacement and substernal extension are clearly depicted. "Cold" regions on isotope scans appear as high-signal areas using long TR/TE. Three "solitary" nodules on radionuclide scans were shown to be multinodular glands by MR.

Hashimoto's thyroiditis appeared as enlarged glands with diffuse inhomogeneous increased signal (greater than fat) on the long TR/TE sequence. Two of 3 showed irregular areas of decreased signal with short and long TR/TE corresponding to regions of fibrosis. Graves' disease showed moderately enlarged, lobulated glands with diffuse increase in signal with both short and long TR/TE. There was only minimal heterogeneity without discrete nodules.

A thyroglossal duct cyst appeared as an anterior midline lesion showing high signal using both short and long TR/TE, possibly due to proteinaceous or hemorrhagic fluid.

The morphology of residual thyroid tissue following subtotal thyroidectomy is clearly depicted.

High-field surface coil MR imaging appears to be a sensitive method for identifying focal, multinodular, and diffuse disorders of the thyroid. This modality permits excellent depiction of the internal architecture of the gland, as well as surrounding structures in the neck and superior mediastinum. MR can accurately identify gross morphologic features of nodules, such as cystic degeneration and hemorrhage. While 2 of 3 carcinomas appeared as poorly-marginated lesions, it seems unlikely that MR will differentiate a focal carcinoma from a benign nodule. Lymphadenopathy, however, is readily identified and may indicate malignancy. MR appears to show distinctive patterns in Hashimoto's thyroiditis, multinodular goiter, and Graves' disease. Further study is required to document this specificity.

P-5
NMR SYSTEM SOFTWARE FOR THE 80'S AND BEYOND

Bradley G. Culter, Robert C. Blencowe, Jr., Debra R. Pheris, Louis Van Houten, Ray L. Nunnally, Ph.D.

Biomedical Magnetic Resonance Spectroscopy Laboratory, Department of Radiology,
University of Texas Health Science Center at Dallas, Dallas, Texas

The rapidly advancing field of NMR imaging and spectroscopy demands a flexible system capable of quickly implementing new techniques such as complex pulse sequences, quadrature coils and more sophisticated data analysis. These demands are being met in this laboratory through the design and implementation of a 1.8 T, meter-bore NMR spectroscopy and imaging system named "Metaview", for metabolic viewing. Specification of Metaview was begun in 1983 due to the unavailablilty of a commercial system satisfying the needs of this research laboratory. Two major requirements were identified: 1) implementation of multi-nuclear spectroscopy and proton imaging on one system, and 2) incorporation of flexibility in pulse sequence design and spectrometer control and hardware components. This provided the opportunity of taking a novel approach to the software design. The final software architecture brings together in one system the often opposing features of real flexibility and performance.

Metaview is organized as a distributed multi-process, multi-user system executable on Masscomp RTU (Real Time Unit) and/or VAX/VMS processors. The processes function in client-server transactions through a mechanism known as Remote Procedure Calls. The System Interface Library, developed as part of this project, permits future portability of the entire system to completely different computers such as the Data General MV series. This architecture provides many direct user benefits, one of which is its intrinsic ability to reformat and transfer data between computers for the purposes of comparison and archiving. Another is the increased computational performance available through combining many Metaview hosts in a network. Many indirect benefits also exist because extensions to a software system organized in this way are safer and more reliable.

The system directly implements object abstraction. Objects can range from the primitive to the complex. For example, a single data point acquired in an FID or echo may be an object as well as an entire NMR study including both the time-domain and processed data sets, the pulse sequence definition, physiologic monitoring data and patient information. Therefore, the user interacts with high-level, user-defined objects whose attributes and internal representations are maintained by the system unlike other systems having objects with rigidly fixed attributes. Metaview incoporates a hierarchical database that supports this more general view of what an object is and allows the user to create objects not previously defined. Hierarchical databases have proven useful in research applications because they facilitate new data analysis through experimentation and discovery.

The Command Language Interface (CLI) provides a powerful set of commands and a macro facility. In many systems the operator and the physician deal with different user interfaces; however, Metaview uses a single CLI for all users. Full on-line help for all commands is available. The powerful macro facility of the CLI is used to define 'MACROS' which are sequences of commands that are frequently required. The CLI also provides the 'ALIAS' command, used to define synonyms. Macros and Aliases allow the emulation of other spectrometer command sets such as those of the commercial systems also used in this laboratory so users are able to quickly learn the new system. Typically, the operator, physician, and researcher use different subsets of the CLI commands and therefore use different pre-defined macros. The commands available through the CLI are divided in groups that correspond directly to each of the server processes. They are: instrument control, data analysis and processing, graphical and image display, and database manipulation.

Metaview is a flexible system capable of being used to quickly develop, test, and implement new NMR techniques. Its capacity for utilizing new and different hardware components with virtually no change in software supports the continual advancement of NMR research.

P-6
MAGNETIC RESONANCE IMAGING OF ACUTE SPINAL CORD CONTUSION: DURATION OF COMPRESSION VERSUS EXTENT OF HEMORRHAGE AND EDEMA

R. Asato, D.B. Hackney, M.J. Carvlin, J.T. McGrath, P.M. Joseph, R.I. Grossman

Department of Radiology, Hospital of the University of Pennsylvania, Department of Radiology, Kyoto University Hospital, and Department of Pathology, School of Veterinary Medicine, University of Pennsylvania

Current experimental models of acute cord compression do not permit determination of the extent or severity of pathologic change in vivo. Hemorrhage, edema, and necrosis are the characteristic histologic findings occurring after cord contusion. We have developed a model in which in vivo magnetic resonance (MR) imaging demonstrates acute hemorrhage and edema with high accuracy. In this report we describe the application of this model to correlate the duration of cord compression with the severity of the resulting pathologic changes

Materials and Methods

Ten adult male Sprague-Dawley rats were anesthetized with pentobarbital and maintained under general anesthesia throughout the study. Laminectomies were performed at T1 and the spinal cord traumatized using a modification of the aneurysm clip compression technique (1). In this study a Heifetz clip (closing force 50 gr) was applied to the spinal cord extradurally for 2 minutes or 5 minutes. The clip was removed and the wound irrigated and closed. MR imaging was performed 2.5 to 3.5 hr after removing the clip to determine the severity of lesions. T2-weighted(TR 2000, TE 100) and T1-weighted(TR 400, TE 15) spin echo images were obtained on a prototype 1.4 Tesla animal system. At the completion of imaging the animals were euthanized. The cords were harvested, inspected, fixed and hematoxylin and eosin stained histologic sections were examined

Results

We have previously documented the accuracy of MR in identifying hemorrhage and edema in the spinal cord after acute trauma (2). This study confirmed these findings and demonstrated a focal band of hemorrhage at the clip application site in every animal. This was displayed as a very low signal intensity region on the T2-weighted images with signal intensity similar to or slightly greater than the intact cord on the T1-weighted images. The 5 minute compression cords demonstrated prominent edema extending proximal to the compression site. The 2 minute compression lesions demonstrated little or no detectable edema about the hemorrhagic lesion.

Discussion

In this study we have confirmed that the severity of trauma induced and the degree of edema displayed by MR imaging are related to the duration of compression at a fixed compressive force. The value of MR of spinal cord contusion lies in the ability to document the severity of pathologic response to trauma in a completely non-invasive manner. MR performed shortly after trauma may be used to confirm that the desired degree of hemorrhage and edema have been produced before therapeutic interventions are attempted. Therefore it will be possible to ensure that experimental and control groups have received comparably severe injuries. Our findings also indicate that the additional 3 minutes of compression to which the 5 minute cords were subjected was highly significant in determining the intensity of the pathologic response to trauma. Similar conclusions have been derived using clinical rather than pathologic criteria of severity of cord damage (1,3).

References

1. Rivlin AS, Tator CH, Surg Neurol 10: 39, 1978.
2. Hackney DB, Asato R, Radiology 161: 387, 1986.
3. Dolan EJ, Tator CH, Endrenvi L, J Neurosurg 53: 749, 1980.

P-7

STIMULATED ECHO MR IMAGING OF BRAIN PATHOLOGY

James C. Ehrhardt, Ph.D.[1], Hisao Tonami, M.D.[1], William T.C. Yuh, M.D.[1], Charles J. Armstrong[1], William Sattin,[2]
[1]Department of Radiology, University of Iowa Hospitals and Clinics, Iowa City, Iowa 52242
[2]Picker International, Cleveland, Ohio 44106

The practicality of using stimulated echoes for MR imaging has recently been demonstrated.[1,2] The Stimulated Echo Progressive (STEP) method uses three 90 degree pulses to generate a stimulated echo. The signal intensity for a single stimulated echo is given by

$$SI=(1/2)H[\exp(-TE/T2)][1-\exp(-TR/T1)][\exp(-TS/T1)]$$

where TE is twice the first interpulse interval and TS is equal to the second interpulse interval. Thus, a STEP image will have the usual positive T2 contrast dependent on TE and negative T1 contrast dependent on TR as seen in spin echo images. However, the final term in the equation above produces a positive T1 contrast dependent on TS. With a proper choice of parameters, both T1 and T2 effects may combine to produce an image with enhanced positive contrast. The formation of a stimulated echo involves an

unavoidable loss of signal as indicated by the factor of 1/2 above.

A multi-slice STEP pulse sequence (10mm slices) was implemented on a Picker International 0.5T MR imaging system. STEP images (using two excitations) were compared to standard 2DFT images (using one excitation) in 20 patients with various pathological conditions and positive findings on the standard images. All acquisitions used a 256x512 matrix. STEP images were acquired with a variety of combinations of TE (40 and 60ms), TR (1250 and 2000ms) and TS (150, 225, and 350ms) values. The goals of this project were to evaluate the contrast and noise characteristics of STEP images in a diversity of brain pathology and to determine an appropriate range of parameters for further clinical use.

When the shortest values of TE, TR, and TS were used, the opposing T1 effects produced an image with dark CSF and little contrast between grey matter (GM) and white matter (WM). When the longest values of the scan parameters were used, the image had excellent GM-WM contrast and very bright CSF. All images were noisier than the comparison spin echo images. Care must be exercised in choosing scan parameters. For example, images with TE=40ms, TR=1250ms, and TS=225ms had a relatively good signal/noise ratio and excellent GM-WM contrast, but lesions were isointense and difficult to visualize. A longer TR (2000ms) provided better T1 contrast in all cases. When the longest scan parameters (TE=60, TR=2000, and TS=350ms) were used, the lesions were intense but the CSF was so bright that it could hinder detection of lesions in some clinical situations. Decreasing either TE or TS from these longest values appeared to provide images with the best visualization of a combination of anatomical detail and pathology. Artifacts from vascular pulsations appear to be diminished while flow void phenomena appear to be more prominent in STEP images.

Although the signal/noise ratio of these images was less than ideal, the contrast/noise ratio was high. Because this technique combines T1 and T2 weighting in an attractive fashion, further study of stimulated echoes are warranted to evaluate their role in a clinical setting.

References

1. Sattin W and Coleman PE, Clinical considerations of STEP imaging, Book of Abstracts, Soc. Mag. Res. Med., 1420-1421,1986
2. Haase A, Frahm J, Matthaei D, Hanicke W, Bomsdorf H, Kunz D, and Tischler R, MR imaging using stimulated echoes (STEAM), Radiology, 787-790,1986

P-8

PROTON IMAGING AND T_1 MEASUREMENTS IN THE DETECTION OF DIABETIC NEUROPATHY AND DERMAL THICKENING

Richard H. Griffey, Charles Gasparovic, Nicholas A. Matwiyoff, Jeffrey D. Wicks, Randy R. Sibbitt, Wilmer L. Sibbitt, Jr., Marina Scavini, and R. Philip Eaton.

Center for Non-Invasive Diagnosis
Department of Rheumatology
Department of Endocrinology
University of New Mexico School of Medicine
Albuquerque, NM 87131

We have studied the water content in rats fed a diet supplemented with galactose for eight months. These animals are not diabetic, but develop many of the complications associated with diabetes, including sugar cataracts. These complications result from the action of the enzyme aldose reductase, which reduces galactose (gal) to galactitol. Galactitol is retained in tissue, and causes an increase in the water content. The dermus in the gal-supplemented animals thickens by 40% relative to the normal rats, as determined from proton images obtained on side-by-side rats at 1.5 Tesla. We measured a 30-35% increase in the water content of the dermus from the relative pixel intensity in the images.

In animals whose diet was supplemented with the aldose reductase inhibitor sorbinil, cataract formation is prevented. We have determined the T_1 relaxation times in 20 mm sections of the sciatic nerve from normal, gal supplemented, and gal + sorbinil rats, at 300 MHz. The values are listed below:

Rat (N=4)	T_1 (sec)
Normal	1.43 ± .04
Galactose	2.01 ± .03
Gal + Sorbinil	1.49 ± .05

In addition, we find the water content of the nerves from the galactose supplemented rats increases relative to the normal and sorbinil-treated animals as determined from the wet weights. The percentages of water in the nerve and the eye calculated after the samples were dried to constant weight are given below:

Rat (N=8)	Eye	Sciatic Nerve
Normal	78.9% ± 0.8%	61.3% ± 2.0%
Galactose	86.2%	64.5%
Gal + Sorbinil	77.8%	58.9%

The differences in T_1 relaxation time for the nerve samples from the gal supplemented rats and the sorbinil treated animals are 34%, while the increases in wet weight are 10%. Both the T_1 time and the water content of the animals on sorbinil are within experimental error

of the corresponding values for the normal animals. Preliminary studies also show a 10% increase in the T_1 of water in the anterior tendon from the leg of the gal supplemented rats relative to the controls. We feel the T_1 relaxation time accurately reflects the increased water content of the tissue induced by the accumulation of polyols. The T_1 parameter is a more sensitive indicator of water accumulation than differences in tissue wet weight. Calculated T_1 relaxation times obtained from images may allow diabetic neuropathy and dermal thickening to be diagnosed in human patients, and may permit therapy to be monitored in patients on inhibitors of the enzyme aldose reductase.

P-9
DETERMINATION OF LOCAL CORRELATION TIMES FOR WATER USING DEUTERON IMAGING AND SPECTROSCOPY

Richard H. Griffey, Beatrice V. Griffey, Randy R. Sibbitt, Nicholas A. Matwiyoff, Mark Brown*, and John C. Gore*.

Center for Non-Invasive Diagnosis
University of New Mexico School of Medicine
Albuquerque, NM 87131
*Department of Diagnostic Radiology
Yale University School of Medicine
New Haven, CT 06510

We have measured deuteron T_1 relaxation times to estimate the ratios of "free" and bound water in rats. The drinking water of the rats was supplemented with 10% deuterium oxide for three weeks. Measurements were performed at weekly intervals on a rat anesthetized with inactin. A birdcage coil tuned to 30.1 MHz was used for imaging and spectroscopy at 4.7 Tesla. The bulk T_1 of the deuterons could be fit with a single exponential curve to a time of .210$\pm$ .005 sec (N=4). The T_1 of a 10% solution of D_2O is .250$\pm$ .005 sec. The correlation times can be determined using theory proposed by Brown, Gore, and Armitage (unpublished results). The relaxation time in the rat corresponds to an effective correlation time of 3.55×10^{-12} sec for the bulk water. When a two site model is used, the percentage of water bound to macromolecules is calculated to be less than 0.01%.

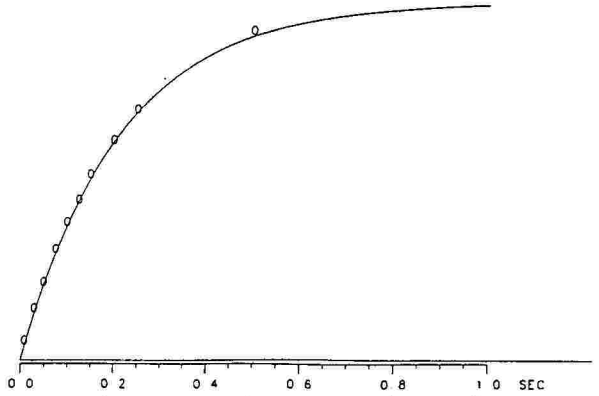

Figure 1. The exponential fit to the data from inversion recovery experiments on a rat. The values for the head, heart, and kidneys all fall within 3%.

P-10
PHOSPHOROUS-PROTON MULTIPLE QUANTUM FILTERING FOR THE SELECTIVE DETECTION OF INORGANIC, β-, AND γ-PHOSPHATES

Richard H. Griffey and Nicholas A. Matwiyoff

Center for Non-Invasive Diagnosis
University of New Mexico School of Medicine
Albuquerque, NM 87131

A new method which selectively detects signals from inorganic, β, and γ-phoshates is described. The phosphorous signals with small three bond couplings to protons (sugar phosphates, 2,3-diphosphoglyceraldehyde, phosphocreatine, and other phosphomonoesters and diesters) can be suppressed by converting their magnetization into phosphorous-proton multiple quantum coherence. Following a 90° pulse on phosphorous, signals from inorganic, β, and γ-phosphates evolve at a frequency determined solely by their chemical shift. The proton coupled signals evolve at rates governed by chemical shift, and by the ~10 Hz P-H

scalar coupling. After a period 1/2J 50 msec, these signals are in antiphase. Application of a proton 90° pulse converts this antiphase magnetization into multiple quantum coherences, which are invisible in the ^{31}P NMR spectrum. The signals from the inorganic, β and γ-phosphates are not affected by the proton pulse, and are detected in the standard fashion as a spin echo, or directly after the proton pulse.

Some sensitivity is sacrificed due to T_1 and T_2 decay during the evolution period following the first 90° phosphorous pulse, and linewidths under 15 Hz are needed to limit T_2* losses. The technique is broadly applicable in vitro and in vivo, even where the 8-12 Hz P-H coupling is unresolved, in the unambiguous estimation of inorganic phosphate, pH, and ATP/ADP ratios. These parameters often are indeterminant because of the overlap among phosphate, phosphomonoesters, phosphodiesters, and phosphocreatine.

P-11

CONTRAST ENHANCEMENT IN LOW ANGLE GRADIENT REFOCUSING TECHNIQUES

S. Vinitski*, M. Fuka, N.A. Matwiyoff, and M. Rifkin*

Los Alamos/UNM Center for Non-Invasive Diagnosis, Albuquerque, NM 87131
*Department of Radiology, Thomas Jefferson University Hospital, Philadelphia, PA 19107

It is well known that the gradient recalled echo technique can produce images in very short periods of time (1). When imaging time is very long (e.g. proton metabolic imaging) the image SNR (2) calculated over that period is slightly higher at low flip angles. However, the increase in the sharpness of the SNR peak at low angles makes errors in sample T_1 estimation very costly in terms of image SNR. Nevertheless, the ability to use a short TR without dead space (at low flip angles) allows acquisition of high 3D resolution contiguous volume data within only a few minutes (Fig. 1).

It has been shown that this type of technique (1) produces image artifacts, probably due to coincidence of the gradient echo with parasitic spin echoes during signal observation (3). It has been further shown (3-5) that an additional phase encoding pulse inserted after the data acquisition, equal and opposite to that before, removes image artifacts and increases signal, but significantly diminishes contrast. Under these circumstances, the diagnostic capability of fast imaging is severely limited.

In this work (performed on a 1.5T GE Signa imager) we demonstrate that by inserting a strong gradient at the end of the pulse sequence in the slice encoding direction, image contrast is restored to the original level with the added benefit of phase artifact absence and enhanced SNR (Figs. 1 and 2). This effect is probably the result of the destruction of the phase coherence in steady state created by the rephasing phase gradient. As theoretically predicted (2) the presence of this 'spoiling' gradient has no effect on the original technique (1), regardless of TR or flip angle. The contrast improvement methodology presented here should greatly enhance the diagnostic usefulness of the gradient refocusing techniques.

REFERENCES

1. A. Haase, et. al., SMRM IV, 980-981 London (1985).
2. J.S. Waugh, J. of Molec. Spectroscopy 35, 298-305 (1970).
3. G. McKinnon, SMRM V, 959-960, Montreal (1986).
4. T.W. Redpath, SMRM V, 963-964 Montreal (1986).
5. M.L. Gyngell, et. al., SMRM V, 666-667, Montreal (1986).
6. F. Wehrli, et. al., Invest. Radiol. 20, 360-369 (1985).

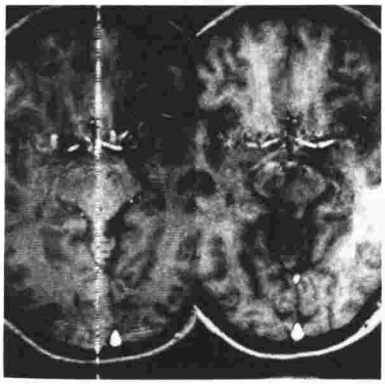

Figure 1. Shows removal of image artifact (left) by proposed technique (right). 32 slices (1mm thick) were acquired within 4 min. Note that contrast is at least as good in the right hand image as in the left hand image.

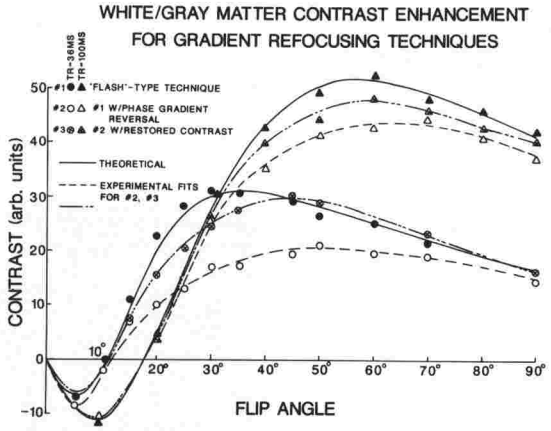

Figure 2. Shows theoretical (2) and experimental results of described methods on a phantom that models white and gray matter relaxation properties within 5% of those reported in the literature (6).

P-12
MRI OF THE PEDIATRIC SPINE

Harold S. Walker, M.D.[1], Rosalind B. Dietrich, M.D.[1], Bonnie D. Flannigan, M.D.,[2] Warwick Peacock, M.D.,[1] Robert B. Lufkin, M.D.[1] Hooshang Kangarloo, M.D.[1]
UCLA[1], Valley Presbyterian Hospital[2]

Evaluation of the pediatric spine has been facilitated by the recent advent of magnetic resonance imaging (MRI). The direct multiplanar capacities, lack of ionizing radiation and non-invasive nature of this technique are particularly advantageous for imaging children. This study was performed to evaluate the ability of MRI to demonstrate normal anatomy and pathology of the pediatric spine.

MR images of 30 normal children's spines were reviewed to evaluate optimal imaging planes and pulse sequences were compared to anatomic sections to define the normal anatomy. Over 70 children with a spectrum of spinal anatomy including congenital anomalies, trauma and tumor were imaged. Whenever possible, surface coils were used.

T1-weighted images best displayed structural anatomy and differentiated extradural, extramedullary and intramedullary lesions. They were particularly useful in the pre-operative evaluation of spinal dysraphic disorders. T2-weighted images were more sensitive for delineating and defining extent of some disease processes. Although lesions were routinely imaged in the sagittal and/or axial plane, the coronal plane often provided additional information and was particularly helpful in children with scoliosis. Magnetic resonance imaging often obviates the need for myelography with anesthesia and can avoid excessive radiation doses to patients undergoing sequential examinations.

P13
NEW MINIMUM ARTIFACT NEEDLE FOR MR GUIDED ASPIRATION CYTOLOGY OF THE HEAD AND NECK

R. Lufkin, D. Wortham, F. Vinuela, J. Bentson, G. Wilson and R. Shenoy and W. Hanafee.

UCLA School of Medicine and Fonar Corporation.

CT guided aspiration cytology of deep lesions plays an essential role in the workup of many head and neck patients. Since MRI is rapidly replacing CT as the imaging study of choice in this region, the ability to perform MR guided aspiration cytology is becoming increasingly valuable.

Attempts at MR guided biopsy with conventional stainless steel needles and MR liver biopsy needles resulted in images with unacceptable ferro-magnetic artifacts for thin section high resolution MR of the head and neck. These artifacts were further exacerbated when gradient echo fast-scanning techniques were employed.

Non-standard needles using a variety of stainless steel alloys including titanium, nickel, and brass were then tested. From this series a new needle was developed which produced markedly diminished artifacts. The position of the needle was easily recognised in 22 and 20 guage sizes as a fine line of signal void superimposed over the lesion. Initial clinical results in patients with head and neck pathology will be presented.

Reference: (1) Mueller P, Stark D, et al. Interventional MR. Successful Design and Use of a Non Ferromagnetic Needle for Aspiration/Biopsy. Society for Magnetic Resonance Imaging 1986 Program.

P-14

MULTIPLE ANGLE OBLIQUE MRI

S. Smith PhD, R. Olsen, D. Wolf, D. Hertz, M. Reicher, R. Lufkin, W. Hanafee.

Fonar Corporation, New York and UCLA

Multiple angle, variable interval, non-orthogonal magnetic resonance imaging (MAVIN) is a new time-saving technique which allows for the independent choice of slice angle and position for each slice in a multi-angle pulse sequence. By appropriate adjustment of the slice select radiofrequency (RF) pulse and the slice select and readout magnetic field gradients, the interval and angle of each slice may be individually chosen.

Magnetic resonance images using MAVIN were produced on normal volunteers using multislice 2D-FT spin echo imaging. The technqiue allows for the choice of slice angle and position individually for each slice in a multi-slice sequence. This was accomplished by appropriate adjustment of the slice select RF pulse frequency and the slice select and readout magnetic field gradients for each image plane. MAVIN has obvious application in studies of the lumbar spine, TMJ, orbits, knees, and other regions where non-parallel oblique scanning is necessary.

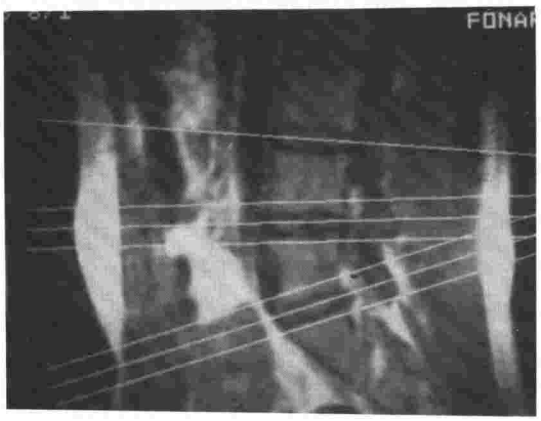

P-15
MRI OF THE CALVARIUM

Marwan Saab M.D., R. Dietrich, R. Lufkin, H. Kangarloo, J. Bentson, G. Wilson, W. Hanafee.

UCLA

With the widespread use of MRI for the diagnosis of cranial disorders, an increasing number of calvarial lesions are being detected. We compared the MR appearance of the calvarium of ten normal subjects to cryosections to define normal anatomy. Twenty cases with calvarial pathology were compared to CT, plain films and clinical examinations. These were divided into three categories: 1) primary processes affecting the calvarium, 2) intracranial or dural processes and 3) superficial processes.

MRI enables more complete visualization of a given lesion through imaging in any desired orthogonal plane. It is also unique in directly visualizing bone marrow involvement of calvarial lesions.

P16
SOLENOID SURFACE COILS IN MR IMAGING

J. Votruba PhD, R. Lufkin, M. Reicher, L. Bassett, S. Smith, W. Hanafee.

Fonar Corporation, N.Y. and UCLA

Surface coils have a strong coupling and high signal to noise response to nearby signals which drops off rapidly beyond one radius from the center of the coil. They are therefore limited to imaging superficial structures only. The planar surface coil may be modified to a solenoidal configuration which surrounds the patient. This allows excellent signal to noise performance without the associated deep signal dropoff of the flat coils.

We used a nonplanar solenoidal surface RF coil as a receiver with a conventional transmitter coil in a magnetic resonance imaging system. The improved signal to noise ratio, compared with conventional fixed saddle or solenoid receiver coils permitted higher resolution imaging and thinner image sections. In addition, the problem of signal dropoff that occurred in deep structures with planar and other noncircumferential surface coils was eliminated.

Solenoid surface coil imaging is very useful in MR imaging of the neck, joints of the extremeties, and/or breasts depending on the orientation of the main magnetic field of the imager. The technique allows high resolution thin section imaging of both superficial and deep tissues not possible with planar surface coils.

P-17
EFFECTS OF ZERO FILLING IN MAGNETIC RESONANCE IMAGING

C. Yoon PhD, R. Lufkin, S. Smith, W. Hanafee.

UCLA and Fonar Corporation, New York

Fast fourier transform algorithms used by most MR manufacturers for 2D-FT MRI require a power of two number of sample points along the phase and frequency encoding directions. Zero filling is a technique that allows smaller sample sizes to be used by adding zeros to bring the dataset to a full power of two. The effect of variable amounts of zero filling on scan time, image signal to noise, contrast and spatial resolution was empirically studied using phantoms and normal volunteers.

Zero filling allows a dramatic reduction in MR scan time at the expense of decreased spatial resolution and increased truncation errors along the phase encoding axis. Unlike most other techniques for shortening 2D-FT scan times, zero filling largely preserves signal to noise response.

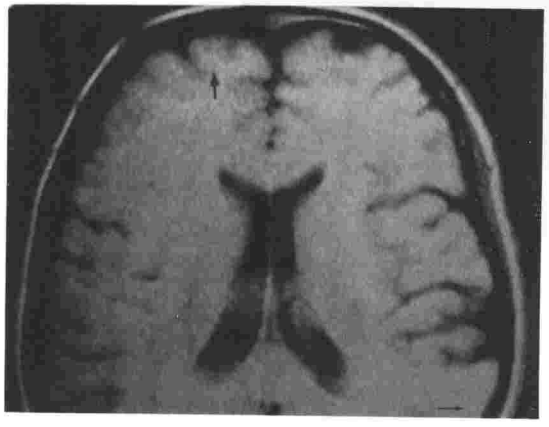

P-18

BIOLOGICAL EFFECTS OF MAGNETIC FIELDS ON THE NEMATODE PANAGRELLUS REDIVIVUS

James Peeling[*], John S. Lewis[*], Martin R. Samoiloff[**], E. Bock[+], Walter H. Huda[++], J. B. Sutherland[***], E. Tomchuk[*]

[*]Department of Physics, Univeristy of Winnipeg, [**]Department of Zoology, University of Manitoba, [+]Department of Chemistry, [++]University of Manitoba, [***]Department of Medical Physics, Cancer Research and Treatment Foundation, Department of Radiology, University of Manitoba, Winnipeg, Manitoba, Canada.

The Panagrellus redivivus bioassay is an established monitor of adverse toxic effects of different environments. Its use as a bioassay of biological effects of magnetic fields involves exposing 100 very young animals to a magnetic field environment and monitoring the survival, growth, and maturation of the test population after a 96 hour exposure period. The exposed animals are compared to a control population. The test is used to determine if a particular test sample has suffered any adverse biological effect, and permits the ranking of the toxic effects in a series of samples. Three distinct effects can be detected: 1)lethality, in which a significant proportion of the exposed animals die; 2) inhibition of growth, in which a significant proportion of the exposed animals fail to grow. This effect indicates damage to the overall physiological activities of the test animal; 3) inhibition of maturation, reflecting significant inhibition of gene regulated activities.

Magnetic environments assayed to date include 1) homogeneous static magnetic fields up to 2.3 Tesla in strength, 2) static magnetic field gradients in which the maximum field strength is .16 T and the gradient is 6 T/m, 3) homogeneous pulsed fields, for which the maximum dB/dt is 640 T/s and the maximum field strength is 64 gauss, or having dB/dt = 2.8 T/s and a maximum field strength of 140 gauss. In both cases the pulsing frequency is 1 Hz, 4) pulsed gradient fields, dB/dt = 800 T/s, dB/dx = .36 T/m, pulsed at 1.2 Hz.

No adverse effects were found for homogeneous or gradient static magnetic fields or for pulsed homogeneous magnetic fields. In the case of pulsed magnetic field gradients, preliminary experiments show a slight inhibition of growth. The biological effects of combinations of these environments, for instance pulsed gradients applied in a residual static magnetic field, have not yet been assayed. However, since the time of exposure (96 hours) and the strengths of the magnetic fields and gradients exceed those of MRI experiments, the Panagrellus redivivus bioassay does not suggest that the separate field compnents present in MRI studies pose a significant biological hazard.

ORAL ABSTRACTS

(Mam-A) NEURO-CLINICAL

Presiding: A. E. James & R. B. Lufkin

10:20 am

RIVER ROOM

12 MINUTES PER PRESENTATION

Mam-A1

MR PROJECTION ANGIOLOGY: APPLICATION IN PATIENTS WITH CEREBROVASCULAR DISEASE

R. Lufkin, L. Chiu, P. Pattany, S. Mohapatra, M. Mehringer, F. Vinuela, J. Bentson,

N. Martin, G Wilson, W Hanafee

UCLA School of Medicine and Picker International Incorporated.

2D-FT thick-slice projection images were obtained on a 0.5 Tesla super-conducting MR system. A flow-senstive image was obtained by suppressing within view motion using the MAST technique. Phase angles in the transverse plane (ϕ) depend on the following parameters: $\phi = \gamma G(t) x(t)\, dt$ where γ equals gyromagnetic ratio, $G(t)$ = gradient pulse at (T), and X (T) is the position of magnetization at (T). By appropriate application of additional gradients, (MAST) completely rephases magnetization within the view. By varying the gradient amplitude, flow at varying velocities is preferentially enhanced.

A standard non-MAST acquisition of the same region was then subtracted from the original image to produce the final vascular image.

This technique was used on normal volunteers as well as patients with a variety of cerebrovascular disease including athrosclerosis, avm's and aneurysms. Comparison was made with other imaging studies such as CT, conventional angiography, and conventional MR. MR projection angiology is capable of producing moderate resolution images of normals and patients with cerebrovascular disease that correlate well with other x-ray imaging studies.

Mam-A2

MR-IMAGING OF ACOUSTIC NEUROMA, PLAIN AND CONTRAST ENHANCED STUDIES

Th. Vogl, M. Bauer, D. Hahn, M. Mees, R. Brüning, J. Lissner

Dept. of Radiology, University of Munich

The diagnostic efficiancy of native and contrast enhanced (Gd-DTPA) MR in comparison to contrast enhanced CT and air-CT-cisternography was studied in 105 patients, suspected of suffering from acoustic neuroma.

Method: the examinations were performed at a 1.5 T MR unit, using T_1 and T_2 weighted sequences and the fast imaging technique (FISP). Before and immediately after the injection of Gd-DTPA fast imaging was used over a period of 10 minutes.

Results: CT and MR were equally accurate (100%) in imaging tumors with an extracanalicular component (n = 65). Fast imaging technique showed an enhancement peak after a period of 5 minutes after injection. In the case of strictly intracanalicular tumors (n = 20), MR imaging using Gd-DTPA was associated with no false positive or false negative predictions, whereas CT failed in 6 patients.

Conclusion: MRI sensitivity is much better than CT in detecting acoustic neuromas. For the intracanalicular tumors contrast enhanced MRI has become the chosen method of investigation, showing clearer delineation between tumor and adjacent pathological changes. Contrast enhancement in acoustic neuromas is very similar to CT and is of help in delineating vital parts of the tumor. Fast imaging techniques enable the differentiation of neuromas from other pathological changes (glomus tumor) in the temporal bone.

Mam-A3

THE IMPORTANCE OF MR IMAGING OF SELLAR-SUPRASELLAR MASSES BEFORE CONSIDERING NEUROSURGERY

Michael A. Mikhael, M.D.[1], Ivan S. Ciric, M.D.[2]

Department of Diagnostic Radiology[1] and Department of Surgery, Division of Neurosurgery[2], Evanston Hospital-McGaw Medical Center of Northwestern University, Evanston, IL

Of the 2800 MR neuro-studies (30 months), 340 were for suspected sellar-suprasellar masses. Of these, 115 studies were abnormal showing: empty sella, 27 cases; cystic sellar tumor, 11 cases; small pituitary adenomas, 37 cases; intrasellar-suprasellar tumors, 29 cases; subarachnoid cyst herniating into the sella, 1 case; tuberculum sellae meningioma with extension to the sella, 4 cases; optic chiasma glioma, 2 cases; craniopharyngioma, 3 cases; and post-traumatic carotid siphon aneurysm, 1 case. Thin sagittal and coronal MR slices (TR 500-2000 ms and TE 30-90 ms) were needed before surgery to help in planning the surgical approach.

From our experience of studying pituitary tumors with MR, the following facts were observed: (1) If the sellar-suprasellar mass is constricted at the diaphragma sellae (11 cases) the transsphenoidal approach is usually not only insufficient for total removal of the lesion, but could also be dangerous because the suprasellar remaining portion can rapidly increase in size from acute postoperative hemorrhage and/or edema, resulting in severe hydrocephalus and/or acute visual symptomatology (2 cases). (2) The coronal slices can visualize accurately the carotid siphon and rule out the possibility of intrasellar aneurysm which can mimic pituitary tumor. We feel that MR can replace preoperative angiography to rule out this possibility. (3) In 16 cases the MR imaging showed correctly the size and the location of the lesion as proven at surgery, while the CT scan of the same 16 cases showed the low density thought to represent the pituitary adenoma on the opposite side. (4) MR was important to obtain before considering radiotherapy to visualize the relation of the optic chiasma to the pituitary tumor. (5) Cases treated with bromocriptine were more efficiently and more accurately followed up by MR imaging.

In conclusion, we feel that MR imaging should be obtained in every case suspected of having a pituitary tumor before considering surgical approach, to visualize accurately the tumor, to rule out the possibility of intrasellar aneurysm, and to detect any constriction of the lesion at the diaphragma sellae. MR imaging is also helpful before radiotherapy and to follow up cases on bromocriptine treatment.

Mam-A4

JUXTRASELLAR MENINGIOMA: HIGH RESOLUTION MR WITH CT AND ANGIOGRAPHIC CORRELATION.

J.W. Yeakley,M.D., M.V. Kulkarni, M.D., C.B. McArdle, M.D., F.L. Haar, M.D.,FACS,PA, R.A. Tang, M.D.

The University of Texas Health Science Center-Houston, School of Medicine, Houston, TX

Magnetic resonance (MR) imaging has demonstrated high sensitivity in the detection of intracranial neoplasm, although, multiple investigators have reported poor differentiation of the meningioma from the normal brain on T1 as well as T2-weighted images. We have evaluated 14 MR studies in patients with juxtrasellar meningiomas because the lesion has excellent inherent MR contrast with the surrounding cerebrospinal fluid spaces, bone marrow and blood vessels. Using high resolution techniques the invasion of tissues surrounding the lesion could be studied.

We retrospectively evaluated 76 high resolution MR studies of sella and juxtrasellar area. 14 MR studies in 11 patients with juxtrasellar meningiomas were examined. 8 Patients had CT correlation while 6 patients had angiographic studies. MR imaging was performed using 1.5-Tesla (T) superconducting magnet. Coronal, sagittal imaging was obtained routinely and in some cases axial images were also obtained. Spin echo sequences with varying TE and TR values were obtained. High resolution images were obtained with 3mm slice thickness, pixel size of 0.39 cm^2. CT scans and angiographic studies were obtained using "state of the art" equipment. The lesions were evaluated in terms of its sellar, suprasellar and lateral sellar extensions. Involvement of the pituitary, optic chiasm, optic nerve, hypothalamus, cavernous sinus and vascular encasements were compared. MR was superior to CT in most instances. Although CT was useful in detecting hyperostosis and calcification it was not considered a drawback for MR in making the diagnosis and determination of the extent of the meningioma. MR was excellent in the determination of postoperative changes. Although MR predicted the results of angiography, it was felt that angiography could still be beneficial.

We conclude that MR is the modality of choice in the evaluation of juxtrasellar meningiomas and their postoperative follow-up. MR does not obviate the need for preoperative angiography at this time.

Mam-A5

THE RELATIVE ACCURACY OF MR IMAGING AND CT SCANNING FOR THE DIAGNOSIS OF CEREBELLOPONTINE ANGLE AND INTERNAL AUDITORY CANAL LESIONS

Michael A. Mikhael, M.D.[1], Ivan S. Ciric, M.D.[2], Allan P. Wolff, M.D.[3]

Department of Diagnostic Radiology[1] and Department of Surgery, Division of Neurosurgery[2], and Division of Otolaryngology & Head and Neck Surgery[3], Evanston Hospital-McGaw Medical Center of Northwestern University, Evanston, IL

Two hundred and fifty-two patients with clinical suspicion of cerebellopontine angle lesions were radiologically evaluated by CT scanning (routine CT scan and CT scan combined with cisternography) and MR imaging in our hospital in the last 36 months. Fifty-two acoustic neuromas, 4 meningiomas and 1 epidermoid cyst were diagnosed and surgically removed.

Routine CT scans were obtained with thin axial slices through the temporal bone before and after intravenous contrast injection. CT scan combined with cisternography was obtained after intrathecal injection of 5-10 cc of air to fill the cerebellopontine angle and internal auditory canal followed by thin axial CT slices. MR images were obtained using spin-echo technique to obtain axial and coronal thin slices (5 mm or smaller) to visualize the 7th/8th cranial nerve bundle on both sides with TR 500-2000 ms and TE 30-90 ms.

Although routine CT scan showed all the extracanalicular large lesions, it missed the lesions in 15 cases where tumors were small and located inside the internal auditory canal. Invasive CT combined with cisternography and the noninvasive MR imaging showed all the small intracanalicular lesions. MR visualized all the lesions including both the large extracanalicular and the small intracanalicular lesions and could differentiate between meningiomas, acoustic neuromas and epidermoid cyst. Meningiomas were shown to arise from the undersurface of the tentorium cerebelli and were separated from the 7th/8th cranial nerve complex. All acoustic neuromas were attached to the 7th/8th cranial nerve bundle. The epidermoid cyst showed high-intensity signal in both short and long sequences with no involvement of the 7th/8th cranial nerve bundle. Acoustic neuromas were shown as high-intensity, isodense, or low-intensity lesions on MR imaging. Their intensity had no correlation with the degree of tumor enhancement on CT scans done after intravenous contrast injection.

We feel that although the routine CT scan can visualize the enhancing cerebellopontine angle tumors, MR imaging could replace both routine CT and CT combined with cisternography without the use of intravenous or intrathecal contrast injection for the visualization and diagnosis of cerebellopontine angle and internal auditory canal lesions.

Mam-A6

CRANIOCERVICAL MANIFESTATIONS OF MUCOPOLYSACCHARIDOSES BY MR IMAGING

J.L. Andrew, M.D., A.J. Jonas, M.D., J.C. Williams, M.D.,Ph.D., C.B. McArdle, M.D., P.A. Narayana, Ph.D., M.V. Kulkarni, M.D.

The University of Texas Health Science Center-Houston, School of Medicine, Houston, TX

The mucopolysaccharidoses (MPS) are inborn error of metabolism in which deficiency of a specific exoglycosidase prevents the normal lysosomal degradation of the mucopolysaccharides. This group of patients have a wide variety of MPS deposition as well as cerebral changes leading to mental retardation, leptomenigeal involvement, spinal stenosis and cord compression. Although computed tomography (CT) and metrizamide CT have been used as a diagnostic tool, we felt that magnetic resonance (MR) because of its high sensitivity and superior inherent contrast could be useful in the diagnosis.

We have evaluated 12 MR studies in 9 patients with MPS. Imaging was performed using a 1.5-Tesla (T) and 0.6-T superconducting magnet. MR of the head was performed with conventional head coils while cervical spine and craniovertebral junction evaluation was performed using surface coils. Multiple pulse sequences were acquirred to provide relatively T1 and T2-weighted images. MR imaging was compared to CT when available. The craniocervical manifestations of MPS included hydrocephalus, multifocal deep white matter abnormalities, deposition of MPS along the dura and around the dens, spinal stenosis and cord compression. MR was far superior compared to CT in the evaluation of periventricular abnormalities. The extent of deep white matter abnormalities correlated well with the disease extent. These areas probably correspond to extensive cribriform and cavitary changes of the subcortical white matter, and the presence of the abnormal viscous fluid and mononuclear cells in the enlarged periadventitial spaces around the cerebral blood vessels, seen on the autopsy sutdies in the patients with MPS. Surface coil MR demonstrated MPS depositions, cervical canal stenosis and cord compression and obviated the need for metrizamide myelography. MR was poor in demonstrating leptomeningeal and dural thickening.

We conclude that MR should be the preferred screening modality in the evaluation of craniocervical manifestations of MPS. MR is more sensitive than CT for intracranial disease, while high resolution MR will probably replace invasive procedures such as myelography and metrizamide CT.

Mam-A7

COMPATIBILITY OF HALO RINGS AND VESTS FOR CERVICAL TRACTION AT 1.5-T

McArdle C.B., Narayana P.A., Kulkarni M.V.

The University of Texas Health Science Center-Houston, School of Medicine, Houston, TX

Cervical traction with halo devices is a popular method for stabilizing acute and subacute cervical spine fractures. To determine the compatibility of these mostly metallic devices, we imaged a variety of commercially available and prototype halo rings and vests with a GE 1.5-T magnet using a specially designed phantom for distortion quantification. Ten different halo rings, 10 skull pins, and 8 uprights (connecting the ring to the vest) were imaged, as well as 10 complete vests with rings. A body coil and surface coil were used to obtain images at the level of the head and the neck, respectively.

Vests made with stainless steel types 1035 or 18-8 have too much iron and preclude imaging. Other stainless steel types 303 and 304 are not as magnetic but cause significant distortion of the images obtained at the level of the offending metal. Stainless steel type 316 produced tolerable images and would be useful as a fastener (bolt, nut, washer) in areas of stress.

Only rings, pins, and vests making use of different types of aluminum and titanium and reinforced plastic were truly MR-compatible and distortion-free. Knowledge of which halo traction devices can be used in MR imaging at 1.5-T will help examine patients with unstable spinal cord injury at all field strengths and will lead to development of other new MR-compatible orthoses.

Mam-A8
DESIGN AND USE OF SURFACE COILS FOR SPINE IMAGING

Barry D. Klein, M.D., William G. Bradley, M.D., Ph.D., Ronald J. Otto, M.D.

MR Imaging Laboratory, Huntington Medical Research Institutes, Pasadena, CA

Surface coils can be customized to the software of the particular MR imaging system and to the particular anatomy to be imaged. The circuit design is relatively simple and the components are inexpensive. Having been disappointed with the limited field-of-view (FOV) of the surface coil supplied by our manufacturer, we built our own. An overview of surface coil design and construction will be presented.

Surface coils can provide superior images of the spine compared with the whole body coils due to increased signal-to-noise ratio and decreased motion artifact from anterior structures. The field-of-view (FOV) must be small enough to give spatial resolution competitive with CT yet large enough to cover the region of clinical relevance. Having tested several sizes of surface coils, we found a FOV of 25 cm to be optimal for general spine work. This gives 0.95 mm pixels on a 256x256 matrix.

In the lumbar spine this size covers T12 to S1 in most patients. The conus and cauda equina are seen routinely allowing exclusion of unusual causes of radiculopathy. Axial images with TR 1500 msec, TE 40 msec, 5 mm slice thickness are frequently performed in addition to a sagittal sequence to give contiguous images from mid L3 to S1. The TR is chosen to give good contrast between the posterior disc margin and dural sac and to give an adequate number of slices.

The thoracic spine images are far superior to body coil studies since cardiac and respiratory motion artifact is essentially eliminated. Most studies cover T4 to T12. Internal cord anatomy is well demonstrated on axial sequences.

The cervical spine can be imaged well in many patients with a specialized head and neck coil which has slots to accept the shoulders. In obese patients or those with prominent shoulders, the coil cannot be positioned low enough and the lower C-spine is not seen. In these cases, surface coil images are superior and usually cover the foramen magnum to T5. The cervical-thoracic junction is particularly well visualized.

(Mam-B) CARDIOVASCULAR

Presiding: R. M. Peshock & M. L. Winkler

10:20 am

ROOM C-107

12 MINUTES PER PRESENTATION

A QUANTITATIVE STUDY OF DYNAMIC VELOCITY AND ACCELERATION PATTERNS IN THE CARDIAC CHAMBERS, USING A FIELD EVEN ECHO REPHASING (FEER) SEQUENCE.
Mam-B1
DN Firmin, GL Nayler, RH Klipstein, SR Underwood, RH Mohaiddin, RSO Rees and DB Longmore.

The National Heart and Chest Hospitals, and Picker International, London, UK.

The recent development of field even echo rephasing (FEER) blood flow measurement sequences has enabled fast accurate evaluation of blood flow in most arteries of the body (1). The techniques have been further developed for measurement of a whole range of flow velocities and accelerations, and then greatly improved by modification for use in oblique planes (2). Previously we have described how the high temporal and spatial resolution of the technique may be useful for investigating quantitative details of flow patterns in the major blood vessels above the heart (3). In this study we have used the techniques to investigate flow patterns in the four chambers of the heart in 12 normal subjects.

The studies were carried out in three oblique planes through the heart. The horizontal long axis or four chamber view clearly shows flow in all the chambers and is particularly useful in displaying flow through the mitral and tricuspid valves. The short axis and vertical long axis views are both important for studying the patterns of flow in the left ventricle. The sequence was repeated at 50 msec intervals

through the cardiac cycle by reducing the flip angle to about 40 degrees, thus producing high temporal resolution without prolonging the scan time.

The following interesting flow patterns were consistently obtained:

i) atrial systolic velocities and accelerations.

ii) velocity and acceleration of blood flowing out of the left ventricle into the aorta during systole.

iii) deceleration of left ventricular blood following closure of the aortic valve.

iv) velocity and acceleration of blood flowing through the mitral valve in early diastole.

v) late diastolic flow down the centre of the left ventricle towards the apex and then up the walls towards the base.

The flow pattern in v) is thought to contribute to the closure of the mitral valve. Flow patterns are best visualised by combining the flow information with anatomy by colour coding the flow (4), and in addition displaying the individual frames dynamically as a cine loop.

To conclude we have developed a technique capable of accurate quantitative measurements of flow velocities and accelerations in and around the cardiac chambers. With these techniques we are establishing the range of normal patterns which will be important in the analysis of cardiac function and in the investigation of patients with anatomical abnormalities of the heart chambers and valves.

1. Nayler GL, Firmin DN, Longmore DB. Cine MR Flow Imaging. J Comput Assist Tomogr 1986;10:715-22.

2. Firmin DN, Nayler GL, Underwood SR, Klipstein RH, Rees RSO, Longmore DB. Oblique Cine Magnetic Resonance Cardiac Blood Flow Imaging. (Abstract) Fifth Annual Meeting of the Society of Magnetic Resonance in Medicine, Montreal 1986.

3. Klipstein RH, Firmin DN, Underwood SR, Rees RSO, Longmore DB. Human Blood Flow Patterns in the Ascending and Descending Aorta studied by Magnetic Resonance. (Abstract) Third Congress of the European Society of Magnetic Resonance in Medicine and Biology, Aberdeen 1986, 128-9.

4. Klipstein RH, Firmin DN, Underwood SR, Nayler GL, Rees RSO, Longmore DB. Colour Display of Quantitative Blood Flow and Cardiac Anatomy in a Single Magnetic Resonance Cine Loop. Br J Radiol 1986, (in press).

Mam-B2

CARDIAC SHUNT ASSESSMENT BY GATED RAPID DYNAMIC ACQUISITION MAGNETIC RESONANCE IMAGING

C.E. Spritzer, M.D., E.L. Effmann, M.D., R.J. Herfkens, M.D., B. Armstrong, M.D., D.F. Merten, M.D.

Department of Radiology, Duke University Medical Center, Durham, N.C. 27710

Magnetic resonance imaging has been shown to be useful in the evaluation of congenital heart disease (1). However, in conventional gated spin echo images, flow related phenomena may make evaluation of vessel or shunt patency difficult. Gated rapid dynamic acquisition magnetic resonance imaging of the heart permits noninvasive assessment of flow related phenomena while assessing complex cardiac function and anatomy.

Seven patients with complex congenital heart disease requiring shunt procedures were evaluated with a General Electric 1.5 Tesla Signa System utilizing a new CINE software package. The CINE technique utilizes a small flip angle (typically 30 degrees) which permits using short repetition times (TR=21 msec) and short echoes (TE=12 msec) which are acquired using gradient reversal. Each cardiac cycle is divided into 16 frames enabling one to assess cardiac function. Data is acquired for 128 consecutive heart beats in order to obtain 128 views in the phase encoding direction. Four images may be simultaneously acquired in 3 to 6 minutes, depending upon the patient's heart rate. The CINE method displays laminar blood flow as increased signal whereas turbulence appears as decreased intensity.

Eight CINE MRI studies performed in seven patients characterize the anatomic features of the underlying congenital heart disease (tricuspid atresia - 3, pulmonary atresia with VSD - 1, common ventricle with pulmonary stenosis - 1, hemitruncus - 1, and Tetralogy of Fallot - 1) in each case. Preoperative atrial and pulmonary artery anatomy was accurately shown in two patients. Postoperative Fontan shunt patency was noted in four patients. Complications of 1) stasis of right atrial blood flow, 2) stenosis of the left pulmonary artery, 3) reduced left ventricular function, and 4) probable graft occlusion were demonstrated in single cases. This rapid acquisition MRI method with sensitivity to flow and turbulence holds considerable potential for the noninvasive evaluation of congenital heart disease.

1. Higgins CB, Byrd II, BF, McNamara MT, et al: Magnetic resonance imaging of the heart: a review of the the experience in 172 subjects. Radiology 1985;155:671-679.

Mam-B3

MRI IN-PLANE FLOW PHENOMENON: CORRELATION OF VELOCITY-DEPENDENT PHASE SHIFT AND IMAGE APPEARANCE

June T. Ruszkowski, PhD. and Antoinette S. Gomes, M.D.

State University of New York Health Science Center at Brooklyn and UCLA Medical Center

The appearance of in-plane flow on gated MR images is described. A flow model was developed consisting of a modified pulsatile flow pump which triggered "gated" image data acquisition at any point in the flow cycle. Water doped with nickel chloride (to provide a fluid with a T_1 similar to blood) was pumped through tubing to simulate arterial blood flow. Spin echo images were obtained of the tubing in longitudinal view. Flow contrast results from the phenomenon of velocity depoendent phase shift, which modulates the signal obtained from fluid flowing along a magneic field gradient. Flow images were obtained which demonstrated the appearance of slow flow, fast flow, turbulent flow, and flow in the region of a bifurcation.

Normal volunteers were studied using spin echo images acquired in oblique planes through the carotid arteries. A high sensitivity surface coil allowed the acquisition of high resolution images of small structures. Cardiac gating was used to synchronize image data acquisition to a specific phase of the cardiac cycle.

Longitudinal views of the carotid arteries were obtained with this method of MRI carotid angiography. Acquisition of the image during end diastole when blood flow is at a minimum results in positive flow contrast. Gating during the systole when flow velocity is high results in negative flow contrast because significant spin dephasing occurs and low signal is received from moving blood. These results suggest that magnetic resonance imaging may be used to visualize vascular morphology and blood flow.

Mam-B4

TECHNIQUE FOR ELIMINATING FLOW ARTIFACTS AND FOR IMPROVING THE DEPICTION OF VASCULAR ANATOMY IN MRI: DESCRIPTION AND CLINICAL APPLICATION

Ehman, Richard L., M.D.; Felmlee, Joel P., M.S.; Julsrud, Paul R., M.D.; Berquist, Thomas B., M.D.; Gray, Joel E., Ph.D.
Mayo Clinic and Foundation 200 1st St. S.W., Rochester, MN 55905

INTRODUCTION

Clinical magnetic resonance images are often degraded by flow artifacts. These zipper-like artifacts radiate in the direction of the phase encoding axis from the position of vessels passing through the plane of section. They are especially bothersome in high-resolution studies with small fields-of-view, in surface coil studies, and with high field strength imagers. These artifacts can obscure anatomic detail and simulate the presence of pathology.

A second kind of vascular artifact that have received less attention is the frequent presence of intraluminal signals in an unpredictable pattern that degrades the flow void. Such artifacts can simulate or mask the presence of important intraluminal pathology such as dissection or thrombus. Successful clinical imaging with conventional spin echo MR pulse techniques requires accurate depiction of vascular structures with reliable flow voids in patent vessels. Currently, many of the vascular applications of MRI that have been reported in the literature cannot be consistently reproduced in clinical practice because of this problem.

OBJECTIVES OF THIS PROJECT

To further investigate the basic causes of flow artifacts in MRI. To develop and evaluate a method for elinimating these artifacts. To improve the reliability of depiction of vascular structures in conventional spin echo MRI.

METHODS

The physical mechanism of flow artifact generation was studied with a laminar and turbulent flow phantom, using continuous and pulsatile flow. This phantom also served as a means for quan-

titatively evaluating artifact suppression techniques. The physical basis was also investigated by a computer simulation which generates a numerical representation of the temporal and spatial distribution of spin density and phase in a complex object containing flow or motion. It then simulates the 2DFT scanning process to generate a data matrix. This data is then reconstructed to yield an image which can be compared to the original numerical object.

These studies suggested a new approach for suppressing flow artifacts and improving the depiction of vascular anatomy. This techique was implemented in the standard spin echo sequences of a GE 1.5T Signa imaging system. The method (which we will refer to as the FLAK technique) utilizes additional radiofrequency pulses and gradients to adjust the spatial orientation of flowing isochromat dipoles in the rotating frame. It typically adds 3 to 6 msec to the minimum time required for acquisition of single view. It differs intrinsically from gradient-nulling techniques for suppression of flow artifacts that have recently been reported. In principle, the method can be applied to any pulse sequence on any imager.

RESULTS

The flow phantom studies and simulations indicate that flow artifacts are not the product of intra-voxel phase dispersion. Rather, the zipper-like artifacts in 2DFT imaging result from temporal modulation of both the magnitude and phase angle of bulk voxel magnetization. The implication is that phase-nulling techniques alone, which can reduce phase modulation but not intensity modulation, cannot completely eliminate flow artifacts. In addition, phase-nulling techniques have the effect of increasing the intraluminal intensity of vascular structures, thereby destroying the flow void. This is objectionable from the clinical standpoint, since it obscures intravascular pathology.

In flow phantom tests, the FLAK technique suppressed the intensity of flow artifacts by more than 90% in spin echo sequences with a variety of clinically pertinent flow rates and patterns. The technique yields a quantitatively similar improvement in luminal signal uniformity.

Volunteer and clinical studies with FLAK have demonstrated a striking reduction in the amount of flow artifact and a marked improvement in the reliability with which vascular structures are depicted. To date, we have found the technique particularly helpful for high resolution surface coil studies of the neck, for detecting thrombus and other intravascular pathology such as dissections, and for delineation of the relationship between hepatic vessels and liver tumors prior to attempted resection. The technique substantially improves the quality and reliability of images obtained with cardiac gating. Advanced clinical trials are continuing.

Mam-B5

OBLIQUE VASCULAR DISPLACEMENT FLOW ARTIFACTS IN CONVENTIONAL MRI SEQUENCES*

P.R. Moran, O. Nalcioglu and S.C. Juh

Department of Radiological Sciences, Division of Physics and Engineering
University of California - Irvine

We have shown elsewhere [1] that the MRI encoding process is described rigorously by solution of the Bloch-Boltzman Transport equations which produce a magnetization expressed by,

$$M(\vec{R},t) = M_o(\vec{R} - {}_0\int^t \vec{u}(t')dt')\exp\{-i\gamma(\vec{R}\cdot {}_0\int^t \vec{G}(t')dt' + {}_0\int^t \vec{G}(t')\cdot {}_0\int^t \vec{u}(t'')dt''dt')\} \quad (1)$$

where $M_o(\vec{R}(0))$ is the initial magnetization, $\vec{R}(0)$ is the spatial position at t=0, and $\vec{u}$ indicates the velocity of spins within the medium,. Thus, $M(\vec{R},t)$ expressed above describes an initialy excited magnetization bolus that subsequently transports under any molecular flow to new positions. In fact, the actual dispersion also is governed by the integral of the distribution of velocities within that particular voxel.

Field gradient modulations, $\vec{G}(t)$, encode the spin system's position and motion variables into Fourier variables. If the pulse sequence shown in Figure 1 is used in acquiring a second echo image, then the y and x positions of the moving bolus of magnetization are encoded at times T_p and 2TE respectively, where these variables are defined in Figure 1. Thus the magnetization distribution is

$$M(x(2TE),y(T_p)) = M(x(0)+2TE\cdot v_x, y(0)+T_p\cdot v_y) \quad (2)$$

This time-of-flight inconsistency in the data generates a displacement artifact, as sketched in Figure 2, for flow-streams having both a v_x and a v_y component of velocity, but it arises from the transport term M_o. The displacement of a vessel occurs perpendicular to the direction of flow and is given by,

$$\vec{d}(v) = v_x v_y (2TE - T_p)/v \quad (3)$$

which is a cross-correlated product of x and y direction velocities of flow and is independent of the gradient strengths. An actual example of the displacement artifact is shown in Figure 3. Two tubes with inner diameters 9.5 mm were filled with water and placed at an angle with the read-out direction (x-in this case). A projection image of the tubes containing stationary water was obtained using a second echo FID with TE=60 msec. A second image having 17.6 cm/s average flow velocity in the tubes was obtained. The flow direction is reversed in the two tubes. The new image was subtracted from the stationary water image and is shown in Figure 3. The black lines correspond to the positions of the stationary tubes. Since in general the tubes contain a distribution of velocities, the amount of shift would depend on the specific velocity at a given point within the object. This would result in a distorted "apparent density" distribution within the tube. All zero-order effects (i.e. all terms relating to average velocity within the $(T_p, 2TE)$ interval) can be compensated by adding to the G_y-pulse a suitable bipolar phase-gradient. If the additional y-gradient is chosen properly, then the transported magnetization encoded as $M_o[x(2TE),y(2TE)]$, independent of velocity and gradient amplitudes, and no discrepancy between x and y encoding times exists.

The above capability suggests some important applications not possible before. For example, we can achieve a direct spatial display of vessel velocity profiles, and the displacement magnitudes are independent of phase-shift or blurring effects, but still depend upon the velocity cross-correlations. Such quantities are important in assessing turbulance behavior quantitatively.

*This work was supported in part by PHS Grant No. 1R01-CA41307 awarded by the NCI, DHHS. PRM gratefully acknowledges research leave from BGSM.

1. P.R. Moran and O. Nalcioglu "MRI Rigorous Solutions for Transport from the Bloch-Boltzman Equation". Presented at this conference.

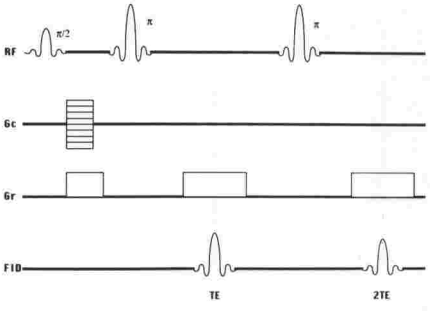

Figure 1. Double echo pulse sequence.

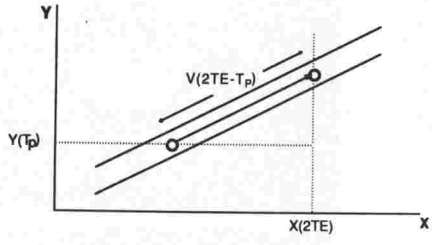

Figure 2. Displacement artifact.

Figure 3. Difference of stationary and moving fluid images.

Mam-B6

MEASUREMENT OF MEAN AND VARIANCE OF VELOCITY WITHIN A VOXEL BY NMR IMAGING*

Q.S. Xiang, S.C. Juh and O. Nalcioglu

Department of Radiological Sciences, Division of Physics and Engineering
University of California - Irvine

NMR imaging has the capability of providing information regarding the magnetization density and motion related parameters if the object has both stationary and moving regions [1]. Furthermore, it is physically possible to have a spectrum of velocities within a voxel in the image. The measurement with finite size voxels results in some sort of spatial averaging of these velocity components. We have shown [2] that the velocity distribution modifies the reconstructed image according to,

$$\hat{\rho}(\vec{r}) = \rho(r) \int d^3 v \; \xi(\vec{r},\vec{v}) \; \exp\,(i\vec{\alpha}\cdot\vec{v}) \qquad (1)$$

where $\hat{\rho}$ and ρ are the reconstructed and actual magnetization densities. In equation (1) ξ represents the velocity spectrum at a location $\vec{r}$ and $\vec{\alpha}$ is the velocity encoding vector. By defining $\vec{u} = \vec{v} - \langle\vec{v}\rangle$, equation (1) can be rewritten for the pulse sequences shown in Figure 1 as

$$\hat{\rho}_a(x,y) \simeq \rho(x,y)\ \exp(i\alpha_x^a \langle v_x \rangle)\ (1-(\alpha_x^a)^2 \langle u_x^2 \rangle /2) \qquad (2.a)$$

$$\hat{\rho}_b(x,y) = \rho(x,y) \qquad (2.b)$$

where we ignored the small velocity encoding due to G_y. Thus $\vec{\alpha}$ is basically determined by the read-out gradient G_x. Images $\hat{\rho}_a$ and $\hat{\rho}_b$ result from Figures 1.a and 1.b respectively. For the sequence shown in Figure 1, $\alpha_x^a = \gamma G_x \Delta\ (TE-\Delta)$ and $\alpha_x^b \simeq 0$. The form given in eq. (2.a) can be obtained from eq. (1) by expanding the exponential term within the integral after substituting $\langle \vec{v} \rangle + \vec{u}$ for $\vec{v}$ and retaining the first three terms [2]. The convergence of the expansion can be assured by choosing α_x^a appropriately. The mean velocity and variance images can be computed from eqs. (2.a-b).

The above theory was tested using a flow phantom which was built by wrapping two 60m tubes connected in series on a plastic spool in the form of two coils wound in opposite directions. The inner diameters of the tubes for the outer and inner shells were 1.07 and 0.81 mm, respectively. The large axis of the coils was placed along the z-axis and two (x,y) projection images were obtained using the pulse sequence shown in Figure 1. Since the Reynolds numbers in the current experiments were within 5-50, the flow within the tubes is believed to be laminar. In the case of laminar flow, the expected images of $\langle v_x \rangle$ and $\langle u_x^2 \rangle$ can easily be calculated. The experimental results shown in Figure 2 agree well with the theoretical predic-

0.07 ± 0.02 and 0.11 ± 0.01, both in $(cm/s)^2$ for the outer and inner shells, respectively. These values agree well with the corresponding theoretical values of 0.06 and 0.16 $(cm/s)^2$. The linearity between $\langle v_x \rangle$ and $\langle u_x^2 \rangle^{1/2}$ was also checked using nine different velocities and the correlation coefficient was found to be 0.95.

*This work was supported in part by PHS Grant No. 1R01-CA41307 awarded by the NCI, DHHS.

1. P.R. Moran, Mag. Res. Imag. 1, 197(1982).
2. O. Nalcioglu, Z.H. Cho, Q.S. Xiang and C.B. Ahn, Proc. SPIE. 671(1986).

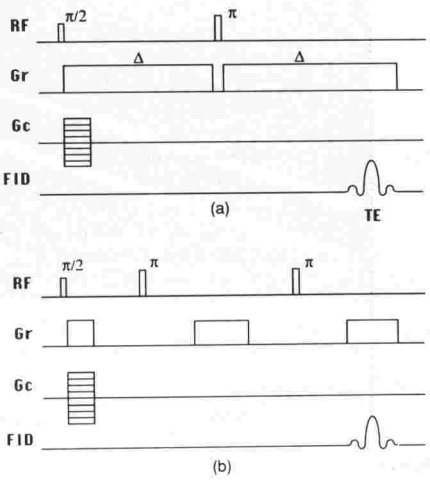

Figure 1. (a) velocity sensitized first echo sequence, (b) velocity rephased second echo sequence.

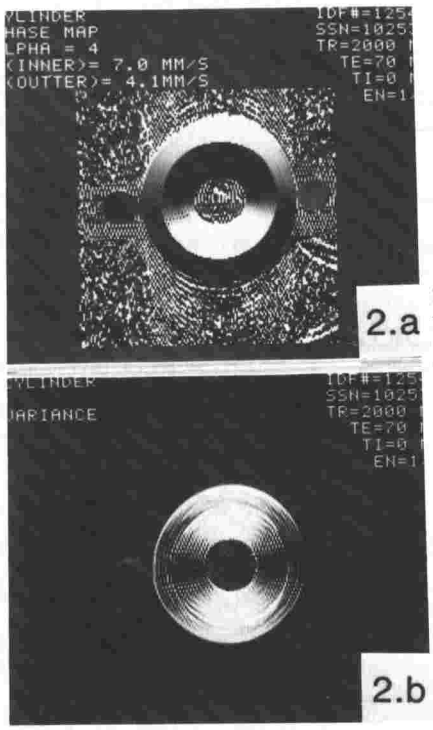

Figure 2. (a) phase map yielding mean velocity distribution, (b) velocity variance map.

Mam-B7

QUANTITATIVE VELOCITY DETERMINATION IN MRI OF FLOW USING A MEASURE INDEPENDENT OF THE ABSOLUTE INTENSITY

D. Saloner, P.R. Moran and B.M.W. Tsui*

Dept of Radiology, Bowman Gray School of Medicine, Winston-Salem, NC and *Dept of Radiology, University of North Carolina, Chapel Hill, NC

Although rapid progress has been made in the ability to use MRI for the qualitative investigation of flow, the reliability of quantitative measures of velocities and volume flow rates is still questionable. Conventional techniques used to determine flow rates rely on relating the observed intensities in the image to intensities predicted for the specific pulse sequence used. There are several effects which can modify the predicted intensity values and thus degrade the ability of conventional techniques to quantify flow velocities. Among these are the fact that in most techniques the acquired signal is dominated by the signal from stationary material resulting in a reduced sensitivity to the flowing material and consequent errors in the intensity determination. In addition any deviation of the values of the relaxation parameters of the flowing material from those assumed in the calculation of the intensity will result in an inaccurate calculation of the time variance of the magnetization in the moving material and hence an incorrect value for the flow velocity. Further, a precise knowledge of the response of the magnetization to the applied rf pulses and imaging gradients is essential to determine the signal strength. Highly simplified assumptions are generally made in the calculation of the magnetization strength, e.g. in slice selective excitation it is commonly assumed that the excited magnetization has the shape of a perfect square pulse although it is well known that this is not the case.

We have previously reported on a pulse sequence which provides a steady state distribution of magnetization and decomposes the excited material into regions characterized by the number of excitation cycles that the given region has experienced.[1] This in turn reflects the transit time of material through the region of excitation. Under appropriate conditions the magnetization is inverted in sign with consecutive excitation cycles. In this case the signal from stationary material is inherently suppressed and the resultant image has a banded appearance reflecting the distribution of velocities across the flowing material.

For simplification we will consider here a modified spin-echo pulse sequence where the initial angle of excitation is nominally $\leq 30^{\circ}$. Assuming ideal conditions such as an accurate knowledge of the relaxation parameters of the flowing material and square edged magnetization distributions, the positions of the intensity maxima and minima can be used to determine the flow velocities. We have investigated the validity of this result for the case that the relaxation parameters are poorly known and for realistic slice-selective excitations where the nominal angle of the excitation and rephasing pulses may be achieved only over a relatively narrow region of the selected slice. In Fig 1 we show the calculated intensity that would be observed in a plane perpendicular to the direction of flow as a function of velocity for a range of T1. We note that although the absolute intensity is different in each case the positions of the intensity maxima and minima are unaffected by the value of T1 assumed. Similarly we will show that provided the rephasing pulse is such that the magnetization is inverted over the region sampled by the excitation pulse, the positions of the intensity maxima and minima are unaffected by the detailed shape of the excitation and rephasing pulses. We thus have a robust measure of the velocities in flowing material determined primarily by the pulse sequence timing parameters and the width of the selected slice as defined by the excitation pulse, rather than by an absolute intensity measurement.

[1] D. Saloner, P.R. Moran and B.M.W. Tsui, Abstracts of SMRM V, Montreal, 1986 p117.

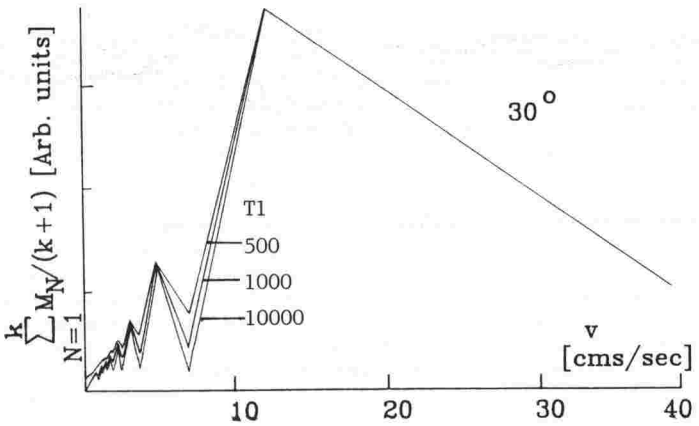

Fig. 1 Intensity measured in a plane perpendicular to the direction of flow as a function of velocity for several values of T1.

Mam-B8

MRI RIGOROUS SOLUTIONS FOR TRANSPORT FROM THE BLOCH-BOLTZMAN EQUATION*

P.R. Moran and O. Nalcioglu

Department of Radiological Sciences, Division of Physics and Engineering
University of California - Irvine

The Bloch equations for the evolution of the magnetization density can be transformed into a modified Bloch-Boltzman equation when the spins are subjected to a velocity field $\vec{v}$ in the rotating frame of reference.

Following Torrey [1], the Bloch-Boltzman equation for the transverse magnetization density of an incompressible fluid is given by

$$\partial M(\vec{R},t)/\partial t = \{i\gamma\vec{G}(t)\cdot\vec{R} - 1/T_2\}\, M(\vec{R},t) - \vec{v}\cdot\nabla M(\vec{R},t) \qquad (1)$$

The last term in eq.(1) describes the transport of the spin density within the medium. Let us eliminate the T_2 term by substituting $m(\vec{R},t) = M(\vec{R},t)\exp(t/T_2)$. Then the Bloch-Boltzman equation becomes,

$$\partial m(\vec{R},t)/\partial t = 2\pi i\, \vec{F}(t)\cdot\vec{R}\, m(\vec{R},t) - \vec{v}\cdot\nabla m(\vec{R},t) \qquad (2)$$

where $2\pi\vec{F}(t) = \gamma\vec{G}(t)$ and includes the phase reversals from rf-echo-pulses. In general, there is also some distribution of spin density given by $\Delta(\vec{R},\vec{v},t)$, which comes from the physics of the flow (e.g. the Navier-Stokes equation); it is not directly available from eq. (2). We can, however, rigorously solve eq. (2) for a particular velocity, $\vec{v}(t)$, and derive a "kernel" solution for $m(\vec{R},t)$, understanding that the physically observable magnetization is an integral over the distribution $\Delta(\vec{R},\vec{v},t)$ for each resolvable imaged-volume and the corresponding velocity-history probabilities. The solution of eq. (2) is,

$$m(\vec{R},t) = M_o\{\vec{R} - {}_0\int^t \vec{v}(t')dt'\}\exp\{2\pi i\{\vec{R}\cdot\vec{A}_1(t|F) - {}_0\int^t \vec{v}(t')\cdot\vec{A}_1(t'|F)dt'\}\} \qquad (3)$$

using the accumulator, cummulant value notation of statistical mathematics,

$$\vec{A}_1(t|F) = {}_0\int^t \vec{F}(t')dt' \text{ and } \vec{C}_1(F) = \vec{A}_1(TE|F) \qquad (4)$$

where TE is the echo-centroid for stationary spins of the MRI echo-FID being acquired. The continuity condition guarantees that one may replace the field variables, $\vec{R}$, by particle positions, $\vec{R}(t)$, by using,

$$\vec{R}(t) = \vec{R}(0) + {}_0\int^t \vec{v}(t')dt' \qquad (5)$$

A substitution of eq. (5) into eq. (3) and performing an integration by parts of the last exponential term in eq. (3) results in,

$$m(\vec{R},t) = M_o\{\vec{R}(0)\}\exp\{2\pi i\{\vec{R}(0)\cdot\vec{A}_1(t|F) + {}_0\int^t \vec{F}(t')\cdot {}_0\int^{t'} \vec{v}(t")dt"dt'\}\} \qquad (6)$$

The new representation given in eq. (6) for the transverse magnetization density $m(\vec{R},t)$ corresponds to treating the flow problem using the Lagrangian point of view. The former expression given in eq. (3), on the other hand, is the expression for transverse magnetization in terms of the Eulerian representation. We have shown above that the two representations yield identical results. The physical meaning of eq. (6) is that an inital magnetization density M_0 generated at location $\vec{R}(0)$ at t=0 moving with velocity $\vec{v}(t)$ evolves through a magnetic field gradient and experiences an overall phase shift which is the summation of phase shifts along the trajectory of motion. The FID signal corresponding to eqs. (3) or (6) can be obtained by distributing $m(\vec{R},t)$ according to $\Delta(\vec{R},\vec{v},t)$ and integrating over the volume of excitation.

These rigorous Bloch-Boltzman solutions provide a novel insight for known flow/motion MRI applications, and give verifiable explanations for a number of motion-artifact phenomena not resolved by current MRI descriptions. For example, any component of $\vec{F}(t)$ produces a specific phase-encoding only to some average position, and never specifically to any motion occuring. Diffusional decay, both molecular and turbulent, derives directly and easily from statistical variations of the velocity-distribution. We shall demonstrate a number of immediate applications, implications, and consequences of the Bloch-Boltzman MRI transport solutions for flow/motion imaging.

*This work was supported in part by PHS Grant Number 1R01 CA41307 awarded by the National Cancer Institute, DHHS. The first author (PRM) acknowledges research-leave support from Bowman Gray School of Medicine, Department of Radiology.

Reference

1. H.C. Torrey, Phys. Rev. 104, 563 (1956). The Bloch-Boltzman equations, developed here, differ from the Bloch-Torrey formulation in the important feature that M is generally a strong and explicit function of position in MRI, $M = M(\vec{R},t)$.

(Mam-C) MUSCULOSKELETAL

Presiding: S. Harms & F. Shellock

10:20 am

ROOM C-101

12 MINUTES PER PRESENTATION

Mam-C1
1.5T FLASH MRI OF THE KNEE

D. Lawrence Burk, Jr., M.D.*; Emanuel Kanal, M.D.**; James A. Brunberg, M.D.**; Richard J. Prorok, RTR**; Joseph S. Gillen, B.S.**; Gerald L. Wolf, Ph.D., M.D.**.

*Hospital of the University of Pennsylvania, Philadelphia, Pennsylvania 19104; **Pittsburgh NMR Institute, Pittsburgh, Pennsylvania 15213.

FLASH (Fast Low Angle SHot) MRI of the knee was performed on 10 patients using a 1.5T GE Signa scanner and a transmit-receive extremity coil. The FLASH images were obtained using a repetition time (TR) of 22msec, a gradient echo time (TE) of 12msec and a flip angle of 30 degrees. Normal menisci were visualized as triangles of low signal intensity, hyaline cartilage demonstrated intermediate signal intensity and meniscal tears, joint effusions and cysts all had increased signal intensity. The findings were correlated with sagittal and coronal spin echo pulsing sequences (TR/TE). Three horizontal meniscal tears, 2 complex meniscal tears and 1 total meniscectomy were visualized on proton spin density (2000msec/20msec) images and on FLASH images. Three popliteal cysts and 3 meniscal cysts were detected on T2 weighted (2000msec/80msec) images and on FLASH images. Four knees were normal on all pulsing sequences. Examination time was significantly decreased with the FLASH technique, but resolution was also decreased due to limitations on the minimum size of the field of view. Despite this loss of resolution, there were no significant diagnostic discrepancies between the two techniques.

Mam-C2
THE TENDONS: HIGH FIELD SURFACE COIL IMAGING

Javier Beltran, M.D., Angela M. Noto, M.D., Leigh J. Herman, M.D., Lawrence M. Lubbers, M.D. (2)

Department of Radiology, OSU Hospital and Department of Hand and Microvascular Surgery, Riverside Hospital (2)

High resolution magnetic resonance (MR) images of the tendons in the hands, wrists, feet and ankles of six normal volunteers and six cadavers were obtained using receive-only surface coils and reduced field of view imaging. Normal anatomy was identified and compared to gross anatomic sections of the six cadavers. Experimentally produced Achilles tendon tears were identified in the legs of domestic swine. The hands and feet of 13 patients were examined and a variety of pathologic lesions were identified including acute post traumatic rupture, acute tenosynovitis, chronic tendonitis and post surgical complications. MR imaging provides inherently greater soft-tissue contrast than any other currently available imaging modality. With the use of surface coils and reduced field of view imaging to enhance spatial resolution, MRI has become a valuable tool for imaging tendons. Advantages over the other available modalities included excellent anatomic detail, superior contrast resolution and the potential for multiplanar imaging.

Mam-C3

SOME PITFALLS OF MAGNETIC RESONANCE IMAGING OF THE KNEE

Leigh J. Herman, M.D., Javier Beltran, M.D., David Hack, MS4, Melinda S. McCall, B.S.R.T.

Department of Radiology, Ohio State University Hospital

MRI provides a technique by which the soft tissues of the knee can be directly visualized with unprecedented detail. Along with new opportunities MRI presents the radiologist with the potential pitfall of misinterpreting familiar anatomic structures now being viewed in unfamiliar ways. The menisci, tendons and blood vessels all have extremely low signal intensity on both T1 and T2 weighted images. When the knee is imaged in the sagittal plane blood vessels and tendons located close to the menisci can simulate meniscal tears. A review of 64 knees imaged on a 1.5 Tesla superconducting magnet revealed six cases in which the anterior inferior geniculate artery simulated a tear of the anterior lateral meniscus, and two cases in which a prominent hiatus for the popliteus tendon simulated a tear of the posterior medial meniscus. Familiarity with the appearance of these potential pitfalls can prevent misinterpretation of the magnetic resonance study.

Mam-C4

MRI OF AVASCULAR NECROSIS OF THE FEMORAL HEADS. PART I: CLINICAL - PATHOLOGICAL CORRELATION.

Jane M. Burk, M.D., Javier Beltran, M.D., Leigh J. Herman, M.D., R. Marvin Freedy, MS4, Jonathan B. Baktari, MS4, Andrea Yang, BS, Wilhelm Zuelzer, M.D. (2)

Ohio State University Hospital, Department of Radiology & Orthopaedic Surgery (2)

Early detection of avascular necrosis of the femoral head is important as early treatment aimed to halt the continued ischemic injury and to thereby prevent collapse of the femoral head can only be instituted once the problem is defined. A total of 65 patients, 129 hips, were imaged to rule out AVN in a symptomatic patient population at high risk for developing AVN due to long term steroid use. Clinical - pathological correlation was obtained in 42 patients (83 hips). Comparison of imaging modality sensitivity showed MRI to be 74% sensitive, 94% specific and 82% accurate. Bone scintigraphy by comparison was 68% sensitive, 79% specific and 72% accurate. MRI proved to be more accurate primarily due to its superior specificity. The high specificity of MRI renders its positive predictive value in detecting AVN to be 95%. This is superior to any other noninvasive diagnostic tool. Additional comparisons between MRI and bone scintigraphy will be discussed as well as our recommendations for approaching the patient with suspected AVN.

Mam-C5

MR IMAGING OF AVASCULAR NECROSIS OF THE FEMORAL HEAD

Jesse M. Cohen, M.D., Jeffrey C. Weinreb, M.D., George Muschler, M.D., Lawrence Wolbarsht, M.D., William A. Erdman, M.D., John Childers, M.D.

University of Texas Health Science Center at Dallas, Dallas, Texas

Magnetic resonance (MR) imaging is the most sensitive non-invasive method for detecting avascular necrosis (AVN) of the femoral head. The principal advantage of MR appears to be the ability to diagnose early AVN before nuclear bone scan or plain x-rays become positive. Advances in the orthopedic management of patients with AVN make early detection critical for surgical success and reduced patient morbidity. Despite resports on the MR appearance of AVN and the sensitivity of MR in comparison with other diagnostic modalities (plain films, bone scan, CT), the precise role of MR in the evaluation of patients with suspected AVN has yet to be established. In addition, the histopathological changes necessary for MR detection, and thereby the potential limitations of MR, have not been defined.

One hundred ten femoral heads (57 subjects) were studied (0.35 Tesla) in the coronal and transverse planes utilizing relatively T1 and T2 weighted multiple spin echo pulse sequences. AVN was diagnosed on the basis of decreased signal intensity involving the weightbearing surface of the femoral head. Results were compared with plain films of the hip (N=37), nuclear bone scan (N=27) and axial CT scans (N=17) obtained within 3 weeks of MR. Seventeen patients (29 hips) underwent surgery to establish the diagnosis of AVN vis-a-vis bone marrow pressures and intraosseous venography. Once AVN was confirmed, treatment consisting of "core decompression" was instituted in 28 cases.

All hips positive for AVN on x-ray, bone scan or CT were positive with MR (N=60). Five cases of surgically proven AVN were detected with MR despite normal radiographs and bone scans. Histopathologic analysis revealed focal areas of intramedullary fat degeneration throughout the bone marrow. Three cases of surgically confirmed AVN had normal MR studies, films, and bone scans. In the cases, only minimal marrow fat degeneration was appreciated with maintenance of the intramedullary lipid spaces.

Fifteen patients underwent serial MR examinations including seven following core decompression. Collapse of the femoral head and/or more widespread low signal correlated with clinically progressive disease (N=2) or persistent postoperative symptoms (N=2). No interval change in the MR signal characteristics or integrity of the femoral head was seen in 5 asymptomatic postoperative patients and in 6 patients with an unchanged clinical course who were not operated on.

In view of our findings, a reasonable and cost-effective approach in detecting AVN should first include a plain film since many patients will have already progressed past the preradiographic phase to Stage II disease. If films prove negative, MR should be the next diagnostic study performed; however, patients with

only minimal marrow fat degeneration may have a false negative study and more invasive diagnostic studies may be necessary. MR also appears to be an effective means of following possible progression of disease in patients with known AVN.

Mam-C6

THE UNIQUE MRI APPEARANCE OF THE REACTIVE INTERFACE IN AVASCULAR NECROSIS: THE DOUBLE LINE SIGN

D.G. Mitchell[1], H.Y. Kressel, V.M. Rao[1], P.M. Joseph, M.K. Dalinka, M. Fallon[2], M.E. Steinberg[3]
Department of Radiology, Pathology[2], or Orthopedics[3], The Hospital of the University of Pennsylvania, Philadelphia, Pennsylvania
1: Present address: Department of Radiology, The Thomas Jefferson University Hospital, Philadelphia, Pennsylvania

INTRODUCTION: The most characteristic histopathologic feature of avascular necrosis (AVN) of the femoral head (FH) is the reactive interface between live and dead bone, which consists of peripheral sclerosis surrounding a zone of vascular granulation tissue. To determine if this reactive interface can be depicted by MRI, we reviewed MRI examinations of 56 proven lesions and 6 resected specimens.

MATERIALS AND METHODS: In-vivo AVN lesions were imaged with a commercially available 1.5T MRI unit using a body coil. Ex-vivo FH's were imaged with a 1.4T research MRI unit using a 7.5 cm cylindrical coil. All in-vivo and ex-vivo MRI examinations included both short (TR 400-1000 msec, TE 15-25 msec) and long (TR 2000-2500 msec) TR/TE spin echo images. Corresponding CT examinations were available for 15 of the 56 in-vivo and all 6 ex-vivo AVN lesions. Following MRI examination, FH specimens were sectioned, photographed, radiographed, and prepared for histologic analysis.

RESULTS: In all 6 resected FH's a peripheral rim of sclerosis was observed surrounding the lesion. This corresponded to a rim of low MRI signal intensity. Inside this was a thin zone of vascular granulation tissue, which had low to intermediate intensity with long TR/TE. On long TR/TE MR images, therefore, the reactive interface was depicted as a characteristic "double line". This "double line sign" was present in 80% (45/56) of in-vivo AVN lesions, allowing a specific MRI diagnosis to be made. In advanced lesions, available CT examinations showed the high intensity zone to correspond to fractures, while in early lesions no fracture was depicted.

CONCLUSIONS: The characteristic reactive interface between live and dead bone at the periphery of AVN lesions has a distinctive appearance on long TR/TE MR images. This consists of a zone of high signal intensity within a low intensity peripheral rim. Because it reflects the unique histopathology of bone necrosis, we consider this "double line sign" pathognomonic of AVN.

Coronal MR images, TR 2500 msec, TE 80 msec. The "double line sign" consists of a low signal rim (black arrows) surrounding a zone of high intensity (white arrows.)

Figure 1: Early AVN lesion in-vivo

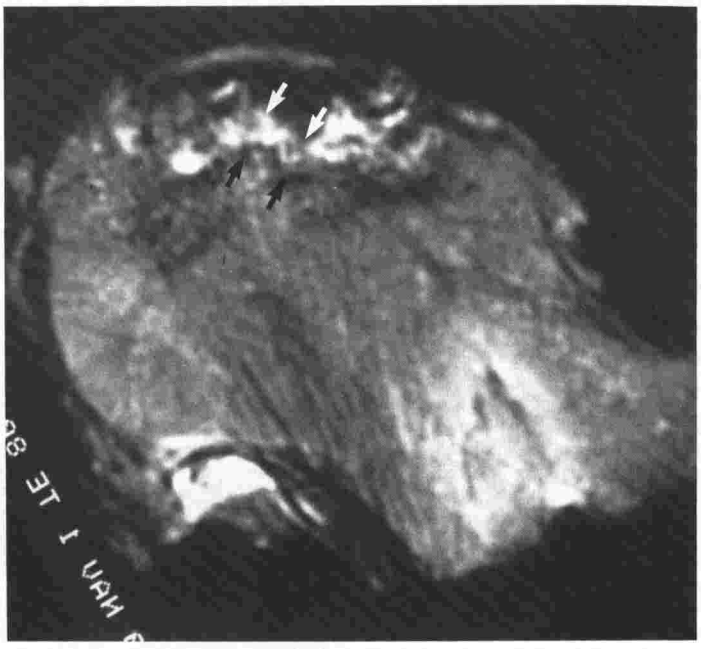

Figure 2: Advanced AVN lesion ex-vivo

(Mam-D) SPECTROSCOPY - MULTINUCLEAR

Presiding: C. L. Partain & R. Nunnally

10:20 am

ROOM C-102

12 MINUTES PER PRESENTATION

Mam-D1

LOCALIZED ^{31}P NMR SPECTROSCOPY IN NORMAL AND INFARCTED HUMAN HEART

P. A. Bottomley, R. J. Herfkens*, L. S. Smith and T. M. Bashore*

General Electric Corporate Research and Development Center, Schenectady, New York and *Duke University Hospital, Durham, NC

^{31}P NMR spectra can be obtained nonivasively from localized volumes in the human anterior myocardium using the depth resolved surface coil spectroscopy (DRESS) technique at 1.5 T in acquisition times of order 5 min (1). The precise locations of localized volumes relative to the heart are preselected in ^{1}H surface coil images recorded immediately prior to the spectroscopy examination. ^{31}P spectra acquired as a function of depth in the chest exhibit a discontinuous drop in PCr/ATP ratio upon moving from chest to heart muscle, and a sudden drop in all metabolites as the ventricle is entered (1). Gated DRESS spectra acquired as a function of cardiac cycle exhibit no significant variation in high energy metabolite ratios, but some variations in blood 2,3 diphosphoglycerate (DPG) are sometimes observed. The absence of blood DPG often encountered in spectra from anterior myocardium may reflect the sharper depth localization sensitivity profile of the DRESS method compared to other current approaches that employ RF gradients: the proportion of blood in cardiac muscle is much less than that in the ventricle.

Clinically stable male and female patients aged 38 to 70 suffering acute anterior myocardial infarction were studied by gated ^{31}P DRESS with image localization as described above (2). Infarction was confirmed by ECG, creatine kinase enzyme levels and cardiac catheterization. Significantly reduced PCr/Pi ratios and elevated Pi/β ATP compared to normal ratios were detected in the anterior myocardium of patients ($p<0.005$). The results are consistent with canine DRESS studies of anterior myocardial infarction produced by coronary occlusion (3).

1. Bottomley PA. Science 229, 769-772 (1985).
2. Bottomley PA, Herfkens RJ, Smith LS, Bashore TM (submitted for publication 1985).
3. Bottomley PA, Smith LS, Brazzamano S, Hedlund LW, Redington RW, Herfkens RJ. (Submitted for publication 1985.

Mam-D2

IN VIVO PHOSPHORUS-31 SPECTROSCOPY AT 1.5 TESLA OF HUMAN MYOCARDIUM

David B. Kaplan*, Mary Osbakken+, Gerald L. Wolf*

The Pittsburgh NMR Institute, 3260 Fifth Ave., Pittsburgh, PA 15213
Biochemistry/Biophysics and Anesthesia Departments, University of Pennsylvania, Philadelphia, PA 19104

Some in vivo spectroscopy experts[1] have stated that the basic instrumentation for excellent MRI and MRS may be mutually incompatible at current field strengths. Further, the unique capabilities of prototype equipment and highly skilled support staff may preclude excellent MRI and MRS in a production device within a clinical setting. We utilized a GE Signa with a spectroscopy research package to perform ^{31}P spectroscopy of the human myocardium. Images were obtained with the normal multi-echo, multi-planar, spin warp sequence, transmitting with the body coil, and receiving with a three-inch surface coil. Spectra were obtained from a selected region of interest via depth-resolved surface coil spectroscopy (DRESS) with an eight-inch transmit, three-inch receive (actively decoupled) surface coil tuned to 25.86MHz. For both imaging and spectroscopy the patient was placed prone such that the heart was centered directly over the coil. It should be emphasized that this was accomplished at a busy clinical site that performs more than 25 high quality MRI scans (in two signa systems) per day. The operator has a B.S. degree with practical experience in spectroscopy, and the co-authors are practicing M.D.'s with biological research expertise.

The myocardial spectrum shown below was obtained by gating the RF pulse to the ECG, with a TR of approximately 800 ms. The selected volume was a 2 cm thick slice through the heart wall, and represents the average of 512 transients. Spectral resolution was superb, clearly delineating resonances from PCr; all three phosphates from ATP with some resolution of J-coupling; P_i; and phospho-mono and -diesters.

Conclusion:
We conclude that state-of-the-art spatially localized ^{31}P spectroscopy can be performed in vivo with a commercial instrument (Signa, General Electric. Milwaukee) that also provides excellent clinical MR imaging.

References:
1. Radda GK: Magnetic Resonance Spectroscopy in Clinical Medicine. Proc XVI International Cong Radiol, 5-10, 1985.

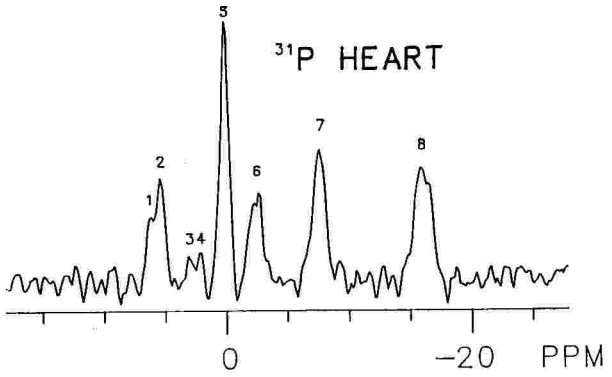

Figure 1. ^{31}P spectrum showing: 1)PM, 2)P_i, 3&4)PD, 5)PCr, 6)γ-ATP, 7)α-ATP, 8)β-ATP

Mam-D3
MYOCARDIAL REPERFUSION: EFFECTS OF VENTRICULAR FIBRILLATION ON LOCAL METABOLISM: A31P NMR STUDY

Roger B. Rehr, M.D., Lewis Wetstein, M.D., James Tatum, M.D., and Geoffrey Clarke, PhD.

Departments of Cardiology and Radiology, Medical College of Virginia, Richmond, Virginia

Introduction: The effects of ventricular fibrillation on myocardial metabolism in acute myocardial infarction with therapeutic reperfusion are potentially important but unknown. The purpose of this study was to compare ischemic-zone myocardial metabolism with one hour of coronary artery occlusion followed by 5 hours of reperfusion in animals with (Group VF:n=5) or without (Group NVF:n=8) ventricular fibrillation. A control group (Group C:n=5) of animals without coronary occlusion was also included for comparison.

Methods: The canine open-chested model of LAD ligation and reperfusion after one hour was used. A 1.5 cm diameter surface coil was sutured to the epicardial surface of the risk zone and 31P spectra acquired at 15 minute intervals, at a frequency of 42 MHz. Intracellular pH (pH), inorganic phosphate (Pi), phosphocreatine (PCR), and adenosine triphosphate (ATP) were compared among groups at baseline and at 0-1, 1-3, and 3-5 hours following reperfusion using the RGEW multiple range multiple comparisons procedure. A p value of less than 0.05 was considered be statistically significant. The REGW procedure was also used to examine the control group for significant variation in any variable over time, as a test of the stability of our model.

Results: The control group showed no significant variation in any parameter over the course of the experiment. There were no significant differences in any parameter among groups at baseline. Both groups VF and NVF exhibited metabolic evidence of severe myocardial ischemia when compared with Group C during the period of total coronary occlusion. There were no significant metabolic differences between groups VF and NVF during total occlusion. Infarct size did not differ between groups VF and NVF, although the risk region was larger ($p<0.05$) in the latter group.

Results of the baseline and post-reperfusion measurements are shown in the table:

Group	Metabolite	Baseline:	0-1 hr#	1-3 hr#	3-5 hr#
Group C	pH	7.22 +/- 0.03	7.26 +/- 0.03	7.21 +/- 0.03	7.25 +/- 0.05
Group NVF	pH	7.24 +/- 0.03	7.30 +/- 0.05	7.25 +/- 0.02	7.27 +/- 0.03
Group VF	pH	7.26 +/- 0.05	7.24 +/- 0.03	7.35 +/- 0.02*$	7.37 +/- 0.02*$
Group C	Pi	0.13 +/- 0.03	0.28 +/- 0.11	0.14 +/- 0.05	0.08 +/- 0.01
Group NVF	Pi	0.22 +/- 0.02	0.33 +/- 0.05	0.30 +/- 0.02*	0.31 +/- 0.03*
Group VF	Pi	0.18 +/- 0.03	0.28 +/- 0.04	0.30 +/- 0.02*	0.34 +/- 0.03*
Group C	PCR	1.12 +/- 0.08	1.08 +/- 0.05	1.11 +/- 0.07	1.10 +/- 0.09
Group NVF	PCR	1.00 +/- 0.02	0.85 +/- 0.04*	0.98 +/- 0.02*	0.94 +/- 0.02
Group VF	PCR	1.02 +/- 0.01	0.76 +/- 0.07*	0.87 +/- 0.05*	0.99 +/- 0.09
Group C	ATP	0.55 +/- 0.02	0.60 +/- 0.05	0.55 +/- 0.05	0.55 +/- 0.03
Group NVF	ATP	0.52 +/- 0.02	0.28 +/- 0.04*	0.28 +/- 0.02*	0.29 +/- 0.03*
Group VF	ATP	0.55 +/- 0.03	0.23 +/- 0.03*	0.25 +/- 0.01*	0.30 +/- 0.02*

All values are mean +/- s.e. #post-reperfusion * vs Group C $ vs Group NVF

Conclusions: No evidence of a significantly detrimental metabolic effect of ventricular fibrillation was noted in infarcted, reperfused myocardium. Reperfused myocardium which had suffered ventricular fibrillation was found to be alkalotic with repect to both control animals and those animals which did not suffer ventricular fibrillation with coronary occlusion.

Mam-D4

THERAPY RESPONSE OF HUMAN TUMORS MONITORED BY IN VIVO 31-P-SPECTROSCOPY

Semmler W, Gademann G, Backert-Bauma P, Zabel M-J, van Kaick G, Lorenz W-J

German Cancer Research Institute, D-6900 Heidelberg 1, Im Neuenheimer Feld 280, W-Germany

PURPOSE

The purpose of this study is to investigate whether tumor therapy can be improved using 31P-spectroscopy as a monitor.

INTRODUCTION

It was shown in experimental animals that 31P-spectroscopy is an effective tool to monitor the high energy phosphorous metabolism. The method can be used for in vivo studies of metabolic disorders of pathological processes like cancer. Tumors as compared to other tissues show elevated phosphomonoester, phosphodiester and inorganic phosphate peaks and reduced phosphocreatinine levels.

MATERIAL AND METHOD

A total of more than 20 patients was examined. In 6 of these patients short and/or long term follow up examinations after chemotherapy and/or radiation therapy were performed. Only patients with superficial tumors were included in the study. An extensive protocol including diagnostic MR-imaging was performed and long term follow up was extended up to 7 months after therapy. In the short term follow up studies, the chemotherapy was started when the patient was positioned in the MR-imager. All images and 31P-spectra were obtained with a 1.5 Tesla imager. Spectra were taken only, if the frequency resolution was better than 0.5 ppm. Spectra were analyzed by a least square fit program. Up to 9 lines could be fitted simultaneously with FWHM, integral and peak position as parameters. The contribution of immobile phosphorous atoms was eliminated by subtraction of the background, which was defined by a spline function.

RESULTS AND DISCUSSION

We observed high quality 31P-spectra with home-built surface coils. In our long term follow up studies after chemotherapy (osteosarcoma, neuroectodermal tumor), we observed an increase in the ratio of PCr/Pi and in the sum of PCr+Pi. No significant change in pH could be observed. In the short term follow up study the immediate effects of chemotherapy were investigated. Up to three hours after application only a slight decrease of PCr/Pi and pH can be detected. In the follow up of a malignant melanoma chemotherapeutics were applied in high dosage by an extracorporal circuit. 31P-spectra show a distinct change after 24 hours before any clinical sign of tumor response can be observed. Our results show that tumor tissue is metabolically almost inactive after therapy whereas muscle tissue is almost not effected by chemotherapy.

CONCLUSION

31P-spectroscopy is capable to monitor tumor response after treatment. 31P-spectroscopy can detect therapy response of tumor within the first 24 hours, when clinical methods still fail.

Mam-D5

PROGRESSIVE DEFECT IN CEREBRAL ENERGY METABOLISM IN PATIENTS WITH HEPATIC ENCEPHALOPATHY (HE)

B D Ross[+*], M Y Morgan[#], I J Cox[+*], K M Hawley[#], and H Hodgson[+]

[+]NMR Unit, Royal Postgraduate Medical School, Hammersmith Hospital, London
[*]GEC Research Laboratories, Hirst Research Centre, Wembley
[#]Medical Unit, Royal Free Hospital, London.

Cerebral energy metabolism is thought to be impaired in patients with persistent hepatic encephalopathy (HE); oxygen consumption and glucose uptake across the cerebral circulation are reduced. Treatment results in improved cerebral oxygen consumption but blood flow may remain lower than normal. This suggests that a residual defect in cerebral energy metabolism occurs even in patients receiving treatment. Successful treatment of complex organic brain disease requires further understanding of the nature of this defect. 31P MRS is ideally suited to examining this problem.

A standard test of cerebral metabolic function has been developed, using 31P phosphorus magnetic resonance spectroscopy, to determine cerebral high energy phosphates ([ATP]; [PCr]), inorganic phosphate [Pi] (Pi/PCr; Pi/ATP) and of intra cerebral pH in a constant volume of the forebrain. Eight patients with proven HE (mean age 56 years), and eight control subjects (mean age 51 years) were examined. In the patients, cerebral blood flow, 0_2 consumption, glucose uptake and blood bicarbonate, phosphate and standard liver function tests were performed. All patients were examined with MRS while receiving their normal treatment. Psychometric tests of cerebral function were also performed, 30 minutes before 31P MRS examination. Spectra were obtained in a 1.5T Picker prototype spectrometer, using separate transmitter and receiver antenna; one 1H and three 31P spectra were completed within 30 minutes. In selected patients the volume of brain examined was also determined using MRI (Picker prototype: 0.15T). The resultant spectra were predominantly from the frontal hemispheres. The contribution of skeletal muscle to the final 31P spectra was consistently less than 5%, while skull and meninges were readily eliminated from the spectrum. Relative concentrations of metabolites in the spectra were determined from peak areas, and pH from the chemical shift of Pi.

Results HE patients had normal 1H and 31P spectra judged from the number and chemical shifts of the peaks. Intracerebral pH was unaltered (6.93 ± 0.06 vs 6.97 ± 0.04 in controls. [PCr]/[ATP] was unchanged.

A significant reduction in intracerebral [Pi] was observed in HE subjects (Pi/ATP = 0.29 ± 0.03; Pi/PCr = 0.17 ± 0.01) compared with normal subjects (Pi/ATP = 0.46 ± 0.06; Pi/PCr 0 0.27 ± 0.03: N = 8, P less than 0.01 (student t test)). Plasma (Pi) was identical in the two groups.

We conclude that 31P MRS demonstrates a defect in cerebral energy metabolism in HE, and suggest that the previously noted reduction in cerebral oxygen consumption may be the direct result of reduction in intracerebral Pi content, below the K_m for synthesis of ATP. In a further series of patients, there were indications that increasing severity of HE, to coma grades II and III emphasised the cerebral energy defect.

MRS could provide a sensitive, non-invasive test of cerebral function in hepatic encephalopathy and other organic brain syndromes.

Mam-D6

RAPIDLY SEQUENTIAL FLUORINE AND PROTON MAGNETIC RESONANCE IMAGING USING A VARIABLE MAGNETIC FIELD STRENGTH APPROACH.

Adam V. Ratner, M.D., David Parish, B.S., Beverly Bradley-Simpson, B.S., Holde Muller, M.S. and Stuart W. Young. M.D.

Stanford University School of Medicine, Stanford, California 94305.

Proton MRI has proven useful in the delineation of anatomy and allows the detection of many pathological processes. This modality, however, often suffers from a lack of specificity in the delineation of disease as well as the inability to characterize many physiologic and pathologic processes. Previous work has shown that F19 magnetic resonance techniques have been able to provide some insight into physiologic and metabolic processes. Because the magnetogyric ratio of the F19 nucleus is roughly 6% lower than that of the proton, raising the ambient magnetic field by 6% will allow imaging of the F19 nucleus in a system previously optimized for proton MRI. Using the Resonex RX-4000 whole body magnetic resonance imaging device with a variable magnetic field strength up to .4 tesla, it is possible to perform proton imaging at .38 tesla and fluorine imaging at .4 tesla at a constant radiofrequency of approximately 16.1 MHz. Initially a phantom consisting of a vial of 1 molar sodium fluoride, a vial of a polyfluorinated low molecular weight chemical (SRI 4552), and a vial of water underwent fluorine imaging on the RX-4000. Only the sodium fluoride and the SRI 4552 vials were detectable. No signal emanated from the water containing vial. Subsequently, the magnetic field strength was reduced to approximately .38 tesla, and proton imaging was performed without repositioning of the phantom. On the proton image all three samples were visualized. Using a similar approach, hamsters injected with perfluorooctyl bromide emulsion, a reticuloendothelial system labelling agent, underwent both fluorine and subsequent proton imaging. Signals coming from the liver and spleen regions were detected on the fluorine image. Anatomic correlation with proton images was obtained subsequently without repositioning the animals.

Performing fluorine and proton imaging using this approach requires no RF retuning at any stage. Thus, the coil used for proton imaging can be used for fluorine imaging without replacement or retuning and repositioning the object to be imaged is not necessary. From a practical perspective this allows optimal registration of image data from the fluorine image with the more anatomical proton image.

Mam-D7

F19 IN VIVO SPECTROSCOPY OF NEOPLASMS.

Adam V. Ratner, M.D., Chris Sotak, Ph.D., Holde Muller, M.S., Ralph Hurd, Ph.D. and Stuart W. Young, M.D.

Stanford University School of Medicine, Stanford, California 94305 and GE NMR, Fremont, California 94539.

F19 NMR techniques may allow the delineation of metabolic processes as well as the detection and characterization of pathology. Previous work in our laboratory has shown that perfluorooctyl bromide (PFOB) emulsion, a reticuloendothelial system labelling agent, can be detected in the liver and spleen using F19 MRI. In addition, this agent also allows the detection of neoplastic processes.

Two mice each with a previously implanted intradermal RIF tumor received 10 ml/kg of PFOB emulsion. One hour after injection of PFOB, proton images were acquired of these mice using a GE NMR CSI-2 2 tesla imaging/spectroscopy system. The positions of the tumors were noted 3-dimensionally by imaging along two different axes. From these images the coordinates of the tumor were determined and used for localization in a 3-dimensional

ISIS F19 spectroscopy sequence. Voxel sizes of 1 cm, 7 mm and 5 mm on a side were used. With this technique, fluorine signal from PFOB was detected in the tumor in all three voxel sizes. The presence of PFOB within this tumor may be due either to leakage of the emulsion through endothelial gaps in tumor blood vessels or possibly from uptake by local macrophages at the inflamed tumor site. This technique, using either PFOB or perhaps some other fluorinated agent may be useful clinically in the detection and perhaps characterization of neoplasms.

Mam-D8

NATURAL ABUNDANCE CARBON-13 NMR IMAGING OF THE HUMAN ARM

J.Hasegawa,N.Iriguchi,Y.Ueshima,T.Yamamoto,S.Yamai,T.Miyazaki,K.Hikida,H.Toyoshima,T.Maki

Systems Engineering Laboratory,Asahi Chemical Industry Co.,Ltd.
221 Tanazawa,Atsugi,Kanagawa 243-02 Japan

Introduction: The interest in human C-13 imaging is significantly increasing. However,C-13 is only 1.1% in natural abundance, has sensitivity of only 1.6% of 1H, and has overall molar concentration of roughly 0.1% of 1H in the subject.

Methods: A cylindrical coil was installed in a 1 m bore 2 tesla system, Asahi Super 200. The right upper arm was put through the coil. Spectroscopy and imaging were carried out. The imaging was by Saturation Recovery for 128×128 matrix size with Tr of 1,000ms. The frequency was set for the C-13 NMR frequency of -CH2-, the fatty acyl chain. No C-13 enrichment nor 1H decoupling was introduced.

Results: Fig.1 shows the C-13 spectrum of the human upper arm. Fig.2 shows the C-13 image of the human upper arm of 10 cm slice thickness. The image was 64 times averaged. The subcutaneous fatty tissue and the bone marrow were recognized. The S/N was around 5.

Conclusion: We attained natural abundance C-13 NMR imaging of the human arm. The investigation should prove to be efficacious in the study of spatial differences in physiochemical structure or function of the human subject.

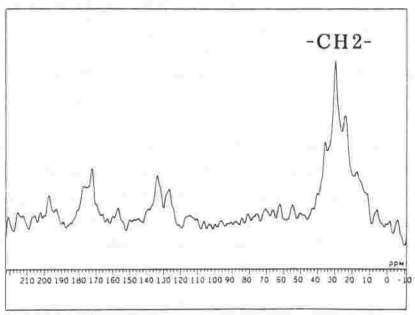

Fig.1

Fig.2

(Mpm-A) VASCULAR FLOW

Presiding: I. R. Young & J. Frahm

3:20 pm

RIVER ROOM

12 MINUTES PER PRESENTATION

Mpm-A1
MAGNETIC RESONANCE ANGIOGRAPHY

D.G. Nishimura, J.M. Pauly, A. Macovski, J.I. Jackson, S.M. Conolly

Department of Electrical Engineering, Stanford University, Stanford, CA 94305

We have studied a variety of methods for projection angiography that isolate blood via mechanisms involving velocity-dependent phase shifts or time-of-flight effects.

In one subtractive method, a first image is based on reduced, incoherent signals from blood due to velocity-dependent dephasing, a second image based on relatively large, coherent signals due to rephasing. Changes in the first moment of the gradient waveform, embodied typically by the phase-encoding or readout gradients, create the dephasing and rephasing effects which lead to flow sensitivity in the direction of the gradient.

A second method under study employs a sequence of excitation pulses in conjunction with flow-encoding gradients to produce a net excitation of flowing blood only, with static material driven back to equilibrium. Care is taken to reduce errors introduced by both main field and RF inhomogeneities. This excitation sequence can be incorporated by other angiography methods to significantly improve the dynamic range of the signals generated.

We have also developed a subtractive method based on time-of-flight effects where the region excited by the 180° inversion pulse in an inversion recovery sequence varies between measurements. Blood flowing into an imaged slab during the interval between the inversion pulse and 90° readout pulse experiences the inversion for one of the two measurements while static material in the slab receives the same excitation for both measurements. Complex subtraction therefore cancels static material and leaves a signal from the differentially tagged blood. By specifying the inverted regions appropriately, one-way direction sensitivity can be established to image either arterial or venous flow. Because time-of-flight effects provide the flow sensitivity, flow-related artifacts and signal loss are minimized by employing flow-insensitive gradient waveforms and timing the readout to diastole. Implementation was done on a GE 1.5 T Signa system, producing a carotid arteriogram shown below (128 x 256 image, 4 min acquisition, 12 cm x 9 cm field of view).

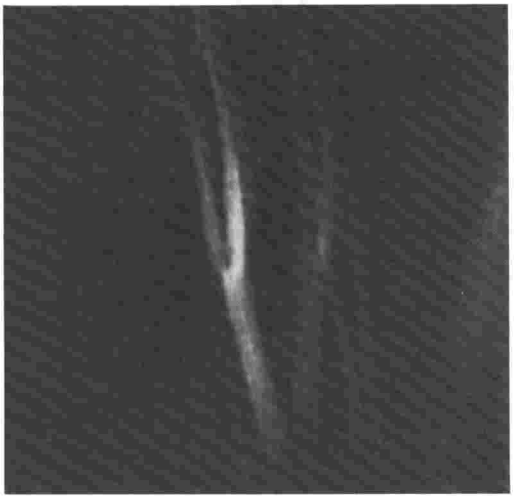

Mpm-A2

MAGNETIC RESONANCE ANGIOGRAPHY - A NEW FAST SCANNING TECHNIQUE

C. L. Dumoulin, S. P. Souza and H. R. Hart Jr.

General Electric Corporate Research and Development Center,
PO Box 8, Schenectady, New York 12301

The phase contrast technique of MR angiography (1) has been modified and extended. The original version of the technique employs a gradient refocused spinwarp imaging pulse sequence which is augmented with bimodal flow encoding gradients. The phase of the RF pulse is kept constant and the phase of the flow encoding gradient pulses is inverted on alternate data acquisitions. The pulse sequence is synchronized to the patient's heart to insure that the blood velocity is consistent for each data acquisition. In the new technique, cardiac gating is not employed and data are acquired as rapidly as possible. Flow compensation gradient pulses have also been added to enhance image quality. A typical pulse sequence uses a TR of 33 msec, TE of 28 msec, a 128x256 data matrix and NEX of 16 to 64. Total scan time can be as short as 1 min. For examinations of the carotid arteries (and other long vessels) a saturating RF pulse can be used to remove venous flow from the image. Projection images can be obtained for any view angle and the projection can be constrained to a thick imaging slice if desired.

The use of a fast scanning technique provides greater suppression of non-moving spins in addition to reducing imaging times. The extensive signal averaging removes artifacts due to the pulsatile nature of the blood flow and also provides a measure of average blood flow instead of flow at a given point in the cardiac cycle.

1. C. L. Dumoulin and H. R. Hart Jr., "MR Angiography" Radiology (December 1986).

Mpm-A3

EVALUATION OF PULSATILE FLOW USING LIMITED FLIP ANGLES AND GRADIENT REFOCUSSED ECHOES

Avery J. Evans, B.A., Robert J. Herfkens, M.D., Laurence W. Hedlund, Ph.D., Russell Blinder, M.D., Evan K. Fram, M.D., Joseph A. Utz, M.D.

Department of Radiology, Duke University Medical Center, Durham, N.C. 27710

The use of magnetic resonance (MR) imaging for evaluating vascular flow, both quantitatively and qualitatively, is now well established. Unfortunately, in spin echo imaging, signal intensity generally decreases with increasing blood flow, conseqently, at physiologic velocities, accurate measurement of flow velocity is not possible. CINE GRASS (gradient refocussed acquisition in the steady state) is an imaging technique that uses gradient refocused echos and limited flip angles with short repetition times (TR=21 ms) to produce rapid (two minutes) and anatomically precise images of the beating heart. Since CINE GRASS signal intensity increases with increasesing flow, this technique may allow the determination of flow velocities.

A flow phantom was constructed with Tygon tubing, and an electro-pneumatic valve controlled by a solid state device created pulsatile flow analogous to that found in large to medium sized arteries. This solid state device also generated an artificial QRS complex that gated the scan. Inline electromagnetic flow probes were used outside the magnet room to determine instantaneous velocities in the lumen. Signal intensity in the lumen was determined using an eliptical region of interest.

In these experiments signal intensity increased linearly with pulsatile flow mean velocity up to 30.1 cm/s ($r=.970$). In addition, the graphs of the change in signal intensity through the "R to R" interval were virtually superimposable on the actual pulsatile flow velocity profiles (changes in instantaneous velocities), $r>.897$ for velocities between 4.0 and 16.6 cm/s.

This functional information can potentially aid in the evaluation of cardiovascular pathology characterized by derangements from normal flow patterns, and is collected noninvasively without the use of contrast media.

Mpm-A4

IN-PLANE FLOW QUANTIFICATION ALONG THE PHASE ENCODING AXIS USING MAST™ GRADIENTS INSENSITIVE TO HIGHER ORDER DERIVATIVE TERMS

J. L. Duerk, Ph.D. and P. M. Pattany, M.Sc.

Mt. Sinai Medical Center, Cleveland, Ohio 44106 and Clinical Science Center, Picker International, Highland Heights, Ohio 44143

Flow quantification in MRI has typically been used for fluids traveling perpendicular to the imaging plane. Flow quantification for in-plane fluid motion is also possible. Recent work demonstrated in-plane flow quantification along the read axis, exploiting the balanced bipolar nature of the gradient by the echo time. This work describes a new method for flow velocity quantification along the phase encoding axis which is both insensitive to higher order derivitive terms and eliminates problems common to quantification along the read axis.

In-plane flow quantification along the frequency encoding axis has been demonstrated in the past by Wedeen, et. al.. However, as Van Dijk and others have recognized, a time dependent phase term evolves during data collection which leads to a complex convolving function in the final image. This convolving function produces errors in phase angle dependent velocity quantification in many few cases. This error may be small if the velocities along the read axis are small, if the vessel is parallel to the axis, and if the flow is steady and laminar. Unfortunately, these situations rarely occur in the body. Secondly, higher velocity flow rates are often seen as "flow voids" in MR images. For these reasons, modified spin echo imaging gradients were developed to completely rephase moving spins, and encode velocity in the phase encoding direction as the phase angle between the real and imaginary images obtained from 2DFT reconstruction.

The phase encoding gradient is split into two sections. The first, before the pi pulse, performs only position encoding with no sensitivity to velocity, acceleration or pulsatility for each view. It is incorporated into an imaging pulse sequence which ha s slice select and read gradients which satisfy the motion artifact suppression technique (MAST™) requirements of zero valued moments at the echo time. The MAST™ gradients allow virtually complete recovery of spins commonly dephased (flow voids) in standard MR imaging gradients by refocusing all velocity, acceleration and pulsatility induced phases. This signal recovery allowed flow quantification over a wider range of in-plane flow velocities than previously attained. The second part of the gradient occurs after the pi pulse. This section is insensitive to position, acceleration and pulsatility. It is sensitive to velocity. It is not scaled during the various phase encodings so that the same velocity encoding is obtained in each view. The position encoding of the first portion and the velocity encoding of the second can be considered separately by the principal of superposition. The image maintains its velocity/phase relationship after 2DFT reconstruction allowing for quantification. Phase images from encoding and non-encoding gradients are subtracted to eliminate static field inhomogeneity, RF inhomogeneity, and incomplete rephasing effects. Further, the two images are obtained interleaved in time to reduce time dependent system errors. Here, identical rows of Fourier space are acquired sequentially using the encoding and non-encoding phase gradients.

The pixel's phase value must accurately reflect that of the mean velocity within that voxel. This requires that velocity induced phase angles be less than or equal to approximately 60 degrees over the velocity range of interest. Flow rates ranging from 0.55 to 2.5 gallons per minute (GPM), corresponding to mean velocities of 13.2 to 55.3 cm/sec were measured using this technique. The maximum flow encoding was set to 180 degrees at 100 cm/sec. Figures I shows the phase difference image of the tubes and static phantom at 1.5 GPM. Note the opposite sign of the pixel values arising from the flow in opposite directions in the inlet and outlet lines. Estimation of the tube radius from the phase image was used to determine the cross-sectional area of the tube. The mean velocity determined from the phase map was then used with the area estimate to predict the total volume flow rate. A comparison of the MR predicted and actual flow rates is shown in Figure II. Errors in predicted both mean velocities and volume flow rates were less than or equal to 8.0% over a velocity range from 13.2 to 55.3 cm/sec.

Initial phantom studies indicate that in-plane flow encoding along the phase axis is an accurate method for flow velocity quantification when combined with motion artifact suppression technique (MAST™) gradients which rephase flowing spins. Accurate flow velocity quantification has been obtained with the further advantage of motion artifact reduction. A wider range of flow velocities was imaged than obtainable using standard imaging gradients with additional bipolor flow encoding lobes. Further clinical experimentation on volunteers is being examined.

FIGURE I

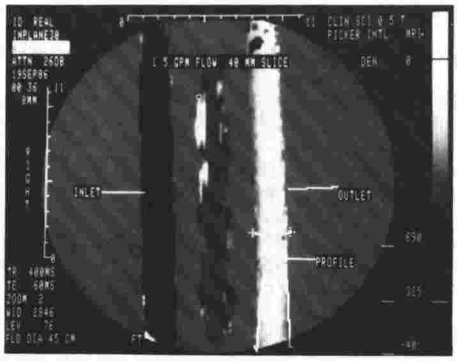

FIGURE II

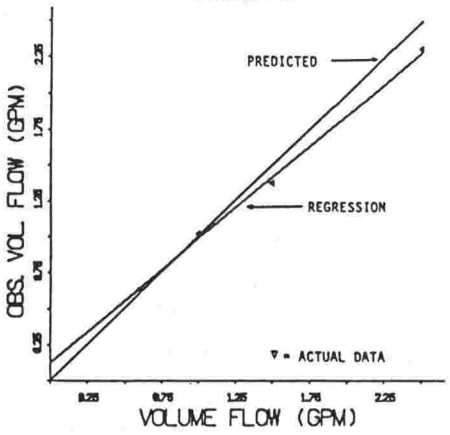

REFERENCES

Wedeen, V. J., et. al., JCAT, Vol. 9, No. 3, pp. 530-536, 1985.

van Dijk, P.. and van Mierlo, C.P.M., Proc. of SMRM Fourth Annual Meeting, pp. 572, 1985.

Moran, P. R.. Mag. Res. Imag., Vol. 1, pp. 195-207, 1982.

Pattany, P.M., et. al., Motion Artifact Supression Technique for MRI, Patent Application 766,757, filed August 16, 1985.

Mpm-A5

PHASE RECONSTRUCTION OF MAGNETIC RESONANCE IMAGES IN THE DETERMINATION OF CARDIAC WALL AND BLOOD VELOCITY AND THE POSSIBLE EFFECTS OF ACCELERATION.

J. Katz, R.M. Peshock, P. McNamee, S. Schaefer, C.R. Malloy, R.W. Parkey

Departments of Radiology and Cardiology, The University of Texas Health Science Center at Dallas

Phase reconstruction of magnetic resonance images can yield useful information regarding cardiac wall velocity and blood velocity. Phase images were evaluated in a phantom of continuous laminar flow and turbulent flow. The phase images were sensitive to small velocities ($v \approx 0.6$ cm/sec) and showed phase shift which were linearly proportional to flow velocity. Aliasing occurred at relatively low velocities ($v \approx 7.5$ cm/sec).

Use of phase reconstruction in the determination of fluid velocity for pulsatile flow or in the case of cardiac wall velocity should, in general, also take into account higher components in the Fourier expansion of the velocity function (acceleration and higher terms). However, at certain points in the cardiac cycle (mid-systole), these terms may be neglected. Permutation of imaging gradients allows one to determine the magnitude and direction of cardiac wall velocity at these points. At other points in the cardiac cycle, additional imaging steps may be necessary in view of the contribution of higher Fourier coefficients.

Mpm-A6

A COMPARISON OF FLOW MEASUREMENT BY NMR AND DOPPLER ULTRASOUND*

S.C. Juh, J.M. Jo, J.M. Gardin, O. Nalcioglu and Z.H. Cho

Department of Radiological Sciences, Division of Physics and Engineering
University of California - Irvine

Recent studies have suggested [1] that nuclear magnetic resonance imaging may be useful in measuring flow. In the current investigation, we used NMR imaging to spatially localize and measure flow in liquids. The component of flow velocity perpendicular to the slice plane was measured by the technique developed by us and reported earlier [2,3]. The NMR pulse sequence used in the current study is shown in Figure 1. The application of the slice selection gradient at the selective 180°-RF pulse results in the encoding of velocity perpendicular to the slice thickness. The reconstructed image in this case is given by,

$$\hat{\rho}(x,y) = \rho(x,y) \exp\{i\alpha v_z(x,y)\} \quad (1)$$

where ρ is the spin density, α a real constant which depends on the duration and amplitude of the slice selection gradient G_z. In equation (1) v_z is the component of flow velocity perpendicular to the slice plane at a location (x,y). We observe from equation (1) that the velocity v_z can be computed by

$$v_z(x,y) = \tan^{-1}\{\mathrm{Im}\,\hat{\rho}(x,y)/\mathrm{Re}\,\hat{\rho}(x,y)\}/\alpha \quad (2)$$

NMR data were acquired with an 0.6T Technicare whole body scanner using the pulse diagram shown in Figure 1. The spin echo time was 18 msec. Non-pulsatile flow rate was varied from 1 to 7 L/min using a Biomedicus constant flow pump to circulate cow blood in 12.7 and 9.5 mm inner diameter tubes. The component of flow velocity perpendicular to the tomographic slice was computed on a pixel-by-pixel basis using equation (2). Average flow rate by NMR was computed as the average flow distribution over the cross-section of the tube and compared with the average flow rate obtained from the flow meter. Doppler measurements were made using the echo image of the tube to correct for the angle between the ultrasound beam and blood flow. Doppler and flow pump measurements were related by: Q (Doppler) = 0.80 Q (pump) + 1.81 (r = 0.92). NMR and pump measurements were related by: Q (NMR) = 0.84 (pump) +0.18 (r = 0.97), where Q is the flow rate in liters/min. Pulsed Doppler tended to overestimate the actual Q measurements, presumably because the interrogated sample volume represents only the highest velocities within the tube. NMR, on the other hand, more closely approximated actual Q due to pixel-by-pixel computation and better cross-sectional averaging. However, NMR estimates of Q became non-linear at 3.4 L/min and 5.3 L/min for 13 and 10 mm diameter tubes respectively.

*This work was supported in part by PHS Grant No. 1R01-CA41307 awarded by the National Cancer Institute, DHHS.

References

1. P.R. Moran, Mag. Res. Imag. 1, 197 (1982).
2. Z.H. Cho et al. J. Appl. Phys. 10, 1256 (1986).
3. C.H. Oh and Z.H. Cho, Phys. Med. Bio. (in press) (1986).

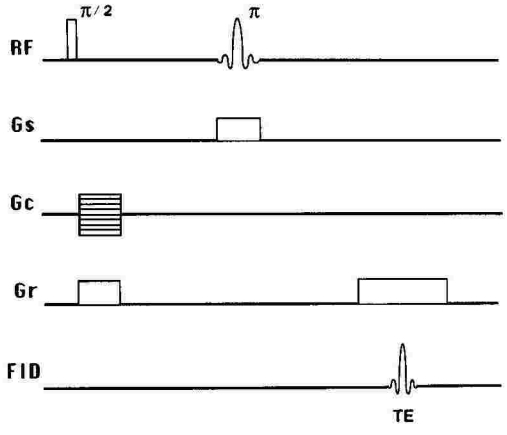

Figure 1. Pulse diagram used in the current study.

Mpm-A7

USE OF AN IMPLANTED FLOWMETER FOR IN-VIVO CALIBRATION OF MRI FLOW MEASUREMENTS

Leon Axel, Ph.D., M.D., Daniel Morton, M.S.S.E., Jeffrey Wortman, D.V.M., Harold L. Kundel, M.D.

Radiology Department, Hospital of the University of Pennsylvania

Although many techniques have been proposed for studying blood flow with MRI, verification and calibration of these techniques has largely relied on measurements of flow in artificial phantoms, such as plastic tubing . While useful as a baseline, such models cannot fully evaluate the usefulness of MRI flow measurements made in vivo, where flow has more complex geometries and time variations. There may be also other effects in vivo such as artifacts from motion.

Conventional electromagnetic flow meters employ magnets and are not suitable for use in an MRI system. We have modified a commercially available implantable ultrasonic flow probe (Transonics, Ithaca, NY), that measures volume flow in a vessel placed within a reflector bracket, to allow flow measurement within a MRI system. The principal modification involved replacing the usual metal reflector bracket with a nonmetallic ceramic material; no ferromagnetic material is employed in the probe. The probe output has been interfaced to a digitizer so that flow measurements can be acquired in synchronization with a cardiac trigger.

Implantation sites that have been used in conjunction with MRI studies include the cat carotid artery and rabbit distal aorta, although many other sites are possible. The presence of the probe produces a minimal effect on the images. Truly simultaneous MRI and flow measurement may result in some interference in the image, although the procedures can be interlaced.

The use of suitably modified implantable flow probes permits nearly simultaneous correlation of MRI flow measurements with an independent measure of flow.

Mpm-A8

APPLICATION OF MRI IN FLUID MECHANICS OF TURBULENT FLOW*

O. Nalcioglu and P.R. Moran
Department of Radiological Sciences, Division of Physics and Engineering
University of California - Irvine

Experimental measurement for detailed properties of turbulent flow in liquids is a very important need for study of fluid mechanics, but it is largely unsolved in methodology. We propose that MR flow imaging can be applied uniquely to quantitative study of turbulent flow, by a modification of the bipolar phase-gradient modulation (BPGM) encoding method. Turbulence is characterized by large random vortical-velocity fluctuations in liquids like water, but these statistically distributed events have strong temporal and spatial correlations over short, but finite, lifetimes. Turbulent velocities are described by their temporal autocorrelation (WEINER spectrum) at a fixed position, and by their spatial correlation during a fixed interval in time.

In the interval $0<t<TE$ (TE is the spin echo time) in an MRI imaging cycle the liquid velocity $\vec{v}(t)$ can be expressed as the summation of a coherent net flow velocity $\vec{v}_0(t)$ and a random turbulent fluctuation $\vec{u}(t)$. The coherent velocity component $\vec{v}_0(t)$ at a given location is determined by performing an ensemble average. Then the reconstructed image $\hat{\rho}$ is given by [1],

$$\hat{\rho}(\vec{r},TE) = \rho(\vec{r})\ \Gamma(\vec{r},TE)\ \exp\{i\int_0^{TE} \vec{v}_0(\vec{r},t)\cdot\vec{k}(t)dt\} \qquad (1)$$

where $\hat{\rho}$ is the actual spin density and

$$\vec{k}(t) = \gamma \int_0^t \vec{F}(t')dt' \qquad (2)$$

The gradient $\vec{F}$ used in defining $\vec{k}$ is chosen in such a way that it encodes velocity only, e.g. see ref.[2]. In equation (1) Γ is defined by

$$\Gamma(\vec{r},TE) = \int d^3u\ p(\vec{r}|\vec{u})\exp\{i\int_0^{TE} \vec{u}(t)\cdot\vec{k}(t)dt\} \qquad (3)$$

Here $p(\vec{r}|\vec{u})$ is the conditional probability distribution function for $\vec{u}$ at a given $\vec{r}$. The effect of

turbulence on the image can be understood by examining Γ . It can be shown that [3],

$$\Gamma(\vec{r},TE) \simeq \exp\{ - \sum_{lm} {}_0\int^{TE} d\tau\ C_{lm}(\tau)\ R_{lm}(\vec{r},\tau)/2\} \quad (4)$$

where $R_{lm}(\vec{r},\tau)$ is related to the Reynold's tensor and given by,

$$R_{lm}(\vec{r},\tau) = \langle u_l(0) u_m(\tau)\rangle \quad (5.a)$$

and

$$C_{lm}(\tau) = \int dt\ k_l(t)\ k_m(t+\tau) \quad (5.b)$$

The gradient tensor C_{lm} depends on the actual velocity encoding gradients interlaced within the imaging sequence. The components of the Reynold's tensor can be determined by choosing C_{lm} appropriately.

It is seen from equations (1) and (4) that the coherent fluid velocity gives rise to phase shifts in the reconstructed image whereas the turbulence term (eq. 4) causes an attenuation of the signal intensity in a similar fashion as spin-spin relaxation and molecular diffusion. For coherent velocities, the measured outputs are the velocity phase-shifts, integrated over all velocities in a resolvable volume, i.e., the velocity Fourier Transform. For turbulence fluctuations, however, only quadratic-products have a non-zero average; the result is a decay-function which is the Laplace Transform of turbulence correlations within a resolvable volume. We can, for example, modulate a gradient so that $C_{lm}(\tau)$ in Eqs. 4 and 5.b is a single pure harmonic modulation over the measuring interval. Then, the resulting $\Gamma(\vec{r},TE)$ decay-function of Eq. 4 encode that single spectral component of the Weiner-spectrum of the Reynold's tensor correlation function.

*This work was supported in part by PHS Grant No. 1R01-CA41307 awarded by the NCI, DHHS. PRM acknowledges research-leave granted by BGSM.

1. O. Nalcioglu, Z.H. Cho, Q.S. Xiang and C.B. Ahn, "Incoherent Flow Imaging", Proc. SPIE 671(1986).
2. Q.S. Xiang and O. Nalcioglu, "A Formalism for Generating Multiparametric Encoding Gradients in NMR Tomography". To be published in IEEE TMI (1987).
3. O. Nalcioglu and P.R. Moran, "Characterization of Turbulent Liquid Flow by MRI" (to be published).

(Mpm-B) NEURO-CLINICAL

Presiding: V. Runge & D. Spigos

3:20 pm

ROOM C-107

12 MINUTES PER PRESENTATION

Mpm-B1
MRI IN THE EVALUATION OF SPINAL TUMORS

Kathleen Davis, MD[1]; Randall James, MD[2]; John C. Stears, MD[1]

[1] University of Colorado Health Sciences Center, 4200 East Ninth Avenue, Denver, CO 80262

[2] AMC Cancer Research Center, 1600 Pierce Street, Denver, CO 80214

Magnetic resonance (MR) imaging has been shown to be useful in evaluation of the spine. We reviewed the MR examinations of 45 consecutive patients with spinal tumors.

MR scanning was done on a Diasonics MT/S imager, Milpitas, CA with a superconducting magnet operating at 0.35 T. Contiguous 10mm and 5mm thick axial, coronal, and sagittal slices were obtained using a multislice spin echo technique with repetition times of 2.0, 1.5, and 0.5 sec. and echo delay times of 30, 40, 60, and 80 msec.

The patients were divided into three groups based on site of tumor origin:

Group I - Intramedullary (12)
7 - primary
5 - secondary
Group II - Epidural (20)
12 - metastatic
8 - direct extension
6 - origin in soft tissues
2 - origin in bone
Group III - Bone (13)
10 - metastatic
3 - lymphoma

Studies were correlated with CT scans, myelograms, angiograms, bone scans, plain films, surgical and pathological findings. MR was comparable to myelography with CT for detection of tumor in Group I and superior for tissue characterization. In Group II MR was comparable to myelography with CT in most cases, but surpassed either myelography or CT alone. MR was the most sensitive technique for detection of Group III tumors. Convenience, comfort, and safety factors were superior with MR and contributed to our use of MR as the (initial) method of choice.

Mpm-B2

MRI FINDINGS IN ACUTE CERVICAL SPINE INJURIES

G. J. Beers, M.D.; G. G. Wagner, M.D.; C. B. Shields, M.D.; J. R. Johnson, M.D.; J. E. Meyer, M.D.

University of Louisville School of Medicine and Humana Hospital University

Magnetic resonance scans were obtained on ten patients within a week after acute cervical spine injuries. Frequent findings included focal swelling of the spinal cord and increased signal intensity within the cord on T2 weighted images. Other findings included disk protrusions as well as edema and hematoma in the epidural soft tissues. Although visualization of fractures was only fair, the scans demonstrated narrowing of the canal by posteriorly protuding vertebral body fragments. A discussion of findings as well as a technique for evaluating these patients and resultant practical applications to clinical management will be presented.

Figure 1: SE 1500/50 image demonstrates swelling of the spinal cord from C2 to C7. There is increased signal intensity within the cord, suggesting the presence of hemorrhage or edema. The body of C5 is traumatically deformed.

Figure 2: SE 1650/50 image demonstrates traumatic deformity of the C5 vertebral body with increased signal indicative of hemorrhage in portions of the body. Edema or hemmorrhage of prevertebral soft tissues, anterior epidural soft tissues, and posterior epidural soft tissues are present. There is suggestion of posterior protrusion of disk material (arrow) posterior to which there is slightly increased signal intensity within the cord.

Mpm-B3

MAGNETIC RESONANCE IMAGING AND CONTRAST CT IN LUMBAR DISC DISEASE: A COMPARISON OF DIAGNOSTIC METHODS AND CORRELATION WITH SURGICAL FINDINGS.

Ronald M. Forristall, M.D., Orthopedic Resident; *Norman T. Pay, M.D., Assoc. Med. Director; Henry O. Marsh, M.D., Director, Orthopedic Residency Program

St. Francis/University of Kansas (Wichita) Affiliated Hospitals Orthopedic Residency Program
*St. Francis Magnetic Resonance Imaging (Wichita)

Twenty patients with suspected lumbar disc herniation were studied with Magnetic Resonance Imaging (MRI) and contrast Computerized Tomography (CT). Seventeen patients underwent surgery for disc herniation, allowing confirmation of the diagnosis.

Four diagnostic categories with specific radiological and surgical criteria were used for classification of each patient. Category I included all normal discs. Category II did include degenerative changes and diffuse bulging without neural compression. None of these patients underwent surgery. Herniated disc lesions with neural compression were placed in Category III, and disc fragments sequestrated from their site of initial herniation were in Category IV.

The MRI diagnosis agreed with surgery in 15 of 17 (88%) of cases. The CT diagnosis agreed with surgery in 12 of 17 (70%) of cases. MRI and contrast CT reached the same diagnosis in 17 of 20 (85%) of cases. When a discrepancy did occur the MRI diagnosis was correct. In 2 cases MRI and surgery confirmed a disc herniation when CT showed diffuse annular bulge. In one case MRI and surgery confirmed a sequestrated fragment when CT showed a herniated nucleus pulposis. Complications did occur in two of twenty patients (10%) both after contrast CT. One patient suffered a lumbar puncture headache requiring hospitalization. Another patient had hives and nausea after contrast injection. No significant complications were noted after MRI studies.

Cost analysis showed that MRI was often less expensive than contrast CT at our facility.

We conclude that MRI shows a clinically significant superiority over contrast CT for the diagnosis of lumbar disc disease. Currently our study size is too small to show a statistically significant difference. MRI also offers economic advantages with fewer complications than contrast CT.

Mpm-B4

MRI IN THE EVALUATION OF METASTATIC SPINAL DISEASE.

E. Unger, M.D., H. Kessler, M.D., R. Gatenby, M.D., P. Moldofsky, M.D., W. Hartz, M.D. and M. Clair, M.D.

Fox Chase Cancer Center, Philadelphia, PA 19111

Magnetic resonance imaging examinations were retrospectively reviewed in 40 patients in whom these examinations had been conducted to evaluate for clinical suspicion of metastatic spinal disease. Spin echo technique was utilized employing a Siemens Magnetom operating at 1.5 Tesla. Both T_1 and T_2 weighted sequences were obtained utilizing TR/TE of 450/16 (4 averages), 2200/28/70 (2 averages) in the sagittal plane at 4 mm intervals and in the transaxial plane at 4 mm intervals. Images were obtained using a surface coil positioned over the region of the spine suspect for metastatic disease or spinal block. In cases in which clinical information could not localize a given level or when multiple levels were suspect, the body coil was utilized to examine the entire spine. Images were correlated with bone scintigraphy and with CT examinations and myelography. Vertebral metastases presented as regions of decreased signal intensity on T_1 weighted images with increase signal on the T_2 weighted images. The T_1 weighted image was most sensitive in depicting the extent of involvement of vertebral bodies by metastatic disease but the T_2 weighted image was necessary to differentiate between the posterior extension of tumor from CSF. The T_2 weighted image was most sensitive in depicting spinal cord compression. In correlating the MRI examinations with bone scintigraphy, it was apparent that MRI showed many more lesions than did bone scanning. In assessing the degree of spinal block, MRI was equally sensitive and accurate when compared to myelography but MRI provided additional information on the extent of involvement of vertebral bodies by metastatic disease. This information was found useful by radiation therapists when planning radiation ports. In comparing MRI to CT examinations, MRI was more sensitive in depicting the extent of involvement of vertebral bodies by tumor and also more accurate in depicting intraspinal extension of tumor and degree of spinal block.

Forty consecutive MRI examinations performed on patients with no history of cancer and no clinical suspicion of metastatic disease were also retrospectively reviewed to determine if the signal intensity characteristics which were observed in metastatic disease might be found in a normal population. In no case was a vertebral body identified in which there was decreased signal intensity on the T_1 weighted image and increased signal intensity on the T_2 weighted image. Acute compression fractures illustrated increased signal intensity on both the T_1 and T_2 weighted images. Old compression fractures more than 6 months old were present in cases with decreased signal intensity on both the T_1 and T_2 weighted image. Spurs and hypertrophic cortical bone caused decreased signal intensity on both the T_1 and T_2 weighted images.

In conclusion, MRI is highly useful in the evaluation of metastatic spinal disease. MRI accurately assesses the degree of spinal block. MRI appears to be more sensitive than bone scintigraphy in identifying metastatic involvement of the vertebral bone marrow over a given region. While MRI and myelography provide comparable data on the degree of spinal cord or nerve root compression, MRI provides additional data on the extent of involvement of marrow by metastatic disease.

Mpm-B5
THE SPECTRUM OF POST TRAUMATIC CHANGE IN THE SPINAL CORD USING MRI

Dreisbach JN,* Edgar RE,** Seibert CE,* Lammertse DP,** Wilhelm MW*

*Radiology Imaging Associates, Englewood, Colorado, **Craig Hospital, Englewood, Colorado

Progressive neurological loss occurs in 1-5% of quadriplegic, quadriparetic or paraplegic patients and is usually secondary to intramedullary necrosis resulting in microcystic and progressive cyst formation. It has been well documented that shunting a post traumatic cyst can arrest further neurological loss. Thus, the identification and separation of the spectrum of injury to the spinal cord has treatment implications. Prior to MRI, the spectrum of injury to the cord seen with imaging techniques was confusing i.e. malacic changes in the cord mimicked cyst formation using non-ionic subarachnoid contrast enhanced delayed CT. MRI has provided a non-invasive method of following patients with cord injury and appears to help define the injury spectrum. We define these patterns as 1) post traumatic cystic myelopathy (PTCM), 2) myelomalacia, 3) progressive post traumatic cystic myelopathy (PPCM).

Post traumatic cystic myelopathy is the residual pathological change in the spinal cord and includes post traumatic atrophy and post traumatic cystic intramedullary change. Clinically, these patients are stable after their injury. On MRI, PTCM demonstrates areas of discreet decreased signal within the cord on T_1WI and mildly T_2WI pulse sequences. The cord may show focal atrophy at the injury site.

Myelomalacia (as we use this term) is a spectrum of pathological change which microscopically may not be separable from PTCM but appears to have different imaging characteristics. It may coexist with PTCM or PPCM or as an isolated finding. It has imaging and clinical significance since we have found that it can be the precursor of advancing cystic formation. Patients with post traumatic myelomalacia may have symptoms that suggest progressive neurological loss but a defined cyst for shunting may not be present. Using MRI, myelomalacia may demonstrate a focal area of decreased signal or multiple small areas of decreased signal within the cord on T_1WI and these may become isointense or hyperintense compared with the cord on the mildly weighted T_2WI sequence. Additionally, myelomalacia may have essentially normal signal on T_1WI and increased signal in the area of abnormality on T_2WI sequence.

Progressive post traumatic cystic myelopathy is a clinical imaging term that refers to a patient with progressive neurological loss and a cyst in the spinal cord. These patients can manifest further loss of neurological function if progressive enlargement of the cyst occurs. MR findings show a discreet area of decreased signal on T_1WI and on T_2WI. Potentially of importance has been the demonstration of areas of myelomalacia adjacent to these cysts which appears to represent the advancing edge of cyst enlargement.

MRI findings have been correlated with operative results thus allowing a better understanding of this spectrum of disease. The theoretical basis for these observations will be discussed and representative case material presented.

Mpm-B6
HIGH RESOLUTION MRI OF THE SPINAL CORD IN HUMANS AND RATS

M. Carvlin, Ph.D., R. Asato, M.D., DSc., D.B. Hackney, M.D., E. Kassab, B.A., R.T., P.M. Joseph, Ph.D.

University of Pennsylvania, Department of Radiology

Spinal cords were harvested from adult male cadavers (C1-T1) or from adult male Sprague-Dawley rats (C1-L1) and were imaged fresh (pre-) and post-fixation. Using an experimental imaging system operating at either 1.4 or 1.9 T, a special purpose receiver coil and a 128x128 data matrix a spatial resolution of either 300 microns or 150 microns per pixel was achieved. The specimens were imaged in the saggital and axial planes giving high resolution images which clearly delineated lateral, and posterior funiculi, the dorsal and ventral horns, and the white and gray commissures. Our findings indicate that: (1) fixed gray matter has a significantly higher spin density, slightly shorter T2 and T1 than white matter; (2) fresh gray matter has a higher spin density, slightly shorter T2, but longer T1 than white matter. Using inversion recovery pulse sequences, the gray matter signal of the cords, fresh or fixed, exceeded the white matter signal for all values of TI (TR = 3000, TI = 2000, 1200, 600, 100). Hence, in relatively "T1-weighted" images of fresh and fixed spinal cords spin density effects appear to predominate rather than T1 differences to the extent that the white matter/gray matter contrast is reversed from that demonstrated in the brain. An in-depth quantitative assessment of the T1 and T2 values for gray and white matter in the spinal cord is now being conducted.

Mpm-B7
MRI OF ACUTE SPINAL TRAUMA

William F. Bennett, M.D., Donald W. Chakeres, M.D., Linda Gray, M.D., Edward Delgrosso, MS4

The Ohio State University Hospitals, Department of Radiology

Plain films, myelography, and CT are the classic modalities for evaluation of spinal trauma. We investigated MRI's potential for evaluation of spinal trauma. We investigated MRI's potential to add significant new information. This study compares MRI findings to the classic exams in fifteen patients

with acute spinal trauma (less than 72 hrs). The patients were examined on a 1.5T GE Signa System. Spin echo images were obtained in both sagittal and axial planes, using TR1500 and TE20 and 60 msec. Comparison of the MRI data was made with the clinical symptoms, plain films, polytomes, myelography and CT. We found that ligamentous injuries, including rupture of the anterior and the posterior longitudinal ligaments were visible. Disc protrusions, epidural fluid or hemorrhage were visible deforming the dura. Paraspinal fluid collections were seen with dural lacerations. Alterations in the shape and endplates suggested compression fractures and large fragments protruding into the canal could be seen. Occasionally low signal was seen in the marrow suggesting acute hemorrhage. Cord contrusions were most commonly seen as areas of mild cord enlargement or increased signal with loss of the internal architecture (seen only on the axial images). Acute cord hemorrhage was seen as low signal region. Cord transection was easily visualized. MRI and myelography demonstrated comparable findings. Vertebral body and posterior element fractures were better seen on CT. In conclusion MRI adds unique information about the spinal cord, disc, and ligaments which is not visible using other techniques; information which is important to patient management.

Mpm-B8

THE ROLE OF M.R. IN THE STUDY OF CHORDOMA

L. Balzarini, J.D. Tesoro Tess, E. Ceglia, R. Petrillo, P. Colombo, R. Musumeci

Section of Urologic Radiology, Lymphangiography and Magnetic Resonance
Istituto Nazionale Tumori - Milano.

M.R. imaging was compared with computed tomography and traditional radiology findings in eight cases of chordoma. Five of these patients were studied as initial staging, two for local recurrence and finally one for methastatic disease.

In all cases Spin-Echo sequences with different echo times were used to obtain images T1 and T2 wheighted.

The usefullness of CT in the demonstration of chordomas is well know. But in some cases CT doesn't provide an adequate demonstration of a local recurrence or infiltration of the soft tissues. On the contrary CT provides a more accurate depiction of calcification inside the mass and bone destruction.

Magnetic Resonance Imaging offers several advantages in the evaluation of these lesions, in determining the estension and relation with adjacent tissues. The free choice of the imaging plane and particularly the possibility to acquire sagittal views, justifies the advantage of this method in the evaluation of the involvement of spinal cord.

For particular behaviour of chordoma it's essential to diagnose recurrences as soon as possible.

Standard X rays and CT can only conferme recurrence mainly when considerable bone changes or discrete masses are present. M.R., for high soft tissues resolution, can differentiate small tumoral lesions from changes caused by therapy (surgery and/or RT).

From these considerations it can be assumed that M.R. is at least equal to CT for a demonstration of the primary lesion but it's the best imaging method during the follow-up of these patients.

Mpm-C1

THE OPTIMUM DATA SAMPLING PERIOD FOR MAXIMUM SIGNAL-TO-NOISE RATIO IN MR SPIN-ECHO IMAGES

John P. Mugler, M.S., James R. Brookeman, Ph.D.

Departments of Biomedical Engineering and Radiology, University of Virginia

Signal-to-noise considerations are of prime importance in MRI because the nuclear magnetic resonance signal is inherently weak. It is well known that the image noise varies as the square root of the reciprocal of the data sampling period[1], T_S, and consequently increasing T_S decreases the noise level[2], but it has not been recognized that for a given $T2$ this dependence leads to an optimum sampling period with respect to the signal-to-noise ratio. This optimum period is dependent on the details of the pulse sequence and on the relaxation times of the tissue. For the spin-echo pulse sequence, we have demonstrated the existence of this optimum sampling period both theoretically and experimentally.

Assuming 2D-FT spin-echo imaging with fixed resolution and slice thickness and a fixed subject/RF coil combination, the image signal-to-noise ratio per unit time, SNR, is[1]

$$SNR = K \cdot \sqrt{T_S} \cdot \sqrt{1/TR} \cdot (1 - \exp(-TR/T1)) \cdot \exp(-TE/T2), \quad (1)$$

where K is a constant. This expression assumes $TR \gg TE$. Maximizing equation 1 with respect to T_S, TR, and TE, considering them to be independent, yields $T_S = \infty$, the familiar result $TR = 1.25\,T1$, and $TE = 0$. In practice, of course, TE cannot be equal to zero. The minimum achievable TE can be written $TE = a \cdot T_S + b$, where a depends on the position of the echo in the data sampling period and on the magnitude of the readout gradient during the dephasing period, and b depends on the duration of the RF pulses and the rise and fall times of the gradients. With this substitution in equation 1, the maximum value of SNR occurs for $T_S = T2/2a$ and so the optimum value for the echo time becomes $TE = T2/2 + b$.

The solid line in Figure 1 is a plot of equation 1 showing the normalized SNR versus TE for fixed TR, $a = 1.00$, $b = 23.3$ms, and $T2 = 30.0$ms. Note the maximum in SNR occurring at $TE = 38.3$ms. The circles in Figure 1 are measured signal-to-noise ratios for an oil phantom having a $T2$ of roughly 30ms. Imaging was performed on a Siemens 1.0T Magnetom whole-body imager. The pulse sequence timing corresponded to the values of a and b used for the plot in Figure 1. The signal-to-noise ratio was calculated as the mean image intensity of the phantom divided by the standard deviation of the image intensity of the phantom. Each data point was calculated from an ensemble of 10 images made under identical measurement conditions. The experimental values show the same behavior as the theoretical curve, and have a maximum at approximately $T2/2 + b$ as predicted by theory.

A general conclusion from this work is that the optimum TE with respect to SNR for the spin-echo pulse sequence depends on the tissue $T2$ values: it does not occur at $TE = 0$ as is commonly stated. In fact, the SNR approaches zero as TE is decreased below the optimum value. While this analysis does not at present address the restrictions on T_S due to artifacts from chemical shift, motion, field inhomogeneities, and $T2$ decay during T_S, other work indicates these effects are manageable and that for particular imaging situations this analysis can provide a basis for improved image quality. We are currently investigating the optimum values of T_S for contrast-to-noise ratios.

REFERENCES:

1. W.A. Edelstein, G.H. Glover, C.J. Hardy, and R.W. Redington, *Magn. Reson. Med.* **3**, 604 (1986).

2. I.R. Young, M. Burl, and G.M. Bydder, *J. Comput. Assist. Tomogr.* **10**, 271 (1986).

FIGURE 1

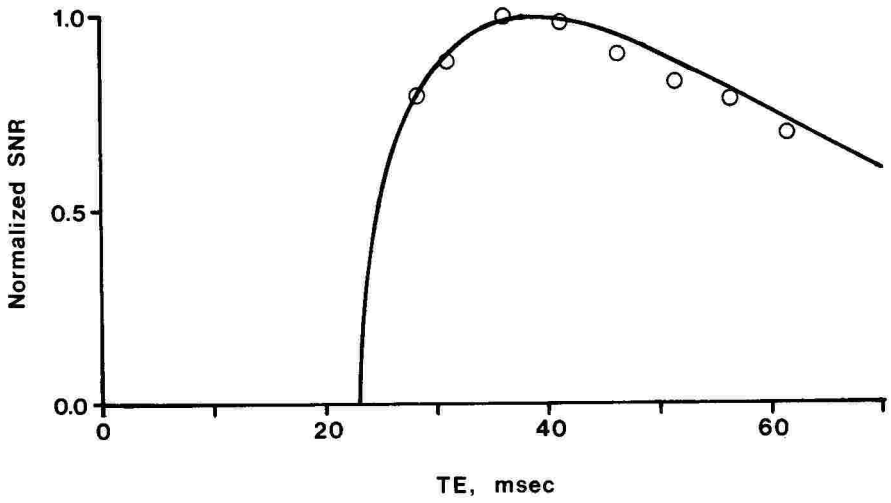

Mpm-C2

A RIGOROUS THERMODYNAMICS OF NMR IMAGE FREE-INFORMATION-ENERGY

Paul R. Moran

WAKE FORFST UNIVEPSITY, THE BOWMAN GRAY SCHOOL OF MEDICINE

A unification theory exists, based on rigorous thermodynamics of system free-energy of information (the Gibbs potential), for the image-information produced in any MRI study. It reduces ultimately to simple and appealing radiological-imaging factors and physically plausible concepts. It is highly useful and practical in assessing MRI scanning parameters, equipment limitations, and strategies. That medical-image properties involve statistical considerations whose treatment resembles the statistics of true thermodynamics has long been known. This observation even extends to borrowing terminology from thermodynamics for analogous concepts, for example, the image power-spectrum content, the image entropy and so on. Magnetic resonance imaging is truly limited ultimately by the thermal properties of the subject/receiver system and, consequently, is particularly interesting in this respect. Unlike x-ray imaging, for MRI it is possible to formulate a rigorous thermodynamics of the physical free-energy; when the electromagnetic signals are detected, stored, and reconstructed into image-arrays, then that free-energy is transformed into free-information-energy of the imaging process.

The MRI subject for medical-imaging is at fixed temperature, so the free-energy function which applies is the Gibbs-potential, F = E -TS, and the physical free-energy incremented in the study is the change in the Gibbs-function, δ F/kT = f/kT = e/kT -s, where "e" is the total energy (normalized to the usual thermal content, kT) delivered to reception system, and "s" is the entropy-increase from disordered random signals. There are two steps in delivery of free-information-energy: (1) there is the physical total "f" produced without regard to its diagnostic usefulness and (2) then total "f" somehow is filtered by a generalized display system (post-reconstruction procession, display medium, and the diagnostician/ observer. The display filtering, which transforms total-f into the diagnostic free information-energy, Dx-f, is a process not unique to the MR modality. Though crucially important, the generalized properties of the DISPLAY are perhaps the least understood scientifically of all imaging-system considerations, except possibly in trivial circumstances. Consequently, in this presentation, we address the total "f" generated from the SUBJECT and delivered into the MRI SYSTEM, and leave modifications to Dx-f, by the DISPLAY system, for subsequent research of adequate display-system concepts.

When the rigorous mathematical theory of the thermodynamics of NMR signal generation and collection, and its reconstruction into image arrays, is completed, then the result factors into four relatively simple term

$$f/kT = (\ \text{SUBJECT}\ )x(\ \text{CONTRAST}\ )x(\ \text{RESOLUTION}\ )x(\ \text{RECONSTRUCTED VOLUME}\ ). \qquad (1)$$

It is very satisfying that the exact derivations of the nexus of terms in each factor turns out, in the end, to be completely independent of the particular scanning strategy, independent of the particular gradient-modulation sequences, and independent of the specific mode of data-set reconstruction into the final image arrays (assuming that no reconstruction algorithm blunders occur). It is also satisfying, and and somewhat surprising, that each factor in Eq.1 is a ratio of terms; in each denominator is a factor which would be equal to unity (corresponding to entropy-preserving reversible second-law conditions) for ideal instrumentation, but which will be greater than unity for real-life instruments (corresponding to entropy-increasing irreversible second-law conditions). This is exceedingly useful information for MRI scanner design; for example, it shows precisely where and how instrumental limitations, which we identify below by < >-terms, influence the final image-information.

The (SUBJECT) factor is a product of the object itself and the magnetic environment including rf-reception coil properties, with a the system <noise-factor> denominator. The (CONTRAST) factor includes how the rf-sequence generates subject contrast, divided by a scanning <data inconsistency factor>. The (RESOLUTION) factor comprises both spatial and time resolution in the resolvable VOXEL-VOLUME and in "[t(data)-voxel]", the total time actually acquiring data used to reconstruct a given single voxel. It has a <bandwidth noise-sampling factor> in its denominator. The (RECONSTRUCTION) factor's numerator turns out to be, simply, the total "reconstructed volume" of the subject, while its denominator is a <sampling convolution-apertured reconstruction factor>, which describes any mismatch due to instrumental or algorithmic bandwidth limitations, between the computer reconstruction volume and the actual non-zero reconstructed values.

As an application example, we can observe that the MRI free-information available grows directly with [t(data)-voxel], the total time that data for a single voxel actually are acquired. However, at a fixed readout gradient strength, the resolvable voxel-volume varies inversely with the time that FID-data are acquired. Thus, in (RESOLUTION), all other things being equal, increasing the VOXEL VOLUME only improves apparent SNR, but it fails to increase the final image free-information actually delivered.

In this presentation, we shall discuss each factor of the Unified Theory in Eq.1 separately, including its sub-terms, in more detail and demonstrate other practical applications to MRI assessment, scanning efficacies, and system design.

Mpm-C3

AN ADAPTIVE FILTER FOR IMPROVING THE SIGNAL-TO-NOISE RATIO OF NMR IMAGES WITHOUT LOSS OF RESOLUTION

Kenneth S. Denison, Ph.D. and William Sattin, Ph.D.

Picker International, Inc., 5500 Avion Park Drive, Highland Hts., OH 44143

Medical NMR images often are degraded by signal-independent, uncorrelated noise, sometimes called "speckle" or "graininess." Such noise tends to hamper effective diagnosis. Traditional techniques for reducing this noise involve applying a filter to the raw data in the frequency domain before reconstructing the image. For example, a low-pass exponential filter might be used. The result is an improvement in signal-to-noise ratio (SNR) at the expense of spatial resolution. This also may hamper diagnosis by blurring fine detail in the image.

An alternative is to perform the filtering in the spatial domain. Several efficient spatial noise filtering methods are based on the computation of local statistics in the neighborhood of individual pixels [1,2]. These techniques combine the local mean, local variance, original pixel value, and assumed noise statistics to give the filtered image. The disadvantage of these techniques is the assumption that the noise statistics are known, i.e., the requirement that the user supply an estimate for the noise statistics. Without an accurate estimate, the result can be little or no improvement in SNR, or improved SNR with loss of resolution.

An improved filtering technique is reported which combines a spatial domain filter based on local statistics with a method for obtaining the noise statistics from the frequency domain data. The noise in the acquired data is assumed to be signal-independent, uncorrelated, and additive. The image noise statistics are determined directly from the data noise statistics before image reconstruction. The image is then reconstructed and filtered to produce an improved SNR image without loss of resolution. The technique requires no user input, and does not require significantly more time than reconstruction alone. In addition, the filter is also implemented in a stand alone configuration which requires the user to input the estimated noise variance and the size of the local neighborhood. Typical results are shown in Figures 1 and 2. In both, the left side is the image reconstructed without filtering, the right with filtering. The noise is significantly reduced in the filtered images without loss of resolution.

References: [1] J.S. Lee, IEEE Trans. Pattern Anal. Mach. Intell., PAMI-2, 165 (1980).
[2] D.T. Kuan, A.A. Sawchuk, T.C. Strand, and P. Chavel, IEEE Trans. Pattern Anal. Mach. Intell., PAMI-7, 165 (1985).

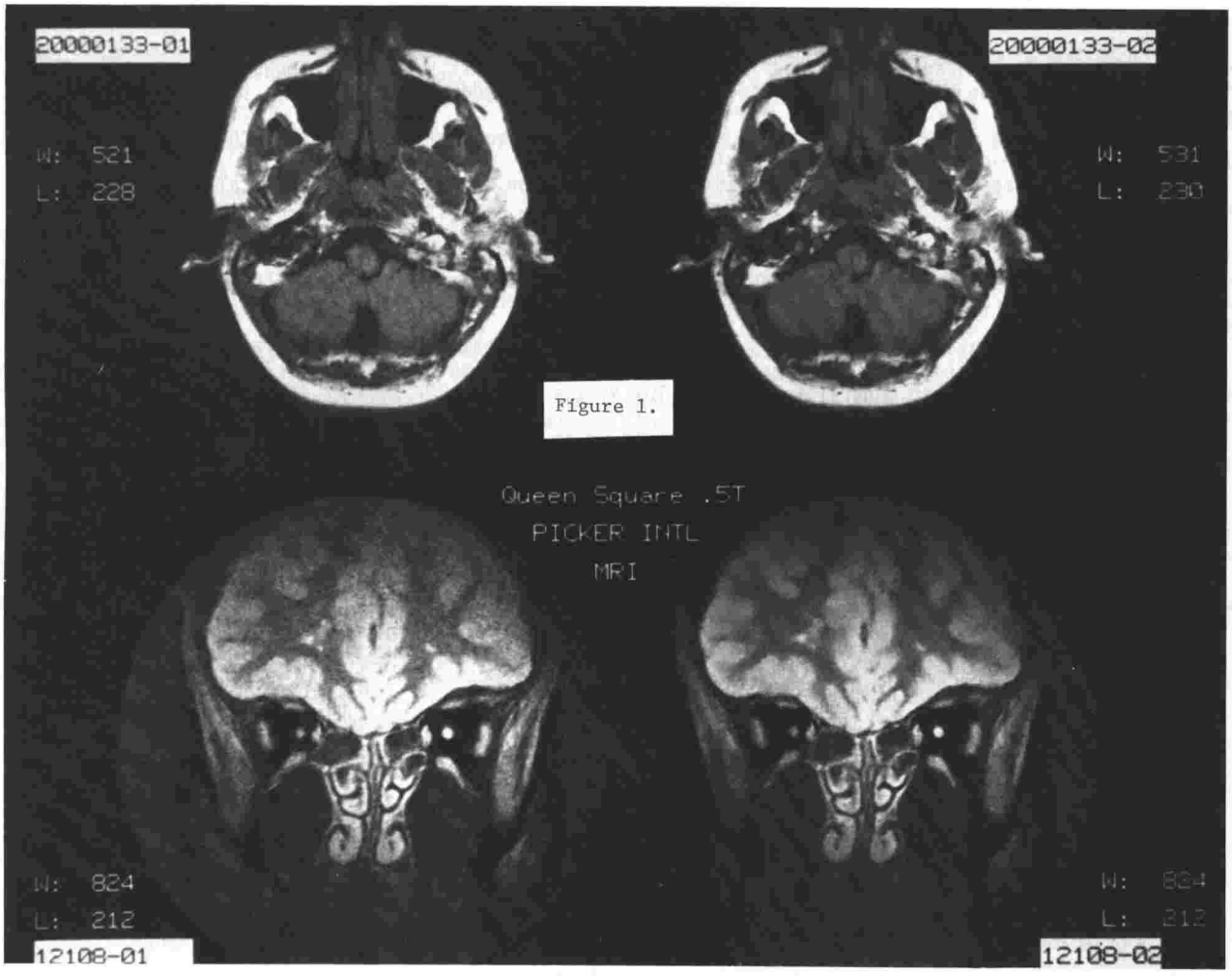

Figure 1.

Mpm-C4 Abstract Withdrawn

Mpm-C5
DISTORTION OF AXIAL GRADIENT BY DEWAR WALL EDDY CURRENTS

Z. J. J. Stekly

Magnetic Corporation of America

Purpose

Quantize effect of dewar wall eddy currents on magnitude and distortion of the axial gradient magnetic field.

Methods

Axial gradient were selected for analysis because of their axial symmetry, thus resulting in a two-dimensional problem. For calculation purposes, the eddy currents were modeled by placing an infinitely long cylindrical "shield" at various radial distances. The boundary condition at this shield was: no penetration of magnetic field. The Poisson magnetic field program was used for the computations.

Results

Selected results are presented in Figures 1 to 4. When current is first applied to the gradient coil the magnitude of the central gradient produced is reduced by eddy currents. Figure 1 shows the magnitude of this attenuation as a function of radius of the eddy currents. As the eddy currents decay, the attenuation approaches unity.

Figure 2 shows the variation along the z axis of the local gradient G relative to the central value for various eddy current radii for the same condition as Figure 1.

Figure 3 shows the variation of the z gradient as a function of radius at the central plane for various eddy current radii.

Figure 4 compares fractional departure of the local magnetic field from a straight line for several conditions. (1) No eddy currents, (2) right after an initial step in gradient current, and (3) after initial eddy currents have adjusted to a pulse train of square waves with 50% "ON" time. Curves are shown for the gradient current "ON" condition as well as for the gradient current "OFF" condition.

Conclusion

The central gradient is attenuated by a time varying factor that depends on the radius of eddy currents. Maximum loss of gradient and distortion occur at the beginning of a pulse sequence. Initial distortions vary from about 1% at z = 10 cm, to generally less than 10% at z = 25 cm. The smaller the radius the larger the distortion.

The radial variation of distortion is less than 1% up to a radial distance of 10 cm. It remains of the order of 1% from up to a radial distance of 20 cm.

Figure 4 shows the departure of the "on axis" field from a straight line for an eddy current radius of 52 cm. The initial distortion is about 1% up to z = 16 cm and increases to about 3% for z = 25 cm. If only a single step occurs the eddy currents decay to the no shield curve which results in a change of 2% at z = 16 cm and 4.5% at z = 25 cm.

As part of a pulse train the eddy currents adjust to an average value. For the case calculated (50% "ON" time square wave), the distortion is less than 1% on the z axis. For the gradient current OFF condition there is still about 3% effect at z = 25 cm.

The computation have demonstrated the ability to quantitatively characterize expected attenuations and distortions of the axial gradient magnetic field.

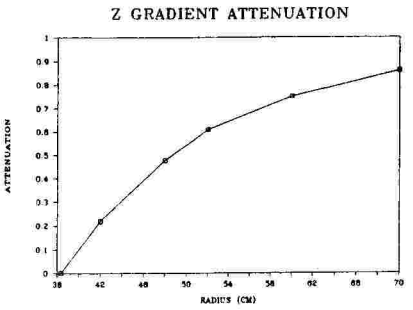

Fig. 1 Initial gradient attenuation

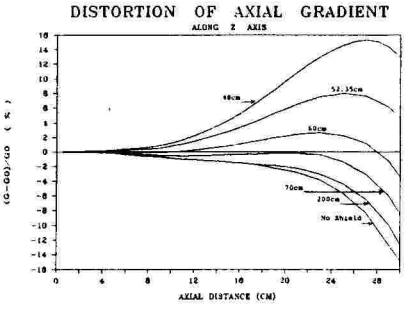

Fig. 2 Variation of the local gradient along the z axis for various radii of eddy currents

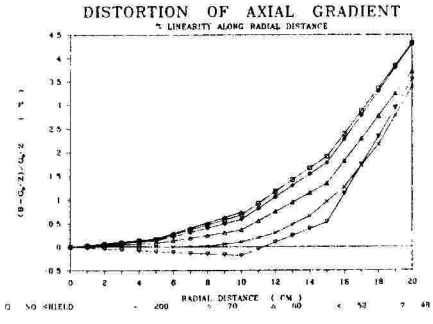

Fig. 3 Variation of the gradient in the central plane for various radii of eddy currents

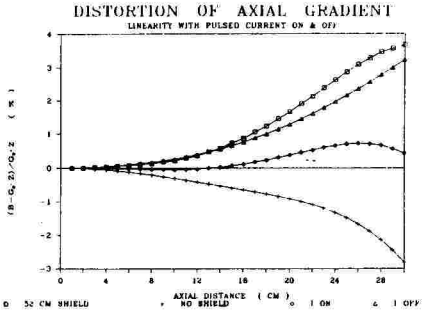

Fig. 4 Departure from linear magnetic field along z axis for several conditions

References: Smythe, W.R., Stat. & Dyn. Elect. McGraw Hill 1968.
Pillsbury, R.D., et al. IEEE Vol MAG 21 No. 6 Nov 1985.

Mpm-C6

REDUCTION OF ALIASING IN 2DFT MRI BY PSEUDOFILTERING

Leon Axel, Ph.D., M.D. and Lawrence Dougherty, B.S.

Radiology Department, Hospital of the University of Pennsylvania

The properties of data sampling and the discrete Fourier transform (DFT) used in image reconstruction in 2DFT MRI lead to the artifact of aliasing when the object extends beyond the boundary of the region being reconstructed. For frequency encoding of position, the aliased components can be supressed by analog attenuation of higher frequencies (filtering) prior to signal digitization. However, there is no direct equivalent to the analog filter to be applied for the case of aliasing with phase encoding of position.

The only direct way to avoid aliasing along the phase-encoded direction is to increase the number of sampling steps in this direction by using smaller gradient increments (sampling more finely in "pseudotime"), use a correspondingly larger DFT and then "throw away" the unneeded portions of the image. An alternative approach can be used in which the more finely sampled phase-encoded data are averaged together to create a new set of data points with the same size pseudotime steps as were used to create the original image. Now there will again be aliasing, but the aliased image will be attenuated, with the spatial dependence of the attenuation of the aliased images depending on the particular averaging process ("pseudofiltering") carried out on the original data (1). At the cost of some residual (attenuated) aliased image, we have thus retained much of the SNR improvement available from averaging the additional data. If the imaging process would have included some signal averaging anyway, the signals to be averaged can be acquired while appropriately incrementing the phase-encoding gradient. Thus the signal averaging can be combined with the pseudofiltering process, accomplishing reduction of the aliasing without requiring any increase in the image data acquisition time. For example, a simple equal-weighted average will yield a sin x/x modulation of the aliased image, and may not require any increase in data processing or reconstruction time.

This approach to pseudofiltering leads to significant attenuation of aliased images without major penalities in SNR or image acquisition time.

References

1. Kurihara N, Kamo O, Umida M, Sato K, Hyakuna K, Megayama K. Applications in one-dimensional and two dimensional NMR of a pseudofilter by jittered time averaging. J Magn Reson 65,405-416(1985).

Mpm-C7

INCREASED NMR IMAGE SPATIAL RESOLUTION VIA NON-LINEARLY INCREMENTED PHASE-ENCODING

William Sattin, Ph.D.

Clinical Science Center, Picker International, Highland Heights, Ohio

This investigation considered the effect upon spatial resolution in NMR images of non-ideal applications of the phase-encoding magnetic field gradient. Specifically, unequally incremented phase-encoding gradients were used as input to correct for imperfections in the amplifiers that drive the gradient coils and result in the applied phase-encoding gradients. These limitations may present themselves as non-linearities as well as asymmetric bipolar responses.

The majority of NMR imaging sequences in commercial use today are based upon the Fourier imaging method (1) and its modifications (2). Typically, slice selection is accomplished by selective excitation, applying an rf pulse while a magnetic field gradient is turned on. With the received NMR signal now spatially limited to originating from a slice, the Fourier imaging method of collecting the signal in the time domain and reconstructing it into the spatial domain is applied.

Fourier space, or k-space (3) is usually sampled on a rectilinear grid. One axis of this grid is determined by the readout gradient, a steady linear magnetic field gradient applied during data acquisition. As long as this gradient remains steady, and the NMR signal is sampled at a constant time interval, then the "steps" along the readout gradient axis of k-space are equal.

The second axis of the rectilinear k-space grid is determined by the phase-encoding gradient, which is also a linear magnetic field gradient. Typically the phase-encoding gradient is applied before data acquisition in an incremental fashion. That is, the amplitude of the phase-encoding gradient is varied for each application of the rf sequence. For example, its amplitude may start at a given negative maximum and incrementally progress to the corresponding positive maximum. If the intermediary values of the phase-encoding gradient amplitude are incremented by a fixed amount, then the "steps" along the phase-encoding gradient axis of k-space are equal.

These equal "steps" along the phase-encoding gradient axis of k-space may be thought of in terms of the relationship between the accumulated phase $\theta(V)$ in the NMR signal introduced by the application of the incrementing phase-encoding gradient, and the incrementation index, or view number V. In a simplified form, this relationship is given by:

$$\theta(V) = \gamma\, gY\tau V \qquad (1)$$

where γ is the gyromagnetic ratio, g is the constant increment of the phase-encoding magnetic field gradient, Y is the field-of-view in the y spatial direction for which the phase-encoding gradient acts, t is the time the phase-encoding gradient is applied, and V is the view number. For an image with N views or increments of the phase-encoding gradient, V is incremented from -N/2 to +N/2 by ones. Thus gV represents the actual amplitude of the phase-encoding gradient for view V. Figure 1 illustrates the ideal gradient response as suggested by equation 1. The negative and positive maximum of the phase-encoding gradient are chosen such that the accumulated phase is single valued, and in the range of 0 to 2π.

Figure 1. Ideal Gradient Response

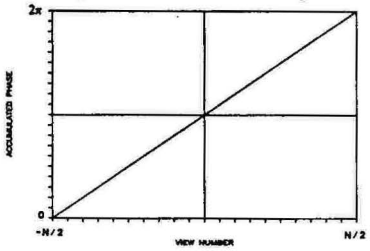

Figure 2. Droopy Gradient Response

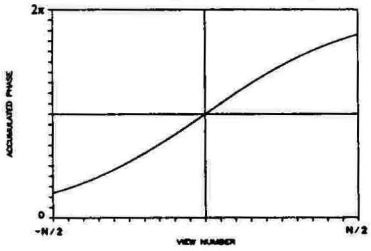

Figure 3. Asymmetric Gradient Response

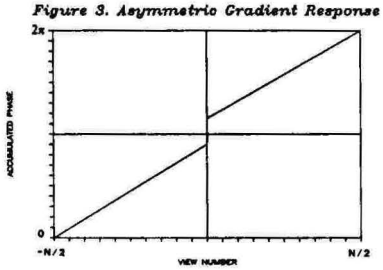

Figures 2 and 3 are extreme but illustrative examples of non-ideal behavior of the applied phase-encoding gradients. Figure 2 represents the case where the amplifiers are able to remain linear when amplitude demands are minimum (about view 0), but are non-linear, or "droopy" when the amplitudes are increased. Figure 3 represents the case where the amplifier response is different for positive versus negative amplitudes; here, for example, the positive and negative zero current conditions are different. In each case, or any combination of or addition to these cases, the resolution along the phase-encoding direction of the resultant NMR image will be compromised, and artifacts could be introduced.

The application of an unequally incremented phase-encoding gradient made it possible to empirically maximize the image resolution in the phase-encode direction. Additionally, this study gave direction for hardware corrections of non-ideal amplifier behavior.

References:

1. A. Kumar, D. Welti, and R. R. Ernst, J. Magn. Reson. 18,69 (1975).

2. W. Edelstein, J. Hutchinson, G. Johnson, and T. Redpath, Phys. Med. Biol. 25, 751 (1980).

3. D. Twieg, Med. Phys. 10, 5, (1983).

Mpm-C8

ANALYSIS OF PULSE SEQUENCE PERFORMANCE IN MR IMAGING

David D. Stark, M.D., Michael S. Middleton, M.D., Ph.D., Jack Wittenberg, M.D., Sanjay Saini, M.D., Rodney J. Butch, M.D., Joseph T. Ferrucci, M.D.

Massachusetts General Hospital & Harvard Medical School, Boston, MA 02114

Introduction: A quantitative method derived from MR image contrast theory (1-4) is applied to actual clinical images. The detection of hepatic metastases is used to demonstrate this method of MR image analysis (5).

T2 weighted SE images acquired in conjunction with the phase contrast (chemical shift) technique are currently recommended for the detection of hepatic metastases. Recently, the minimal achievable echo delay (TE_{min}) has been reduced to 18 msec or less, increasing T1 contrast and signal-to-noise ratios of IR and short TR SE sequences (7).

Methods: We compared T2 weighted conventional and phase contrast images with T1 weighted IR and SE images. Forty patients with cancer metastatic to the liver were imaged with 20 different pulse sequences (avg. 8.6 seq/patient) to allow direct comparison of pulse sequence performance. The cancer-liver signal-difference (SD) was measured and scaled to background image noise (SD/N)(5). All data were corrected to account for imaging time (5).

Results. As predicted by MR image contrast theory, the SD/N ratio was found to correlate with subjective (visual) assessments of lesion detectability (Figs. 1,2).

Quantitative results are ranked (Table) using the SD/N parameter as well as the ratio of SD/N to its standard deviation, known as the "confidence factor" (4).

Conclusion: These results show that the phase contrast technique improves T2 weighted SE images but is detrimental to T1 weighted SE and IR images (5,6). At our field strength (0.6T) TR should be at least 2000 msec for T2 weighted SE images, as the TR 1500 sequences were inferior. T1 weighted IR and SE techniques benefit by reduction of TE_{min} to 18 msec or less.

Quantitative image analysis allows practical confirmation of image contrast theory and provides a scientific basis for pulse sequence selection that can be applied to a variety of clinical tasks.

PULSE SEQUENCE	(N)	CANCER-LIVER SD/N MAGNITUDE	Rank order of performance SD/N	CONFIDENCE FACTOR*
SE 1500/30	7	1.9 ±0.9	19	
SE 1500/30 PC	7	3.0 ±2.4	15	
SE 1500/60	7	3.5 ±3.0	14	
SE 1500/90	6	5.5 ±4.2	10	
SE 2000/30	27	2.4 ±2.1	18	10
SE 2000/30 PC	25	4.2 ±3.1	13	8
SE 2000/60	33	4.7 ±3.6	11	9
SE 2000/60 PC	6	6.9 ±2.7	7	
SE 2000/90	27	7.5 ±5.3	5	7
SE 2000/120	5	7.7 ±3.4	4	
SE 2000/180	4	4.2 ±2.0	12	
IR 1500/450/30	33	6.2 ±3.6	9	5
IR 1500/450/30 PC	1	1.6	20	
IR 1500/450/18	35	7.9 ±4.2	3	3
IR 1500/280/18	30	7.2 ±3.7	6	2
SE 500/30	37	6.4 ±4.1	8	6
SE 500/30 PC	6	2.9 ±2.1	17	
SE 260/30	32	8.1 ±4.6	2	4
SE 260/30 PC	5	3.2 ±0.9	15	
SE 260/18	39	10.3 ±5.2	1	1

*Confidence factor is calculated only when the number of patients (N) is >25. PC = phase contrast

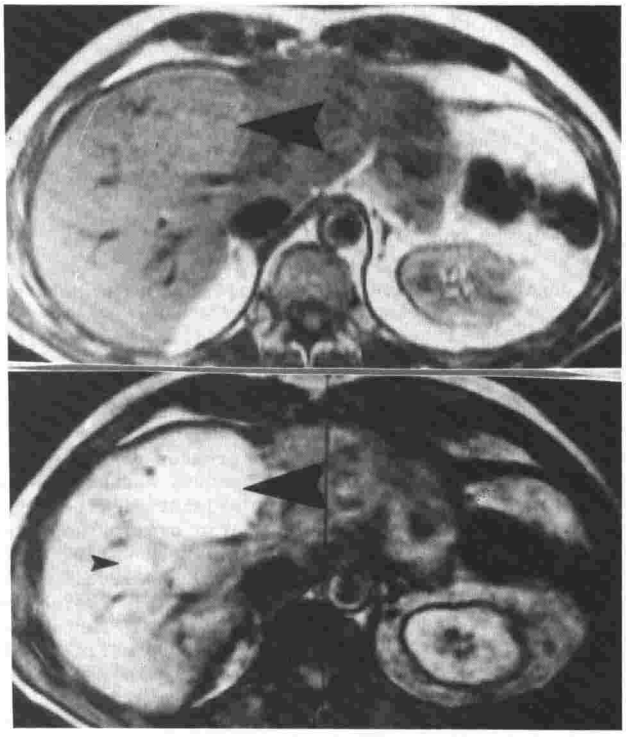

Fig. 1: Liver metastases SE 2000/30 sequence shows a low contrast lesion (arrowhead) in the right hepatic lobe.

Fig. 2: SE 2000/30 PC (phase contrast) sequence has improved contrast & shows additional lesions in the right hepatic lobe.

References:
1. Hendrick RE: Mag Res Imag 2:193, 1984.
2. Wehrli FW: Mag Res Imag 2:3, 1984.
3. Edelstein WA: JCAT 7(3):391, 1983.
4. Rose A: Vision: Human and Electronic. Plenum Press, New York, 1974.
5. Stark DD: Radiology 158:327, 1986.
6. Lee JKT: Radiology 156:429, 1985.
7. Stark DD: Diagn Imag 7(11):118, 1985.

(Mpm-D) RELAXOMETRY

Presiding: S. McCarthy & N. Matwiyoff

3:20 pm

ROOM C-102

12 MINUTES PER PRESENTATION

Mpm-D1

ROLE OF WATER CONTENT AND WATER STRUCTURE IN THE EARLY DETECTION OF STROKE BY CT AND MR IMAGING

Evan Unger, M.D., James Littlefield, M.D. and Mohktar Gado, M.D.

Fox Chase Cancer Center, Phila., PA 19111 and Mallinckrodt Institute of Radiology, St. Louis, MO 63110

Recent work by the authors and others has shown that Magnetic Resonance Imaging (MRI) is more sensitive than transmission Computed Tomography (CT) in the detection of acute stroke. In order to provide an understanding of this greater sensitivity, two sets of experiments were performed using simple model systems. A comparison was made of CT and MRI of gelatin gels with increasing water content and hardened hens eggs. Relaxation times of samples were measured by spectrometer. Varying the concentration of water in gelatin over a range seen in non-ischemic and infarcted cerebral tissue confirmed the linear relationship between water content and spin lattice (T_1) and spin spin (T_2) relaxation times. A simple cellular system using hen's eggs demonstrated that there was a significant decrease in T_2 and a lesser shortening of T_1 which accompanied egg hardening although there was no significant change in water content. On CT there was a direct linear relationship between CT attenuation (Hounsfield Units) and the specific gravity of the gelatin gels and an inverse relationship with water content. There was no change in specific gravity of egg samples with hardening and as expected on CT no change in linear attenuation accompanied hardening. The dramatic shortening of T_1 and T_2 relaxation times of egg samples which occurred within egg hardening likely reflected the transfer of bulk egg intracellular water into a bound or structured form. Although there is a well known change in water content which accompanies stroke and which accounts for the changes seen on CT, the increased sensitivity of MRI in stroke is related not only to this minor change in water content but importantly to changes in subcellular water structure as well. We hypothesize that the increased sensitivity of MRI to the detection of stroke is due to changes in the bulk water content within cerebral tissue accompanying infarction.

Mpm-D2

ANALYTICAL NUCLEAR MAGNETIC RESONANCE STUDIES OF TUMOR METASTASIS IN RATS, RABBITS AND MAN AT 30, 60 AND 200 MHZ

J.W. Frazer[1], C. Hazlewood[4], M. Hebert[4], L. Wood[1], S. Tomasovic[1], S. North[1], A.W. Boddie, jr[1] and L. Dennis[4]

1. M.D. Anderson Hosp. & Tumor Inst., Houston, Tx. 2. U. Kentucky Sch. Med., Louisville,Ky 3. Exxon Res.& Eng. Corp., Baytown, Tx. 4. Baylor Univ. Sch. Med., Houston, Tx.

VX2 tumors implanted in rabbit hind limbs were shown to have differences in Folch extracted lipids in the region1.2-2.5 ppm downfield from TMS standard in 1H spectra when compared to normal tissue. Metastasis of this tumor to the lungs produced tumor spectra quite different from the parent tumor and from non-involved lung tissue. We have shown (Bines et al, submitted to Jour. Clin. Exp. Metast.) that rat mammary tumors with high metastatic potential (13762NF clone MtLn3) had spectra in the 3-4 ppm range markedly different from clones with lower metastatic potential (clone MTC) as well as differences in the 0.9-2.5 ppm range.

Rats implanted with clones MtLn3 or MtPa had blood samples removed at weekly intervals during the period of tumor growth. Serum T_1 was measured at 30 and 200 mhz, the A and B relaxation constants calculated and compared. Both constants varied in tumor bearing anim-

als after the tumor burden had become appreciable in contrast to controls in which both constants remained level for the duration of the experiment.

Human colon tumors, explanted incidental to normal therapeutic procedures, were examined for differences between de novo colon tumors, liver metastasis, and tumors formed by metastasis from other tissues. Tumors were marked by peaks at 3-4 ppm and 1-1.5 ppm, but the most striking difference was the number of definable peaks found in contrast to the poorly resolved peaks usually found in tissue samples,

The findings suggest that part of the spectral differences found is due to structural disruption of tissue with decrease in nuclear Overhauser effects. These effects are strongly dependent on separation distance, either within or between molecules and may also explain the lack of resolution improvement found at higher frequencies in the absence of pulse techniques in normal tissue. Such a tissue disruption would have dramatic effects on solvent relaxation times if hydrophyllic groups such as glycosides were to be exposed to solvent.

Mpm-D3

STUDIES OF T1 CHANGES IN RAT LIVER PROTONS AS A RESULT OF INJURY NOT INVOLVING LIVER

D.J. Pizzarello, Ph.D., R. Chandra, Ph.D., J. Ziegler, M.D., A.D. Steinfeld, M.D. and D. Bimston

New York University Medical Center, Department of Radiology, 550 First Avenue, New York, NY 10016

The longitudinal relaxation time, T1, of protons in rat liver has been shown by us and others to increase after partial hepatectomy as well as sham operations (abdominal incision, liver handled but not removed). This suggested that either stress, tissue injury or its repair accounts for the increase. Our later experiments showed that stress alone does not affect liver proton T1. In the present study we report the affect on liver proton T1 of two kinds of tissue injury and repair: surgically produced wounds of differing severity and radiation damage. Neither the surgical cuts nor irradiation involved liver.

METHODS. (a) Care and Maintenance of Rats. Male Sprague Dawley rats weighing 90 to 100 grams each were used in all experiments. Food and water was always available. The light cycle was 12 hours light, 12 dark: lights on at 7:00 a.m.

(b) Surgical Wounds. Animals were placed under light ether anesthesia and either the skin or skin and peritoneum were slit from the xiphoid notch along the midline to the level of the bladder. These were immediately repaired with suture. Liver was not touched or handled in any way.

(c) Radiation Damage. The hind legs, bladder, part of the large intestine and tail were exposed to 1200 rads of 4 MeV x rays. Liver was not in the field, but the affect of radiations scattered to liver was determined by irradiating the livers of some control animals with the calculated scattered dose.

(d) Tissue Sampling. Surgical injury. A small sample of liver was taken from living animals under heavy ether anesthesia either 24 or 48 hours after wounding, placed in a glass NMR tube, corked and T1 and T2 measurements made. Radiation injury. Whole liver was removed from the heavily anesthetized animals. This was weighed and a sample taken from it either at 3, 10 or 28 days after irradiation. At the same time, one kidney, one testis and 1 ml of blood were also removed. T1, T2 and water content measured for all save blood. In addition the remaining testis and kidney were removed and weighed. In order to determine whether there was radiation induced weight loss or retardation of growth, the rats themselves were weighed before irradiation and at the time of sacrifice and these weights compared.

(e) T1/T2 Measurements. Measurements of T1 and T2 were performed at room temperature (22+0.5°C) using a commercial pulsed NMR spectrometer which operates on a fixed frequency of 10.7 MHz (0.25T - magnetic field) within 5 to 15 minutes of the removal of tissue samples from the animals. Pulse sequence, data acquisition and analysis were controlled by a dedicated microcomputer. T1 was determined by a saturation recovery pulse sequence; i.e., 90°-t-90°. Thirty sequentially increasing pulse delays (step = 15 msec) were used and each point was an average of three measurements (spectra). The pulse repetition time (TR) was 1 sec. These measurements described the recovery of longitudinal magnetization as a function of time. A least-squares single exponential fit was made to these data by computer which then printed the relaxation time and the correlation coefficient of the fit to the data. T2 was measured immediately following the measurement of T1 using Hahn's spin echo sequence; i.e., 90°-t-180°. The effect of diffusion on the pulse echo was found to be negligible as was evident from the observed mono exponential decay of echo amplitude with pulse delay. Again, 30 sequentially increasing pulse delays (step = 2 msec) were used, and each point was averaged from three measurements. T2 was calculated by computer by a least-squares fit to a single exponential.

(f) Water Content. After the T1/T2 measurement, the tube was uncorked and weighed, thus determining the wet weight of the tissue. They were put in a hot air oven at 55°C and weighed periodically until no further weight change was noted. This dry weight was subtracted from the wet weight, the difference being the weight of water evaporated from the liver piece, and the result expressed as percentage wet weight.

(g) Analysis of Data. Group means and their standard deviations (S.D.) were computed and the significance of the differences between means was determined using student's t test for two groups.

RESULTS. Surgery. Twenty-four hours post surgery mean T1 values were significantly different from controls (238±7 vs 217±12) for deep wounds (skin and peritoneum): no significant differences between the mean T1 of livers of superficially wounded animals (skin) and controls. Forty-eight hours after operation significant differences persisted in the mean liver T1 between rats with deep wounds and controls. Irradiation. Mean liver proton T1 differed significantly from controls only at 28 days post-irradiation. The mean T1 of other sampled organs did not differ from controls nor did the water content. Body and testis weights in irradiated groups were significantly different from controls. Scattered radiations had no affect on any parameter measured. T2 values were never affected.

CONCLUSIONS. Our results suggest that repair of tissue damage anywhere in the body results in an increase in liver proton T1. This is true whether or not the liver itself is injured. It further suggests that lengthened T1 of liver protons can be an indicator of damaged tissue(s) being repaired.

Mpm-D4

NMR RELAXOMETRY AS A POTENTIAL INDICATOR OF THE PHYSIOLOGICAL AND PATHOLOGICAL RESPONSE OF THE KHT SARCOMA TO RADIOTHERAPY.

Charles A. Belfi, Siglinde Emerson and Frank Q.H. Ngo

Laboratory of Radiobiology and NMR Research
Department of Immunology and Cancer Research, Cleveland Clinic Foundation, Cleveland, Ohio 44106.

NMR imaging has a broad potential for the non-invasive study of tissues and tumors. It may also open up new vistas in the study of the effects of radiotherapy. Since radiotherapy is known to alter the physiological state of tumors and cause tissue injury, it may be possible that NMRI would be able to differentiate between irradiated and non-irradiated tumors in a time dependent manner. In this study, the proton NMR relaxation times and water content values of control and irradiated KHT tumors have been studied as a function of time post-irradiation (P.I.).

Proton NMR relaxometry (T1 and T2) was obtained from excised KHT tumors (Kallman et al, JNCI 39:539-549, 1967) which had been implanted into the leg of C3H/HeJ mice. T1 and T2 were also obtained from excised tumors which had undergone single dose radiotherapy (35 Gy). NMR relaxometry was obtained on the irradiated and non-irradiated, excised tumors using an IBM Multispec spectrometer operating at 20 MHz and 37 C. T1 and T2 were obtained using the IR and CPMG methods respectively. Water content was determined by calculating the ratio of the wet weight over the wet plus dry weights of the excised tumor (Figure 1).

The dose employed caused a substantial delay in tumor growth but was insufficient for complete tumor eradication. A linear correlation between relaxation times and water content was found for the control tumors. The irradiated tumors had a significant increase in water content and a concomitant increase in relaxation times for the first four days P.I. (Figures 2 and 3). The continued NMR reaction to radiation therapy was a fall in T1 below the control tumor T1 value during days 4-9 followed by a gradual T1 increase for the rest of the time the tumors were monitored while remaining below those of the controls. Changes in T2 in the first few days were qualitatively similar to the changes in T1, but the values remained high compared to the T2 of the controls for the rest of the P.I. time. Correlation of relaxation times, T1 and T2, with water contents were strong for control tumors (r= 0.88, 0.81). Interestingly, for irradiated tumors the correlations appeared to break down (r= 0.48, 0.72). The lack of correlation of T1 and T2 with water content may be attributed to radiation-induced edema and necrosis in KHT tumors. (Supported by NCI grant Ca 39032).

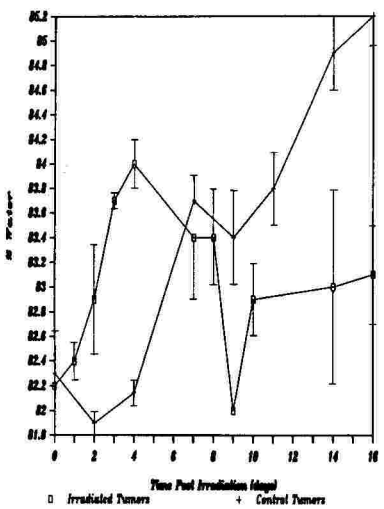

Figure 1.

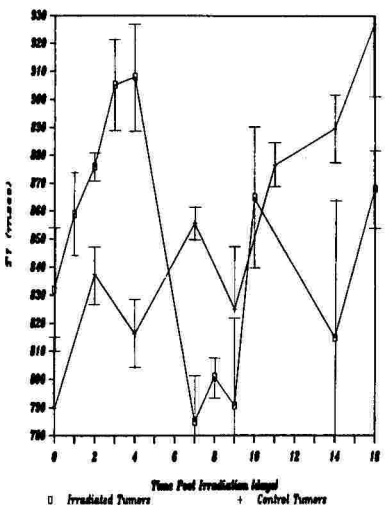

Figure 2.

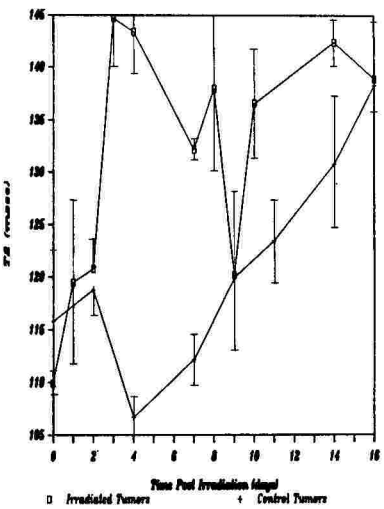

Figure 3.

Figure 1. Water content values for irradiated and control tumors as a function of time P.I. Standard error is shown for each point. Tumor system was KHT and dose used 35 Gy X-rays.

Figure 2. T1 (msec) relaxation time is shown for irradiated and control tumors. T1 was obtained at 20 MHz and 37° C with IR pulse sequence.

Figure 3. T2 (msec) relaxation time is shown for irradiated and control tumors. T2 was obtained at 20 MHz and 37° C with the CPMG pulse sequence.

Mpm-D5
ORIGIN OF MRI CONTRAST: CORRELATION OF KNOWN WATER CONCENTRATION SAMPLES AND IN VIVO BRAIN IMAGING

Donald W. Chakeres, M.D., Charles Dietz, BS, Paul Keller, Ph.D., Petra Schmalbrock, Ph.D., Kenneth Weiss, M.D.

The Ohio State University Hospital, Departments of Radiology and Chemistry

This study investigates the relative magnetic resonance imaging (MRI) pixel intensities of mixtures of quantitatively known water concentration using a clinical MRI unit. We simultaneously imaged these samples with normal brains to develop a model to better understand MRI image contrast. Normal white matter (70% water content) and gray matter (80% water content) structures are known to have a narrow range of water content allowing for correlation of living tissue to experimental mixtures of similar water content. Mixtures of gelatin and water, and polyalcohol polymer and water, ranging from 100% to 50% water were made. These mixtures as well as vegetable oil, paramagnetic (Gd-DTPA) enhanced water, plasma, serum, and whole blood were simultaneously imaged with a normal volunteer head. Spin echo images with TR's 150-4000 msec, and TE's of 20-100 msec were obtained for T1, T2 relaxation times, and relative pixel intensities of the samples and normal brain tissues. A proton density image using a gradient refocused technique with a TR 1000 msec, TE 12 msec, and a flip angle of 22.5 degrees was also made. We found that the proton density image pixel intensities were proportional to the water concentration of the gels. The inverse of the relaxation vs the percent water for the gels and polymer was nearly linear as would be expected with a contrast agent. The pixel intensities on the proton density image for specific regions of the brain having known water concentrations and the polymer solutions were lower than those of the same water concentrations in the gels. Therefore there is a profound proton density effect on imaging. The signal intensities from the spin echo images of the gels and the brain all followed similar patterns of signal and relaxation times based on water concentration but with varying degrees. This suggests that the brain lipids and proteins effect the water in similar fashion to the gels but to a different degree. The spin echo image signal was not unique for each gel. Mixtures of widely different water content could have the same signal intensity producing a confusing inaccurate display of the gels based on their water content. Therefore, we feel that a proton density image will be very important in the evaluation of the brain since it most directly reflects the water content. The proton density image is the only single pulse sequence, other than a very long TE spin echo image which has an umbigous proportional signal based on water content. We conclude that this model accurately explains most of the imaging phenomonon of normal brain with the water content as the ultimate basis for the measured T1, T2 and proton density.

Mpm-D6
WATER CONTENT AND NMR CHARACTERISTICS OF FOETAL AND NEONATAL TISSUES: AN INTER-COMPARISON OF RESULTS IN VITRO AND IN VIVO DURING DEVELOPMENT.

M. A. Foster, P.A. Fowler and J. R. Mallard

Department of Bio-Medical Physics & Bio-Engineering, University of Aberdeen, Foresterhill, Aberdeen, U.K.

In this study NMR is being used to examine the maturation of tissues during foetal and early post-natal life. A large-scale study of young rat tissues has shown overall agreement with findings of earlier authors (1,2,3) and has extended the available information on comparative maturation rates of water content and T1 value between different tissues. In general the water content and T1 value show a relationship close to linear (e.g. in liver tissue) but in some tissues, e.g. thigh muscle, the relationship is more complex (Fig. 1a and b).

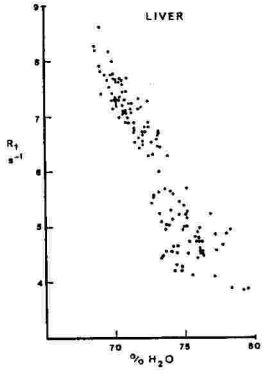

Figure 1a

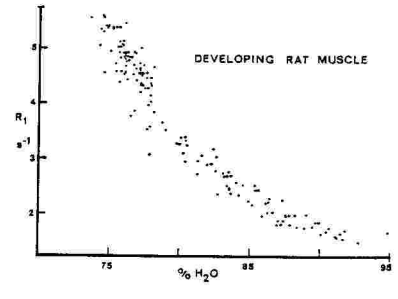

1b

Water content values were obtained by drying tissues at 60°C to constant weight. NMR T1 relaxation time values were produced at 2.5MHz and room temperature (18° to 25°C) on a home-built system using a Hahn spin echo sequence with prior inversion. A minimum of 10 tau values were obtained and each point was the average of five repetitions. A weighted linear regression method was used to calculate T1.

A similar study of goat maturation was undertaken for two reasons. Firstly the goat tissues mature more slowly and may, therefore, be a better model of the human situation. Secondly the young goat is sufficiently large to examine in the head coil of a human NMR imager, hence allowing intercomparison of results obtained in vivo and in vitro. Results in vitro were obtained with the methods stated above. In vivo imaging was undertaken at 0.04 Tesla using an inter-leaved IR/SR pulse sequence to allow calculation of a T1 value using a 2-point method. Ti of the IR sequence was 200ms and the overall Tr was 1 second.

In general the maturation pattern of goat tissues was similar to that of the rats but with a longer time-course. No difference in pattern was detected between the in vivo and in vitro examination although problems such as partial voluming and lack of tissue specificity gave a wider variation in results obtained in vivo. Figure 2a and b show the maturation pattern observed in vivo for several tissues and Figure 3a and b provides a comparison of changes in T1 and water content of goat CNS tissues and tendon observed in vitro.

REFERENCES

1. Widdowson E M and Dickerson J W T (1964): Chemical composition of the body. In: Mineral metabolism, Vol.2 part A, Comar C L and Bronner F (eds.) Academic Press, New York.
2. Hazlewood C F, Nichols B L, Chang D C and Brown B (1971) On the state of water in developing muscle: A study of the major phase of ordered water in skeletal muscle and its relationship to sodium concentration. Johns Hopkins Med. J. 128, 117-131.
3. Foster M A (1985) Tissue discrimination by NMR in the foetus and neonate; in vivo and in vitro studies. J. NMR Med., 5, 51-56.

Figures 2a 2b 3a 3b

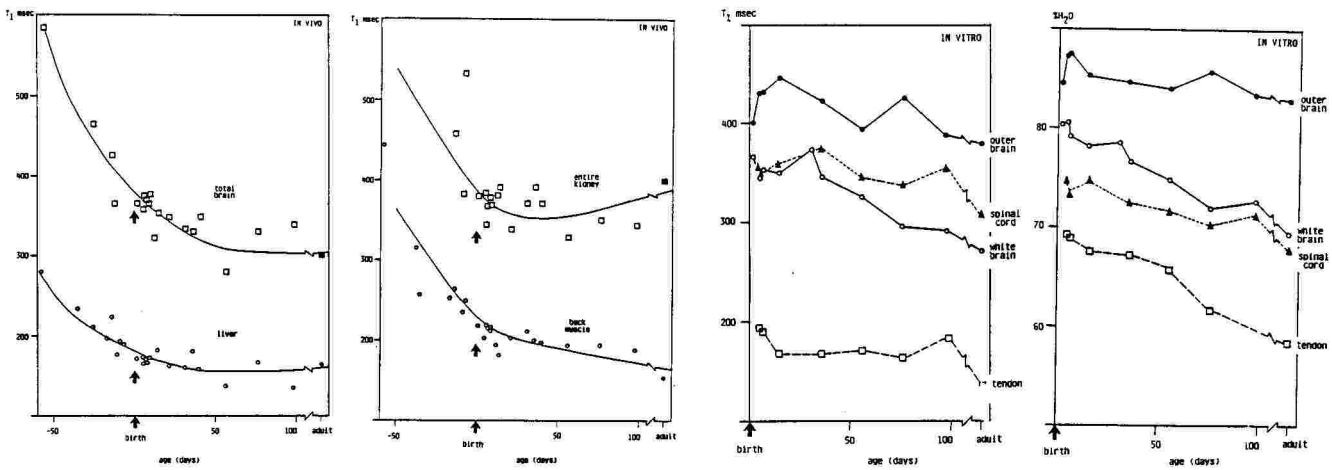

Mpm-D7

Studies on the Release Rate Behaviour of Tetracycline from Sustained Release Dosage by Pulse Nuclear Magnetic Resonance.

by

R. Azoury[1], R. Elkayam[2], S. Abrashkin[1] and M. Friedman[2].

[1]Soreq N.R.C. Yavne, [2]School of Pharmacy, The Hebrew University, Jerusalem, Israel.

A preliminary study to explore the behaviour of a sustained release dosage composed from ethyl-cellulose, polyethylenglycol (PEG) and tetracycline (TET) was carried out using a Bruker PC Multispec at 20 MHz and by means of u.v spectroscopy.

The TET release rate was examined as function of two variables: the gradual changes in the relative concentration (% w/w) of the embedded TET and PEG respectively. T_1 and T_2 relaxation times were measured after the immersion of the film in 1ml of DDW.

As a function of time, pronounced T_1 and T_2 shortening was noted. However the changes in T_2 relaxation time were sharper and seem to be more consistent than in T_1.

High correlation between T_2 relaxation times and TET release as measured by u.v spectroscopy was found. These results may indicate that T_2 could be employed as a method for measuring TET release.

Embedded PEG enhanced significantly the release rate of TET. The enhancement was linearly increased in the presence of up to 5% PEG (30% TET) and then reached a saturation.

When the concentration of embedded TET was gradually increased (up to 40% and in the presence of 5% PEG) a linear enhancement in TET release was observed. A saturation of the release rate was noted when TET concentration exceeds 40%.

Gradual changes in PEG and TET concentration respectively lead to different changes in the hydrophilic / hydrophobic characteristics of the supporting polymer. These changes were reflected in significant differences in T_1 and T_2 relaxation time measurements. The enhancement in TET release rate may be attributed to the hydrophilic character improvement of the supporting polymer. These improvements allowed better penetration and better contact of water with the whole matrix of the sustained release dosage. Thus improved dissolution of TET. The same phenomenon could explain the shortening of relaxation time T_2. The changes in Proton MR relaxation times as correlated to TET release rate may provide a new mean to explore the behaviour Kinetics as related to structural feature of a sustained release dosage.

(Tam-A) BODY - ARTIFACTS

Presiding: P. Joseph & S. Thomas

10:20 am

RIVER ROOM

12 MINUTES PER PRESENTATION

Tam-A1

WHY ARE RESPIRATORY MOTION ARTIFACTS MORE CONSPICUOUS IN HIGH FIELD MRI?

Michael L. Wood[a], Val M. Runge[a], and R. Mark Henkelman[b]

[a]New England Medical Center and Tufts University School of Medicine
[b]Ontario Cancer Institute and University of Toronto

Anatomical structures that move during breathing, particularly the fat in the anterior abdominal wall, often present as multiple ghosts in the phase encoding direction of magnetic resonance (MR) images. The ghosts are a consequence of periodicity between the motion and the technique of Fourier imaging. The overlap of the ghosts with other structures degrades image contrast, interferes with diagnosis, and adds inaccuracy to quantitative measurements. Images of the same human subject under similar conditions at 0.15 Tesla (T), 0.5T, and 1.5T demonstrated that these ghosts are more conspicuous at higher magnetic field strength. Analysis of the images was supplemented with theoretical images of a hypothetical point object in periodic motion.

Respiratory motion artifacts were more conspicuous in the higher field strength images when the structures producing the ghosts were more intense, and also when particular operating conditions increased the intensity of ghosts relative to the structures producing them. Specifically, the following reasons made the artifact more conspicuous in higher field strength images.[1]

(a) Most importantly, there was less noise to hide the ghosts.

(b) Greater contrast between fat and muscle caused more degradation when ghosts from moving fat overlapped with imaged muscle tissue.

(c) The receiver coil was more sensitive near moving anatomical structures, compared to the 0.15T saddle coil, where the image intensity from fat on the anterior abdominal wall was only one-half as great as that from fat in the posterior region.

(d) Motion occurred over a greater number of pixels, because the pixels were narrower. Ghosts with higher intensity were the result.

(e) There was less or even no averaging of data, because noise was already low enough. Consequently, the attentuation of ghosts by averaging was missed.

Motion artifacts are more conspicuous in high field MRI, but they are not detrimental, because there are effective methods, such as rapid imaging[2], for suppressing them. In fact, rapid imaging is actually more feasible at higher magnetic field strength.

1. Wood, ML; Henkelman, RM. The magnetic field dependence of the breathing artifact. Magnetic Resonance Imaging. 4(5):387-392; 1986.

2. Haase, AJ; Frahm, C; Matthaei, W; Merboldt, KD. FLASH Imaging. rapid NMR imaging using low flip angles. Journal of Magnetic Resonance. 67:258-266; 1986.

Tam-A2

EVALUATION OF SHORT TI INVERSION RECOVERY PULSE SEQUENCE IN PATIENTS WITH PRIMARY AND METASTATIC MALIGNANCIES

J.A. Frank,* A.J. Dwyer, A. Hickey, J.L. Doppman*

Diagnostic Radiology Department, Clinical Center, National Institutes of Health, Bethesda, MD and Georgetown University Hospital*, Washington, DC.

Although the inversion recovery (IR) pulse sequence is commonly accepted as a pulse sequence producing

excellent display of gross anatomy, it is commonly held to be inferior to the T2-weighted spin echo (SE) in its sensitivity to and display of pathology. This is a potentially misleading doctrine based on traditionally used IR sequences with long inversion times (TI). Although this is an excellent design for maximizing contrast among normal tissues, exploiting their disparities in T1, it is an incomplete assessment of the full potential of the IR and its applications in cancer imaging. Shortening of the TI, in addition to reducing the total acquisition time per slice, increases the sensitivity to neoplasia and other pathology. This results from the effects of increases in spin density, T1, and T2 (a frequent finding in malignancy) on signal intensity being additive. With other pulse sequences, these effects are opposed, cancelling one another and reducing contrast between tumor and host tissue. In addition, the short TI markedly reduces or nulls the signal from adipose tissue and fatty marrow serving to make tumors more conspicuous, as well as reducing motion artifacts transmitted from body wall and mesenteric fat. Shortening TR, as well as TI, reduces signal intensity from the structures with very long T1s, thereby improving distinction of some tumors from bowel and other fluid collections. In concert, these effects of the short TI IR pulse sequence (STIR) produce images in which the tumor burden appears conspicuously bright in a dark background with muted but discernible anatomic detail.

To assess the utility of the STIR pulse sequence, we examined 300 patients with various malignancies, including liver metastases, bone marrow metastases, soft tissue sarcomas, lymphomas, renal cell carcinoma, lung and breast carcinoma at 0.5 Tesla (Picker International). IR 1500/100 images were compared with T1-weighted SE 500/26 and T2-weighted SE 2000/80. Signal intensities were taken from regions of interest in the tumors, fat, muscle, and host tissues. Noise was estimated as the mean signal of the surrounding air. From these, contrast-to-noise ratios were calculated (difference in mean signal/noise) between tumor and normal host and background tissues.

The STIR sequence was superior to both the T2-dependent (SE 2000/80) and T1-dependent (SE 500/26) sequences in detection and delineation of the tumor burden. In general, tumor was conspicuously bright contrasting markedly with adipose tissue, fatty marrow, muscle, liver, and bone cortex. Problematic was distinction between tumor and normal tissues with prolonged T1s and T2s (i.e., kidney, spleen, and neurovascular bundles)--the distinction resting primarily on considerations of morphology and location. In comparison to the T2-dependent SE 2000/80 sequence, the STIR sequence was superior in producing contrast between lesion and adjacent tissues, achieving as much as a three to fourfold increase in displaying anatomy contrast-to-noise. This was particularly striking with tumor abutting or imbedded in adipose tissue or metastatic to marrow. Contrast-to-noise ratios for tumor versus fat for the SE 2000/80 and IR 1500/100 were 3.6 and 18.8 respectively. For tumor versus muscle, 6.8 and 13.0 respectively (45 cases). In addition, the STIR sequence was more efficient, resulting in a savings of approximately 25% in acquisition time. In comparison with the T1-weighted SE 500/26 pulse sequence, the STIR pulse sequence was inferior in displaying anatomy and demonstrated little advantage in displaying tumor/fat interfaces. However, it was clearly superior in displaying bone metastases interfaces between tumor and muscle and cortical bone. Hence, in cancer imaging, the STIR pulse sequence combines desirable properties of both the T1 and T2-weighted spin echoes, providing the most complete display of the tumor burden and its relationships in a single image.

We, therefore, recommend the IR 1500/100 pulse sequence be used with the T1-dependent spin echo pulse sequence in anatomic staging of malignancy.

Tam-A3
CLINICAL APPLICATIONS OF FLASH AND FISP

Mark A. Osborne, Val M. Runge, Michael Wood, and John Kirsch

New England Medical Center and Tufts University School of Medicine

The clinical application of two "fast scan", gradient echo techniques, FLASH and FISP, is currently being investigated. In the FLASH technique (Fast, Low Angle SHot) TR = 20-80 msec, TE = 10-16 msec, and flip angle = 10-90°. In the FISP technique (Fast Imaging with Steady-state free-Precession) TR = 25-1000 msec, TE = 12 msec, and flip angle = 10-180°.

To date 48 patients have been studied with FLASH and/or FISP. Cases have included primary and secondary hepatic neoplasms, neoplasms of the neck, avascular necrosis, and a variety of vascular abnormalities including aneurysm, thrombosis, and arteriovenous malformation. Both scans afforded decreased respiratory motion artifact compared to traditional spin-echo techniques, and scan time is very short (approximately 5-30 sec). Although initial scans suffered from poor tissue contrast and low signal-to-noise recent changes in the three main variables (TR, TE, flip angle) have resulted in both improved tissue contrast and increased signal-to-noise. Additionally, due to the short scan time vascular structures are easily identified, (high signal intensity), which aids in distinguishing tumor from adjacent vessels, and it offers the potential of imaging vascular abnormalities.

We conclude that both FLASH and FISP do have clinical application to imaging the neck, abdomen, pelvis, and extremity.

Tam-A4

UTILITY OF MODIFYING PHASE/FREQUENCY GRADIENT DIRECTIONS IN CLINICAL MRI

Emanuel Kanal, M.D., Richard J. Prorok, R.T., James A. Brunberg, M.D., Peter L. Davis, M.D.

The Pittsburgh NMR Institute, 3260 Fifth Avenue, Pittsburgh, Pa. 15213

Magnetic resonance imaging is accompanied by artifacts that are unique to this imaging modality. Flow and/or motion of protons during imaging can be manifest as either a) signal void over the region of flow, b) signal increase from the region of flow, or c) increased signal from the region of flow that is artifactually phase-shifted throughout the image. The artifact associated with the last type of flow-related signal phenomena may potentially obscure image data over which this signal is misregistered. Additionally, the spurious smearing of the signal intensity from such flowing protons across the phase encoding direction also results in artificially decreased signal intensity from the region of origin of this signal. Such a phenomenon is virtually universally experienced with long TR imaging of the cerebrospinal fluid (CSF), and may result in decreased image contrast between the CSF and its adjacent lower intensity structures on long TR, long TE images. This problem has limited the current diagnostic capabilities of MRI in areas subject to flow/motion artifacts.

Additional limitations exist in areas subject to either respiratory or cardiac motion, where the phase- shifted signal can obscure adjacent regions such as the thoracic spine. While cardiac gating has been shown to effectively improve the accuracy of phase-encoded spatial localization, this technology is presently neither universally available nor applicable or even successful. For example, successful gating may not be possible on certain patients such as those with arrhythmias. Cardiac gating would also potentially limit the range of pulse sequence parameter selection due to its cardiac cycle dependency. Respiratory gating has not been demonstrated as yet to be either efficient or reliable.

For such circumstances, interchanging the directions of the phase and frequency encoding gradients may allow the phase-shifted artifact to be redirected over a portion of the image that may not be crucial for diagnostic purposes, while sparing the region(s) of interest. Such phase/frequency encoding direction interchange is achievable on many clinical MR systems with minimal effort, and may have considerable utility in areas prone to motion and/or flow including the spine, head, abdomen, and pelvis.

The accompanying figures illustrate the applicability of selective gradient orientation for studying the cervical spine. Figure 1 was acquired with the system-standard gradient directions employing a relatively long TR and long TE with 2 excitations. Figure 2 was acquired with identical scan parameters settings but with the phase encoding direction reoriented along the vertical axis. While still present, the phase shifted signal from the flowing CSF has been redistributed over the image in such a way as to considerably decrease the degree of its superimposition over the cervical spinal cord, the anatomic region of interest.

Limitations of this approach are the same as that of routine imaging; it must be remembered that the phase shifted signal has not been removed, only redirected. Especially kyphotic or lordotic cervical spines may not demonstrate as much benefit from such a scanning approach as the phase shifted signal may still be superimposed over the cord from superior or inferior flowing CSF. While the change is technically minor, the resultant effect upon image quality is frequently substantial, and may frequently salvage an otherwise undiagnostic study.

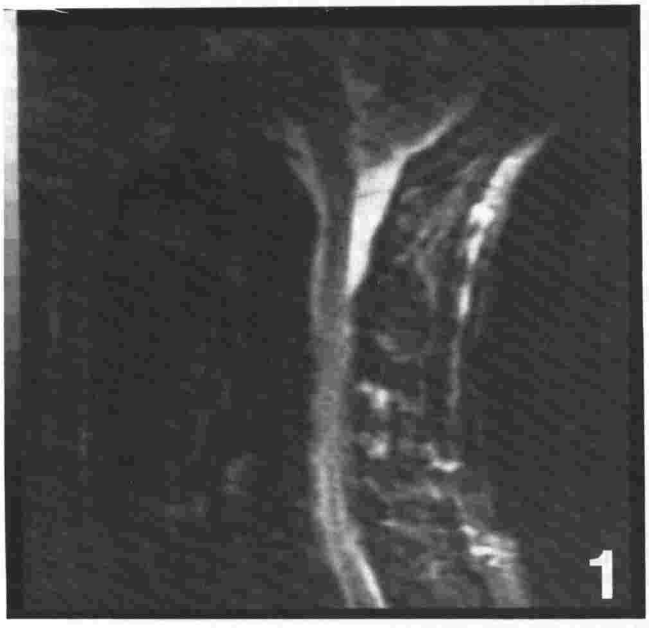

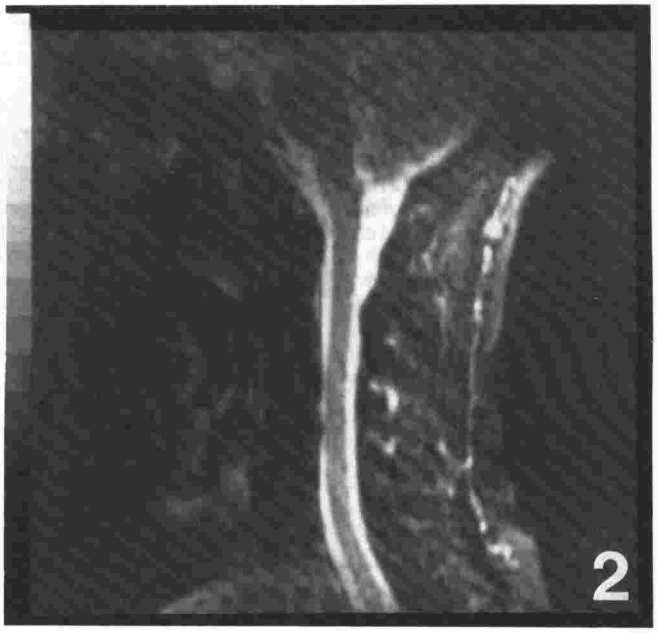

Tam-A5

MOTION ARTIFACT SUPPRESSION TECHNIQUE (MAST^{tm}) IN MAGNETIC RESONANCE IMAGING: CLINICAL RESULTS

Patrick M. Colletti, MD; Pradip Pattany, MSc; Robert Benson, MD; James McNally, PhD; Janak Raval, MD; Chi Zee, MD; William D. Boswell, MD; Philip W. Ralls, MD; Hervey D. Segall, MD

Department of Radiology, Los Angeles County-University of Southern California Medical Center, Los Angeles, California, and Picker International, Inc., Highland Heights, Ohio

Pulsatile flowing blood or CSF cause apparent random phase change which appears as random noise in the phase encoding direction on 2DFT MRI. MAST^{tm} (Picker Int.) is a technique which reduces these artifacts by using a gradient echo sequence computed to cancel velocity, acceleration and pulsatility components. This essentially rephases in-view magnetization. 2DFT spin echo TE 40, 80, and 100 were available. These techniques were clinically tested in 535 patients including 262 brains, 50 head and neck exams, 101 spines, and 122 body scans. Images of the head were sharper with TE 100 MAST. CSF flow artifacts and arterial pulsations were reduced. Rephasing often caused increased signal in moving blood. Excellent T2 spines and improved T2 body scans resulted. TE 40 MAST of the chest showed improved pleural detail. A MAST multiecho 26/100 sequence is also available as is a MAST STIR TI 160. MAST^{tm} is compatible with gating and surface coils and has replaced conventional T2 imaging in our center.

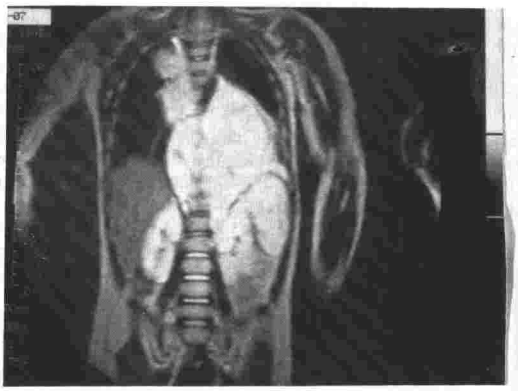

SE2000/100 MAST
Neuroblastoma

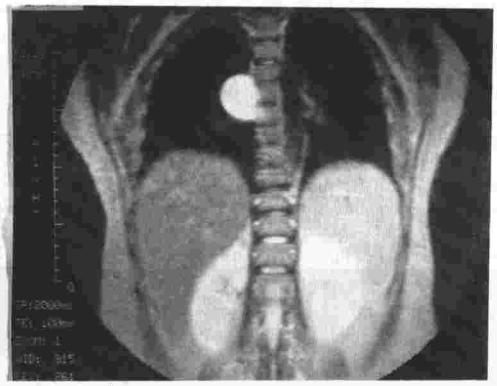

SE 2000/100 MAST
Bronchogenic Cyst

Tam-A6

CLINICAL APPLICATIONS OF THE MOTION ARTIFACT SUPPRESSION TECHNIQUE (MAST)

Phillips JJ, Chiu LC, Pattany PM, Lipcamon JD

Harbor-UCLA Medical Center, Torrance, California

Various techniques have been employed in Magnetic Resonance Imaging to overcome the deleterious effects of physiologic motion on image quality. These include data acquisition during periods of minimum motion, obtaining multiple averages and fast scanning during periods of suspended respiration. The motion artifact suppression technique (MAST) represents a mathematical solution which uniquely takes into consideration motion occuring between the time of the 90° Rf excitation and the echo time (within-view motion). Modifications made on the gradient waveforms refocus magnetization in the transverse plane and zero the within-view random phase terms due to respiratory, cardiac, orbital, peristaltic and blood flow motions. The result is high quality T2- and T1-weighted images with as few as one to two acquisitions per view.

Our ten months experience with the technique on the Picker 0.5T Vista 2055 system will be briefly reviewed, with discussion of its utility in the various imaging areas. Notable improvements in detail within the liver and upper abdomen are obtained on T2-weighted images. In the central nervous system, refocused signal from CSF results in a more uniform appearance, and reduction of flow-related artifacts. Preliminary results also show that signal intensity from the intravascular space will be useful in blood flow quantification and in imaging of vascular abnormalities.

Tam-A7

MOTION ARTIFACT REDUCTION BY FAST SPIN ECHO IMAGING

David D. Stark, M.D., R. Edward Hendrick*, Ph.D., Peter F. Hahn, M.D., Ph.D., Susan A. Stafford, M.D., Joseph T. Ferrucci, M.D.

Massachusetts General Hospital, Harvard Medical School, Boston, MA 02114, and
*University of Colorado Health Services Center, Denver CO.

Introduction: Short TR/short TE spin echo imaging has dramatically improved the quality of abdominal MR images (1). In this study we analyze complex ghost artifacts resulting from all types of physiologic motion in the upper abdomen of 50 patients and volunteers. The levels of systematic noise due to ghosting are measured and compared to statistical (thermal) noise levels. We quantitate the dependence of systematic and statistical noise levels on signal averaging and the choice of spin echo interpulse delay times (TR and TE). This leads to a straight-forward procedure for reducing motion-induced noise and maximizing signal and contrast relative to noise in abdominal imaging.

Methods: Using a Technicare 0.6 Tesla system planar transverse sections were obtained through the abdomen using spin echo techniques varying TR from 260-2000 msec, TE from 15-180 msec, and averaging from 1-18 acquisitions. Measurements of signal intensity were obtained from images using operator defined regions of interest. Systematic noise was measured outside the patient along the same phase encoding axis as moving structures (2). Statistical noise was measured outside the patient along the frequency encoding axis. Noise measurements were scaled to the signal intensity of subcutaneous fat and liver tissue.

Results: We confirmed the theoretical expectation that statistical noise would decrease as the square root of the number of acquisitions (n) averaged (3). Systematic noise dominated images obtained with TE <100 msec and was 2-10 fold greater than statistical noise. All types of systematic noise (cardiac ghosts, vascular ghosts, and subcutaneous fat ghosts) decreased at the same rate as statistical noise in response to averaging.

Varying TR affected the time between phase encoding steps, ghost position and the relative intensities of fat, liver and other tissues due to relaxation effects. Normalization of noise data to fat or liver showed an increase in systematic noise at long TR with the number of acquisitions held constant; this is attributed in part to ghosting from structures with long T1 and T2 relaxation times such as bowel contents (Table). Statistical noise increased at the same rate as signal with increasing TR.

Decreasing TE reduced the contribution of systematic noise relative to statistical noise as the signal intensity of ghosts decreased at the same rate as the signal intensity of their tissue of origin (e.g. subcutaneous fat), while statistical noise remained constant.

Pulse sequence*	Noise#	Fat	Noise%	Liver	Noise%
SE 2000/60/2 9 minutes	11.8	218	5.4	121	9.7
SE 2000/15/2 9 minutes	9.2	343	2.7	255	3.6
SE 260/15/2 1 minute	5.0	176	2.8	73	6.9
SE 260/15/16 9 minutes	2.5 (1.8)	178	1.4 (1.0)	74	3.3 (2.4)

* Spin echo TR/TE/number of data acquisitions.
\# Standard deviation of background ventral to the abdomen.
Noise% is (100 x noise)/(fat or liver signal intensity)
( )Predicted noise% based upon theoretical $\sqrt{n}$ reduction of noise with signal averaging.

Conclusion: Averaging is a powerful technique for reducing both systematic and statistical noise on MR images. Short TR/short TE SE imaging allows extensive averaging without a time penalty and reduces ghosting from bowel contents. Furthermore, short TR/short TE imaging increases signal-to-noise per unit time (Table) and increases T1 dependent image contrast (2). Mathematical techniques developed to predict pulse sequence performance for applications in the central nervous system (4,5) must be modified to account for the relationship of systematic noise to averaging, TR, and TE on abdominal MR images.

References:
1. Stark DD: Diagn Imag 7(11):118, 1985.
2. Stark DD: Radiology 158:327, 1986.
3. Wood ML: Med Physics 12(2):143, 1985.
4. Wehrli FW: Mag Res Imag 2:3, 1984.
5. Hendrick RE: Mag Res Imag 2:193, 1984.

Tam-A8
ARTIFACTS IN CLINICAL MAGNETIC RESONANCE IMAGING

Errol M. Bellon, M.D.[1,3,4], E. Mark Haacke, Ph.D.[2], Damon C. Sacco, M.D.[1,3]

Departments of Radiology[1] and Physics[2], Case Western Reserve University and Cuyahoga County Hospital[3], Cleveland, Ohio and the Clinical Science Center[4], Picker International, Highland Heights, Ohio

The process of creating magnetic resonance images frequently gives rise to artifacts in the final display. These may arise during each step of the scanning process. Many may be corrected through an understanding of their causation; this requires familiarity with scanner design, theory of operation, and image acquisition, generation and display.

The various artifacts are categorized as sequence, reconstruction algorithm, field, or noise artifacts. Each category is further subdivided into system- and patient-related artifact.

Some artifacts are obvious, totally degrading the image; other are regional, affecting only portions while leaving much of the field undisturbed and diagnostically usable. Some artifacts are overt and easily identified, while others, such as those due to phase-shift or gradient strength effects, are quite subtle.

The presentation will consist of an extensive review, emphasizing causation, recognition and correction, with demonstration of specific examples of each type of artifact.

(Tam-B) CHEST - VASCULAR

Presiding: R. Pettigrew & M. Bronskill

10:20 am

ROOM C-107

12 MINUTES PER PRESENTATION

Tam-B1
PULMONARY VESSEL IDENTIFICATION WITH MAGNETIC RESONANCE IMAGING

E.M. Haacke [1], B. Fletcher [2], G.W. Lenz [2], M. Jacobstein [3]

Case Western Reserve University, Departments of Radiology and Physics [1], Department of Radiology,[2] Department of Pediatric Cardiology [3], Cleveland, Ohio 44106

Currently, visualization of the intrapulmonary vessels requires contrast angiography. In patients who have congenital heart disease, magnetic resonance imaging has potential value in order to evaluate peripheral pulmonary stenosis, and hypoplasia as well as abnormal arborization due to pulmonary arterial hypertension. Identification of the first few levels of brachiation of the pulmonary arteries would make MRI techniques valuable for the detection of pulmonary emboli as well.

In abnormalities, blood is often identified by flow void, especially with longer TE values. Longer TE images can suffer significantly from motion artifacts (1)Flow void identification of blood may be ambiguous since the airways and lungs also appear dark. By applying rephasing spin-echo sequences both of the above problems can be unambiguously resolved. Blood is purposely rephased in one sequence while it is dephased in a second. Subtraction then yields a map of blood filled regions. This technique can be applied with low TE values and image quality is excellent.

This rephased technique is then extended to refocus moving blood in both the read gradient direction and the slice select direction. With a spin-echo TE=38 ms sequence, images with 0.5-1.0 mm resolution of pulmonary vessel brachiation have been imaged. Regions of confluence appear as bright circles. The associated phase images give a clear identification of blood flow. This MR angiography technique is an excellent way to visualize and quantify pulmonary blood flow.

1. E.M. Haacke and G.W. Lenz
Improving resolution and signal-to-noise in the presence of motion using rephasing gradients. Submitted to Radiology, August, 1986.

Tam-B2

MAGNETIC RESONANCE AND THALLIUM 201 MYOCARDIAL IMAGING IN PATIENTS WITH MYOCARDIAL INFARCTION AND ISCHEMIA: A SEGMENT TO SEGMENT COMPARISON

Masood Ahmad, M.D., Raleigh F. Johnson, Jr., Ph.D., H. Daniel Fawcett, M.D., Dennis J. Dornfest, R.T., and Melvyn H. Schreiber, M.D.

University of Texas Medical Branch, Galveston, Tx.

Magnetic resonance imaging characterizes acute myocardial infarction as an area of increased signal intensity and prolonged T_2 relaxation time. Reversibly ischemic myocardium, however, has not been identified by magnetic resonance imaging. To determine whether magnetic resonance imaging can distinguish reversible ischemia from normal and from infarcted myocardium, we performed stress thallium scintigraphy (Tl-201) and gated multislice magnetic resonance imaging in 27 patients. Nine patients were imaged within 2 weeks of acute myocardial infarction and 18 patients from 4 to 12 weeks of acute myocardial infarction. Multiple Tl-201 views and multiple magnetic resonance imaging slices along the left ventricular short axis allowed precise comparison of a total of 108 segments. Based on thallium 201 images, EKG and cardiac enzyme data, 65 segments were classified as normal, 14 as acute myocardial infarction, 9 as old myocardial infarction and 20 as reversible ischemia. Mean T_2 relaxation times in myocardial segments in the magnetic resonance images are tabulated.

Segments	Total No.	T_2 (msec)±SD	%increase in T_2 from normal	p(compared to normal)
Normal	65	37 ± 9		
Acute myocardial infarction	14	60 ± 15	62	<0.001
Old myocardial infarction	9	52 ± 13	41	<0.001
Reversible ischemia	20	51 ± 10	38	<0.001

Signal intensity ratios (abnormal/normal) increased from echo 1 to echo 2 in acute myocardial infarction and in reversible ischemia ($p<0.005$) but were not significantly different in old myocardial infarction. These data confirm the previously reported prolongation of T_2 in acute myocardial infarction. Prolonged T_2 in our patients with old myocardial infarction may be related to the age of myocardial infarction (all <12 wks). Reversibly ischemic myocardium in patients with previous myocardial infarction was characterized by prolongation of T_2 and increased signal intensity ratio from echo 1 to echo 2.

We conclude that prolongation of T_2 relaxation time and increase in signal intensity are not specific for the presence of acute myocardial infarction and may be seen in reversibly ischemic regions. The possibility that these changes may be secondary to islands of myocardial necrosis interpersed with the reversibly ischemic tissue cannot be excluded. The separation of reversibly ischemic tissue with areas of incipient myocardial necrosis from completely reversible ischemia is of prognostic importance. Our data suggest that magnetic resonance imaging may be able to further characterize and possibly stratify the reversibly ischemic regions of myocardium.

PANEL 1

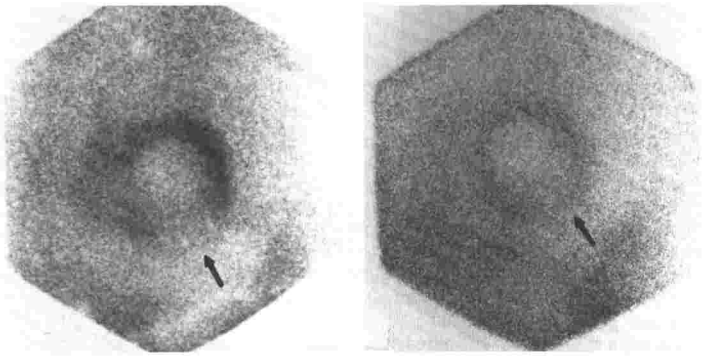

Panel 1 shows stress (A) and redistribution (B) Thallium—201 LAO images.

PANEL 2

Panel 2 shows 32 msec echo (A) and 64 msec echo (B) short axis MR images. Arrows point to the posteroinferior region of reversible perfusion deficit in the Thallium—201 images and to the corresponding area of abnormal signal intensity in the MR images.

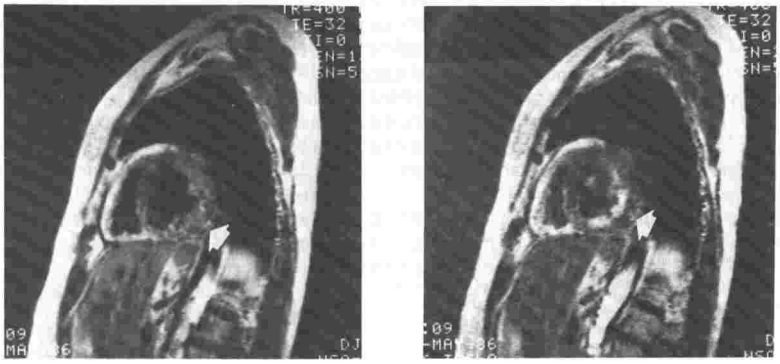

Tam-B3

ROLE OF M.R.I. AND 2D ECHO IN EVALUATING INTRACARDIAC MASSES.

S. Biasi, F. Casolo, M. Borroni, L. Balzarini, E. Ceglia, R. Petrillo, P. Piotti, J.D. Tesoro Tess, R. Musumeci

Section of Magnetic Resonance
Istituto Nazionale Tumori - Milano.

Nine patients with intracardiac masses were studied by two dimensional echo (2D Echo) and gated magnetic resonance (MRI) in order to compare their accuracy for the non invasive imaging. Two patients had atrial mixoma, two intraventricular and one intraatrial metastases, one had an intraatrial septic thrombus, one a parietal left ventricular thrombus in post infarctional area and, finally, two pediatric patients affected by tuberous sclerosis had cardiac rhabdomyomas. In four patients diagnosis was confirmed by surgery and with autopsy in one.

The initial 6 patients have been imaged by a 0.5 T superconductive magnet whereas a 1.5 T magnet was used for the following 3; SE pulse sequences were obtained with echo delay times at either 36 ms or 36 and 68 ms. The TR was set according to each patient's heart rate. All the patients were imaged using paraxial planes.

MRI depicted shape and surface characteristics of the masses more clearly than 2D Echo because of better spatial and contrast resolution: 2D Echo was however superior in showing masses mobility within the cardiac chambers and eventual intrusion into valvular orifices. Both methods could accurately show the sites of attachment.

MRI and 2D Echo are complementary in the evaluation of intracardiac masses: 2D Echo can be considered a first-choise examination because has a shorter acquisition time, is less technologically sophisticated and is significantly less expensive; increased information on the tissutal characterization and anatomical configuration can be obtained by MRI.

MRI provides further insights on tissue characteristics and constantly allows better global view of the heart.

Tam-B4

LEFT VENTRICULAR WALL MOTION ASSESSMENT WITH MR

Madeleine R. Fisher, M.D.

Fred Steinberg, M.D., James Talano, M.D., David Mehlman, M.D.
Daniel Fintel, M.D., Kerry Kaplan, M.D., Richard Davison, M.D.

The purpose of this study was to evaluate a new MR gating technique to evaluate regional wall motion abnormalities. A prospective evaluation of 10 patients approximately 10 days status post myocardial infarction were studied with MR and echocardiography for evaluation of segmental wall motion abnormalities. MR imaging was performed with a 1.5T superconducting MR system operating at 0.5T. Images of the heart were acquired with a fast field echo technique allowing acquisition of 16 images of the heart at one anatomic level. The data was then formatted into a movie mode and analysis of regional wall motion abnormalities for the septum, anterior, and lateral walls were recorded. A similar criteria used for interpretation of regional ventricular performance from contrast ventriculography was employed. Comparison of these results to those of echocardiography in each patient was done. Results showed this MR gating technique was capable of demonstrating wall motion abnormalities in the post MI patient. Echocardiography and MR provided similar information for wall motion abnormalities. The findings of echocardiography were known at the time of the MR exam therefore, the specificity and sensitivity of MR can not be evaluated from this study.

Tam-B5

GAMUT: HYPERINTENSE INTRATHORACIC LESIONS ON T1-WEIGHTED MRI STUDIES

Anthony R. Lupetin, M.D.; Nilima Dash, M.D.; Rolf L. Schapiro, M.D.;

Allegheny General Hospital, Pittsburgh, Pennsylvania

PURPOSE: To discuss the differential diagnosis of thoracic abnormalities demonstrating a signal intensity greater than striated muscle on T1-weighted studies.

METHODS: A retrospective review of thoracic MRI studies performed at the Allegheny General Hospital since December, 1983, generated a series of intrathoracic abnormalities demonstrating a signal intensity greater than striated muscle on T1-weighted studies (TR = 0.5, TE = 17 or 35 msec). A gamut was then compiled.

RESULTS: The high signal intensity of the lesions in this gamut related to four main types of internal composition: those containing blood, fat, complex fluids, and a miscellaneous group of tumors.

Lesions in our series demonstrating a high signal intensity due to their blood content included hemothorax, hemomediastinum, postoperative hematoma, and intravascular thrombus. Lesions in which the high signal intensity related to fat content included superficial and deep lipoma and diaphragmatic hernia containing omental fat. Lesions containing complex fluids included esophageal duplication cyst, bronchogenic cyst, pericardial cyst, Zenker's diverticulum, and achalasia of the esophagus. A miscellaneous group of intrathoracic neoplasms demonstrated a signal intensity greater than striated muscle including a large neurofibroma, a primary leiomyosarcoma of the superior vena cava, and an intracardiac hemangioma.

A general discussion of this gamut and reasons for high signal intensity related to internal content will be attempted.

CONCLUSION: We have generated an MRI gamut that we hope will be useful in the differential diagnosis of intrathoracic lesions with a high signal intensity on T1-weighted exams.

Tam-B6

PERCUTANEOUS SUBCLAVIAN CENTRAL VENOUS CATHETERIZATION:
DETERMINATION OF OPTIMAL PATIENT POSITIONING BY MR IMAGING.

Jerry M. Jesseph, M.D., Ph.D., Dewey J. Conces, Jr., M.D., Gary T. Augustyn, M.D.

Indiana University School of Medicine, Indianapolis, Indiana.

By virtue of its excellent ability to demonstrate vascular anatomy, Magnetic Resonance (MR) imaging has the potential of assisting in the planning of interventional procedures. As an example, we demonstrate the use of MR imaging in the planning and optimization of percutaneous subclavian central venous catheter placement.

The subclavian vein is a commonly used central venous access route. Complications of percutaneous catheterization may occur during venipuncture or subsequent positioning of the catheter witin the great veins. In order to minimize the occurance of these complications and maximize chances for successful catheterization, we studied the effects of different patient positions using multiplanar MR imaging. The MR imaging findings were verified by comparison to gross dissection of cadaver specimens in the pathology lab.

We found that variations in patient position play a critical role in the configuration of the venous anatomy. Our findings show that traditional recommendations for patient positioning, shoulder retracted posteriorly and head turned to the contralateral side, act to distort the venous anatomy and make successful catheterization more difficult. We found that retraction of the shoulder decreases the anteroposterior diameter of the subclavian vein by compressing it between the clavicle and the first rib, and thereby lessens the likelihood of successful venipuncture. The MR images also demonstrated that turning the head to the contralateral side increases the angle formed by the jugular and subclavian veins, and thereby increasing the probability of malpositioning the catheter within the internal jugular vein. Furthermore, we found that the Trendelenburg position did not substantionally change the subclavian vein diameter.

As an alternative to these traditional recommendations for patient positioning during percutaneous subclavian vein catheterization, our study suggests that the patient be placed flat with the head and shoulders in a neutral position. This will result in the greatest subclavian vein diameter and a favorable jugular/subclavian angle; thereby maximizing chances for successful venipuncture and subsequent catheter advancement into the brachiocephalic vein, respectively.

Tam-B7
MAGNETIC RESONANCE IMAGING OF THE RENAL VEINS

Anthony R. Lupetin, M.D.; Nilima Dash, M.D.; Jeffrey K. Cohen, M.D., Douglas M. Landwehr, M.D., Ph.D.;

Allegheny General Hospital, Pittsburgh, Pennsylvania

PURPOSE: Demonstrate the usefulness of MRI in the evaluation of the renal veins.

METHODS: A retrospective review of the abdominal MRI studies performed at the Allegheny General Hospital since December, 1983, generated a series of twenty patients with renal vein abnormalities. Etiologies included: acute and chronic bland thrombus formation with or without associated IVC thrombus or venous collateral formation; tumor thrombus related to hypernephroma or malignant retroperitoneal adenopathy with or without associated IVC thrombus; compression by retroperitoneal primary and secondary neoplasm with or without occlusion; congenital anomalies (retroaortic renal vein; in conjunction with IVC anomalies); enlargement due to renal AVM.

The usefulness of MRI was estimated in staging the renal vein in patients with hypernephroma or adrenal carcinoma and screening patients with chronic nephritis for renal vein thrombosis. We then estimated the frequency with which the left and right renal veins appear on MRI studies in the various scanning planes.

RESULTS: MRI will uniformly demonstrate the renal veins because of flow void phenomenon in normal patients. Axial sections are most useful, and the left renal vein is easier to visualize and evaluate.

MRI is a useful modality for demonstrating renal vein tumor thrombus in association with primary neoplasms. It will demonstrate the primary tumor, the renal vein thrombus, and associated inferior vena caval extension.

MRI can be utilized to screen patients with chronic nephritis for development of renal vein thrombus. In addition, T1-weighted MRI studies will demonstrate a lack of corticomedullary differentiation indicating the presence of chronic renal disease.

MRI is very helpful in checking renal vein status in the presence of retroperitoneal lymphoma or other primary or secondary neoplasms.

CONCLUSION: MRI uniformly demonstrates the normal renal veins and can be utilized to screen the renal vein for thrombus formation, extrinsic compression or occlusion, and for congenital anomalies.

Tam-B8
A COMPARATIVE STUDY OF THE ACCURACY OF MAGNETIC RESONANCE IMAGING AND VENOGRAPHY IN THE EVALUATION OF INTRAVASCULAR TUMOR IN RENAL CELL CARCINOMA

J.T.Simmons*, P.J. Choyke**, D.L. Miller*, J.A. Frank*

Diagnostic Radiology Department, Clinical Center,* National Institutes of Health, Bethesda, MD and Georgetown University Hospital**, Washington, DC.

Twenty-two patients with metastatic renal cell carcinoma (RCC) and primary tumor in place underwent evaluation at the National Cancer Institute Surgical Branch in preparation for nephrectomy and resection of locally invasive disease followed by adoptive immunotherapy. Both Magnetic Resonance Imaging (MRI) at 0.5 Tesla and venography (VEN) was utilized to detect intravascular thrombus within the inferior vena cava (IVC) and renal vein. Subsequent operative and pathologic findings were compared. Coronal and axial MRI T1-weighted (T1W) spin-echo images displayed IVC involvement with tumor thrombus in all four cases. IVC thrombus was present in four patients at the time of operation. MRI and VEN equally predicted the presence of thrombus in all four cases. Seven/22 patients were found to have renal vein thrombus operatively and/or pathologically. In four patients, the distal renal vein was not adequately seen at venography to exclude thrombus, with thrombus detected in six of the remaining patients. There was one false positive and one false negative venogram. MRI accurately detected thrombus in all seven cases, with one false positive.

These results indicate that MRI is an accurate non-invasive imaging technique for the evaluation of IVC and RV tumor thrombus in patients with RCC. The avoidance of intravenous contrast, minimum surgical clip artifact and coronal imaging capability provide advantages to VEN that may make MRI a preferred modality for preoperative staging.

(Tam-C) NEURO-TECHNIQUES

Presiding: K. Davis & H. Stein

10:20 am

ROOM C-101

12 MINUTES PER PRESENTATION

Tam-C1

HIGH-CONTRAST CSF IMAGING WITH MR:- AN UNEXPLOITED DIAGNOSTIC OPPORTUNITY

B Condon, J Patterson, D Wyper, R Grant, A Jenkins, D Hadley, G Teasdale, J Rowan

MRI Unit, Institute of Neurological Sciences, Southern General Hospital, Glasgow, Scotland

Introduction

There is considerable confusion in the medical literature regarding the true relaxation times of CSF. In 15 recent publications the variation in quoted T_1 between publications was by a factor of 5 (range 1000 to 5500 ms) whilst T_2 varied by a factor of 16 (range 166 to 2640 ms). Such gross differences cannot be simply ascribed to variations in operating frequency. That the T_1 and T_2 of CSF are longer than other tissues in the brain is widely appreciated; that the difference in relaxation times is so marked that a significant diagnostic opportunity is available is not appreciated.

In this paper three independent sets of evidence are provided that indicate that the T_1 of CSF is > 3000 ms and that the T_2 of CSF is ~ 2000 ms. It will be shown how pulse sequences can be constructed which produce signal ratios between a unit volume of CSF and a unit volume brain of better than 200 to 1. This approach is applied to obtain high contrast images of CSF in the brain from which can be calculated not only the volume of CSF in the lateral ventricles but also, for the first time with any diagnostic modality, the extra-ventricular and total intracranial CSF volumes.

This technique can also be applied to produce non-invasive high contrast images of CSF in the spine but also any other organ or tissue where unbound water predominates; for example the eye, bladder and seminal vesicles.

Measurement of T_1 and T_2

Two direct and one indirect sets of measurements are used to determine the relaxation times of CSF:-

(i) **Spectrometer estimates:-** A Bruker PC6 non-imaging spectrometer operating at 6.0 MHz was used to obtain accurate relaxation times for 10 samples of biochemically normal CSF at body temperature. T_1 was calculated from an IR sequence with incremental T_I and 16 averages. T_2 was calculated from a 10-echo CPMG sequence with 36 averages. All measurements were performed with the repetition time > 20 seconds. T_1 of CSF was found to be 3302 $\pm$ 170 ms, T_2 was 2269 $\pm$ 128 ms.

(ii) **Imager estimates:-** A pooled CSF sample was imaged using a Picker 0.15 Tesla (6.3 MHz) resistive system. T_1 was estimated by determining the null-point using an IRSE sequence with incremental T_I. T_2 was calculated from a 7-echo CP sequence. The repetition time used was the maximum available namely 9999 ms. The T_1 of CSF was found to be between 3140 and 3434 ms, the T_2 was found to be > 1500 ms (pulse imperfections on the CP sequence will make this an underestimate).

(iii) **Comparison with the relaxation properties of water:-** In the above two experiments the relaxation times of distilled water were measured in the same way as for the samples of CSF. No significant difference was found in any of the measurements between CSF and singly distilled water. The previously published estimates of the relaxation times of water are variable due to the differences in the operating temperature and the grades of distilled water measured but all when corrected for operating temperature would indicate a T_1 > 3000 ms and a T_2 ~ 2000 ms.

CSF Imaging

In comparison with CSF the T_1 and T_2 values of grey matter (513, 118 ms) and white matter (242, 86) are greatly different at 0.15T. Sequences may be constructed to effectively destroy signal from grey and white matter whilst still retaining high signal from the CSF. Such a sequence is an IRCP300/400/5000 (an inversion recovery sequence with a Carr-Purcell data collect with an overall T_E of 400 ms and a T_R of 5000 ms) (1). By ensuring the inversion time of the IR is adjusted to fall between the null-points of white and grey matter cancellation of these signals will always occur to some extent when these tissues exist within the same volume element. This is particularly important as thick slices are used in the quantification of ventricular volume (~ 8 cm) and total intracranial CSF volume (~ 20 cm). Figures 1 and 2 demonstrate the images for a 20 cm thick sagittal slice through a normal volunteer and a patient with normal pressure hydrocephalus (NPH). Each image was acquired in 5.3 minutes. This technique may be of considerable potential utility in the diagnosis and serial assessment of treatment in conditions such as benign intracranial hypertension, cerebral atrophy, NPH and the blockage of ventriculo-peritoneal shunts. The differential volumes of CSF in the

ventricular and extra-ventricular CSF spaces may provide a simple non-invasive means of differentiating between NPH and true cerebral atrophy (2).

In both figures it is evident that high signal is also obtained from fluid in the eye. Indeed such sequences can be used to image concentrations of unbound water throughout the body. High contrast images have been obtained of CSF in the lumbar spine and fluid in the bladder and seminal vesicles.

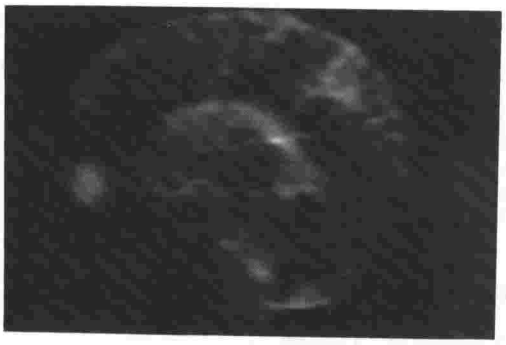

Figure 1 20 cm thick slice through a normal volunteer.

Figure 2 20 cm thick slice through a patient with normal pressure hydrocephalus.

References
(1) B Condon et al. J Comp Assist Tomog 1986; 10:784-792.
(2) B Condon et al. Lancet 1986; 8494:1355-1357.

Tam-C2

INVERSION RECOVERY MRI FOR THE DIAGNOSIS OF HEAD AND NECK MALIGNANCY

F.W.Smith, A.R.Law, K.McLay, C.W.Rayner, E.R.Robertson, J.Weir

Departments of Radiology, Surgery and Medical Physics, Aberdeen Royal Infirmary, Scotland.

109 consecutive cases of suspected head and neck malignancy have been entered into a comparative study of M.R.I. and X-ray CT. All patients were studied by both X-ray CT and low field (0.08T) M.R.I. within 24 hours of each other and histological confirmation of the diagnosis obtained.

There were 78 male and 31 female patients included in the study whose mean age was 66 years, range 16-84 years. Within this group three main subgroups were identified: 32 cases had disease of the salivary gland, 16 tumours of the larynx and 10 malignant lesions of the tongue. Of the remaining cases, 6 were normal, 15 had benign conditions, 17 other malignant tumours and 7 were examined after treatment.

In all groups there was general agreement between M.R.I. and X-ray CT as to the site of primary tumours. In all groups M.R.I. tended to stage tumours more accurately than CT, presumably due to the improved contrast resolution between tumour and surrounding soft tissues obtained using short TI inversion recovery sequences. A similar degree of difficulty was found in separating benign from malignant tumours of the salivary glands. In the staging of laryngeal tumours M.R.I. tended to be more accurate than CT. In the definition of the extent and boundaries of tumours in all regions M.R.I. defined the boundaries as well defined in 14 of 32 cases of malignant tumour, whereas CT said only 3 of 29.

It is concluded that inversion recovery M.R.I. is a sensitive method for the localisation of tumours and other diseases of the head and neck region, but that more experience is required to improve its specificity above that of X-ray CT.

Tam-C3

COMPARISON OF LOW FIELD (0.08T) INVERSION RECOVERY M.R.I. AND X-RAY CT FOR THE DIAGNOSIS OF INTRA-CRANIAL DISEASE

F.W. Smith, R. Donald, A.R. Law, A.F. MacDonald

Departments of Radiology and Medical Physics, University of Aberdeen, Scotland

In an effort to assess the diagnostic accuracy of low field (0.08T) Inversion recovery M.R.I. for the diagnosis of Intra-cranial disease, 230 patients who had been examined by X-ray CT were also examined by M.R.I. and detailed follow up obtained. 176 of these patients had both examinations, 54 were lost to the trial

because they were either "too ill" for M.R.I., refused examination, were sent for surgery after X-ray CT, or were discharged home because the X-ray CT was normal.

The patients' ages ranged from 1-84 years, mean age 53 years. There were 81 males and 95 females. 31 of the cases were normal, 57 had tumours, 45 cerebrovascular disease, 43 other conditions.

Each examination was divided into three areas: posterior fossa, pituitary fossa and supratentorial. A questionnaire was completed by one of the Radiologists at the time of reporting the X-ray CT or M.R.I. A total of 528 areas of investigation was therefore possible and 477 were completed by both CT and M.R.I; 159 posterior fossa, 154 pituitary fossa, 164 supratentorial. CT and M.R.I. agreed in 434 cases; 310 were normal and in 124 abnormalities were found. In 43 cases (9%) there was disagreement; in 27 M.R.I. found an abnormality and CT did not, and in 16 cases CT was abnormal and M.R.I. normal.

Of the 27 cases where M.R.I. demonstrated a lesion, 14 were in the posterior fossa, 2 in the pituitary fossa and 11 above the tentorium. In the 16 cases where CT was positive and M.R.I. normal, 4 were in the posterior fossa, 1 the pituitary fossa and 11 above the tentorium.

Broad agreement between the two imaging methods was found in the detection of lesions above the tentorium although M.R.I. tended to oversize both tumours and recent infarcts due to its sensitivity in demonstrating oedema. In the posterior and pituitary fossa M.R.I. was more sensitive in demonstrating disease than X-ray CT.

Tam-C4

VISUALIZATION OF INTRACEREBRAL HEMATOMAS WITH WITH T1, T2, T1ρ AND T1ρ DISPERSION IMAGING AT 0.02

Sepponen RE[1], Tanttu JI[1], Suoranta H[2], Suramo I[2]

1) NMR Laboratory, PLK RTG, 2) Dept. of Radiology, Helsinki University Central Hospital, Haartmaninkatu 4, 00290 HELSINKI, Finland

PURPOSE OF THE STUDY: The visualization of intracerebral hematomas (ICH) with MRI is dependent on the strength of the polarizing magnetic field and the age of the hematoma [1,2,3,4,5,6,7,8]. At 0.02 T the acute hematoma is visualized as an area with shorter T1 than that of white matter which enables the differential diagnosis of the lesion based on the relaxation time T1. At field strengths 0.12 T and above the acute hematoma has equal or longer T1 than that of white matter.

In addition to the standard T1 and T2 information it is possible at low field strengths to obtain relaxation information in the rotating frame characterized by the relaxation time T1ρ[9]. T1ρ is obtained by the utilization of the spin locking technique and is effectively T1 at very low field strengths. T1 is dependent on the strength of the locking field (T1ρ dispersion) just as T1 is dependent on the strength of the polarizing magnetic field. The T1ρ and T1ρ dispersion imaging provides information about macromolecular processes at very low frequencies and therefore provides additional information for tissue characterization[10,11].

In this study we have imaged patients with ICH at various times after the onset of the symptoms in order to find the characteristics of visualization of ICH at 0.02 T. The results of the study provide hints for the processes behind the dynamics of ICH.

METHODS: The T1 weighted images were obtained with the IR 1000(247)/40 sequence and 1000(47)/40. The T2 weighted images were obtained with SE 2000/150 sequence. The spin locking sequences SL 1500(100,1.3)/40 and SL 1500(100,13)/40 were used for collecting T1ρ weighted and T1ρ dispersion images. Designation of the spin locking sequence SL TR (TL, F1L)/TE, where TR is the repetition time (ms), TL is the length of the locking pulse (ms), F1L describes the Larmor frequency in kHz corresponding to the strength of the locking pulse and TE is the time to echo (ms). A commercial MRI unit operating at 0.02 T (Acutscan^{R}, Instrumentarium Corp., Helsinki, Finland) was used. The unit was modified for T1ρ imaging by the installation of a 300 W excitation RF amplifier and a necessary change in the software.

RESULTS: In the acute phase (within days after the onset of symptoms) the center of the ICH has shorter T1, shorter or equal T2 and T1ρ than white matter and it demonstrates negligible T1ρ dispersion in the locking field range 0.03 - 0.3 mT (corresponding frequency range 1.3 - 13 kHz). The area surrounding the center of an ICH has long T1, T2 and T1ρ compared to white matter and it has negligible T1ρ dispersion. The relaxation times of the ICH increase by the age of the lesion and the T1ρ dispersion remains small. The T1ρ dispersion of white matter is considerable. Subcutaneous fat and CSF have small T1ρ dispersion.

DISCUSSION: The relatively short T1 and T2 may be due to the coagulation of blood which increases the viscosity in the clot and reduces the mobility of water molecules in the center of the lesion. The clot has a large concentration of medium size proteins which reduces T1 at low frequencies. The high protein content and reduction of mobility (reduction of the motional narrowing effect) reduces T2. However, the center of the lesion possesses no T1ρ dispersion in the frequency range 1.3 - 13

kHz. This indicates that there are no significant relaxation mechanisms which are effective only at this low frequency range which may be an indication of the lack of large macromolecules normally found in tissues like white matter. The surrounding area with long relaxation times and small dispersion is probably serum around the clot.

REFERENCES:
1) Sipponen JT et al., J. Comput. Assist. Tomogr., 7:954 - 9, 1983
2) DeLaPaz RL et al., J. Comput. Assist. Tomogr., 8:599 - 607, 1984
3) Zimmerman IA et al., Neuroradiology, 27:16 - 20, 1985
4) Swensen SJ et al., AJR 145:921 - 7, 1985
5) Bradley WG et al., Radiology 156:99 - 103, 1985
6) Sipponen JT et al., J. Comput. Assist. Tomogr., 9:698 - 704, 1985
7) Gomori JM et al., Radiology 157:87 - 93, 1985
8) Di Chiro G et al., AJNR 7:193 - 9, 1986
9) Sepponen et al., J. Comput. Assist. Tomogr., 9:1007 - 11, 1985
10) Sepponen RE et al., SMRM, Proc. 5th Ann. Mtg., 639 - 40, 1986
11) Tanttu JI et al., SMRM, Proc. 5th Ann. Mtg. 1137 - 8, 1986

Tam-C5

UTILITY OF LOW FLIP ANGLE, GRADIENT RECALLED ECHO FAST SCANNING IN CLINICAL MRI IN NEURORADIOLOGIC IMAGING

Emanuel Kanal, M.D., James A. Brunberg, M.D., Richard J. Prorok, R.T.

The Pittsburgh NMR Institute, 3260 Fifth Avenue, Pittsburgh, Pa. 15213

While there are numerous accepted methodologies for performing spin echo MR examinations, many start with a relatively short TR, short TE series of images for anatomic delineation. These are often followed by a relatively long TR, long or multiple TE study to attempt to obtain a metrizamide, or myelogram-like effect, yielding images where the cerebrospinal fluid (CSF) and most lesions demonstrate relatively greater signal intensities than the adjacent neural and bony structures. One disadvantage of the latter imaging strategy is the relatively long image acquisition times, generally of ten or more minutes. CSF and vascular flow as well as respiratory and gross patient motion can all increase background noise by inducing phase shift in the signal originating from the flowing/moving protons. This can result in a decrease in signal- (SNR) and contrast-to-noise (CNR) and an overall decrease in image quality.

Fast scan techniques have the advantage of markedly reduced scan acquisition times. The potential for less flow and especially respiratory and patient motion with scans that may typically last only several seconds helps prevent such image SNR degradation. Furthermore, the $T2^*$ and proton spin density dependence of the resultant image signal and contrast enables a myelogram-like picture to be obtained with excellent contrast between CSF and the adjacent neural tissues.

Figure 1 demonstrates marked phase shift artifact on a routine spin echo study acquired with a long TR (3500 ms), long TE (120 ms) study in 15 minutes and 7 seconds. Figure 2 demonstrates the result obtained on the same patient with a fast scan technique utilizing a flip angle of 4 degrees, a TR of 100 ms, and a TE (time to gradient-recalled echo) of 12 ms acquired in a scan time of 27 seconds per selected slice when utilizing a non-interleaved mode of data acquisition. Voxel dimensions are 1.9 x 0.94 x 5.0 mm in each image; each study was acquired with 2 excitations. While the amount of phase shift artifact in Figure 1 is far worse than is generally seen with such scan parameter settings, the case demonstrates the utility of the fast scan gradient recalled technique in general and in the setting of clinical patient throughput in particular.

We conclude that such fast scan techniques may be of considerable clinical utility in patients in whom flow/motion is a limiting factor in image interpretation. Furthermore, interleaved mode multislice acquisition fast scan is presently available. With further increases in SNR accomplished through multiple excitations or other techniques, scanning strategies utilizing such fast scan sequences may well rival the more traditional long TR studies in CNR and diagnostic potential while enabling a marked reduction of scan time and concomitant increase in patient throughput.

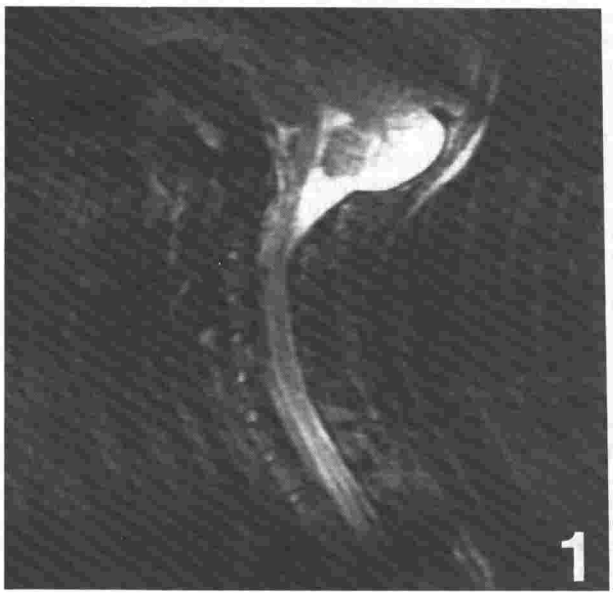

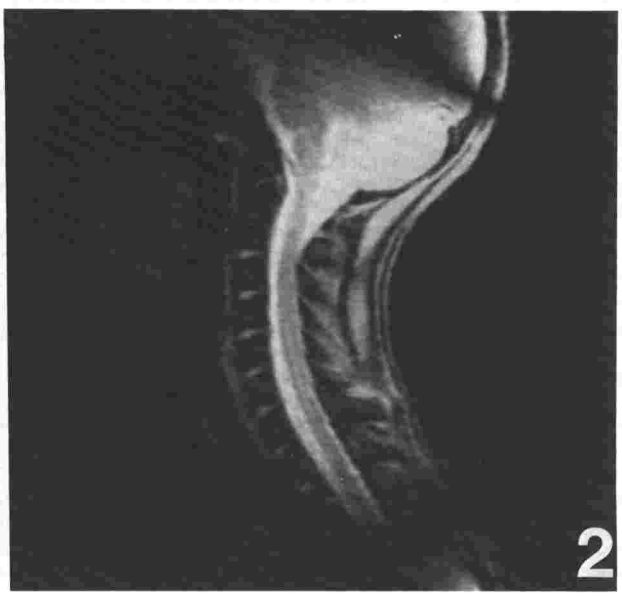

Tam-C6

THE APPLICATION OF PARAXIAL SCANNING TO MRI OF THE CNS

Val M. Runge, M.D., Mark A. Osborne, M.D., Samuel M. Wolpert, M.D., Eddie Kwan, M.D., Dean M. Kaufman, M.S., Michael L. Wood, Ph.D.

Division of Magnetic Resonance, Department of Radiology, New England Medical Center Hospital, Boston.

Straight axial and tilted axial (parallel to the orbito-meatal line) MR examinations of the head were compared in 34 patients for diagnostic efficacy.

A standard anatomical line, between the nasion and the most caudate portion of the cerebellum (NC line), was defined for use with MR sagittal examinations. The reference points for this line are readily recognizable on MRI even with relatively poor resolution fast scout sagittals. The angle between the NC line and straight axial (as defined with reference to the magnet axis) was measured in 156 consecutive MR examinations. In 34 of these patients, mild T1 weighted examinations (TR/TE= .8/25, 1.0 zoom, 256x256 matrix, 1 acquisition, multislice technique with 11 slices) were obtained both in the straight axial plane and tilted - parallel to the NC line. Two of these cases further included the use of Gd DTPA (0.1 mmol/kg IV, Berlex Laboratories). All images were acquired using a Siemens Magnetom operating at 1.0T. Thirty-two of the 34 examinations were read by four radiologists independently. Two cases were excluded for technical reasons. The scans (tilted axial vs. straight axial) were assessed for relative merit in identification of normal anatomical structures. In 11 instances, the x-ray CT was also available for comparison. In 20 of the mild T1 MR examinations (tilt and straight axial), pathological lesions were present. The readers were also asked in these cases to grade the two scans in terms of visibility of the lesion, anatomical localization, and margin definition.

From results with five normal patients using sagittal multislice images, it was determined that the NC line is approximately parallel to the orbito-meatal line. Marked variability from patient to patient in the angle between straight axial and the NC line was noted due to differences in patient positioning (head tilt). In the 156 patient cases which were assessed, the mean angle was -24 degrees with a standard deviation of 8 and extremes of +5 to -39. In a subsequent series of 25 patients, the technologists were instructed to attempt uniform positioning of the patients' heads. In this series, the mean angle was -25 degrees with a SEM of 4 and extremes of -15 and -34.

Overall, the tilted axial (or paraxial) scans were superior for visualization of normal cerebellar structures and the optic chiasm. The straight axial examinations were felt to improve depiction of the brain stem, cerebral aqueduct, and orbit. Examination of low frontal and cerebellar lesions was improved by utilization of the tilted MR sequence. This conclusion however is based on a small number of cases, 3 for the cerebellum and 5 for the frontal region. Image quality was equivalent for both the straight axial and tilted axial sequences, as assessed both visually and by signal-to-noise measurements. In comparison of the MR to the CT examinations, the tilted axial MR scans were heavily favored (98%) for correlation.

Positioning of the head for MR examinations should be standardized to eliminate potential variability in anatomical plane. This can be accomplished (as illustrated) by specific instructions to the technologist. If this is not done, head tilt may vary dramatically from scan to scan and play a detrimental role with regards to clinical interpretation. Tilted axial scans (parallel to the orbito-meatal line) may be superior for examination of low frontal and cerebellar lesions and are without question preferred for comparison with x-ray CT. The availability of correlative CTs and the anatomical region of interest should dictate the choice between straight axial or tilted axial sequences.

(Tam-D) RELAXOMETRY

Presiding: G. Fullerton & R. Dietrich

10:20 am

ROOM C-102

12 MINUTES PER PRESENTATION

Tam-D1
NMR RELAXATION IN HYDROGELS: A MODEL FOR TISSUES

M.S. Brown and J.C. Gore, Dept. Diagnostic Radiology, Yale University, New Haven, CT 06510

The NMR relaxation properties of a class of cross-linked hydrophilic polymeric gels (1) have been investigated and found to closely simulate the behavior of tissues. In particular the gels show strikingly similar T_1 dispersion profiles tissues, and may be manipulated at constant water content to replicate a range of frequency dependences (NMRD). They thus serve not only as a versatile material for test objects but also as a model system for investigating water relaxation properties in a disordered arrangement of hydrophilic interfaces where cross-relaxation may be expected to be important. The gels have been extensively investigated by other means[2] and consist of polytetramethylene oxide diol macromer (PTME, MW=2000) cross-linked by co-polymers of dimethylacrylamide (DMA), methylmethacrylate (MMA) and 2-hydroxyethylmethacrylate (HEMA). The gels are solid, thermally stable and may be mechanically machined. They swell in H_2O (or D_2O as appropriate) and trap in their interstitial spaces an amount of water which is controllable by varying the amount of DMA, which is hydrophilic. At constant DMA composition, the proportions of MMA (which is hydrophobic) to PTME can be altered and this induces dramatic alterations in relaxation rates and NMRD profiles at relatively constant water content. Figure 1 shows the NMRD results for a typical hydrogel superimposed on the curves for different rabbit tissues[3], while Figure 2 shows the behavior for different MMA concentrations. When MMA content is low the macromer chains are linked by many short chains of DMA, but as MMA content increases the cross-linking chains are longer and form copolymers of both hydrophilic and hydrophobic regions. We have investigated the relaxation behavior of these gels in both H_2O and D_2O, when cross-relaxation effects are negligible, and have demonstrated the dependence of T_1 and T_2 on water content. There exists a linear weak dependence of relaxation rate on water content that also mimics the behavior of tissue, but the dispersion profiles and deuteration studies emphasize that the water content alterations are merely correlates and not causes of the relaxation changes. The implications of these measurements for relaxation in tissue are under investigation.

(1) Ciba-Geigy Corporation, Ardsley, New York
2. Lee H, Ph.D. Thesis, University of Utah, 1974
3. Koenig SH, Brown R.D. III, Adams D, Emerson D and Harrison CG: Invest. Radiol. 19:76 (1984).

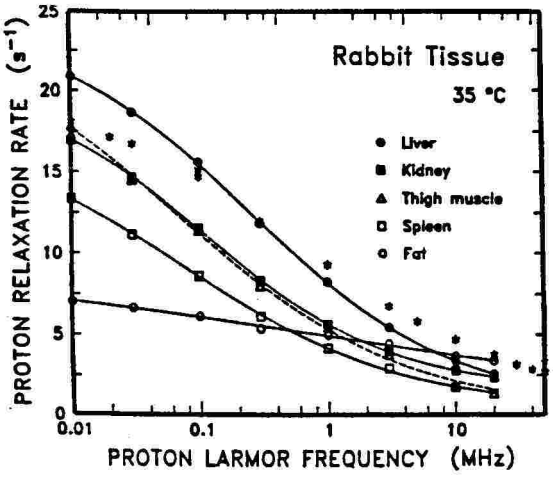

Fig. 1 Plot of N.M.R.D. for a hydrogel of composition 30% DMA, 40% MMA, and 30% PTME (shown as unconnected stars *). For comparison, the dispersion curves for various rabbit tissues are also shown.

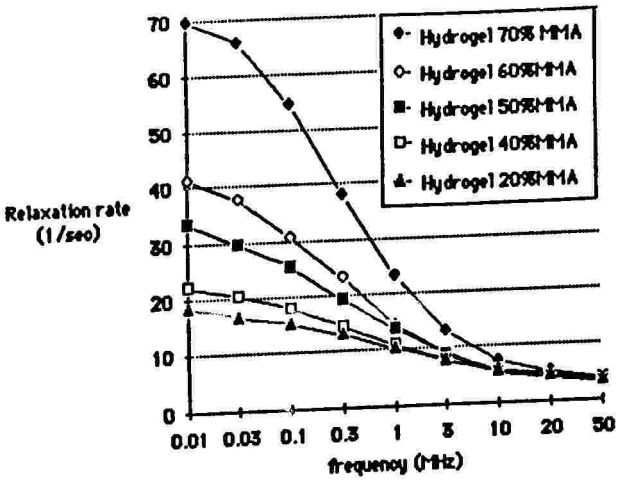

Fig. 2 N.M.R.D. curves for hydrogels in which the DMA content is held constant at 30% and the MMA content is varied from 20% to 70%, and PTME varying from 50% to 0%.

Tam-D2

REHYDRATION PROFILES OF LYOPHILIZED URINE SAMPLES FROM NORMALS AND FROM PATIENTS WITH DIFFERENT RENAL PATHOLOGIES

R. AZOURY*, S. ABRASHKIN*, A. IAINA**, AND J. WEININGER*
*SOREQ N.R.C. YAVNE, **BARZILAI HOSPITAL, ASHKELON, ISRAEL

Proton MR measurements were performed in small lyopilized urine samples collected from normals and from patients with different renal pathologies. T1 and T2 were measured with a Bruker PC Multispec at 20 MHz and 37 C in the lyophilized samples and in samples gradually rehydrated. Prolonged T1 and T2 relaxation times were measured after addition of water; the initial values of the two groups didn't differ among themselves but their prolongations were significantly different in the two groups.

The preliminary results we obtained when the relaxation times were represented graphically as a function of the water content of the samples or of the added water amount are significantly different. The rehydration curve of the pathological samples is sigmoid with a relatively short lag, much shorter than that of the rehydrated normal samples.

The calculations of total water (PW) and of its compartmentalization, may indicate that similar PW changes determine significantly different hydration fraction (HF) and fraction bound (FB) changes in the two groups. These results may reflect their differences in the hydration layer thickness and also in their macro-molecular contents and properties.

The important hydrogen MR differences which wre found between normal and pathological urine samples must be correlated with parameters characteristical to the different pathologies in study.

The changes in MR properties as reflected in the rehydration profiles, i.e. rehydration curves as a function of relaxation times, may provide new diagnostic possibilities of different renal pathologies.

Tam-D3

A THEORETICAL DESCRIPTION OF DIFFUSION IN RANDOM SUSCEPTIBILITY DISTRIBUTIONS

S. Majumdar and J.C. Gore
Yale University School of Medicine, New Haven, CT 06510

The effects of diffusion and other motions of the spins in a linear gradient are well known and lead to a reduction in the apparent transverse relaxation time T_2. The effects of diffusion in such a gradient may be compensated by using multiple echoes in the manner described by Carr and Purcell. However, there has appeared no adequate description of the behavior of the net magnetization from nuclei diffusing in more complex static field arrangements. At a microscopic level, tissue samples are magnetically inhomogeneous and possess regions of different susceptibility which give rise to magnetic field gradients that are in general arranged in a disordered fashion. Diffusion of nuclei within such field distributions gives rise to an attenuation of echo amplitude that depends on the statistical properties of the distribution of field gradients. There is then an additional apparent contribution to the rate of decay of transverse magnetization that depends linearly on the variance of the gradient probability function. This effect is particularly important when the susceptibility variations are large, such as occur in the lung with air interfaces or in other tissues when particles of high susceptibility are present, such as occurs in the use of superparamagnetic (magnetite) contrast agents as well as in some naturally occurring disease states that produce iron deposition. We have derived theoretical expressions for the dependence of the apparent relaxation time on the parameters that describe the field distribution and are able to relate measurements of T_2 to the number density and spacing of point susceptibility variations caused by various materials. Analytical results have been verified by computer simulations of diffusing spins in various arrangements of point susceptibility variations, achieved by simultaneously solving the Bloch equations with the equation of motion of the spins and the magnetostatic field distribution. Experimental verification of the model has been achieved using CPMG measurements of T_2 in arrangements of glass beads in water, and is being investigated by imaging experiments of iron particle distributions. The significance of these results for a better quantitative understanding of diffusion effect in random media will be discussed, and their relevance to the design of contrast agents that use this effect will be described.

Tam-D4

VARIATION IN TISSUE T1 RELAXATION TIME WITH MEASUREMENT TEMPERATURE AND FREQUENCY. AN IN VITRO STUDY OF RAT TISSUES.

M. A. Foster, J. E. Rimmington and J.R. Mallard

Department of Bio-Medical Physics and Bio-Engineering, University of Aberdeen, Foresterhill, Aberdeen, U.K.

Spin-lattice relaxation time of tissues and doped gels is known to vary with both temperature and measurement frequency. In addition to yielding fundamental information about the state of contributing protons, these dependencies are important in assessing contrast in NMR images. This study has been undertaken to compare frequency dependence between different body tissues and with certain model systems such as doped gels. It has also provided information on the inter-dependence of T1 on temperature and frequency, this also varying between tissues.

A variety of tissues were obtained from rats which had been sacrificed by cervical dislocation. These were placed in pieces into NMR tubes and examined within a few hours of the death of the animals. The T1 relaxation times were measured using an inversion recovery sequence and calculated using a weighted least squares fit method which assumed single exponential relaxation characteristics. (More detailed examination suggested that this was the case in the tissues used here). The measurements were made in a Bruker CXP100 spectrometer over a temperature range of 4° to 40°C and a frequency range of 4 to 90MHz. Standard samples of CuSO4 in solution were run along with the tissues to assess instrument accuracy and precision.

Figure 1 demonstrates variation in T1 value with temperature of samples of thigh muscle, white brain tissue, spleen and liver. Figure 2 demonstrates variation in R1 (1/T1) with frequency in spleen, thigh muscle and white brain, and compares this with the standard solution and with agar gel with and without manganese doping.

Variation in temperature dependence is clearly seen between, for example, spleen with only a small change over the temperature range and muscle which shows the largest temperature sensitivity of the tissues examined. Muscle also shows a very strong frequency sensitivity as compared to other tissues and to agar gels. It is also notable that the frequency dependence of undoped gel is less than for doped gel or paramagnetic metal ion solutions. This is possibly related to the contributions from bound and free water molecules to the overall relaxation rate.

Figure 1

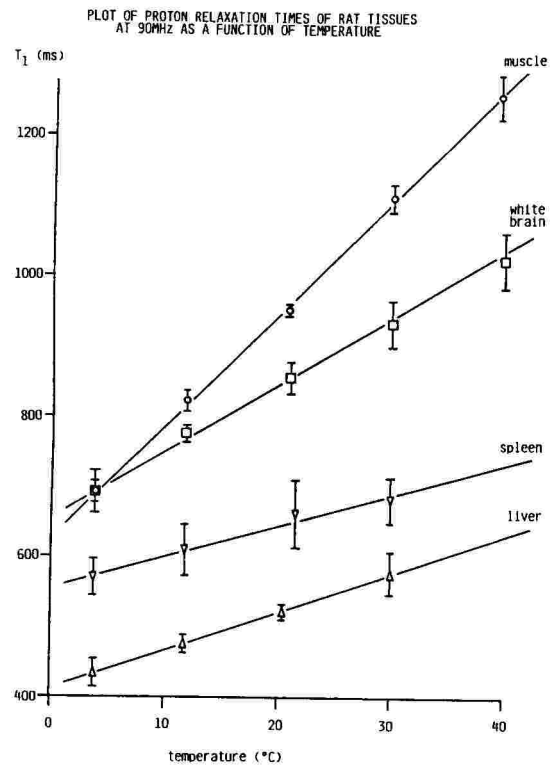

Figure 2

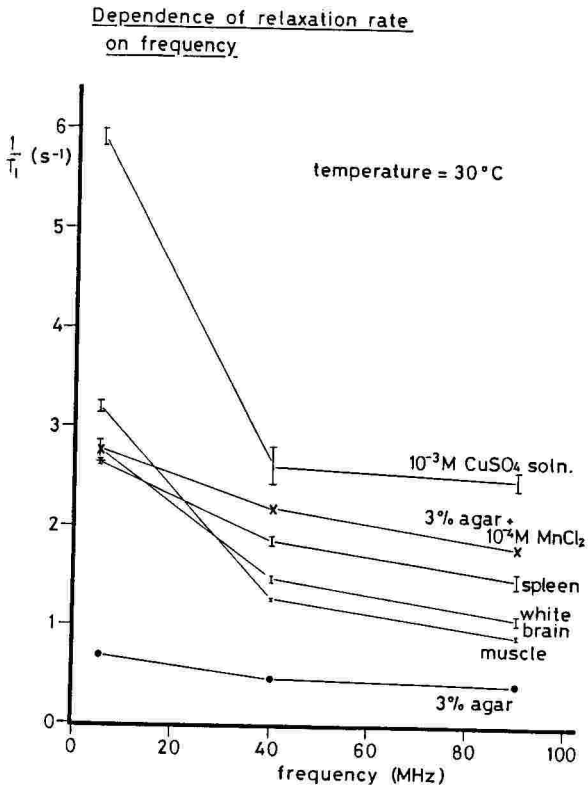

Tam-D5

THE EFFECTS OF TEMPERATURE UPON PROTON RELAXATION RATES IN BIOLOGICAL TISSUES

Gerald L. Wolf, Peter C. Sullenberger, Kathryn J. Bickerstaff

Pittsburgh NMR Institute, Pittsburgh, PA 15213

Among the many variables known to influence proton T1 relaxation in biological tissues are temperature and field. To study the reversibility of temperature changes between 5-37°C, we obtained fresh skeletal muscle, liver, fat, kidney cortex, and kidney medulla from euthanized rabbits. Each tissue was subject to Nuclear Magnetic Relaxation Dispersion measurement of spin-lattice relaxation from 0.1-50 MHz. The tissues were alternately studied at 37°, then 5°, then back to 37° for complete temperature cycles over six hours. As expected, each tissue had its own NMRD curve and relaxation rates were significantly faster at any field at the lower temperature. However, upon return to a previous temperature, there was no difference in the NMRD profile for any tissue. These results suggest that for reasonable periods of time and over the temperature range studied, the effects of temperature change upon the T1 of biological tissue are completely reversible.

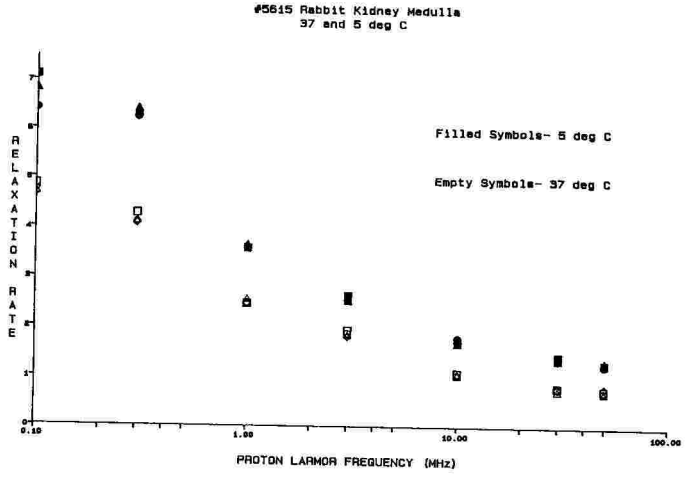

Tam-D6

FREQUENCY DEPENDENCE OF PROTON RELAXATION TIMES T1 AND T2 IN PARAMAGNETIC SOLUTIONS, NiC12 AND MnC12

William S. Yamanashi, David W. Anderson, Stanley Fricke, Robert Stewart*, George Thyvellikakath, B.M. Fung+, Daryl Doughty++, and Patrick D. Lester

City of Faith Medical and Research Center, Tulsa, Oklahoma; *Amoco Production Research Center, Tulsa, Oklahoma; +University of Oklahoma, Norman, Oklahoma; ++National Institute for Petroleum and Energy Research, Bartlesville, Oklahoma.

Aqueous solutions of MnC12 and NiC12 of several concentrations were analyzed for relaxation times over the range of operating proton resonance frequency of clinical MRI. Data were evaluated for the use of these paramagnetic solutions for (i) quality control and for (ii) contrast media. NMR spectrometers at several sites which operate at frequencies of 10.7 MHz, 20 MHz, 60 MHz, 80 MHz, and 270 MHz at temperatures near 25° C were used to obtain relaxation times. Plots of 1/T1 and 1/T2 vs concentration were made at each frequency and were found to increase linearly according to the empirical expressions,

$$R1 = 1/T1 = k1\ c + 0.31 \text{ and } R2 = 1/T2 = k2\ c + 0.59,$$

where c is the concentration in (millimole), k1 and k2 are in $(\text{second-millimole})^{-1}$, and T1 and T2 are in (seconds). Plots of k1 and k2 for both NiC12 and MnC12 solutions were obtained (5-170 MHz) using the data from this study and data reported previously by other authors (Ref). Plots of k1 for NiC12 and MnC12 are shown on the next page.

For NiC12 solutions T1 and T2 were nearly equal and little change was observed in values of either in the frequency range from 10 to 70 MHz. Thus NiC12 solutions may be most useful in phantom studies comparing different MRI units which operate at different magnetic field strengths. For MnC12 solutions the T1/T2 ratio is more similar to human tissues and changes appreciably over the frequency range. Thus phantoms using MnC12 solutions may be more appropriate for evaluating imager performance at a particular clinical site.

REFERENCES: Morgan L.O. and Nolle, A.W.; Proton Spin Relaxation in Aqueous Solutions of Paramagnetic ions II Cr+++, Mn++, Cu++, and Gd+++, J. Chem. Phys. 31-265-368, 1959.

ACKNOWLEDGEMENT: We wish to acknowledge Radiation Measurement Inc. for partial support of this research.

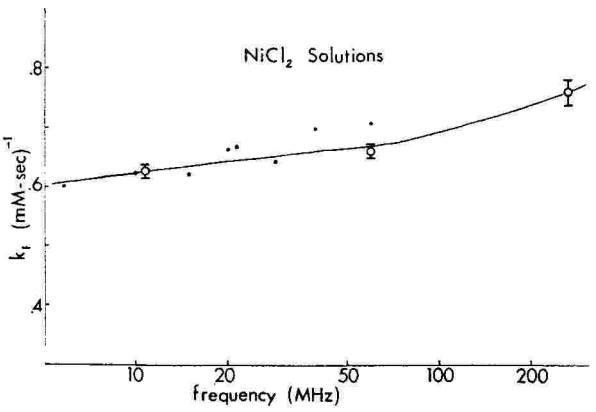

K1 vs frequency in NiC12 Solution

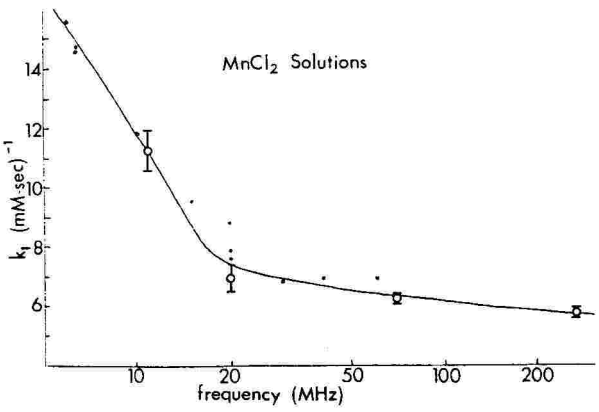

K1 vs frequency in MnC12 Solution

Tam-D7

MAGNETIC RESONANCE (MR) IMAGE RESPONSE CURVES FOR MnCl2 SOLUTIONS: TESTS FOR MRI CONTRAST, LATITUDE, AND CONTRAST INVERSION TIMES.

David W. Anderson, William S. Yamanashi, Stanley Fricke, John Ross-Duggan, and Patrick D. Lester

City of Faith Medical and Research Center, Tulsa, Oklahoma

Values of T1 and T2 obtained from NMR spectrometer for MnCl2 solutions over a wide range of frequencies were utilized to calculate theoretical MRI intensities for spin echo, I(SE), and inversion recovery with spin echo detection, I(IRSE), the expression used were:

$$I(SE) = C1\ \rho \exp(-TE/T2)\ \{1 - 2\exp[(-TR + TE/2)/T1] + \exp(TR/T1)\},$$

$$I(IRSE) = C2\ \rho \exp(-TE/T2)\ \{1 - 2\exp(-TI/T1) + 2\exp[(-TR + TE/2)/T1] - \exp(-TR/T1)\},$$

where the C1 and C2 are arbitary constants, ρ is the proton density, TE is the echo delay time, TI is the inversion time and TR is the repetition time. The theoretical intensities were calculated at TE and TR values appropriate for T1 and T2 weighted spin echo images and T1 and TR for inversion recovery images for magnetic field strengths from 0.3T to 1.5T. When intensity values are plotted vs. log T1 and log T2 the response curves obtained can be utilized to compare contrast, latitude (the range of T1 or T2 available for linear intensity response), and contrast inversion times (T1 or T2 values for which the intensity peaks) for different MR scanners. A phantom made with MnCl2 solutions with relaxation times which span the range of common tissues has been used to measure actual MRI T1 and T2 latitude and contrast inversion times. The results are compared to theoretical expectations and conclusions related to effects on actual images. Several MR response curves are shown on the next page.

ACKNOWLEDGEMENT: We wish to acknowledge Radiation Measurements, Inc. (RMI) for partial support of this research.

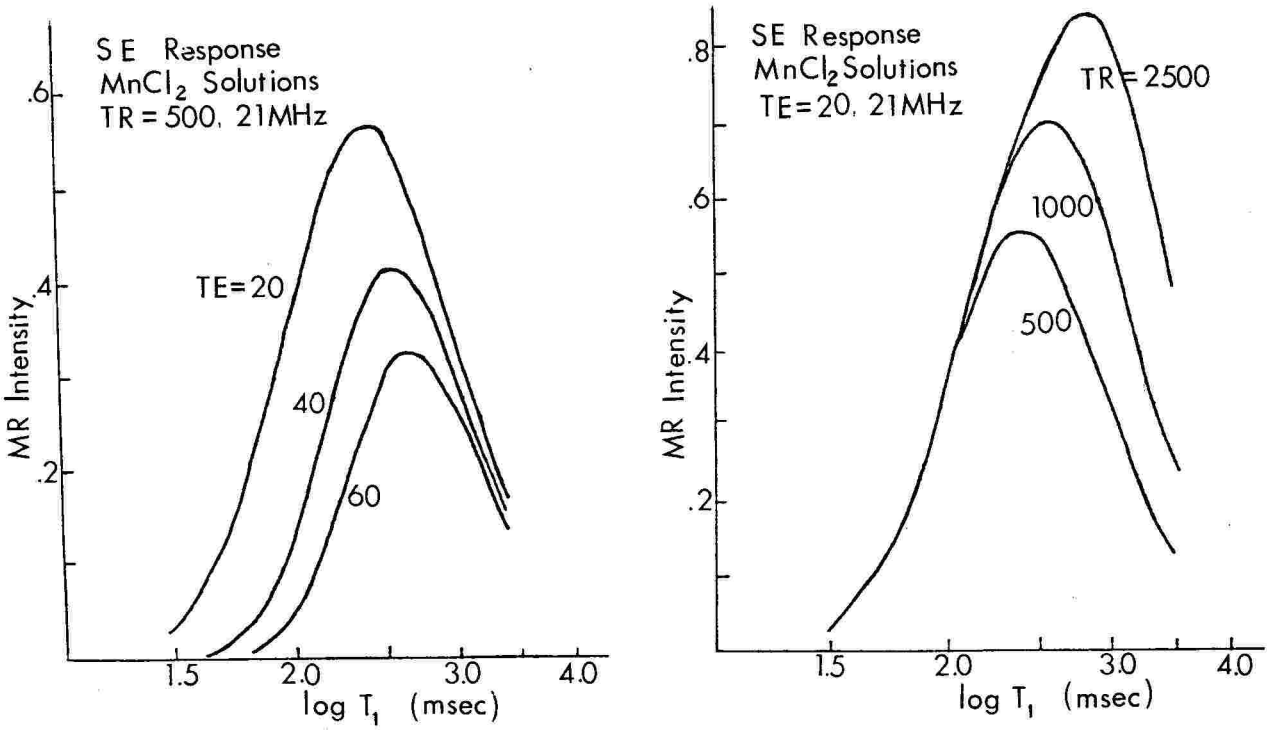

Several MnCl2 response curves for spin echo operation on a 0.5T MRI.

Tam-D8

CONSIDERATIONS IN CHOOSING PARAMAGNETIC DOPANTS FOR TISSUE EQUIVALENT PHANTOM MATERIAL

K.A. Kraft, P.P. Fatouros, G.D. Clarke, and P.R.S. Kishore

Department of Radiology, Medical College of Virginia, Richmond, Virginia 23298

The use of paramagnetic relaxation modifiers in magnetic resonance imaging phantoms is commonplace. Desirable characteristics of such phantom materials include long term stability and similarity of relaxation parameters to those of physiological fluids and tissues. One frequently overlooked phenomenon in choosing paramagnetic solutes is the temperature and magnetic field dependence of their relaxation rates. Due to normal variations in room temperature as well as instrumental RF heating effects, it is advantageous for the phantom material to exhibit a minimal temperature dependence in its relaxation properties. Similarly, it may be desirable to have a material with field independent relaxation characteristics for evaluating several imagers operating at different Larmor frequencies. That the phantom relaxation rates be independent of temperature and frequency is perhaps most important when quantitating image T_1 and T_2 times, and when correlating spectroscopic results with imaging data.

Paramagnetic ions have been used for decades to modify the proton relaxation rates of aqueous solutions. Theoretical expressions, developed principally by Solomon and Bloembergen[1,2], have been found to adequately explain experimental relaxation data for a number of paramagnetic solutions, including those of Co^{2+}, Cr^{3+}, Cu^{2+}, Fe^{3+}, Gd^{3+}, Ni^{2+}, and Mn^{2+}. These equations predict that when the dipolar correlation time (Tc) is controlled by the rotational motion of the hydrated ion, the proton T1 and T2 will be strongly influenced by temperature, since Tc has an exponential temperature dependence in that case. In addition, there is predicted a significant dependence of the proton relaxation times on the Larmor frequency over the approximate range 1 to 100 MHz.[3] Behavior consistent with this scheme is exhibited by solutions of Cr^{3+}, Cu^{2+}, Fe^{3+}, Gd^{3+}, and Mn^{2+}. However, for other paramagnets (e.g. Co^{2+} and Ni^{2+}) their fast electronic relaxation rate will dominate the dipolar correlation time, resulting in virtually no dependence of the proton relaxation parameters on temperature or magnetic field strength (below ca. 10 T).

Although aqueous paramagnetic solutions are adequate for use as T1 modulators in phantoms, they generally constitute a poor simulation of tissue because of their long T2 times. Pure gels, on the other hand, may be likewise unsuitable as tissue equivalent materials because their T2 is too short relative to T1. Paramagnetically doped agarose has been proposed as a phantom material whose T1 and T2 rates may be altered over a wide range to simulate a variety of tissues.[4] From the known temperature dependence of paramagnetic aqueous solutions, it might be predicted that paramagnetically doped gels will behave analogously. Figure 1 shows the variation of T1 and T2 with temperature in 2% agarose gels doped with either 2 mM $CuSO_4$ or 5 mM $NiCl_2$. Between 20° and 30°C, the T1 of the copper doped gel rises from 405 to 520 ms, whereas the nickel containing gel varies only from 225 to 230 ms in the same interval. The T2 behavior of the two gels, on the other hand, is nearly indistinguishable.

These and other data demonstrate that large variations in measured relaxation times due to temperature fluctuations may be expected from commonly used paramagnetic dopants such as Mn^{2+} and Cu^{2+}. Moreover, the proton T1 rates of gels prepared from these same ions are also predicted to vary over the Larmor frequency range normally employed in imaging (1 to 100 MHz). Conversely, Ni^{2+} or Co^{2+} doped gels exhibit T1 rates which are much less sensitive to variations in both temperature and magnetic field strength, and for quantitative work may be more desirable relaxation modifiers.

REFERENCES

1. I Solomon. Phys. Rev. 1955, 99:559-565.
2. N Bloembergen. J. Chem. Phys. 1957, 27:572-573.
3. SH Koenig and RD Brown. Magn. Reson. Med. 1984, 1:478-495.
4. MD Mitchell, et al. Magn. Reson. Imaging 1986, 4:263-266.

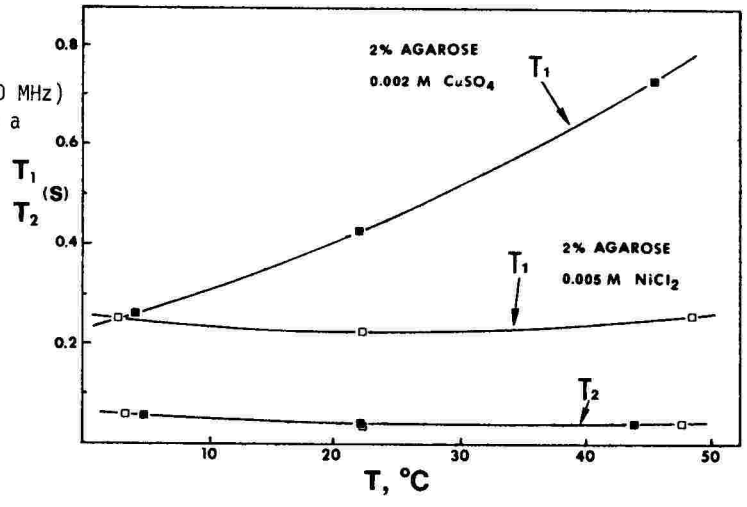

Figure 1. Proton relaxation times (100 MHz) of Cu^{2+} and Ni^{2+} doped agarose gels as a function of temperature.

(Tpm-A) CONTRAST AGENTS

Presiding: B. Englestad & H. P. Niendorf

3:20 pm

RIVER ROOM

12 MINUTES PER PRESENTATION

Tpm-A1
FLASH/FISP - APPLICATIONS WITH Gd DTPA

Val M. Runge, M.D., Michael L. Wood, Ph.D., Mark A. Osborne, M.D., John E. Kirsch, Ph.D., Dean M. Kaufman, M.S.

Division of Magnetic Resonance, Department of Radiology, New England Medical Center Hospital, Boston, and Siemens Medical Systems, Inc., New Jersey.

Two to ten second single slice acquisition times are possible utilizing FLASH or FISP techniques, resulting in relatively high signal-to-noise images with either predominately T1 or T2 weighting. Combined with the use of intravenous gadolinium DTPA (Berlex Laboratories, New Jersey), these techniques open a new door to clinical applications of MRI.

FLASH (Fast Low Angle SHot) and FISP (Fast Imaging with Steady Precession) use gradients instead of RF pulses to refocus the magnetization. FISP achieves a state of dynamic equilibrium with respect to magnetization. On the other hand, the objective of FLASH is to destroy the coherence between individual components contributing to the magnetization. FLASH has been advocated as a technique to achieve rapid and high signal-to-noise (S/N) images with T1 contrast, although it is possible to achieve T2 weighting by using very low tip angles (near 10 degrees). With FISP, tissue contrast depends primarily upon the ratio of T1 to T2.

In vitro studies were performed to evaluate the potential for detecting Gd DTPA with FLASH and FISP pulse techniques. With FLASH, tip angle was varied from 10 to 60 degrees, TE from 10 to 18 msec, and TR from 20 to 80 msec. With FISP, TE and TR were held constant (TR/TE= 30/12) and tip angle was increased from 20 to 160 degrees at 20 degree increments. Slice thickness was variable from 3 to 15 mm. and images in all three orthogonal planes were possible. Twelve patients were examined (9 head, 3 body) combining the use of Gd DTPA with FLASH acquisition technique. The abdominal scans were performed with breath holding. In six of these patients, the time course of lesion (intracranial mass) enhancement in the first two minutes following IV Gd DTPA was observed utilizing 10-20 second duration FLASH images. Clinical trials with FISP are in progress.

The best contrast-to-noise (C/N) and S/N were achieved for Gd DTPA in solution using FLASH with a very short TE (10 msec.). Larger tip angles (40 to 60 degrees) also provide greater sensitivity to changes in T1 and T2 produced by Gd DTPA in vitro. FISP with an 80 degree flip angle gave the best S/N while the 60 degree flip angle gave the best C/N in vitro. Enhancement was observed on FLASH images in clinical cases following Gd DTPA administration, although the magnitude of enhancement was typically less than that observed on more traditional Hahn spin-echo images (such as that with TR/TE= 800/17). The number of cases in which the immediate time course of contrast enhancement was observed was too small to make conclusions regarding diagnostic utility. Renal enhancement was observed in abdominal images obtained with FLASH technique and breath holding.

FLASH and FISP combined with the use of Gd DTPA hold promise for the assessment of tissue perfusion. If large contrast agent dosages can be utilized safely and administered as a bolus intravenous injection, differences in cerebral blood flow might potentially be assessed by MRI. Assessment of the immediate time course of enhancement following 0.1 mmol/kg Gd DTPA IV with both cerebral and renal neoplasms is currently possible and may improve diagnostic specificity. The acquisition of body images during breath holding is also possible, thereby circumventing the problems imposed by respiratory and peristaltic motion. FISP also offers the potential for "T2-like" images, but with sensitivity to Gd DTPA resembling FLASH. These two techniques may also be utilized with 3-dimensional image acquisition to produce high quality, thin sections in a reasonable scan time.

Tpm-A2

FOLLOW UP IN BRAIN TUMORS AFTER HIGH DOSE EXTERNAL STEREOTACTIC IRRADIATION: CORRELATION OF STEREOTACTIC BIOPSIES AND RADIATION FIELD WITH CONTRAST ENHANCED MRI

Semmler W, Gademann G, Niendorf HP*, Wowra B, Kimmich B, Sturm V, van Kaick G

German Cancer Research Institute, D-6900 Heidelberg 1, Im Neuenheimer Feld 280, W-Germany
*Schering AG Berlin/Bergkamen, Dept. of Radiology, W-Germany

PURPOSE

The purpose of this study is to correlate stereotactic biopsies and contrast enhancement in MRI of brain tumors before irradiation. The effect of irradiation in tumor tissue and in normal brain tissue is monitored then with Gd-DTPA enhanced MRI.

INTRODUCTION

It is accepted by convention to interpret contrast enhancing areas in brain tumors as vital tumor tissue. The possibility to do biopsies, MR- and CT-examinations and radiation therapy under reproducible conditions allows for the correlation of histological diagnosis and of the radiation field, respectively, with contrast enhancement behaviour in MRI before and after irradiation.

MATERIAL AND METHODS

Nine patients with histologically confirmed brain tumors (astrocytomas III, IV, n = 7; metastasis, n =2) were examined. Biopsies (n = 5) and radiation therapy (15 MeV photons, spherical field, > 30 Gy/fraction, 2 fractions/patient) were performed under stereotactic conditions based on contrast enhanced CT and MRI (0.1 mmol Gd-DTPA/kg b.w.). Biopsies were taken in 3 sites: adjacent to and within peripheral and central enhancing tumor areas. Controls of baseline scans (including dynamic MRI) were done with MRI and CT within 1 - 7 days, and 4 and 8 weeks post-treatment.

RESULTS AND DISCUSSION

In 3 of 5 cases Gd-DTPA enhanced MRI was successfully correlated with biopsies. In biopsies from outside the enhancing area no histological evidence for tumor growth was found. Biopsies from within the enhancing area showed tumor cells and necrotic and/or vascular tissue. Contrast enhancement of irradiated normal brain tissue showed no evidence for tissue damage at the times of the control examinations. The evaluation of dynamic MRI after bolus injection of 0.1 mmol Gd-DTPA/kg body weight shows that signal intensity increases are steeper and maintain higher levels after radiation treatment as compared to pre-radiation.

CONCLUSION

(i) There is evidence that it is justified to interpret enhancing areas of brain tumor as vital tumor tissue.
(ii) Normal brain tissue showed no evidence of radiation damage with the used radiation dose.
(iii) Tumor tissue showed stronger and faster increase of contrast enhancement after radiation therapy which may be interpreted as increased permeability of the blood brain barrier. Further investigations are needed to confirm these preliminary results.

Tpm-A3

CONTRAST AGENTS BASED ON OXYGEN-17

Amos L. Hopkins(1), Richard G. Barr(2) and Clyde B. Bratton(3)

Dept of Anatomy(1), Dept of Biochemistry(2), Case Western Reserve University, Cleveland, Ohio 44106. Dept of Physics(3), Cleveland State University, Cleveland, Ohio 44115.

The non-radioactive stable isotope of oxygen, O-17, can be a major determinant of the proton T_2 of solutions. At a neutral pH the proton T_2 of water and buffer solutions is significantly shorter than T_1. This difference is caused by the small amount of naturally present $H_2{}^{17}O$ in the $H_2{}^{16}O$. The change in T_2 resulting from $H_2{}^{17}O$ enrichment is indicative of the proton-^{17}O resident lifetime or exchange rate (1). We have shown that in both living muscle (2) and *in vivo* human ventricular CSF (3) , the T_2 is also less than T_1 - although not all of this difference is due to O-17. Factors affecting the application of these findings on ^{17}O enrichment, to the protons of living systems have been investigated. It is possible that the distribution, diffusion and macroscopic mobility of enriched water molecules can be followed through the effect of ^{17}O on their protons. Since changes in T_2 can alter image intensity, localized variation in $H_2{}^{17}O$ concentrations can be directly visualized, as well as monitored in samples by the usual proton T_2 procedures. Oxygen-17 water, in contrast to heavy water (D_2O), has no known toxicity. It is a natural constituent of all living systems with more than 2X the natural abundance of D_2O.

The effect of O-17 enrichment on the T_2 of biological solutions was determined using a CPMG six-echo pulse sequence. The results shown in Fig. 1 in which the difference in rate between the experimental value (with added $H_2{}^{17}O$) and the rate for the same solution with only the natural abundance is plotted against the concentration of $H_2{}^{17}O$. Enrichment produces a marked effect on the relaxation rate in the presence of proteins, but not in solutions whose pH is far from neutrality. The effect of 0.05M phosphate buffer on albumin solution T_2 is indicated by Δ.The buffer considerably diminishes the effect without changing the pH but does not eliminate it. (Except were indicated otherwise all solutions are at pH 7.3. Measurements made at room temperature. Increasing the temperature will effect T_2 but to a lesser extent than T_1).

The distribution of perfused $H_2{}^{17}O$ can be visualized in living tissue with the use of clinical imaging equipment operating with a T_2 weighted pulse sequences. Under these conditions there is both a loss of image intensity and a fall in T_2 in those areas of the tissue with the highest concentration of $H_2{}^{17}O$(4).

The injection of a 50% solution of $H_2{}^{17}O$ into the mealworm *Tenebrio molitor* produces a marked change in the width of the water proton peak but little effect on the lipid protons. When measured with a CPMG sequence the T_2 was found to be shortened by 50%. Data from these injections falls within the dashed circle in Fig.1. There was no effect on survival rate of the experimental larvae as compared to the controls.

The issue of potential toxicity is of considerable importance since ^{17}O is a weak proton-relaxing agent which therefore must be used at relatively high concentrations. The relative effect on T_2 of O-17 is shown in Fig. 2 in which it is compared to Mn data from Zimmerman (5). There is no *a priori* reason to think that even water with 100 atoms % ^{17}O is any more toxic than ordinary water. The literature does not indicate any toxic effects of $H_2{}^{17}O$.

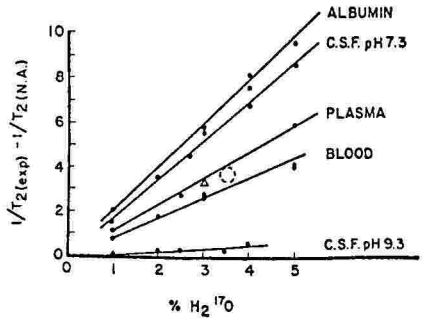

Fig. 1

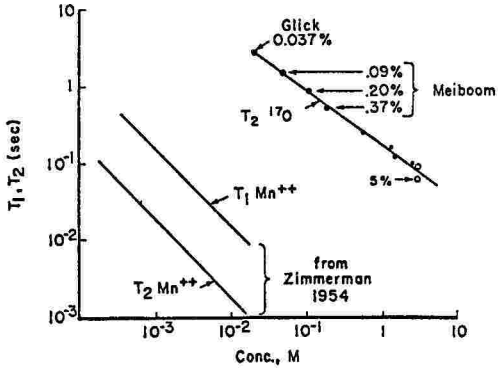

Fig. 2

As a contrast agent the greatest merit of $H_2{}^{17}O$ may possibly be in the area of measurement of capillary and membrane diffusion rates. However, in anticipation of other, more specific applications, we have incorporated ^{17}O into larger molecular species. For example, those compounds in which a high percentage of the oxygen is metabolized to water can be enriched with ^{17}O, possibly allowing visualization of the regions of highest metabolic activity. Experiments with enriched glucose, designed for application to the human cortex, are already underway.

Supported by Endowment Funds of the School of Medicine, Case Western Reserve University. We are indebted to Dr. Henry Sable of the Department of Biochemistry for many helpful ideas and discussions on glucose metabolism which preceded their presentation on June 27th, 1985 to the scientific staff of Technicare Corp.

References: [1] S. Meiboom, *J. Chem. Phys.* **34**, 375 (1961). [2] C. B.Bratton, A. L. Hopkins, J.W.Weinberg, *Science*, **147**, 738 (1965). [3] A. L. Hopkins, H. N. Yeung, C. B. Bratton, *Mag. Reson. Med.* **3**, 301 (1986). [4] A. L. Hopkins, R. G. Barr, and H. N. Yeung, Soc. of Mag. Reson. in Med., Scientific Program. 5th annual meeting, pp 1123-1124.1986. [5] J.R. Zimmerman, *J. Chem. Phys.*, **22**, 950 (1954).

Tpm-A4

FE-HBED AND FE-EHPG: IRON COMPLEXES EXHIBITING HEPATOBILIARY ENHANCEMENT IN MRI.

Homer Macapinlac, Barry Engelstad, Emiliano Ramos, David White, Thomas Johnson, M. Moseley.

University of California, San Francisco, CA.

HBED and EHPG form high-spin ferric iron complexes that are promising as contrast agents for MRI, producing prompt hepatobiliary enhancement in MRI at 0.05-0.2 mmole/kg iv on T1-weighted images. Fe-HBED and Fe-EHPG differ in stability (log K_{aff} = 40 & 34 respectively), lipophilicity (octanol/water partition coefficients 0.048 & 0.014, respectively in our lab), and albumin binding (19% & 11% respectively, in our lab). Although both complexes are efficiently cleared (<5% whole body ^{59}Fe at 1 week & hepatobiliary excretion accounting for up to 60% of dose), fecal and/or bowel ^{59}Fe levels are greater for Fe-HBED than for Fe-EHPG in comparative experiments in mice and rats. For both complexes: a) BSP suppresses common bile duct recoverable ^{59}Fe in rats, whereas oxyphenonium and taurocholate do not; b) enterohepatic recirculation accounts for <2% of duodenally administered drug over a 2 hour collection in rats; and c) excreted complexes exhibit minute differences in HPLC retention times from administered complexes, implying absence of major metabolites. Fe-EHPG, composed of two stereoisomers, exhibits similar urinary/hepatobiliary excretion of HPLC-separable isomers, suggesting that isomeric purification is unwarranted. Mice exhibit similar survival after maximal iv Fe-EHPG and Fe-HBED (5/5 surviving at 1.0 & 1.2 mmole/kg, limited by solubility).

These results indicate that either Fe-HBED or Fe-EHPG could be suitable for clinical use; Fe-HBED has a slight advantage in efficacy.

FE-HBED AND FE-EHPG: IRON COMPLEXES EXHIBITING HEPATOBILIARY ENHANCEMENT IN MRI.

Homer Macapinlac, Barry Engelstad, Emiliano Ramos, David White, Thomas Johnson, M. Moseley.

University of California, San Francisco, CA.

Figure 1. Simultaneous side-by-side MRI comparison of Fe-EHPG (Mouse 1) and Fe-HBED (Mouse 2), with each agent at 0.05 mmole/kg. Sequential spin echo coronal MR images (TR= 0.3 sec, TE= 16 msec) before (A) and at 15, 25, and 45 minute intervals (B - D respectively) after intravenous contrast agent administration. Enhancement of liver, gall bladder, small intestine and bladder was observed.

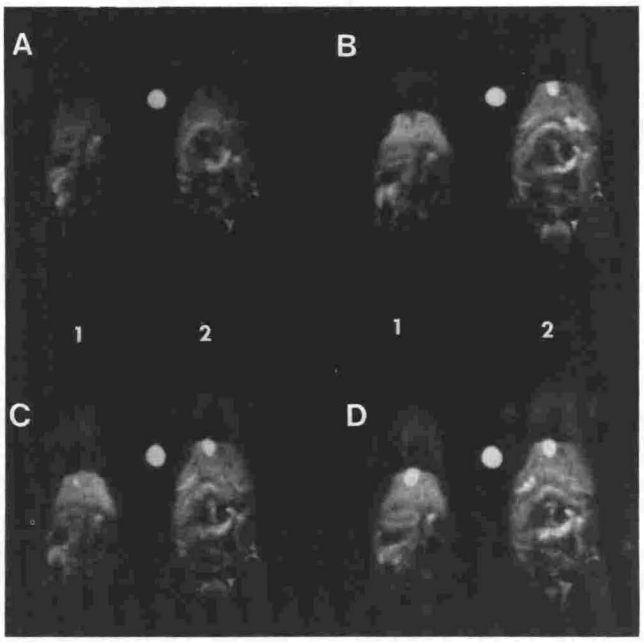

Tpm-A5

THE MECHANISM OF FERROMAGNETIC CONTRAST AGENTS IN PROTON RELAXATION

P. Hardy and R.M. Henkelman

Department of Medical Biophysics, University of Toronto, 500 Sherbourne Street, Toronto, M4X 1K9, Canada

Ferromagnetic particles are presently being tried as contrast agents for the blood and liver.[1] This type of contrast agent, called magnetopharmaceuticals, shows great promise because the large magnetic moment of the particles profoundly affects T2, permitting their use in relatively low, and therefore safe, concentrations.

However, a good understanding of their mechanism of inducing proton relaxation is lacking. We propose that the ferromagnetic particles, with a field resembling a magnetic dipole, create microscopic magnetic inhomogeneities. Their field defines a spectrum of environments distinguished by their different Larmor frequencies. The exchange of water molecules between environments increases the relaxation rate, 1/T2, because the protons accumulate irreversible phase shifts as they move through different magnetic environments during the time before a spin echo is formed.

We have measured the relaxation times of water in suspensions of 100A magnetite particles imbedded in an agar matrix. The measurements were made over the frequency range of 6 to 60 MHz and for a wide range of particle concentration. The decay of the magnetization is multiexponential, becoming more so with increasing particle concentration. The relaxation time T2 was measured using a Carr-Purcell sequence for a range of pulse spacing parameter tcp. The relaxation rate shown in Fig. 1 increases with t_{cp} in a manner consistent with an exchanging process.[2]

We have modelled this system using the Bloch equations modified to include exchange between several sites with different relaxation times and chemical shifts. Computer programs were written to predict the echoes in Carr-Purcell pulse sequences.[3] The modelled decay curves exhibited the nonexponential behaviour and the tcp dependence seen in measured data. Ferromagnetic particles are thus shown to affect the proton relaxation times in a manner distinctly different from paramagnetics.

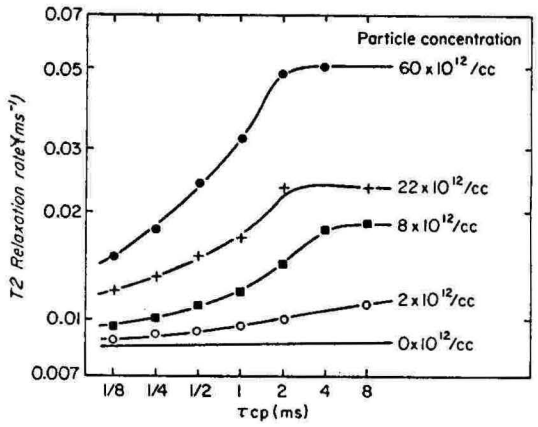

Fig. 1

References

1 Sanjay, S., Stark, D., Ferruci, J.T., Sullivan, J., Wittenberg, J., Mag. Res. Imaging, 4, 144 (1986).

2 Carver, J.P., Richards, R.E., J. Mag. Res., 6, 89-105 (1972).

3 Allerhand, A., Gutowsky, H.S., J. Chem. Phys., 42, 1587 (1965).

Tpm-A6

FERRITE: A SUPERPARAMAGNETIC CONTRAST AGENT FOR MR IMAGING

David D. Stark, M.D., Sanjay Saini, M.D., Peter F. Hahn, M.D., Ph.D., Bruce R. Bacon, M.D.*, Carolyn C. Compton. M.D., Ph.D., Joseph T. Ferrucci, M.D.

Massachusetts General Hospital, Harvard Medical School, Boston, MA, and *Case Western Reserve University, Cleveland, Ohio

Introduction: A ferrite is a metal oxide having the molecular formula of $Fe^{+3}_x M^{+2}_y O_z$. The ferrite magnetite ($Fe^{+3}_2 Fe^{+2}O_4$) forms crystals of varying size (0.01-1.0u) that have been applied to MR imaging (1-4). Particles of this size show a highly specific biodistribution following intravenous administration with uptake by normal reticuloendothelial cells in liver and spleen, where ferrite selectively enhances T2 relaxation. As particles are excluded by cancerous tissues, cancer-liver contrast is dramatically increased on MR images (1,2).

On a molar basis, iron as ferrite has a much larger magnetic susceptibility than paramagnetic agents (metal ions or nitroxides) due to magnetic ordering of the unpaired electron spins of the iron ions in the crystal (5,6). This magnetic ordering results in a net magnetic susceptibility per iron atom which is 10-1000 fold larger than the magnetic susceptibility of non-interacting paramagnetic ions. Crystals of sufficient size (> 0.035 u) behave as a unit of magnetic order or "domain" in a magnetic field and as a result are "superparamagnetic" (5,6).

Two major obstacles remain in the development of ferrite particles as a safe and effective intravenous contrast agent: 1) Little is known about the powerful and selective T2 mechanism of proton relaxation enhancement by superparamagnetic materials; and 2) the prolonged retention of magnetite observed in early studies (1-4) raises serious concerns about possible long term toxicity. A series of ferrite particles with varying magnetic, chemical, and biological properties have been studied. This report describes techniques for magnetic characterization of ferrite particles, assessment of proton relaxivity in vitro and in vivo, and the development of biodegradable particles which show less acute toxicity than Gd-DTPA and have no observable chronic toxicity in rats.

Methods: Ferrite particles varying in composition, surface coating, and size were synthesized at Advanced Magnetic Inc. Cambridge, MA. We have evaluated their magnetic susceptibility from 0-0.6T using a vibrating sample magnetometer (Princeton Applied Research, Model 155) and proton relaxivity in agar gels and rat liver tissue at 0.47 Tesla using IR and CPMG pulse sequences (IBM pc/20 spectrometer). It is known that interpulse timing delays and field strength both affect observed transverse relaxation rates; these factors were not studied and have not yet been clarified. Toxicity studies have included assessment of immunoreactivity (anaphylaxis, complement activation, and cell mediated immunity) and serologic studies (SMA-20 assays) in rats chronically

receiving high doses of ferrite particles as well as target organ studies to assess free radical formation and iron induced toxicity via conjugated dienes (7). Histologic studies using light and electron microscopic techniques were employed to assess the intracellular form of ferrite, tissue distribution, and to search for morphologic evidence of acute or chronic toxicity.

Results: At 0.4T the magnetic susceptibility of ferrite measured 105 emu/gm Fe, compared to 1.2 emu/gm Fe for $FeCl_3$. In agar gels the T2 proton relaxivity of ferrite was 116 $(mM\text{-}sec)^{-1}$ compared to 2.1 $(mM\text{-}sec)^{-1}$ for $FeCl_3$. The intravenous dose sufficient to reduce rat liver T2 to 50% of its normal value (ED_{50} = 4.0 mg Fe_3O_4/kg) was 60 fold lower ("safety factor") than the dose which killed 50% of animals acutely (LD_{50} = 250 mg Fe_3O_4/kg). This compares favorably with the safety factor of Gd-DTPA, <30, and iodinated contrast materials, <10. All other studies have shown no evidence of acute or chronic toxicity. Some ferrite formulations were biodegradable, clearing the liver within 7 days.

Conclusion: Ferrite materials show powerful and selective T2 relaxation similar to the naturally occurring iron-oxy-hydroxide crystals in ferritin and hemosiderin (8). The ferrite magnetite is found naturally in butterflies, tunafish, birds, and bacteria (6) and appears to be non-toxic when administered intravenously to rats. Our preliminary morphological, chemical, and biological data suggest that ferrite may be safe and effective for use in humans.

References:

1. Wolf GL: Magnetic Resonance Imaging Raven Press pp231, 1985.
2. Stark DD: Diag Imag 7(11):118, 1985.
3. Mendoca-Dias MH: SMRM Abstract 2:887, 1985.
4. Olsson M: SMRM Abstract 2:887, 1985.
5. Bean CP: J Applied Physics 26(11):1381, 1955.
6. Blakemore RP: Scientific American 246(6):58, 1981.
7. Bacon BR: J Clin Invest 71:429, 1983.
8. Stark DD: Radiology 154:137, 1985.

Tpm-A7

EFFECT OF HEPATIC MR CONTRAST AGENTS ON GHOST ARTIFACTS DURING ABDOMINAL MR IMAGING

Ralph Weissleder, M.D., Sanjay Saini, M.D., David D. Stark, M.D., Peter F. Hahn, M.D., Ph.D., Jean-Claude Bousquet, M.D., Ernst Rummeny, M.D., Joseph T. Ferrucci, M.D.

Department of Radiology, Massachusetts General Hospital, Harvard Medical School, Boston, MA

Introduction: Ghost artifacts arise due to physiologic motion (respiratory, cardiac, peristaltic) and are the single greatest factor determining the quality of abdominal MR images. Subcutaneous fat has been implicated as the principle offender (1). Motion artifacts hinder image interpretation and can obscure lesions with low contrast (false negative) and can also mimic focal liver abnormalities (false positive). Although other factors such as signal averaging, TR and TE influence ghost artifacts, the effect of contrast agents has not been evaluated.

Gadolinium-DTPA and ferrites are two MR contrast agents that have opposite effects on liver signal intensity (2,3). Paramagnetic Gd-DTPA increases liver signal intensity while superparamagnetic ferrites reduce liver signal intensity. This study was undertaken to study the effect of the SE contrast agents on ghost artifacts during liver imaging.

Methods: Fourteen rats were imaged before and after contrast administration using a 1.4 Tesla superconducting system with SE 250/15 pulse sequence (scan time 1 minute). Serial post contrast MR imaging was done for up to 30 minutes. We utilized a dose of .2 mmol/kg Gd-DTPA and 50 u mol/kg ferrite.

Ghost artifacts were quantitated as the pixel standard deviation over a region of interest outside the animal, anterior to the liver in the phase encoding direction. Corrections were made for thermal noise which was measured using a region of interest lateral to the liver, displaced in the frequency encoding direction.

Results: Ghost artifacts increased following Gd-DTPA administration (Figure) and correlated with increasing signal intensity of the liver. At one minute following Gd-DTPA infusion, there was a 121% increase in liver signal intensity and a 154% increase in ghost artifacts. At 10 minutes there was a 29% increase of hepatic signal intensity and a 38% increase of ghost artifact.

Ferrites reduce ghost artifacts (Figure). While liver signal intensity decreased 38%, the ghost noise was reduced by 44%. This was noted immediately after contrast infusion and remained unchanged for up to 30 minutes as ferrites remain in the liver during this time period.

Conclusions: An important characteristic of paramagnetic agents is their ability to increase signal and hopefully signal to noise which determines scan time and resolution. Our data suggests that signal from hepatic tissue makes a significant contribution to overall ghost noise. Therefore MR contrast agents that increase liver signal intensity, such as Gd-DTPA, cause an accompanying increase in ghosting artifacts. As a result, overall S/N gains are reduced. We conclude that evaluations of new MR techniques such as pulse sequences (STIR) or contrast agents (ferrite) should include an assessment of ghost artifacts as well as other types of image noise.

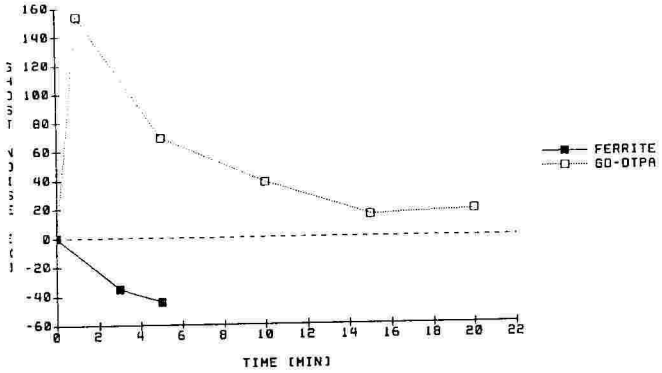

Figure: Percent change of ghost artifacts following administration of Gd-DTPA and ferrite.

References:
1. Bydder GM, Steiner RE, Blumgart LH, et al: MR imaging of the liver using short TI inversion recovery sequences. JCAT 9:1084-1089, 1985.
2. Saini S, Stark DD, Brady TJ, et al: Dynamic spin-echo MRI of liver cancer using Gd-DTPA: animal investigation. AJR 147:357-362, 1986.
3. Saini S, Stark DD, Hahn PF, et al: Ferrite particles: a superparamagnetic MR contrast agent for enhanced detection of liver cancer. Radiology (in press).

(Tpm-B) TECHNICAL DEVELOPMENTS

Presiding: R. E. Hendrick & J. Heiken

3:20 pm

ROOM C-107

12 MINUTES PER PRESENTATION

Tpm-B1

EVALUATION OF THE MULTIPLE INVERSION RECOVERY METHOD

I R Young*, G M Bydder+, A S Hall*

*GEC Research Limited, Hirst Research Centre, Wembley, Middlesex HA9 7PP, UK

+NMR Unit, Hammersmith Hospital, London W12 4RS, UK

Purpose of Study The magnetisation inverted by a 180° pulse can be interrogated several times during its recovery, using reduced precession angles so as to distribute signal between successive excitations. In principle, this approach allows the mapping of the recovery curves for tissues and permit accurate measurement of T1 from at most two scans. This paper reports on the evaluation of this technique as a means of measuring T1, comparing it with a conventional approach using saturation recovery and inversion recovery scans.

Description of the Multiple Inversion Recovery Sequence Following a period to permit substantial recovery of the magnetisation, a 180° inverting pulse is applied. Following this, during the recovery period, the magnetisation is interrogated by a set of rf pulses all except the last substantionally below 90°. The choices of precession angles in the set are dictated by the characteristics sought. For example, if one or more high quality images of a set are needed for diagnostic purposes, additional magnetisation can be concentrated in them, even if the others are sacrificed to some extent. Alternatively, the set can be adjusted to obtain constant contrast. The alternatives are illustrated in the theoretical projection in the table below, which gives the signals and contrasts (taken as signal differences) for grey and white matter (WM and GM) in the former using two sets of acquisitions each of four images, with precession angles respectively of 14.5°, 19°, 30°, and 90° for the one and 27°, 45°, 45° 90° for the other.

	Set of angles 14.5°, 19°, 30°, 90°			Set of angles 27°, 45°, 45°, 90°		
Image No	WM signal	GM signal	Contrast (W-G)	WM signal	GM signal	Contrast (W-G
I	-0.07	-0.09	0.02	-0.10	-0.14	0.04
II	0	-0.04	0.04	0	-0.04	0.04
III	0.09	0.04	0.05	0.11	0.06	0.05
IV	0.30	0.21	0.09	0.23	0.19	0.04

Table I Signals and Contrast for grey and white matter

The first set is designed to give one high quality image, even at the expense of some loss of quality in the others; while the second set is designed to give approximately the same contrast in each of the four images. (Contrast is defined as signal difference in this context, since the signals can be either positive or negative). In this analysis the interval between the 180° pulse and the first interrogating pulse is 120msec, and this interval is the same between all subsequent pulses. (This is not, clearly, necessary, but it makes analysis of the sequence much easier.)

The sequence is free of many slice shape artifacts, with the form being accurately reproduced from one slice to another of a set for tissue of any given T1. However accurate calibration shows that there are errors dependent on T1 - due to the tendency for there to be more magnetisation available in the sloping sides of the slice for excitation by later elements of the set than would be predicted by simple theory. However, since slice shape is well maintained, this can be allowed for by calibration.

The optimum method of measurement of T1 using this technique is to determine from the set of images, by plotting signal amplitudes, the times at which the signals from the various tissues are zero. This implies that images are reconstructed so as to obtain real images (1, 2) using a pilot FID scan, so that positive and negative signals can be obtained. This is preferable to estimating the time from a set of magnitude images (3). Some iteration is required to obtain the values, except if the zero crossing lies between the inversion and first acquisition, although this implies that the last interrogation is at a sufficient time after its predecessor to allow some estimate of proton density to be made (ie, recovery or short T1 tissue is largely complete in it).

Results Typical results for T1 measured from a 14.5°, 19°, 30°, and 90° set on the one hand, and on the other from the same sites on a conventional IR 1500/500/22.5 and PS 1500/22.5 pair of images are given in Table II. Each result is the average of at least four samples, and the table shows reasonable consistency although the range of tissues is small.

Tissue	Value from Multiple IR Sequence	Value from Conventional Sequences
White matter	365 (± 10)	380 (± 25)
Grey matter	545 (± 13)	520 (± 18)

Table II

Discussion

The multiple inversion recovery method is relatively simple to implement on an imager using standard multi-echo software. It is a relatively swift method of obtaining data to construct a magnetisation recovery curve, and appears to result in reasonably accurate data.

References

1 Young I R, Bailes D R, Bydder G M, Mag. Res. Med. 2, 81-85 (1985)

2 Park H W, Cho M H, Cho Z H, Mag. Res. Med. 3 (1) 15-2 (1986

3 Grossmann M, Deim Irving M, Heilmann T, Oppelt A, Proc. 5th Ann. Mtg. Soc. Mag. Res. Med. Montreal, pp 922-923 (1986)

Tpm-B2

ULTRA SHORT TE SEQUENCES

G. Neil Holland, David Lampman, Gordon DeMeester, Terrence Provost and Michael Morich

Picker International, Inc., 5500 Avion Park Drive, Highland Hts., OH 44143

Partial Saturation (PS) is now widely used for acquiring T1 weighted images. It has been shown however that contrast-to-noise in PS spin-echo sequences is critically dependent on the choice of TE, and that as short a TE as possible should be used in order to optimize tissue contrast [1]. This finding has been reinforced by the clinical work of Stark in studies of the liver, where tumor detectability was enhanced by using short TE [2].

Manufacturers shortest TE sequences are generally in the range 20-35 ms; shorter TE's being difficult to implement because of hardware (generally gradient, or RF power) limitations. A systems approach has allowed us to design multiple slice, spin-echo sequences with a TE as short as 10 ms without using additional hardware.

The approach we have taken involves the following measures:

- switching the gradient amplifiers, normally connected in parallel, into series mode to give a higher voltage output in order to reduce gradient risetime;
- the use of RF pulse profiles which minimize bandwidth per unit time of RF excitation;
- the use of asymmetric sampling and conjugate symmetrization [3,4] to minimize sampling prior to the echo maximum, and therefore to allow as much time as possible for gradient switching on all three axes before sampling begins. Asymmetric sampling also reduces the need to increase sampling rate, and therefore prevents having to widen the receiver bandwidth which would degrade signal-to-noise; and
- the use of split phase encoding and rephasing either side of the 180° RF pulse to allow smaller field-of-view (FOV) without increasing gradient amplitude.

The architecture of a typical TE10 sequence is shown in Figure 1. This particular version has a total time duration of 16.5 ms, including sampling, operates with FOV as small as 30 cm, and allows up to 12 sections in a TR of 250 ms to be collected.

Results of clinical images obtained with a TE10 sequence are shown. In conclusion, this paper demonstrates that with careful design, true spin echo sequences with TE as short as 10 ms can be produced on a standard clinical imaging system.

References: [1] J.C. Gore, C.F. Pope and H.D. Sostman, Mag. Res. Imaging 4, 251 (1986).
[2] D.D. Stark, et al.,Radiology 159, 365 (1986).
[3] T.J. Provost and G.C. Hurst, S.M.R.M. Book of Abstracts, p. 265 (1986).
[4] G.D. DeMeester and J.L. Patrick, S.M.R.M. Book of Abstracts, p. 267 (1986).

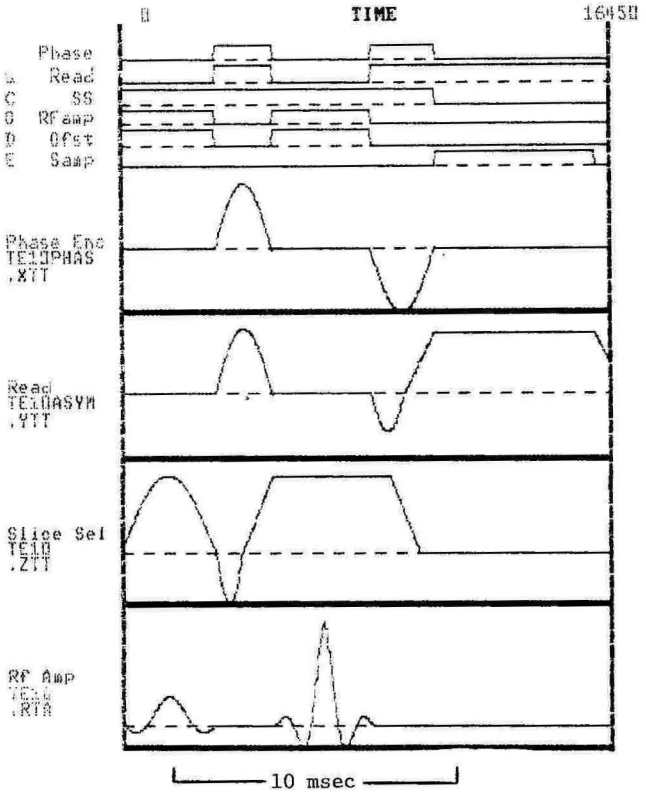

Figure 1. Gradient and RF waveforms for a TE10 sequence. This figure was taken by using the plot utility on the system pulse programmer, and shows the actual waveforms used. The diagram illustrates the use of split phase encoding and asymmetric sampling.

Tpm-B3

IN VIVO RELAXATION TIME MEASUREMENTS FROM A SINGLE DYNAMIC EQUILIBRATION ACQUISITION SEQUENCE USING LIMITED ANGLE RF EXCITATION SEQUENCES

W.H. Hinson, M.S.; W.T. Sobol, Ph.D.; P.R. Moran, Ph.D.; D.A. Saloner, Ph.D.

Bowman Gray School of Medicine, Wake Forest University, Winston-Salem, NC 27103

MR techniques using small-tip angle RF pulses and gradient reversal echos have primarily been used for rapid partial saturation imaging in the steady state. These sequences, however, also offer a wealth of information on the relaxation properties of the subject during the dynamic equilibration to the

steady state which is established after the first several pulses. In an earlier paper, we proposed a "multi-excitation" pulse sequence which provides six magnetization samplings during equilibration for relaxation time extraction from a single pulse sequence. (1) The technique is an adaption of the method proposed by Look and Locker(2), and has been recently introduced to MRI by Graumann, et.al.(3) We have additionally demonstrated that the summation of these individual samplings provides the full T1 contrast discrimination with signal-to-noise higher than that obtainable from a similar sequence using 90 degree pulses. We have implemented this sequence in vivo to obtain both T1 relaxation time measurements and low noise anatomical summation images for normal and pathological tissues. The summation image of the first six echo images, shown in Figure 1, has high signal-to-noise allowing better anatomical evaluation. Figure 2 shows that the six echo samplings for a normal brain obtained at 0.5T with 128 view-encodings, 4 repetitions, a repeat time of 1000ms, and a tip angle of 30°. Our preliminary single exponential extraction of T1 for a region of white matter from this data yields a value of 240ms.

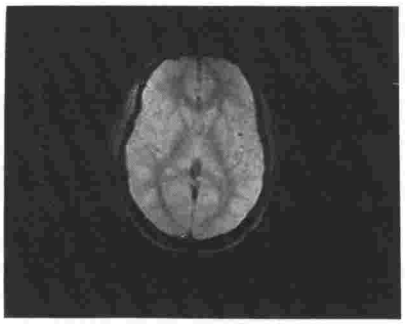

Figure 1: Summation image of first six magnetization samplings

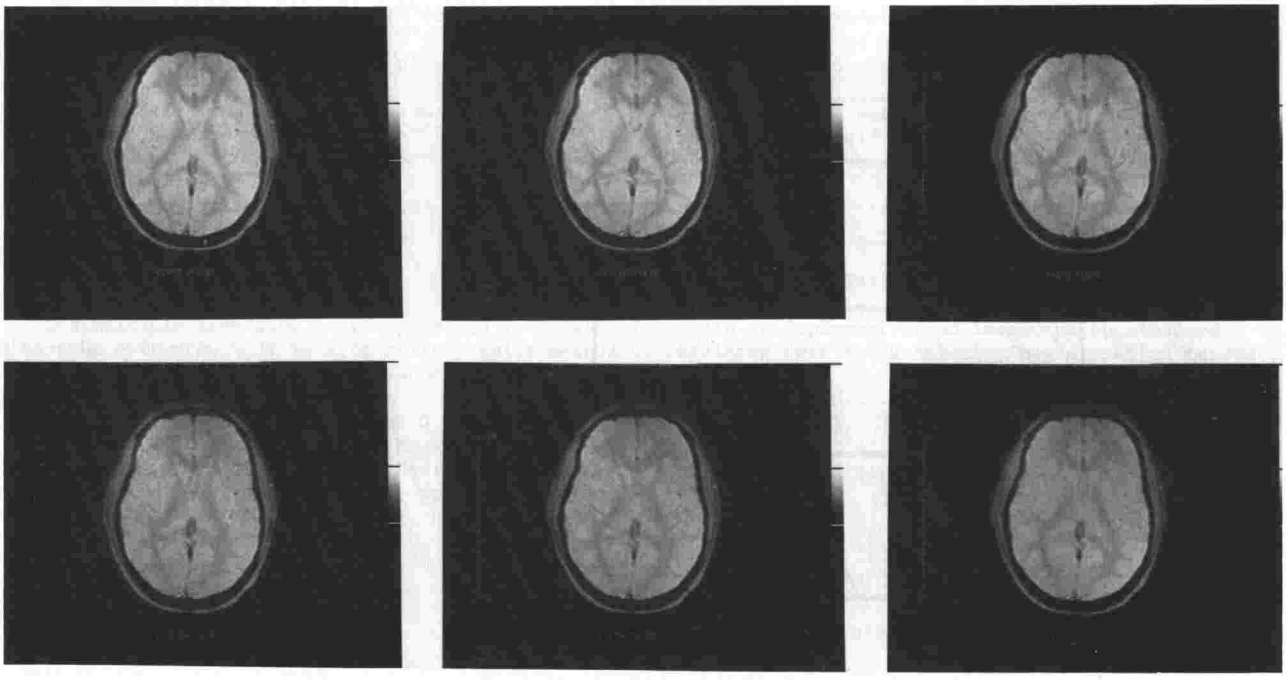

Figure 2: Individual field echo images after first six excitations

REFERENCES

1. W.H. Hinson, P.R. Moran, D.A. Saloner; **Radiology**, 1986 RSNA Abstract Edition, in press.
2. D.C. Look, D.R. Locker; **Rev. Sci. Instr.**, 41 (2), (1970), 250.
3. R. Graumann, M. Deimling, T. Heilmann, A. Oppelt; Abstracts of 5th Annual Meeting of the Society of Magnetic Resonance in Medicine, Vol. 3, (1986), 922.

Tpm-B4

THE DISTINGUISHING PROPERTIES OF GRADIENT-RECALLED ACQUISITION IN THE STEADY STATE (GRASS)

F. Wehrli, Ph.D., J. Hecker Prost, M.S., and F. Roberts

General Electric Company Medical Systems Group, Milwaukee, Wisconsin 53201

This paper discusses several salient features of gradient recalled acquisition in the steady state (GRASS). Besides small flip angles $\theta < 90°$ and gradient echoes (1), this technique is characterized by the use of phase inversion on alternate RF pulses and rephasing gradients which eliminate view-to-view phase changes of the residual transverse magnetization (2). Both have contrast implications which will be one of the subjects of this paper.

Understanding of contrast requires an appreciation of its dependence on the operator-adjustable parameters (TR, TE, flip angle θ) and the intrinsic parameters (T_1, T_2^* and proton density). Peculiar to GRASS is the establishment of a steady state in which, for moderate and large flip angles, the signal in the short-TR short-TE regime becomes a function of both T_1 and T_2^* (3). At increased TR and small flip angles, however, the density effect prevails as a contrast mechanism (4), whereas at long TR ($\geq$ 200 ms), short TE (10 - 20 ms) and large flip angles (60° - 90°), T_1 effects dominate. Finally, T_2^*-weighted images can be obtained by increasing TE ($\geq$ 30 ms) and suppressing T_1 effects by minimizing the flip angle. The quality and contrast characteristics of such images obtained with TR's as short as 200 ms is found to compare favorably with long-TR, long-TE spin echo images.

Another feature of the gradient recalled echo is its sensitivity to chemical shift effects. The presence of more than one spectral component in the imaging voxel causes an amplitude modulation of the signal with TE. This effect is most prominent in subcutaneous tissue where water and the various spectral components of triacylglycerides (methylene, methyl, unsaturated protons) add in a constructive or destructive fashion leading to a sinusoidal modulation of the pixel values with echo delay. It will be shown that by judicious choice of the echo delay fat/water contrast can be maximized.

The sensitivity of the gradient-recalled echo to magnetic field is manifested by signal losses caused by spatial variations in diamagnetic susceptibility and/or B_0 inhomogeneity. This behavior is illustrated with images comparing Carr-Purcell and gradient echo-derived anatomy in the head. The discontinuity of the magnetic susceptibility at the air/tissue boundaries induces intrinsic field gradients causing rapid dispersal of isochromats which lead to signal voids.

Finally, time-of-flight flow effects are more prominent with GRASS, in particular, for vessels transecting the imaging plane. This enhancement has three principal causes (5):

a) The images are typically acquired in a sequential fashion. Therefore, each slice behaves more like the entry slice in a slice-interleaved spin echo scan.

b) In (Carr-Purcell) spin echo imaging, signal loss usually occurs due to failure of the flowing spins to detect both 90° and 180° pulses. Such washout effects do generally not exist with GRASS since a gradient echo is generated irrespective of the location of the bolus at the time of detection (as long as it remains within the active volume of the RF coil).

c) The use of gradient moment nulling (6) causes rephasing of spins dispersed by velocity gradients across the vessel and misregistration losses due to bulk flow-induced phase shifts (7).

References:

1. Haase A, Frahm J, Matthaei D. J Magn Res 67:258-266;1986.
2. Glover G. General Electric Technical Report, 1985.
3. Perkins T, Wehrli FW. Magn Res Imaging, 1986, in press.
4. Karis JP, Framm EK, Johnson GA, Herfkens RJ. Society of Magnetic Resonance in Medicine, 5th Annual Meeting, Montreal, 1986.
5. Wehrli FW, Shimakawa A, Gullberg GT, MacFall JR. Radiol 160:781-785;1986.
6. a) Glover GH. General Electric Medical Systems Technical Report, 1985.
   b) Pattany PM, Marino R, McNally JM. Magn Res Imaging 4:154-155;1986.
7. Ehman RL, McNamara MT, Brasch RC, Felmlee JP, Gray JE, Higgins CB. Radiol 159:777-782;1986.

Tpm-B5

THE RELATION OF T1 AND T2 CONTRAST OF FLIP ANGLE AND FAST FIELD ECHO MR IMAGING.

Nelson RC, Malko JA, Long RC, Coumans J, Bernardino ME.

Department of Radiology, Emory University School of Medicine, Atlanta, Georgia 30322

The Fast Field Echo (FFE) which utilizes a gradient reversal echo, short echo (TE) and repetition times (TR), and variable excitation pulse angles (flip angles) has the potential for yielding high signal to noise images with decreased motion artifact when TR is small, and with overall decrease in acquisition time. According to the equation

$$S = K \cdot P \cdot (\sin A \, (1-e^{-TR/T1}/1\cos A e^{-TE/T1})$$

where S = signal intensity, K = a scaling constant, P = proton density, and A = the flip

angle, more T1 weighted images can be obtained by using large flip angles and less T1 weighted images (T2 weighted) can be obtained by using small flip angles. To verify, this theoretical concept on a clinically oriented MR imaging system, a phantom was designed with 7 vials containing different concentrations of copper sulfate doped water. The T1 and T2 relaxation times were determined on an NMR spectrometer operating at 60MHz and 21°C. The T1 values ranges from 303-1587 msec and the T2 values from 292-1533 msec. For these seven samples, the T2 values are large relative to the short 15msec TE and, therefore, the T2 contribution to the image should be relatively constant. The phantom was imaged on a 1.5 Tesla whole body imaging system (63.9MHz) with TE/TR = 15/300msec and flip angles ranging from 11-80°. The intensity of the vials was plotted versus the log-T1. The experimental results showed that the slope of the curve for the 80° angle was the largest and for the 11° flip angle was the smallest as its curve was essentially flat. A least-squares fit between the experimental data and the theoretically predicted intensities showed them to be in qualitative agreement. The theory of T1 weighting with large flip angles and T2 weighting with small flip angles can, therefore, be reproduced on a clinically oriented MR imaging system.

Tpm-B6

FAST NMR IMAGING BY MODIFIED ECHO PLANAR TECHNIQUE*

G. Kashmar, O. Nalcioglu and Z.H. Cho

Department of Radiological Sciences, Division of Physics and Engineering
University of California - Irvine

Echo planar imaging (EPI) proposed in ref.[1] utilizes an oscillating gradient field applied simultaneously with a low amplitude constant gradient to generate multiple gradient spin echoes for each slice selection RF pulse. It is well known that the use of such gradients results in the measurement of the FID signal along a zig-zag trajectory in the two dimensional q-domain as seen in Figure 1 where spatial frequency q is related to the time integral of the gradient waveform. When the FID is measured along such a trajectory one can not simply apply the two dimensional FFT (2DFFT) to reconstruct the image. Various problems arising from the measurement of the FID along the zig-zag trajectory are discussed in refs.[2,3].

In the present work, we introduce a Modified Echo Planar Imaging (MEPI) technique which enjoys the advantages of the EPI without suffering from some of its shortcomings. The proposed MEPI pulse sequence is shown in Figure 2. The FID signal corresponding to the odd and even echoes is given by,

$$S(t,m) = \int dx'dy'\rho(x',y') \exp\{i\gamma\sqrt{2}G[(-)^{m+1}x't+(m-1)y'\Delta]\} \qquad (1)$$

with m=1,2..., Δ defined in Fig.2 and $G_x=G_y=G$. In equation (1), the (x',y') system is obtained by rotating the (x,y) coordinate system 45° clockwise. The FID measurement trajectory corresponding to the proposed MEPI pulse sequence is shown in Fig.3. It consists of a cartesian coordinate system along (q_x',q_y') which is rotated 45° with respect to the (q_x,q_y) axes. The variables q_x',q_y' are defined by,

$$2\pi q_{x'} = \gamma \sqrt{2}\, Gt \qquad (2.a)$$

$$2\pi q_{y'} = \gamma \sqrt{2}\, G\, (m-1)\Delta \text{ with } m \geq 1 \qquad (2.b)$$

It is important to note that the even echoes (i.e. m even) are time reversed with respect to the odd ones as in the case of the standard EPI technique. The same point was also discussed in ref. [4]. The two dimensional images can be obtained by applying a time reversal operation on the even echo FID's and performing the 2DFFT in the cartesian domain.

The MEPI technique is based on the generation of multiple spin echoes by gradient reversal similar to the EPI method but also enjoys the additional advantage of measuring the FID on a cartesian trajectory. The gradient rise time effects which would occur at the gradient switching points are not expected to cause any problems since we do not measure the FID while we switch from one line to the other (c.f.Fig.2). Finally, the image quality may be improved further by interlacing various MEPI trajectories for a finer data sampling.

*This work was supported in part by PHS Grant No. 1R01-CA 41307 awarded by the NCI, DHHS.

1. P. Mansfield and I.L. Pykett, J. Mag. Res. 29, 355(1978).
2. L.F. Feiner and P.R. Locher, Appl. Phys. 22, 257(1980).
3. M.M. Tropper, J. Mag. Res. 42, 193(1981).
4. G. Johnson and J.M.S. Hutchinson, J. Mag. Res. 63, 14(1985).

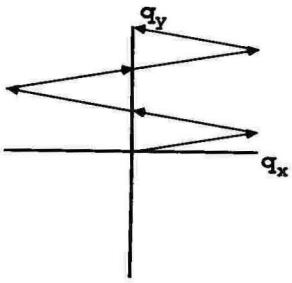

Figure 1. EPI q-domain trajectory.

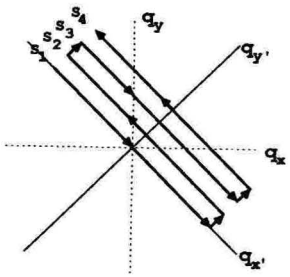

Figure 2. MEPI pulse sequence.

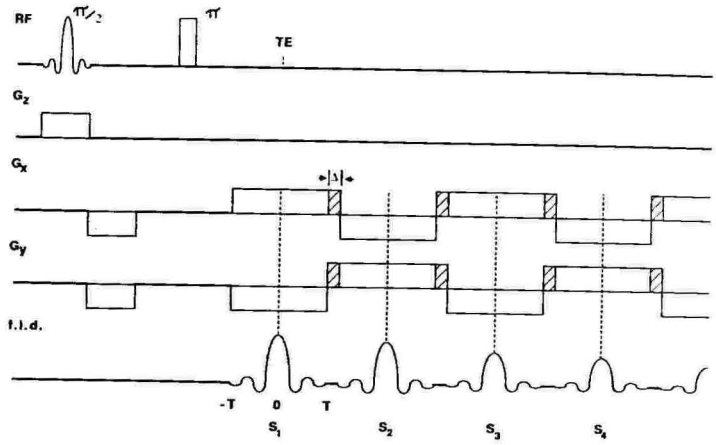

Figure 3. MEPI q-domain trajectory.

Tpm-B7

MOTION ARTIFACT SUPPRESSION TECHNIQUE (MAST^{TM}) IN MULTISLICE MR IMAGING

P. M. Pattany, M.Sc., J. L. Duerk, Ph.D., and J. M. McNally, Ph.D.

Clinical Science Center, Picker International, Highland Heights, Ohio

Artifacts and signal loss due to object motion and blood flow obscure the fine detail structure in 2DFT multislice imaging when using long TE/TR spin echo sequences. This is due to incomplete rephasing of the moving object at the end of the slice select gradient and at the center of data collection gradient.

Complete rephasing of the static and dynamic material within the slice is achieved by setting Ø to zero in the equation shown below.

$$\emptyset = \int_0^t \gamma\, G(t)\, X(t)\, dt = 0 \quad \ldots\ldots\ldots 1$$

where: γ = Gyromagnetic ratio
G(t) = Gradient pulses applied at a given time t in a given gradient profile.
X(t) = Position of the material at a given time t.

The term X(t) can be expanded in a Taylor series as shown below.

$$X(t) = X_o + \frac{Xt}{1!} + \frac{Xt^2}{2!} + \frac{Xt^3}{3!} + \ldots \text{etc}$$

Each order of the above Taylor series equation has been integrated seperately using equation 1, thus completely rephasing static and dynamic material in the slice direction and read direction.

These studies include gradient profile simulation. Comparison of orbits, liver and lumbar spine images obtained with the conventional spin echo sequences and motion artifact suppression technique sequences are presented to show artifact reduction as higher order terms of X(t) are incorporated in the new sequence profiles.

The images obtained with the motion artifact suppression technique reduces/eliminates the artifact due to cardiac, respiratory, orbit and CSF and blood flow motions and signal intensity of the CSF is highlighted.

Reference:

1. Motion Artifact Suppression Technique (MAST^{TM*}) of Magnetic Resonance Imaging. P. M. Pattany, J. M. McNally. Patent Apllicaiton Number 766, 757. Filed August 16, 1986.

* MAST is a trademark of Picker International.

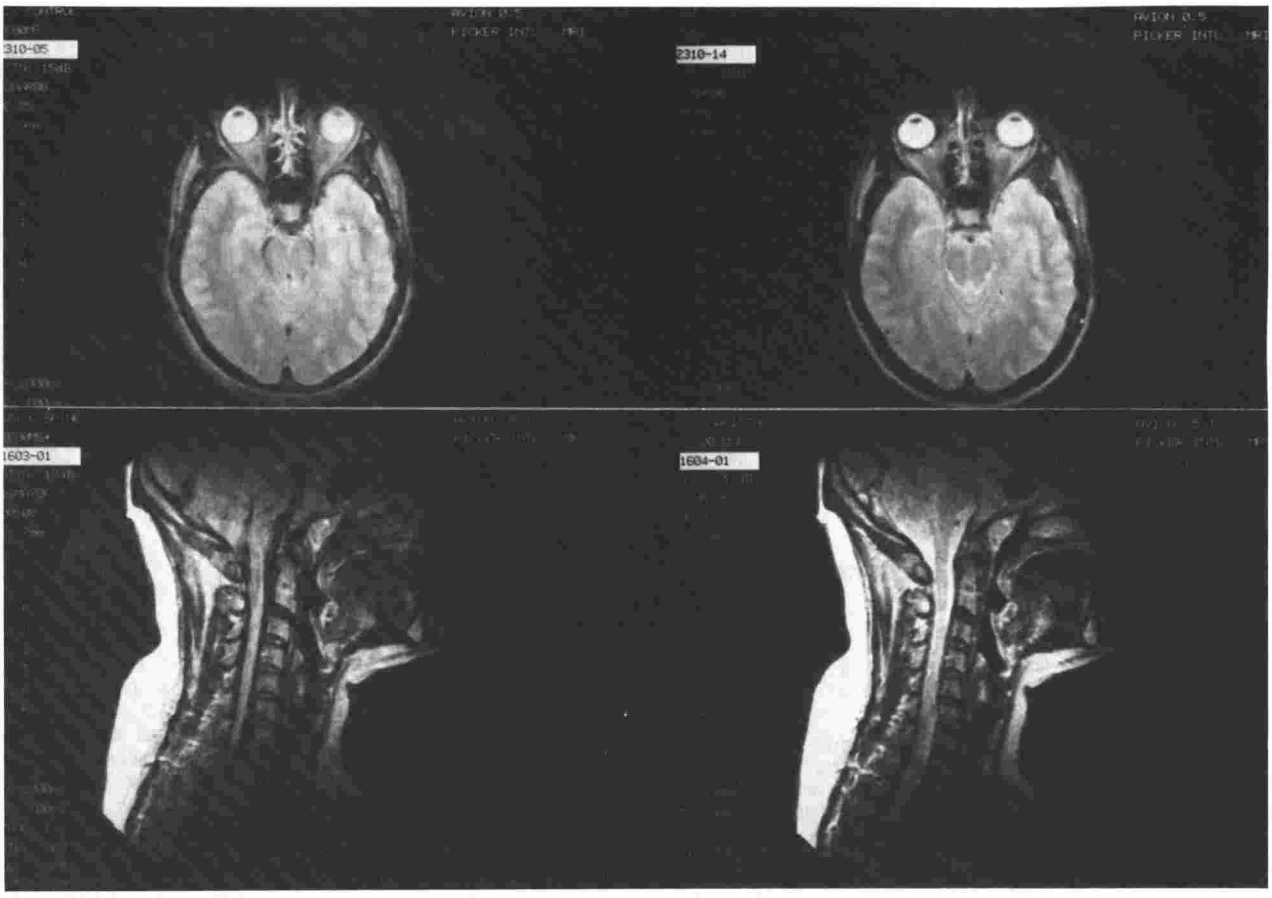

Conventional Spin Echo
Sequence
TR 2000 mSec
TE 100 mSec
1 Excitation
256 Views

MAST™
Spin Echo Sequence
TR 2000 mSec
TE 100 mSec
1 Excitation
256 Views

Tpm-B8

ANALYSIS OF IMAGING AXES SIGNIFICANCE IN MOTION ARTIFACT SUPPRESSION TECHNIQUE (MAST™) REFOCUSSING OF MOVING SPINS

J. L. Duerk, Ph.D. and P. M. Pattany, M.Sc.

Mt. Sinai Medical Center, Cleveland, Ohio 44106 and Clinical Science Center, Picker International, Highland Heights, Ohio 44143

Significant advances have been made recently in producing motion artifact reductions, and flow void refocussing in non-gated MR imaging. Specifically, MAST™ sequences, which employ imaging gradients designed to eliminate the interaction of velocity, acceleration, and higher order terms from the imaging equations, have been demonstrated to be effective without the need for increased imaging time, or additional hardware. This work presents an experimental analysis of the relevance of refocussing gradient lobes along the slice select, frequency encoding and phase encoding axes in standard spin echo imaging. Experiments were performed using a static resolution phantom, flanked by 19. mm I.D. glass tubes carrying $CuSO_4$ doped water (1.0 mg/ml) at 1.5 gallons per minute (Reynolds number= 6900). Images were obtained in coronal and transverse orientations, and various phase encoding directions to allow analysis of MAST™ gradients importance when turbulent motion exists along any imaging axis.

Initial experiments were performed with turbulent flow along the slice select axis. MAST™ gradients, for each axis, which eliminated zero through third moment (static through pulsatility) effects from the imaging equation were used in six different combinations in TE=60 msec pulse sequences. For example, scans using MAST™ gradients along the slice select axis alone, along only the slice select and frequency encoding axes and those using MAST™ gradients along all axes were three of those evaluated. The read and

slice select axes were found to be most important in refocussing the turbulent flow. The amount of signal recovered from the flowing fluid was compared to that of the fluid when it was static. Signal to noise ratios in the tubes were defined as the mean signal value divided by the pixel standard deviation over the same region of interest. The region of inter est was chosen as close to the actual size of the tubes as possiibe using standard viewing console options available on the imager. The magnitude of the flow artifact reductions were determined from the standard deviation of the pixel values in the small artifact resulting from incoherent or uncorrected motion terms. Then, the number of moments in each of these axes was varied from zero through third moment (static to pulsatility) compensation to zero through first (static to velocity) moment compensation, with improvements in motion artifact suppression related directly to increased moment compensation.

Further experiments evaluated combinations of MAST^{TM} gradients when turbulent flow existed in-plane. The phase encoding axis was varied so that the turbulent motion was parallel to the phase encoding direction in one set of experiments and then along the frequency encoding axis in the following trials. Then, the gradient moment compensation was varied as in the previous cases. Similar results were obtained as those above, indicating that the slice select and frequency encoding axes are most important for both motion artifact reduction and flow refocussing in both through-plane and in-plane motion. Approximately 90% of the signal strength of moving spins was recovered using these methods, whereas without them the signal is completely absent. Likewise, motion artifacts were successfully reduced, or even eliminated, in not only scans of the static phantom with turbulent flow, but also in initial clinical trials.

Examination of standard slice select and read gradients provide insight to their contribution to dephasing moving spins. Typical slice select gradients are applied at a specific gradient strength during RF application to give the correct slice thickness. A rephasing lobe is then applied after completion of the RF pulse. This rephase lobe can be applied either before or after the subsequent pi RF pulse. In any event, standard slice select gradients have large first moments, corresponding to significant dephasing from velocity components along this axis. That is, standard slice select gradients rephase static material, yet not those with constant velocity. In addition, the transverse imaging experiments were performed when the tubes were along the slice select axis. Although turbulent flow was used to ensure velocity and higher order terms to be present along each axis during the encoding of any view, the greatest velocity component was along the slice select axis. Therefore, the significant first moment of the slice select gradient, and the large velocity component make the dephasing and signal loss significant along this axis.

Likewise, typical read axis gradients have both dephase and rephase lobes. At the echo time, the read gradient appears as a balanced bipolar gradient, which Moran (1982) showed to have a significant first moment as well. Therefore, standard slice and read gradients significant first moments (velocity sensitivity) lead to signal loss, or phase errors which lead to artifacts in MR imaging. MAST^{TM} gradients remove this sensitivity to velocity or higher order motion terms by having zero valued moments by the echo time, thereby completly rephasing flowing material. In both in-plane and through-plane experiments, the large first moment of the standard read axis gradient combined to make this axis dephasing significant. The signal loss was more dramatic when the tubes were oriented along the read axis, making the product of the large first moment and principle velocity component correspond to a larger dephasing.

The phase encoding axis is not as important as other axes for rephasing moving material, or reducing motion artifacts. First, the single lobe phase gradient is short in time, typically three to five milliseconds long. Therefore, its first and higher mome nts are small, which leads to minor dephasing. Secondly, the moment values are linear with the gradient amplitude. Yet, since most of the signal in MRI occurs at low spatial frequency's (and hence low phase gradient amplitudes), the significance of the dephasing is less than along other axes. Therefore, the frequency encoding and slice select axes are the most important of the three imaging axes to consider for motion refocussing and artifact reduction gradient waveforms.

REFERENCES

Moran, P. R., Magnetic Resoance Imaging, Vol. 1, 1982, pp. 197-203.
Constantinesco, A., Mallet, J., et. al., Magnetic Resonance Imaging, Vol. 2, 1984, pp. 335-340.
Duerk, J. L.. and Pattany, P. M., Proceedings of SMRM Fifth Annual Meeting, Works in Progress, 1986, pp. 3-4.
Pattany, P.M. et. al., Motion Artifact Supression Technique for MRI, Patent Application 766,757, filed August 16, 1985.

(Tpm-C) SURFACE COILS

Presiding: B. Kneeland & S. Saini

3:20 pm

ROOM C-101

12 MINUTES PER PRESENTATION

Tpm-C1
ADAPTIVE HISTOGRAM EQUALIZATION FOR SURFACE COIL IMAGES

Richard Jones

Department of Bio-Medical Physics & Bio-Engineering, University of Aberdeen, Foresterhill, Aberdeen AB9 2ZD

Introduction

Surface coil images generally show significant variations in sensitivity over the imaged area, producing a large dynamic range in the image intensity data. Conventional grey scale display of surface coil images generally results in the contrast range being used to display the disparity in coil response, rather than the difference between tissues. One method of overcoming this problem is to use adaptive histogram equalisation (1). This has been shown to improve the contrast in conventional N.M.R. images (2) and is particularly suitable for surface coil images since it improves the intensity distribution in the image.

Method

In histogram equalization one attempts to re-order the intensity distribution in the total image such that each intensity level represents an equal number of pixels (3). Applying this technique to the whole image improves the contrast between different regions of the image but does not improve the contrast within a particular region. Adaptive histogram equalization attempts to overcome this problem by dividing the image into a number of equally sized contextual regions and performs histogram equalization on each separate region. This serves to improve the contrast within the regions but produces an image with a discontinuous, 'blocky' appearance since the equalization in one region bears no relation to that in the adjacent regions. To overcome this problem it is necessary to interpolate between four adjacent regions, as shown below:

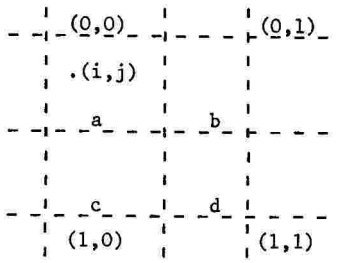

For a pixel of value x whose co-ordinates relative to the upper left contextual region are (i,j). Then if $M_a(x)$,$M_b(x)$,$M_c(x)$ and $M_d(x)$ are the mapped intensity values corresponding to x in the four contextual regions a, b, c and d, then the mapping value for the pixel is given by:

$$M(x) = (i-1)((1-j)M_a(x) + jM_c(x)) + i((1-j)M_b(x) + jM_d(x))$$

The spacing of the contextual regions is taken as unity, so yielding fractional values for the weighting factors i and j. The corners and edges are treated separately.

Results

The original image of the cervical spinal cord (Figure 1, top left) was collected using a specialised receiver coil on our 3.4MHz system using a saturation recovery pulse sequence with a TR of 1000ms and a 90 gaussian RF pulse. Adaptive histogram images were produced using 16, 64 and 256 contextual regions (Figure 1, top right, bottom left and bottom right respectively). All of the images are 8 bit and are displayed using a 256 level grey scale. All of the adaptive histogram images can be seen to exhibit an improved intensity distribution and an increase in contrast. Increasing the number of contextual regions increases the contrast but with very large numbers of contextual regions the increase in contrast produces a very grainy image.

It should be emphasised that the adaptive histogram method has the important advantage of being generally applicable to all types of surface coils. Unlike the non-linear transfer functions used by some groups (4) it does not employ arbitary scale factors. It can also be used to improve the contrast in images collected with conventional RF coils. The contrast in the images can be further manipulated by altering the histogram equalization for the contextual regions by making the frequency with which each intensity level occurs a function of the intensity level.

References

1) Pizer,S.M., Zimmerman, J.B., Stabb, E.V. J.Comp.Tomogr. 8,300 (1984).

2) Ridgeway, J., Sharp, P.E. Phys.Med.Biol. 31, 2; 171-179 (1986).

3) Gorris, M.L., Scheibe, P.O., Kriss, J.P. Comput.Biomed.Res. 9,571 (1976).

4) Noeuer, T., Eisner, R.L., Sprawls, P., Coumans, J.J., Hoffman, J.C. Proc. S.M.R.I. 4th Annual Meeting, Philadelphia (1985).

Figure 1.

Tpm-C2

A VARIABLE FREQUENCY BIRDCAGE RESONATOR FOR IMAGING AT HIGH FIELD

W.G. Holcomb and J.C. Gore
Yale University School of Medicine, New Haven, CT 06510

Radiofrequency coils using lumped element delay lines (so called birdcage resonators (1)) provide a means of producing a homogeneous transverse B field that is especially useful with high field magnets with a static Bo field in the axial direction. Such resonators differ markedly in their design and theory of operation from conventional tuned circuits. They develop the transverse field secondary to a set of furfact currents which are formed along the axis of a cylinder and which vary sinusoidally with azimuthal angle. The design rationale has been described by Hayes et al (1). We here describe our experience in developing imaging coils for small animals (5 - 10 cm diameter field of view) for use in a 2.0T imaging magnet.

The performance characteristics of coils with different numbers of columns (8, 16 and 32) have been evaluated for resonators in which the distributed capacitance and conducting elements were produced from a single etched sheet of printed circuit material. These devices were configured in the model of a low pass network. However the final adjustment to the exact desired operating frequency was tedious and time consuming. We therefore investigated methods of adjusting the frequency. A mechanical design was developed using 16 columns in which each column is a concentric pair of tubes that are separated by a thin layer of teflon shrink tubing (see figure 1). The inner and outer tubes in each pair are connected to opposite ends of the coil and all 16 can be moved in and out together. Variable tuning is achieved by a long threaded screw which transports the two halves of the cylinder in opposite directions, varying the length from 7.8 to 9 cm. In an early version, 16 columns around a 5 cm field of view gave a tuning range of 146 to 232 MHz, but could not be tuned as low as 85 MHz because the maximum column capacity was only about 10 pF. To lower the frequency range, 16 small inductances were placed around the perimeter of each end ring of the birdcage, which resulted in a tuning range of 64 to 100 MHz. This coil may be used to image both proton and fluorine in the same object. The coupling network must be adjusted independently, and variation in the matching can be achieved by varying the spacing, and therefore the inductive coupling, between the coil and a secondary loop that is directly connected to the receiver. Such variable coils may be adjusted so they are immune to different loading effects, they may be used with more than one magnet (e.g. 1.5T and 2.0T) and may permit the detection of more than one nuclear species.

(1) C.E. Hayes, W.E. Edelstein, J.F. Schenck, O.M. Mueller and M. Eash J. Magnetic Resonance, 63, 622-628 (1985).

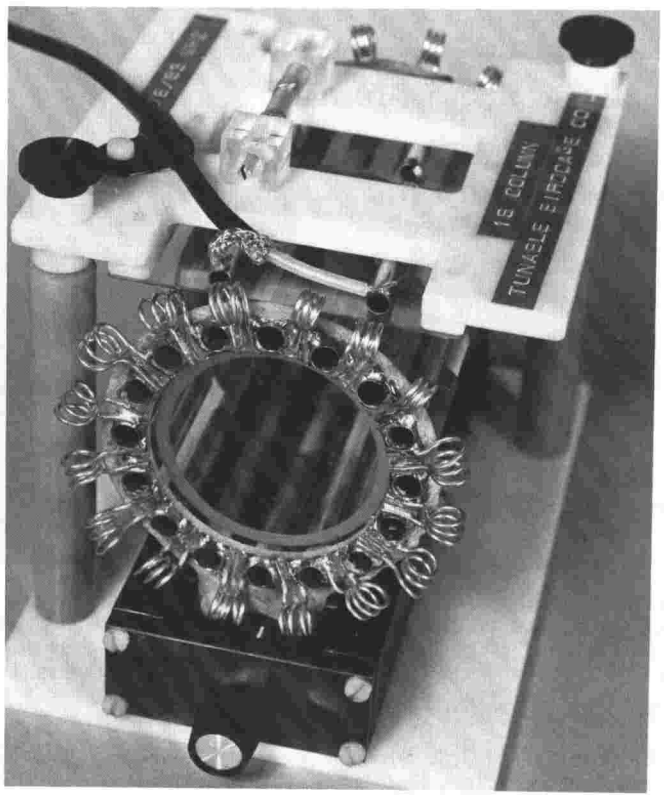

FIGURE 1

Tpm-C3 THE DESIGN OF A TRIPLE TUNED COIL BASED ON FOSTER NETWORK PRINCIPLES

W.G. Holcomb, J.C. Gore and H.D. Sostman, Department of Diagnostic Radiology
Yale University, New Haven, CT 06510

An important problem for successful in vivo spectroscopy is the design of RF coils simultaneously tuned and matched to different frequencies. Such coils permit rapid switching between nuclei or even multiplexed data acquisitions. A common constraint however is that the dimensions of the sample coil itself are determined by geometrical considerations of surrounding the required volume so that the receiving element inductance may not be freely specified. We have encountered such a problem specifically in designing a coil to simultaneously acquire spectra from protons, phosphorus and sodium in an elongated specimen containing a perfused cell culture, designed to investigate tumor metabolism in a 2T magnet. Figure 1 depicts the simple circuit that produced the impedance-frequency variation shown in Figure 2. L_o is the inductance of the probe, contrained in our case to be 83 nH. The choice of the other components may be made by recourse to the theoretical framework provided by R.M. Foster.[1] Using Foster's theorems, the expression for the total complex impedance may be expanded as a sum of partial fractions, each of which has a simple physical interpretation as a null or pole in the impedance characteristic. At each resonant frequency a further problem is matching the low impedance of the circuit to the 50 ohms of the preamplifier. Using a microstrip 50 ohm line and variable capacitors to serve as stubs, we were able to correct the high standing wave ratio presented at the network's open terminals. This is equivalent to using a variable parallel capacitor for transmission line matching. Martin and Daly (2) recently used a similar method with an adjustable coaxial line. Of course only one stubb can be activated at a time using this method.

1. Foster RM, Bell Systems Technical Journal, 3:259-267, 1924.
2. Martin JF and Daly CP: Magnetic Resonance in Medicine, 3: 346-351, 1986.

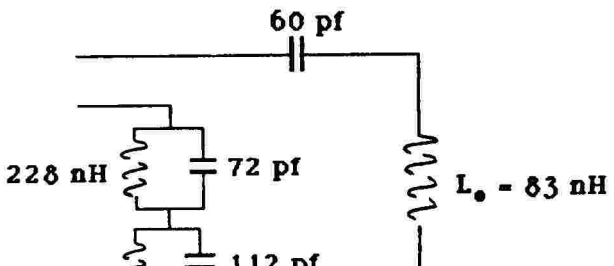

FIGURE 1

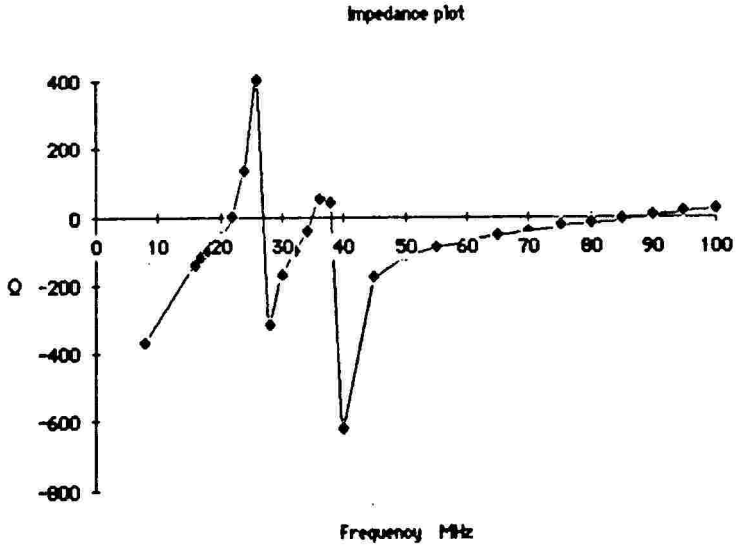

FIGURE 2

Tpm-C4

OPTIMIZING SURFACE COIL GEOMETRY AT 0.15T

J.R. Fitzsimmons, T. Gillespy III, M. Boucher

Department of Radiology, University of Florida, Gainesville, Florida

The application of surface coils to MRI has developed rapidly over the past several years. The increase in signal to noise (S/N) which results from their use is well documented. However, an analysis of some of the basic variables which determine surface coil performance has been lacking. The purpose of this experiment is to examine how different surface coil geometries affect coil sensitivity.

METHODS

A plexiglass box was constructed to contain a conductive solution (0.45% NaCl) which would approximate the loading effects of the human body. The box was scaled to approximate the torso (40 cm. square on the bottom and 20 cm. deep). A 2 cm loop connected to a coaxial wire was fixed to a movable arm which could be positioned anywhere in the conductive solution to provide a variable oscillating magnetic field. This loop was connected to a signal generator which put out a constant voltage at 6 MHz. Most of the measurements were done on axis by calibrating the vertical support arm in 1 cm intervals. The entire box was elevated by supports to permit the insertion of the surface coils under the box.

Signal intensity measurements were made by positioning the 1 cm transmitter loop at distances of 0, 3, 6, 9 and 12 cm from the surface coil on axis with an rf millivoltmeter attached to the output of the coil. The measurements were first made with the surface coil in free space and then repeated with the coil directly underneath the plexiglass box with 0.45% NaCl solution. The following coils were built and tested.

The effect of conductor diameter on coil sensitivity was evaluated by building 4 single turn 13 cm diameter coils with different diameter conductors: #12 solid wire, 5/16" copper tube, 3/8 " tube and 1/2" tube. The effect of varying the coil radius was evaluated by building a set of three single turn loop coils with different radii: 5 cm, 7.25 cm and 10.5 cm. The simple loop geometry was compared to the oval shape by constructing two coils each having the same surface area (346 sq. cm.). The loop had a 16.5 cm. diameter

while the oval had a minor axis diameter of 14 cm. and a major axis diameter of 32 cm. Adding turns to the simple loop geometry (i.e., a solenoid) was assessed by constructing a set of 3 coils. All coils has a 13 cm diameter, with the first having one turn, the second, two turns and the third, three turns. Finally, a comparison was made of the 2 turn loop geometry (solenoid) and the 2 turn spiral keeping the outer diameter of the two coils constant.(13 cm).

RESULTS

The diameter of the conductor was found to be positively correlated with the signal amplitude from depths of 1 to 12 cm away from the surface of the coil in both the unloaded and loaded case. Surface coil radius was inversely related to sensitivity at depths <6 cm; however, at depths >6 cm there was no difference in coil performance. When comparing the simple loop to an oval shape geometry of the same surface area, no significant difference is found in sensitivity for depths ranging from 0 to 15 cm in both the loaded and unloaded case. The two turn loop (solenoid) coil was more sensitive than the simple loop. The three turn version, however, was less sensitive than the simple loop. For the unloaded case, these differences are only apparent at depths of less than 6 cm. When loaded, the two turn coil was more sensitive at depths up to 9 cm. Finally, the 2 turn spiral was significantly more sensitive than the 2 turn loop (solenoid) at depths of less than 3 cm, while the solenoid does somewhat better at depths of greater than 6 cm. Overall, the effect of loading was to reduce signal intensity at all depths by about 50%.

CONCLUSION

The results of the experiments have direct implications for surface coil design. For areas of the body which are superficial and which require high resolution capabilities such as the TMJ, the spiral geometry is highly desirable. In the spine where structures are somewhat deeper in the body and have a fixed distribution, an oval or elliptical shaped coil is more appropriate than a simple loop. There is no loss in sensitivity at depth with an oval coil compared to a loop and the sensitivity profile can be matched to the structure of interest. In almost all cases some advantage is obtained from adding a turn to the coil design although the same sensitivity would probably be obtained from an even larger tubular diameter. Finally surface coil performance is severaly limited beyond a distance of about 6 cm regardless of the coil design. For greater depth penetration one must consider a volume coil design.

Tpm-C5

REMOTELY TUNED RF COILS FOR NMR

M.J. Hennessy and E. Kwok

Intermagnetics General Corporation, MRI Laboratory, Troy NY

For many practical reasons, there is an increasing need to tune RF coils remotely by separating the coil and capacitor by a transmission line. Remote tuning allows greater flexibility in the placement of RF coils, leading to more compact designs since bulky tuning capacitors may be placed elsewhere. Recently, there have been reports of remotely tuned surface coils which have given good results.

It is commonly known that inserting a transmission line between the coil and capacitor degrades the Q and hence the overall sensitivity and signal-to-noise ratio of the NMR signal. The purpose of this work is to quantify the amount of degredation that can be expected in a practical system using a half-wavelength cable. A half wavelength cable was chosen for simplicity for two reasons. Ideally, the load impedance appears at the half-wavelength position and capacitors may be used to tune the coils.

It can be shown from transmission line equations(1) that the impedance of a one-half wavelength lossy transmission line terminated by an impedance Z_L can be written as

$$Z = Z_0 \frac{1 + R e^{-\alpha\lambda}}{1 - R e^{-\alpha\lambda}}$$

where

$$R = (Z_L + Z_0)/(Z_L + Z_0)$$

α = characteristic line attenuation constant
λ = wavelength of propagation in the cable.
Z_0 = characteristic line impedance.

Measurements were taken at 104 MHz using RG 58/U cable. Using manufacturer's propagation velocities the half-wavelength of this cable should be 95.1cm compared to 96.1cm measured. The impedance is 2910 ohm which compares well to the calculated value of 3060 ohm based on the equations above.

Two terminations were tested. The first configuration consisted of a 3-1/2 turn solenoidal coil with a diameter of 0.9cm. Using a variable capacitor, the coil was tuned on resonance at 104 MHz. The measured Q and impedance on resonance was 361 and 25k ohm respectively. With the half-wavelength transmission line inserted in between, the Q as measured at the capacitor dropped to 97 with an impedance on resonance of 2190 ohm. The impedance on resonance as computed by the parallel

combination of the tuned circuit and transmission line resistance is 2014 ohms in good agreement with the measured data.

The second configuration consisted of the same coil with a 2.2k ohm resistor in parallel with the coil. A variable capacitor was used to tune the network on resonance at 104 MHz as before. This circuit had a lower Q of 29 and an impedance on resonance of 2100 ohm. With the transmission line inserted, the Q at the capacitor actually went up to 61. This is due to the fact that the transmission line itself is resonant. The impedance on resonance measured 1302 ohms compared to the computed parallel value of 1245 ohms.

Conclusions

The actual sensitivity of the NMR experiment is proportional to the effective Q of the RF coil which consists of coil losses, sample losses and transmission line losses. For the case studied, a good model is to represent the transmission line loss as a resistor in parallel with the tuned NMR coil. This means the NMR sensitivity will drop as the transmission line losses increase. The transmission line loss and its equivalent resistance can be estimated on the basis of conventional lossy transmission line analysis.

1. M.J. Hennessy to be published.

Tpm-C6

LOCALIZED MR UTILIZING A FERROMAGNETIC CYLINDER

K.Hikida, N.Iriguchi, T.Yamamoto, Y.Ueshima, J.Hasegawa, S.Yamai, T.Miyazaki, Y.Wada*, H.Toyoshima, T.Maki

Systems Engineering Laboratory,*Atsugi Mfg. Works, Asahi Chemical Industry Co.,Ltd.
221 Tanazawa, Atsugi, Kanagawa 243-02 Japan

Introduction: The field, r vertically apart from the center of a ferromagnetic bar which is r_m radial , $2l$ long, and put in a homogeneous field B_o,

$$B = B_o - \frac{m}{2} \frac{r_m^2}{l^2\{1 + (r/l)^2\}^{3/2}} ,$$

where m is the magnetization of the bar. Utilizing a ferromagnetic cylinder, we obtained a localized MR image of the human calf.

Methods: A cylindrical RF coil, 24 cm diametric and 20 cm long, was installed in a 1 m bore 2 Tesla system, Asahi Super 200. A ferromagnetic cylinder, 15 cm diametric and 20 cm long, made of symmetrically arranged 16 straight iron wire pieces of 0.2 mm diameter, was set axially palallel to the RF coil. Putting the right calf through the ferromagnetic cylinder, ^1H imaging was carried out.

Results: Fig.1 shows the normal image (folded) of the calf, obtained without the ferromagnetic cylinder. Fig.2 shows the localized image of the calf, obtained with the cylinder. The sensitive portion was homogeneous and the edge was sharp.

Conclusion: Localized MR imaging, with slice selection, has been practicably performed by focusing the static field with a ferromagnetic cylinder. The concept should prove to have a great potential for localized imaging, and hence, also for localized spectroscopy.

Fig.1

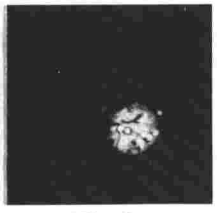

Fig.2

Tpm-C7

A TECHNIQUE FOR MATCHING TRANSMITTERS TO RF COILS

T.W. Redpath and J.M.S. Hutchison

Department of Bio-Medical Physics & Bio-Engineering, University of Aberdeen, Foresterhill, Aberdeen AB9 2ZD,UK

Introduction

A common technique is to match coil and transmitter to 50Ω to avoid standing waves on the connecting coaxial cable, so that the cable length is irrelevant. Here we describe a method in which the line is used as an integral part of the matching network. In this case a substantial standing wave may exist and that choice of the lumped matching elements depends on the line length.

Theory

Figure 1 shows the matching network which consists of a cable of length x and characteristic impedance Z_0, and a terminating π network of impedances Z_1, Z_2 and Z_3.

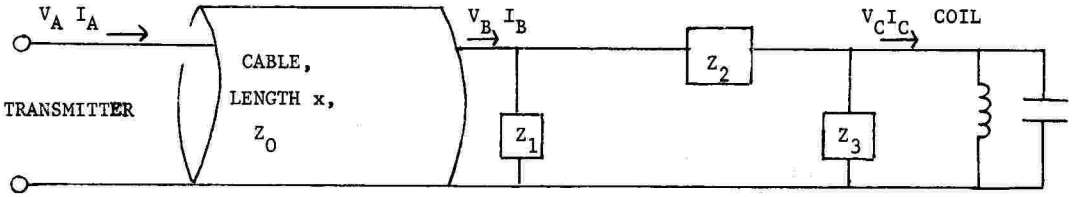

The voltages and currents at the points A,B and C are calculated by a matrix technique (1). For the transmission line of propagation velocity u

$$\begin{pmatrix} V_B \\ I_B \end{pmatrix} = \begin{pmatrix} \text{Cos}\alpha & -jZ_0\text{Sin}\alpha \\ -j\text{Sin}\alpha/Z_0 & \text{Cos}\alpha \end{pmatrix} \begin{pmatrix} V_A \\ I_A \end{pmatrix}$$

where $\alpha = \omega x/u$. The π network gives

$$\begin{pmatrix} V_C \\ I_C \end{pmatrix} = \begin{pmatrix} (Z_1+Z_2)/Z_1 & -Z_2 \\ -(Z_1+Z_2+Z_3)/Z_1Z_3 & (Z_2+Z_3)/Z_3 \end{pmatrix} \begin{pmatrix} V_B \\ I_B \end{pmatrix}$$

The relation of (V_C I_C) to ($V_A I_A$) is found from the product of these matrices.

The values of Z_1, Z_2 and Z_3 can be chosen, for a given length of cable, to give matrices of the form

$$\begin{pmatrix} V_C \\ I_C \end{pmatrix} = \begin{pmatrix} 0 & jZ_L \\ j/Z_L & 0 \end{pmatrix} \begin{pmatrix} V_A \\ I_A \end{pmatrix}$$

or

$$\begin{pmatrix} V_C \\ I_L \end{pmatrix} = \begin{pmatrix} t & 0 \\ 0 & 1/t \end{pmatrix} \begin{pmatrix} V_A \\ I_A \end{pmatrix}$$

where t is a simple ratio. It is desirable to deliver a constant voltage to the coil, regardless of variable patient loading, in order that a constant current flow in the coil, otherwise the pulse angle will vary. The first case is therefore suitable for constant current rf generators, while the second is a voltage transformer and is suited to constant voltage generators. When Z_L and t are real quantities, Z_1, Z_2 and Z_3 are reactive, either capacitors or inductors, depending on cable length and the desired matrix. In the first case

$$Z_1 = jZ_LZ_0\text{Cos}\alpha/(Z_0+Z_L\text{Sin}\alpha)$$

$$Z_2 = -jZ_L\text{Cos}\alpha$$

$$Z_3 = jZ_L^2\text{Cos}\alpha/(Z_L+Z_0\text{Sin}\alpha)$$

The second case has solutions

$$Z_1 = jtZ_0\text{Sin}\alpha/(1-t\text{Cos}\alpha)$$

$$Z_2 = -jtZ_0\text{Sin}\alpha$$

$$Z_3 = jt^2Z_0\text{Sin}\alpha/(t-\text{Cos}\alpha)$$

Conclusion

The matching network parameter Z_L allows the required transmitter output current for a given pulse angle to be calculated directly from coil inductance and field per unit current, assuming the coil has $Q \gg 1$. Similarly the parameter t allows straightforward calculation of the required transmitter voltage. Knowledge of coil Q is not necessary.

Reference

1) H.H. Skilling, 1951. Electric Transmission Lines, New York: McGraw-Hill, pp.274-9.

Tpm-C8

A Transmission Line Resonator for High-Quality Surface Coil Imaging

Reiner Bader, Hans-Joachim Zabel, Joachim Gehrig, and Walter J. Lorenz

Institute of Nuclear Medicine, German Cancer Research Center, Heidelberg, West Germany

High spatial and contrast resolution MR imaging of areas of the human body has been achieved by using surface coils (1). However, because their sensitive volume has to be adapted to the specific area to be examined in order to increase the filling factor, this leads to a high signal-to-noise ratio (S/N) and a compromized quality of the MR image. In addition, since these surface coils are usually components of a resonant circuit, the dielectric and inductive losses in conductive samples must be compensated for by capacitive tuning both to the Larmor frequency and to the 50 Ω -transmission to the preamplifier. It is true that coils with low Q-values significantly reduce the effect of this capacitive detuning (2), but these coils also diminish the S/N proportional to the square root of Q. In addition, the Q-value of loaded coils is far lower, if the energy loss per time in the body increases compared to the energy loss in the resonant circuit. In order to eliminate at least the dielectric losses, it has been suggested that a Faraday shield be interposed between sample and coil (3), but this is often impractical, if not impossible for MR imaging in humans.

In order to circumvent the disadvantages of surface coils we have developed a completely different RF receiver system (Fig. 1). The resonant circuit has been replaced by what we term a coaxial Transmission Line Resonator (TLR); the short-circuited end of which is bent to form a loop for receiving the inductive part of the MR signal. Analogous to the principle of the coaxial frame or ring antenna, the shielding of the loop is cut at a suitable point, usually directly opposite the short-circuit point to provide symmetrical receiving conditions. Thus a functional RF receiving system is obtained along with, except for the small gap, a nearly complete Faraday shield, rendering the two tuning capacitors unnecessary.

The simplest way to produce a receiving system is to use a $\lambda/4$-resonator with a receiver loop as a terminal reactance. The length (l) of the resonator may be calculated by using the equation in Fig. 1, where Z_L is the characteristic impedance of 50 Ω and L and C the inductance and capacitance of the loop. As the $\lambda/4$-resonator has a high ohmic resistance at its preamplifier end, which is also transformed to the end of the $\lambda/2$-resonator by the transmission line, an impedance matching must be set up for the 50 Ω -coupling. This is readily accomplished by the capacitance C_K and a field effect transistor.

This novel type of RF resonator has been developed for use at magnetic fields of 1.5 Tesla, but there are no restrictions for the application of the TLR at lower magnetic fields or frequencies, except for the decrease of the Q-value. For a 1.5 T-tomograph with a 64 MHz resonant frequency, Q-values of more than 200 are usual for commercial coaxial cables. The great advantage of the TLR is that the Q-value of the $n \cdot \lambda/4$-resonator (n = 1,2,.) is independent of the resonator length and less affected by the loss of reactances at one end of the TLR, if the resonator length is increasing. If the loop is connected to a λ-transmission line consisting of a coaxial cable (RG 214) with a Q-value of 166, Q_O is 180 and Q_L becomes 140.

Another feature of the TLR, compared to surface coils, is the minimal effect of detuning. For a loop in connection with a $\lambda/2$-transmission line the detuning of the signal intensity is only 0.5 dB. This means a negligible loss of signal and makes tuning between imaging of patients absolutely needless.

The axial sensivity profile in Fig. 2 shows that the S/N ratio close to the loop is very high compared to body resonators and therefore responsible for the high-quality imaging. Obviously, the best spatial and contrast resolution will be obtained when the region to be examined is situated inside the loop.

As the TLR can easily be made in a relatively short time, immediate adaptation to the individual body contour of a patient is possible. TLRs with loops of different shapes and sizes have been particularly well suited for examinations of the spinal cord, the extremities, the face, and the fairly inaccessible throat. The TLR's high filling factor, Q-value, and stability against detuning significantly improve the quality of the image over standard surface coils.

(1) L. Axel, J Comput Assist **8**, 381 (1984).
(2) P.T. Cahill, J.R. Knowles, J.B. Kneeland, Radiology **153(P)**, 243 (1984).
(3) D.I. Hoult, P.C. Lauterbur, J Magn Reson **34**, 425 (1979).

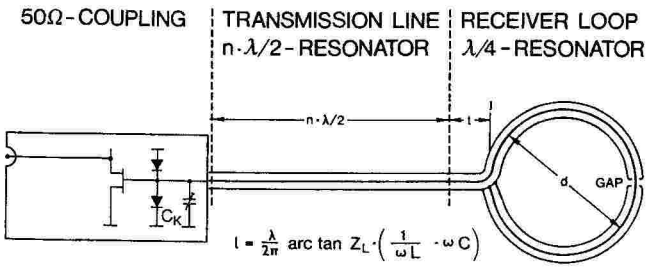

Fig.1: Line drawing of the TLR

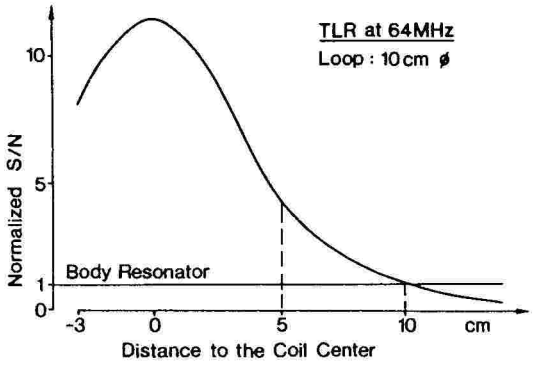

Fig.2:Sensivity profile of the TLR

(Tpm-D) NEURO-CLINICAL

Presiding: B. Flannigan & G. Sze

3:20 pm

ROOM C-102

12 MINUTES PER PRESENTATION

Tpm-D1
MR IMAGING: CONTRIBUTION OF MR IN BRAIN INJURY

Seibert CE, M.D.*, Dreisbach, JD, M.D.*, Smazal SF, M.D.*, Cilo M, M.D.**, Hsu M, M.D.**, Weintraub A, M.D.**

*Radiology Imaging Associates, **Craig Hospital

The authors review the MR findings in 75 patients referred for study from a rehabilitation brain trauma setting in which the majority of patients were greater than three months from the date of their injuries. In most cases, CT's were available for comparison and all clinical material, histories and physicals were reviewed. Qualitative impressions of the review became apparent even though the case numbers were small and may not have statistical significance. These findings are:

1. MR was more valuable than CT in certain local injury patterns e.g. residual subdural hematoma was more easily characterized on MR than on CT. Residual resolving hemorrhage in the brain was more easily identified on MR than on CT.
2. Prognostic findings: Foci of frontal and temporal brain injury were better identified on MR than on CT--useful information in rehabilitation. Secondly, of the spectrum of shear injuries, the most severe was characterized by extensive high signal seen on T_2 weighted images (T_2WI) extending from the ventricles through the white matter to cortical medullary junctions and this pattern was associated with poor clinical outcome.
3. Hydrocephalus: The degree of post traumatic hydrocephalus was difficult to follow on sequential T_2WI alone; T_1WI or CT were necessary. Hydrocephalus with periventricular hyperintensity (PVH) was common. Varying degrees of hyperintensity did not correlate with radionuclide studies (RNS) for CSF flow and ventricular obstruction, however, the PVH associated with advanced shear injury pattern was a negative predictor for clinical outcome if a ventricular shunt was performed. In patients meeting imaging criteria for ventricular shunt for obstructive hydrocephalus, clinical parameters seem to be the most reliable criteria in patient selection for shunt and subsequent improved clinical outcome.

Tpm-D2

MR IN THE EVALUATION OF THE COURSE OF DISEASE IN MULTIPLE SCLEROSIS

W.M.Bauer[1], M.Reichel[1], K.Sigel[2], G.Fenzl[1], P.Baierl[1]

Dpts. of Radiology[1] and Neurology[2] of the University of Munich

MR has shown to be a very sensitive method for detecting lesions in multiple sclerosis. Demyelinating plaques are represented on T2-weighted images as areas with a higher signal intensity. An acute lesion with an active process of inflammation and edema or hypervascularisation is supposed to be the pathological anatomical substrate of these plaques with high signal intensity. With respect to older lesions with gliosis and scarring no increased signal intensity is expected (1). There exist no detailed experiences yet about signal characteristics of MS-plaques during the time-course of the disease.

Therefore 15 patients with MS have been selected with a primary MR-examination during the first phase of an acute attack. The control study comprising a thorough clinical neurological examination and MR was done after a period of 1 1/2 - 2 years. The study was performed by means of superconducting magnet (Magnetom, Siemens AG) with T1- and T2-weighted spin-echo-sequences. For the evaluation the actual neurological status, the course of the disease (number of attacks) and the MR-images were compared with the initial findings.

The results of our study demonstrate a correlation between the clinical neurological course and the MR-findings. In patients without further deterioration since the basic MR-examination there was no change in size, number and signal intensity of the demyelinating plaques. In one case there was a decrease of size, number and signal intensity, partially even complete regression. On the other hand we could recognize an increase in size and number of the plaques in patients with a relapsing course of the disease.

The results of this study extend the knowledge about the time-course of demyelinating alterations. We conclude that MR-examination provides further information about the history of the disease and might be helpful in therapeutic trials.

Ref.: (1) D.Uhlenbrock et al.: KST bei gesicherter Multipler Sklerose
Digit. Bilddiagn. 5(1985) 1-7

Tpm-D3

PROGRESSIVE SUPRANUCLEAR PALSY: MAGNETIC RESONANCE IMAGING AT 1.5 T

S. Patel, M.D., W. Sanders, M.D., A. Haggar, M.D., R. Boulos, M.D., B. Mehta, M.D. and J. Froelich, M.D.

Department of Diagnostic Radiology, Henry Ford Hospital, Detroit, Michigan 48202

Progressive supranuclear palsy (PSP) is a neurodegenerative disorder characterized clinically by supranuclear opthalmoparesis, pseudobulbar palsy, Parkinsonian signs without tremor but with axial rigidity, broad based gait and postural instability. Dementia follows later in the disease.

Five patients with established diagnosis of PSP were studied by MRI on a GE Signa system operating at 1.5 T. Both T-1 weighted (SE TR600, TE 2 MS) and T-2 weighted (SE TR2500, TE25, 50, 75, 100 ms) images were obtained. Following morphologic observations were made on MRI images:

1. Brainstem atrophy more marked in the mid brain
2. Periventricular hyperintensity on T2 images
3. Hyperintense foci on T2 weighted images in white matter of frontal lobes mainly
4. Cortical atrophy involving frontal lobes
5. Corpus callosum atrophy
6. Abnormal iron accumulation was looked for but was not found.

Findings on MRI parallel the pathologic findings.

Tpm-D4
MRI OF NEUROCYSTICERCOSIS

Russell S. Rhee, M.D.; Don Kumasaki, M.D.; Mohammad Sarwar, M.D.

Cook County Hospital and University of Illinois Hospital

A comparison was made of CT and MRI findings in 15 patients with neurocysticercosis. MRI demonstrated greater sensitivity in detecting lesions than CT and also provided a better evaluation of the extent, location and morphology of lesions. Ventricular and cisternal lesions as well as smaller lesions were particularly better demonstrated. In one instance, calcified lesions interpreted as parenchymal in location on CT were actually found to lie deep within cortical sulci on MRI. Calcifications that were present in most of the cases were clearly better demonstrated on CT while vascular structures caused confusion in identifying calcifications on MRI. However, at the level of the lentiform nuclei, small foci of low signal intensity medial to the external capsule on MRI corresponded well with calcifications seen on CT: those located lateral to the external capsule were more likely to represent vascular channels. A highly characteristic finding of neurocysticercosis is the identification of a scolex within a cystic lesion. Scolices were more often seen on MRI than CT and one lesion seen on MRI demonstrated multiple scolices. In one case, multiple hyperintense lesions were seen in each centrum semiovale representing vasculitis which is part of the neurocysticercosis spectrum.

Tpm-D5
PRECISE ANATOMIC LOCALIZATION OF CEREBROSPINAL FLUID LEAKS BY MRI (for oral presentation)

Randy R. Sibbitt, M.D. *, William Orrison, M.D. **, Jeffrey Wicks, M.D. *, and Glen Morradian, M.D. **

*UNM/Los Alamos Center for Non-invasive Diagnosis
1201 Yale Blvd NE, Albuquerque, NM 87131
**University of New Mexico School of Medicine
Dept. of Radiology, Albuquerque, NM 87131

Cerebrospinal fluid fistulas are extremely difficult to identify at surgery with inadequate closure having recurrent episodes of meningitis and a high mortality. Although nuclear studies allow gross determination of CSF leakage exact localization has been most effective with metrizamide computed tomography with the attendant morbidity of intra-thecal contrast administration.

MRI images obtained on a 2.0T GE Signa operating at 1.5T confirmed suspected CSF leakage in 4 of 6 paients identifying alternate fluid collections in the remaining 2 patients. Of the 4 CSF leaks identified the exact site of the dural defect was identifed in each of 8 scans with followup scans confirming surgical success or failure. MRI impressions of the initial leak locations and sites of failed surgeries were all confirmed at surgery. Negative exams were confirmed through tissue diagnosis. No false positive, false negative, or inaccurate leak locations were found. The heavily T2 weighed images (TE80/TR2000) appear most obvious with CSF high in intensity. Thus, MRI is highly accurate in the detection of CSF leaks and is the method of choice for exact pre-surgical localization and followup.

Tpm-D6
PEDIATRIC MR IMAGING OF THE SPINAL CORD

P. Baierl[1], G.Fenzl[1], M.Naegele[1], B.Krauß[1], Th.Vogl[1], C.Förster[2], D.Vogl[2], H.Obermüller[3]

Departments of Radiology[1], Pediatrics[2] and Neurosurgery[3], University of Munich, F.R.G.

Introduction

MR Imaging has been shown to be an effective method for the evaluation of the spinal cord (1,2). In pediatrics, the non-invasiveness and the absence of ionizing radiation appear to be of even greater value than in adults.

Purpose of the study

This study was aimed to ascertain the diagnostic accuracy (sensitivity and specifity) of spinal cord MR Imaging in children. The results were compared with other methods (CT, metrizamide cisternography, myelography).

Materials and Methods

60 children aged between one week postnatal and 16 years were examined. 45 examinations concerned the lumbar spine, the other 15 the cervical and the thoracic spine. In all patients, sagittal and transversal spin echo images were obtained. T1- and T2-weighted pulse sequences were used, as well as gradient (short) echoes. The MR system consisted of a 1.5 T superconductive magnet run at 0.35 and 1.0 T. Total examination times ranged from 30 to 60 minutes. Children up to 6 years were either sedated or examined under general anesthesia with intubation and controlled artificial ventilation (3).

Results

45 of the patients showed pathologic findings (spinal dysraphism, tumors, hemorrhage, degenerative or inflammatory disorders).

- in most cases, MRI showed the intraspinal and soft-tissue changes better than other methods
- cortical bone destruction was best seen in the CT scans
- MRI was superior to all other methods regarding the detection of cystic lesions
- extramedullary space-occupying lesions were depicted in metrizamide cisternography as well as in MR Imaging. The cranio-caudad extent of the disease was delineated better in the sagittal MR slices.
- intramedullary lesions often could only be seen by MRI
- spinal dysraphism was diagnosed by both MRI and metrizamide cisternography. However, because of its invasiveness, cisternography was abandoned during the study in favour of MRI.

Conclusions

MR Imaging of the spinal cord proved to be a rapid, non-invasive method in children. In these patients, MRI should be applied as the method of choice in spinal cord diseases.

References

(1) M.T.Modic, M.A.Weinstein, W.Pavlicek, D.L.Starnes, et al.
Radiology 148, 757-762 (1983)

(2) J.S.Han, B.Kaufman, S.J.El Yousef, J.E.Benson, et al.
AJR 141, 1137-1145 (1983)

(3) J.Groh, P.Baierl, M.Naegele, H.Fendel
submitted to Radiology

Tpm-D7
MR EVALUATION OF MYELINATION PATTERNS IN INFANTS

RB Dietrich, M.D.[1], W G Bradley, Jr., M.D., Ph.D.[2], EJ Zaragoza, B.S., MS IV[1], RJ Otto, M.D.[2], GH Wilson, M.D.[1], H Kangarloo, M.D.[1]
1. UCLA Medical Center, 2. Huntington Memorial Hospital

Previous studies evaluating the brain of infants with MR spin echo pulse sequences suggest isointensity between gray and white matter during the first 6 weeks of life (1,2). Following a transient appearance of white matter hyperintensity relative to gray matter at 4 to 6 months, gray-white differentiation has reportedly reverted to a normal adult pattern at approximately 9 months to 1 year (1). As our preliminary observations were discrepant with these findings, we evaluated 57 children less than 3 years of age. Relative intensity of gray and white matter was evaluated in the regions of the internal capsule, centrum semiovale, frontal and temporal lobes. Clinical correlation was obtained in all cases and developmental delays noted.

Studies were performed using either a 0.3 Tesla permanent magnet or a 0.35 Tesla superconducting magnet and T2-weighted sequences (SE 2000/84) were obtained in all cases. Myelination patterns observed were divided into infantile (white matter more intense than gray matter), isointense and adult (gray matter more intense than white matter). All children less than 5 months of age had the infantile pattern and no child less than 9 months of age had the adult pattern. The age range for developmentally normal children with the infantile pattern was birth to 6.5 months, and for the isointense pattern 5 to 12 months. When developmental delay was present, the infantile pattern extended to 16 months and the isointense pattern to 33 months in this series.

Progression of myelination generally followed established patterns, ie, posterior limb of internal capsule, followed by thalamo optic tracts, followed by posterior centrum semiovale, anterior centrum semiovale and finally temporal lobes. On children scanned sequentially, progression of this pattern was noted.

Using T2-weighted sequences, it is possible to distinguish gray and white matter by MR in infants and to demonstrate early progression of myelination. At birth and generally for the first 6 months, there is a reversal of the normal adult pattern on T2-weighted images, white matter being more intense than gray matter. This pattern passes through a transient isointense stage on its way to the normal adult pattern where white matter is less intense than gray matter. In children scanned sequentially, the isointense zone is noted to proceed in a rostral direction, the temporal lobes myelinating last. When the infantile and isointense pattern persisted into an older age group, there was a significant correlation with developmental delay.

References

1. Holland BA, Haas DK, Norman D, et al. MRI of normal brain maturation. AJNR 7:201-208, 1986.
2. Lee BCP, Lipper E, Nass R, et al. MRI of the central nervous system in neonates and young children. AJNR 7:605-616, 1986.

Tpm-D8

MRI OF THE DISEASED EYE, ORBIT, AND OPTIC CHIASM USING SURFACE COILS AND CONTRAST AGENTS.

A.F. Markl[1], K.G. Riedel[2], R. Oeckler[3], Th. Vogl[1], D. Hahn[1], J. Lissner[1]

Dpts. of Radiology[1], Ophthalmology[2], and Neurosurgery[3], University of Munich, West Germany

Purpose:
Evaluation of the usefullness of paramagnetic contrast agents and surface coils regarding morphological details and the diagnosis of benign and malignant space-occupying lesions in the region of the eye, orbit, and optic chiasm.

Introduction:
MRI has improved the means of investigating the eye, orbit, and optic chiasm. The advantage of MR as a noninvasive method is given up using paramagnetic contrast agents like Gadolinium-DTPA.
The aim of our study was to find out whether the administration of this contrast agent is advantageous over plain MR.

Methods:
More than 135 patients with a wide range of orbital pathology (tumors, inflammatory and vascular diseases) were examined by MR, 89 of them with surface coils of various types. 36 of these patients were scanned before and after administration of intravenous Gadolinium-DTPA.
MR images were obtained by means of a 1.5 Tesla superconductive magnet (MAGNETOM/Siemens), which was run at 0.35 Tesla (12 patients with Gd-DTPA) and 1.0 Tesla (24 patients with Gd-DTPA). The patients were examined using either the head coil (10 patients with Gd-DTPA) or various surface coils of our own design (26 patients with Gd-DTPA). The acquisition matrix size was 256 x 256 pixels. The slice thickness was 5 mm and the zoom factor (hardware zoom) was set to 1.4. Data acquisition utilized 2 averages of the signal. The spatial resolution of the head coil was 1 x 1 x 5 mm, of the surface coil 0.5 x 0.5 x 5 mm.
In all patients the spin echo technique was used with T1- (TR/TE: 600/30) and T2-weighted (TR/TE: 2000/90) pulse sequences. The multi echo sequence (TR/TE: 1600/30-240) was used only in plain MR. Additionally short sequences like FISP and FLASH were used in 5 patients.
The images were measured routinely in transverse and frontal slice orientation, additionally sometimes in paraxial (oblique-sagittal) slice orientation.
The contrast agent was Gadolinium-DTPA-Dimeglumin (Schering), the dosis was 0.1 mmol/kg bodyweight.
Diagnoses were confirmed
a) in tumors by surgical specimen and histology,
b) in inflammatory diseases by clinical data, in some cases by surgery and histology.

Results:
The orbital space-occupying lesions of the patients with administration of Gd-DTPA were separated into 5 groups:
1) 15 cases with primary or secondary intraorbital tumors (choroidal melanomas, capillary hemangiomas, metastases, optic-nerve-sheath-meningeomas etc.), and tumors of the optic chiasm,
2) 14 cases with external tumor infiltration of the orbit (meningeomas, carcinomas from paranasal sinuses etc.),
3) 3 cases with inflammatory diseases (pseudotumor orbitae etc.),
4) 3 cases with vascular disease (orbital varix etc.),
5) 1 case with Graves' disease.

All space-occupying lesions of the orbit and optic chiasm could be identified by plain MR with T1-weighted, T2-weighted and multi echo sequences. Using the paramagnetic contrast agent, most of the tumors, particularly the meningeomas showed a moderate enhancement. But the differentiation of the tumors from the surrounding structures was somewhat better in the contrast scans in comparison to plain MR.
There was a marked enhancement in orbital hemangiomas and in an orbital varix after Gadolinium-DTPA application. These lesions showed in plain T2-weighted images also an increase of signal intensity, but somewhat lower than in the contrast scans. In inflammatory diseases and in Graves' disease the application of Gadolinium-DTPA yielded no significant change of the signal of the pathological tissue except for the case of acute inflammation.

Conclusions:
1) Extent and location of all orbital and chiasmatic space-occupying lesions as well as the differentiation from surrounding anatomical structures could be visualized by plain MR including heavily T2-weighted images (multi echo imaging).
   Particularly the use of surface coils and multiaxial views allowed a better visualization, delineation and differentiation of orbital structures and pathology.
2) Contrast enhanced MR showed sometimes a better delineation between tumor and surrounding anatomical structures in T1-weighted images.
3) Contrast enhancement in tumors seemed to be similar to iodine enhancement on X-ray computed tomography. The amount of enhancement itself yielded additional information over plain MR in identifying the type of tumor (vascular tumors, avascular tumors).
4) The application of paramagnetic contrast agents and the use of short sequences like FISP and FLASH shortened the acquisition time in patients who did not tolerate the long examination times required for plain MR with T1- and T2-weighted sequences and a multi echo sequence.

(Wam-A) SPECTROSCOPY

Presiding: M. Barany & F. Wehrli

10:20 am

RIVER ROOM

12 MINUTES PER PRESENTATION

Wam-A1

THE POTENTIAL IMPACT OF SUSCEPTIBILITY MAPPING ON THE UTILITY OF SPECTROSCOPY

I R Young*, B D Ross+, G M Bydder+, I J Cox+, A G Collins*

*GEC Research Limited, Hirst Research Centre, Wembley, Middlesex HA9 7PP, UK

+NMR Unit, Hammersmith Hospital, London W12 4RS, UK

Purpose of Study The presence of significant susceptibility variations in a number of pathological conditions has recently been reported (1, 2). Because the changes occur over short distances, which are substantially smaller than the dimensions of spectroscopic voxels, they potentially affect the quality of shimming that can be obtained, even with spatial localisation. This study is an attempt to evaluate the likely level of the changes over a significant population, and suggest the likely effects of this problem on spectroscopic studies.
Methods In order to obtain data including the effects of tissue susceptibility, it is necessary to avoid the use of spin echo methods, and to deploy long delayed field echos (3) as the means of recovering information for the reconstruction of images. These images have proved to be useful in their own right (4) and relatively easy to obtain. The phases of each voxel of two images, one with, the other without, delayed acquisition are calculated from the results of two dimensional complex Fourier transformation. The phases are then subtracted, and represents the resultan difference is proportional to $\delta B_j t_D$ where $\delta B_j = (B_{oj} - w_o/\delta)$ [w_o being the frequency to which the system is tuned, Bo_j is the field at the voxel (j) and t_D the relative delay time between the two sequences]. The map of the phases of the individual voxels is then displayed with a sawtooth scale spanning ± 180°. Since the effects being sought are small compared with field inhomogeneities, correction for these is desirable either, as proposed by Faul et al (5), by obtaining a similar map from a large phantom, and subtracting the two, or by using a set of maps obtained at the same time using reduced amplitudes of rf pulses so that some magnetisation is left along the z axis after each interrogation. Different delays are used after each sampling of the magnetisation so allowing easy determination of the development of the field errors, which permits relatively simple unwrapping of the errors. Alternatively a slight modification of the data acquisition allows reconstruction of what is, in effect, a real image (using the form of correction employed for obtaining real inversion recovery images (6)) with the "zebra stripe" appearance used by Edelman et al (2).
Results Analysis of results obtained from the first 80 patients confirms the initial perception that susceptibility effects are associated with blood breakdown products. As a result, lesions where there is no bleeding show negligible changes, whereas regions of hemorrhage display effects, generally, in the range of 0.4 to 1ppm. (Reference (1) suggests that this is the likely range of expectations for the results of hemoglobin degeneration). Measurements from around 40 tumours of various kinds suggest that around one third show no significant effect, one third changes in the range 0 to 0.2 ppm and the remainder in the range 0.2 to 1.0 ppm. Regions of infarction show no significant changes unless they are hemorrhagic, in which case they tend to behave as do other bleeds.
Discussion The effect of these changes on spectroscopic studies is of interest, since they are potentially the same of several artifacts.

1 Short term perturbations of the magnetic field cannot be shimmed out inside the large voxels used in detecting low concentrations of metabolites, resulting in broadened lines and loss of resolution.
2 If the field inside a voxel is such that one part of the voxel is in one field while the rest is in another, lines may be split - giving the appearance of spin-spin coupling effects which are spurious.
3 In proton spectroscopy, where solvent suppression is necessary, whatever procedure is chosen will be less efficient than it should be, and the choice of the frequency to be used as the centre frequency for the experiment is uncertain.

4 Selective saturation or excitation techniques may fail to a greater or lesser extent.
5 Because of the uncertainty as to whether all the spatial lines being used in an analysis are from regions in the same field, there must be care, for example, in such things as making assessments of tissue pH. However, the information to be gained from observation of susceptibility effects is not negligible, and can offset the relative lack of efficiency of the spectroscopic experiment. The problems are potentially more worrying with high resolution spectroscopy, such as that of the proton, and may only occur in some pathological conditions.

References
1 Cox I J, Bydder G M, Gadian D G, Young I R, Williams S R, Proctor F, Hart I, J.Mag. Res. (in press) (Oct. 1986)
2 Edelman K R, Johnson K, Buxton R, AJNR (in press) (1986)
3 Edelstein W A, Hutchison J M S, Johnson G, Redpath T, Phys. Med. Biol. 25, 751-756 (1980)
4 Young I R, Payne J A, Collins A G, Bydder G M, Mag Res. Mid. (in press) (March 1987)
5 Faul D, Abert J, Margosian P, Radiology 153P, 303 (1984)
6 Young I R, Bailes D R, Bydder G M, Mag. Res. Med. 2, 81-85 (1985)

Wam-A2
IMPROVING RESOLUTION IN SPECTROSCOPY through T2 DECONVOLUTION

E.M. Haacke [1], Z.-P. Liang [2] and J. Tkach [2]

Case Western Reserve University, Departments of Physics and Radiology [1], Department of Biomedical Engineering, [2] Cleveland, Ohio 44106

Recent developments in image reconstruction (1,2) have made it possible to account for the effects of low T2 values in the image. These effects include a loss of resolution, a change in contrast and an introduction of systematic noise. Fortunately, in spectroscopy the major effect is the increase in linewidth (or full width half maximum) of the point spread function or equivalently the loss of resolution in the spectra.

When two lines overlap, the area calculation normally used to estimate the spectral value is further complicated by the need to extrapolate the spectra into the overlap region. Recall that the intensity is conserved in the presence of T2 decay if the area of the spectra is used. If several lines overlap, the extraction becomes more suspect. Actual spectral values also depend on the starting point of the measurement, so that the correct relative determination of several lines depends on the time of the first sampled point.

The Fourier transform reconstruction technique does not account for the T2 decay and hence the above problems arise. By using a matrix or generalized transform approach, the T2 effects can be accounted for. For example, the signal can be written as s=Mp where M is the usual discrete Fourier transform matrix and p is the discrete spectral line contribution for a finite number of points. Before T2 broadening the linewidth is taken to be zero. By taking 2N sample points and reconstructing two separte spectra from the first N and second N points, the T2 values can be estimated. Using these estimates, T2', M is modified to M' where

$$(M')_{lm} = (M)_{lm} \exp(-l\Delta t / T2'(max))$$

where Δt is the sampling interval and Δx is the resolution or spatial sampling. Now the estimate for p is $(M')^{-1}s$ and after iteration to update T2' no overlap of the spectra occurs.

This technique has been applied to various spectral data to illustrate the separation. The method is shown to be insensitive to the first sampling point. Extension to zero time is also considered. In particular, the phosphorus ATP spectra are significantly improved since the T2 values are several to tens of milliseconds and the sampling times are tens of milliseconds.

(1) E.M. Haacke. The effects of finite sampling on image quality in MRI. SMRM abstract, 1986.

(2) E.M. Haacke. Solving for non-ideal conditions in 2DFT imaging. Submitted to Inverse Problems.

Wam-A3
QUADRATURE SPECTROSCOPIC IMAGING WITH A STATISTICAL PHASE CORRECTION METHOD*

C.B. Ahn, O. Nalcioglu and Z.H. Cho

Department of Radiological Sciences, Division of Physics and Engineering
University of California - Irvine

Quadrature spectroscopic imaging (QSI), which is a variation of Dixon's method [1], for separate water/fat imaging with a single scan was introduced by several investigators [2,3]. A description of the method and pulse sequence can be found in reference [3]. The essential part of image reconstruction is how to decompose the water and fat signals orthogonally along the real and imaginary axes. However, in a real NMR system such decomposition may not be easy to achieve due to various systematic errors such as the first and zero order phase errors and external field inhomogeneity.

In a previous study [3], we had used an external phantom of single composition (i.e. water) which was attached to the scanned object. The first and zero order phase corrections were performed based on the phase obtained from the phantom.

We found out that the above technique works well if a small phantom is attached to the surface of the scanned object and the field homogeneity is high. In the present work, we applied a statistical phase correction method which utilized autocorrelation and histogram analysis. A description of the algorithm is given in reference [4]. Here we will briefly describe the application of the algorithm to the QSI technique. The reconstructed image ρ in the QSI method can be written as,

$$\rho(x,y) = (w(x,y) + iF(x,y)) \exp(i(\phi_0 + x\varepsilon_1)) \qquad (1)$$

where W and F denote respective water and fat distributions. In equation (1), ϕ_0 and $x\varepsilon_1$ indicate the zero and first order phase errors. The variables ε_1 and ϕ_0 can be estimated by the autocorrelation and histogram analysis. Then W(x,y) and F(x,y) can be obtained by dividing ρ (x,y) by the estimated phase terms and separating the real and imaginary parts of the resultant function.

An example of the application of the new phase correction method is shown in Figure 1. The real and imaginary parts of the reconstructed image without any phase corrections are shown in Figures 1.a and 1.b. The magnitude image obtained from Figs. (1.a-b) is shown in Figure 1.c. Note that the first and zero order phase errors cause a sinusoidal modulation of the intensity in the image (Fig. 1.a-b). The separated water and fat images after the statistical phase correction are shown in Figures 1.d and 1.e respectively. Finally, Figure 1.f shows the phase histogram computed from the phase corrected images. Two conspicuous peaks which are 90° apart are well expected and correspond to the orthogonal phases of water and fat. Figure 2 is an example of application of the statistical phase correction technique to the knee joint of a human. All the images given in the current investigation were obtained with a 0.6T whole body scanner.

Since the phase error terms are determined from regions of interest in a statistical fashion, the new technique also appears to be more robust to external field inhomogeneity effects as well as the inherent signal-to-noise ratio.

*This work was supported in part by PHS Grant No. 1R01-CA41307 awarded by the NCI, DHHS.

References

1. W.T. Dixon, Radiology 149, 238(1983).
2. Z. Paltier and A. Ban, Proc. SMRM Annual Meeting, p. 172(1985).
3. C.B. Ahn, S.Y. Lee, O. Nalcioglu and Z.H. Cho, Mag. Res. Imag. 4, 110(1986).
4. C.B. Ahn and Z.H. Cho, "A New Phase Correction Method in NMR Imaging Based on Autocovariance and Histogram Analysis". To be published in IEEE Trans. Med. Imag. (1987).

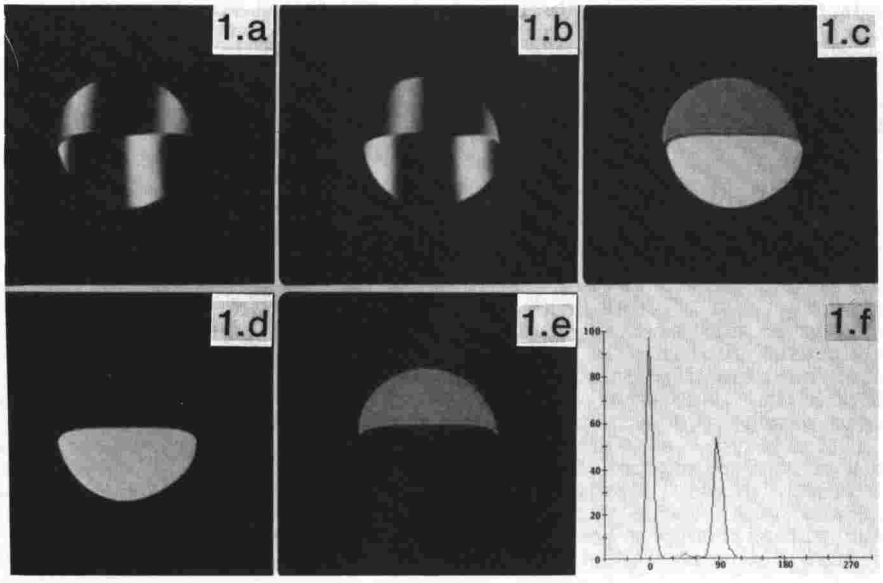

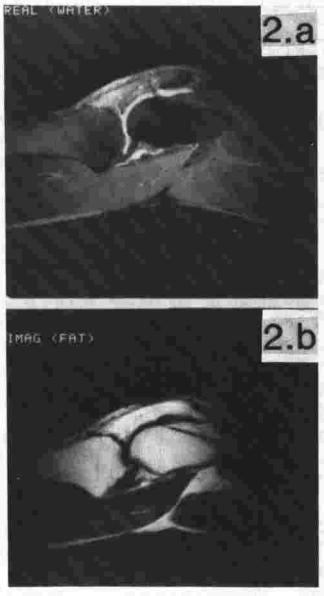

Wam-A4
MULTINUCLEAR HUMAN MR SPECTROSCOPY

M. Bárány, D.G. Spigos, T.M. Grist*, E. Mok, and P.N. Venkatasubramanian

Department of Biological Chemistry and Magnetic Resonance Center, College of Medicine, University of Illinois at Chicago, IL. 60612, and *Department of Radiology, Medical College of Wisconsin, Milwaukee, WI. 53226

^{1}H, ^{31}P, and ^{23}Na MR spectra were recorded from live human tissues using the General Electric (GE) SIGNA MR scanner. The pulse programs used are described in the GE spectroscopy research accessory manual. Surface coils were obtained from either GE or Medical Advances, Inc. Depth resolved spectra were recorded following the procedure of Bottomley and collaborators (1). An extra-sensitive remote control box was enabled in order to shim on the tissue slices. The 12 shim controls were adjusted to obtain a water peak with a line width of 0.075 ppm. In human tissues, the line width of the water signal ranged from 0.17 to 0.55 ppm using the Z, X, Y, and $X^2 - Y^2$ shim controls.

The SPECSUP2.PSD program was optimized for ^{1}H spectroscopy by decreasing the spectral width and increasing the τ value so that the spectra could be phased without the use of magnitude calculation. The standard solution, 100 mM creatine, exhibited two resonances: 2.98 ppm for the $N-CH_3$ and 3.88 ppm for the $N-CH_2$ (with reference to the water resonance at 4.77 ppm). The exchangeable amino protons of creatine which resonate at 6.71 ppm (2) were not visible in the spectrum. Furthermore, the creatine spectrum was free of artificial peaks.

The extent of water suppression in human tissues was estimated from the ratio of the area under the water peak to that of the fat peak. Without water suppression, SPECFID.PSD, this ratio ranged from 15 to 40. With water supression, SPECSUP2.PSD, the ratio was less than 1 and frequently was as low as 0.1.

With good water suppression, the ^{1}H spectrum showed resonances from metabolites in spite of the presence of a major resonance from the repeating $-CH_2-$ protons of neutral fat. Thus, in the aliphatic region of spectra obtained from leg muscle, resonances from creatine, choline, β-alanine in carnosine, glutamine, and taurine (3) were seen (Fig. 1). In the aliphatic region of a liver spectrum, the minor resonances were derived from aspartate, creatine, carnitine, taurine, glutamate, and glutamine.

The total fat and fatty acid content in human liver was quantitated as follows: To eliminate any contribution from subcutaneous fat, a small receiver coil was used such that all the fatty acyl chain resonances originated only from the liver. In fully relaxed spectra we compared the integers of protons under the fatty acyl chain peaks relative to the water peak. Since the water content of the liver is 75 percent and the distribution of saturated and unsaturated fatty acids in liver is known, we were able to calculate that there are 43 g fatty acyl chains per kg normal human liver. Furthermore, ^{31}P spectroscopy on the same liver revealed the presence of a high concentration of glycerol-3-phosphorylcholine (GPC), suggesting that a considerable portion of the fatty acyl chains is in the form of free fatty acid.

In the ^{31}P spectra of healthy human leg, GPC, a marker for human muscular diseases (4), has been clearly resolved. The average pH value in normal human muscles, calculated from the chemical shift of P_i, was found to be 7.1. However, in the muscle of a patient with osteosarcoma the pH was elevated to 7.4. In the same muscle the resonance of ATP-β-P was at -21 ppm as compared to 19.2 ppm for normal muscle, suggesting a lack of Mg^{2+} in the muscle containing the bone tumor.

A $^{1}H/^{23}Na$ double coil prepared by one of us (T.M.G.) was used to record ^{23}Na spectrum of human brain. The ^{23}Na resonance appeared as a single peak with a line width of 1 ppm (Fig. 2).

We thank the enthusiastic assistant of S.D. Thomas, K.M. Pazdra, S.M. Ringquist, J.T. Henderson, and A. Lukas (supported by MDA, CTR, and RRC of UIC).

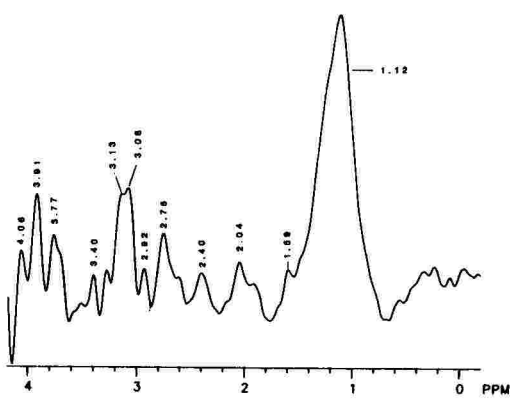

Fig. 1. ^{1}H spectrum of human leg

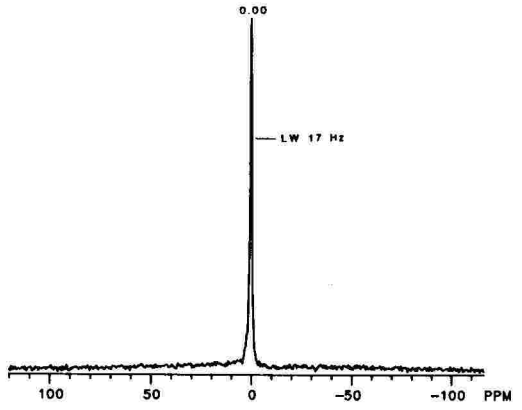

Fig. 2. ^{23}Na spectrum of human brain

References: (1) P.A. Bottomley, et al., J. Magn. Reson. 59, 338, 1984.
(2) C. Arús, et al., FEBS Lett. 165, 231, 1984.
(3) C. Arús and M. Bárány, Biochim. Biophys. Acta 886, 411, 1986.
(4) M. Bárány and T. Glonek, in Phosphorus-31 NMR (D. Gorenstein, ed.) p. 511, Academic Press, 1984.

Wam-A5

QUANTITATIVE ANALYSIS OF FATTY LIVER USING SPECTROSCOPIC IMAGING BY DEPHASING AMPLITUDE CHANGING (SIDAC)

K. Ohtomo, K. Yoshikawa, M. Minami, M. Iio,[1] S. Yamada,[2] T. Miyazaki, N. Iriguchi, T. Maki.[3]

1) Dept of Radiology, Univ. of Tokyo. 2) Dept of 1st Internal Medicine, Univ. of Tokyo.

3) Asahi Chemical Industry Co., Ltd.

Experimental rat model of fatty liver (ethanol and cholesterol induced) was evaluated by a new developed simple technique for spectroscopic imaging, "spectroscopic imaging by dephasing amplitude changing (SIDAC)" 1).

In this technique, one spatial axis is encoded dually with frequency and phase and chemical shift is distinguished and consequently spectrum corresponded to each pixel on an image can be obtained. Sixteen images of rats in which the frequency changes stepwise by 0.79 ppm were obtained and fat to water ratio (F/W) was calculated from "in vivo" spectroscopy and then compared to "in vitro" F/W obtained by FT-NMR spectroscopy. "In vivo" F/W values ranged from 0.07 (normal) to 0.25 (cholesterol induced fatty liver) and well corresponded to "in vitro" F/W values (r=0.8). These values were also compared to the water and fat content within liver tissue and histologic correlation was also attempted. Our results suggest that this new technique is a promising method for quantitative analysis of fatty liver.

1) T. Miyazaki et al.:Presented at the 5th meeting of SMRM, '86.

Wam-A6

STATE-OF-THE-ART OF CLINICAL ^{31}P NMR SPECTROSCOPY IN HUMAN DISEASE

Paul A. Bottomley

General Electric Corporate Research and Development Center, Schenectady, New York 12301

A review of the current status of clinical applications of *in vivo* ^{31}P spectroscopy to human disease is presented, based on a survey of the published literature dating from the initial studies on McArdles syndrome in 1981. The principle findings are reported classified by organ and by pathology and observations of metabolic disturbances noted. It is found that a surprisingly large amount of clinical data is available for human muscular metabolic disorders (McArdles Syndrome, amyloglucosidase deficiency, phosphofructokinase deficiency, postviral exhaustion/fatigue syndrome, mitochondrial myopathies, NADH-CoQ reductase deficiency, Duchenne muscular dystrophy), human brain disorders (neonatal birth asphyxia, meningitis, congenital abnormalities, hypotonia, hyaline membrane disease, polycythaemia, septicaemia; mitochondrial encephalomyopathy; chronic cerebral infarction; adult degenerative diseases; brain tumors), human heart disorders (cardiomyopathy, anterior myocardial infarction), and many other human tumors. The studies suggest that ^{31}P spectroscopy provides diagnostically and prognostically useful information for some of the muscular metabolic disorders and neonatal cerebral disorders. While disturbances in tumor metabolism are often observed, these may vary from tumor to tumor. Variations in tumor metabolism with therapeutic intervention offers hope for the application of spectroscopy to monitor the efficacy of therapy, although specific responses may again vary with tumor type.

Wam-A7
PULSE SEQUENCE FOR DEPTH RESOLVED PROTON SPECTROSCOPY FOR DETECTION OF LACTATE

P.A. NARAYANA, W.W. BREY, D.J. JENSEN AND M.V. KULKARNI

DEPARTMENT OF RADIOLOGY, UNIVERSITY OF TEXAS MEDICAL SCHOOL, HOUSTON, TX

In vivo high resolution MR spectroscopy has a high potential to yield detailed information about the tissue metabolic activity. The two major problems encountered in exploiting this potential are: 1) localizing the region of interest and 2) detecting weak metabolite signals in the presence of strong water and lipid resonances. A number of spectral editing techniques have been proposed to selectively detect the metabolites of interest. In particular the detection of lactate resonance has attracted considerable attention(1,2) because of its important role in tissue metabolism. Of all these spectral editing techniques for detecting lactate, the method proposed by Williams, Gaidan and Proctor (2) has the advantage of using a single RF irradiation. These authors used this method to detect lactate from the rat brain relying on the surface coil RF profile alone for localization. However, surface coil alone provides inadequate localization. Since a good localization is an integral part of in vivo spectroscopy experiments, it is essential to combine the spectral editing techniques with efficient localization schemes. In this work we report the results of the combination of spectral editing proposed by Williams et al(2) with the water suppressed localization sequence(3) based on the one dimensional version of the spatially resolved spectroscopy sequence(4).

The two basic sequences used for observing the lactate doublet signal from a localized region are shown in Fig. 1. Each of these two sequences can be divided into a preparation part and a read part. The preparation part along with the surface coil provides the localization by leaving the magnetization from the selected region along the z-direction. The read sequence contains either a full water suppression sequence $1\bar{3}3\bar{1} - \tau - 2\bar{6}6\bar{2} - \tau$(echo) (Fig. 1a) or only one pulse providing the suppression viz. $1\bar{3}3\bar{1} - \tau - 180^0 - \tau$(echo) (Fig. 1b). By properly adjusting the parameters in the read sequence, it is possible to selectively observe the lactate resonance(2).

All the experiments were performed on a 2T imager/spectrometer built in our laboratory. A 15 cm slotted tube resonator was used to provide uniform excitation over the whole sample. A 2 cm diameter surface coil etched on a printed circuit board was used as the receiver coil. The two coils were decoupled from each other using crossed diodes. The performance of this sequence was tested on a gelatin-fat phantom (5% fat by weight) doped with 0.05 mM of MnCl2 and 10 mM of sodium lactate.The RF frequency was centred on the water resonance. The region of interest was determined by obtaining the proton MR image using a standard 2D FT spin warp technique. The separation T between the pulses in the sequence $1\bar{3}3\bar{1}$ (and $2\bar{6}6\bar{2}$) was chosen such that the CH2 lipid frequency was off resonance by 1/2T. An echo time of 136 ms was chosen. This corresponds to 1/4J where J is the coupling between the CH3 and CH protons of lactate (J=7.35 Hz). To minimize the effects of RF inhomogeneity, spectra were recorded using these two sequences with phase cycling based on Exorcycle scheme. Sequence 1a yields a spectrum with the lactate doublet out of phase with the rest of the spectrum while sequence 1b produces a spectrum with the lactate doublet in phase with the rest of the spectrum. Addition of these two spectra, therefore, should give a single line. As expected, a single line at 1.3 ppm (water assumed to be at 4.7 ppm) from the lactate CH proton was observed. The origin of this line was further confirmed by repeating these experiments with a second gelatin-fat phantom without any lactate. These experiments demonstrate that it is possible to selectively observe resonances from weak metabolites from a localized region of interest.

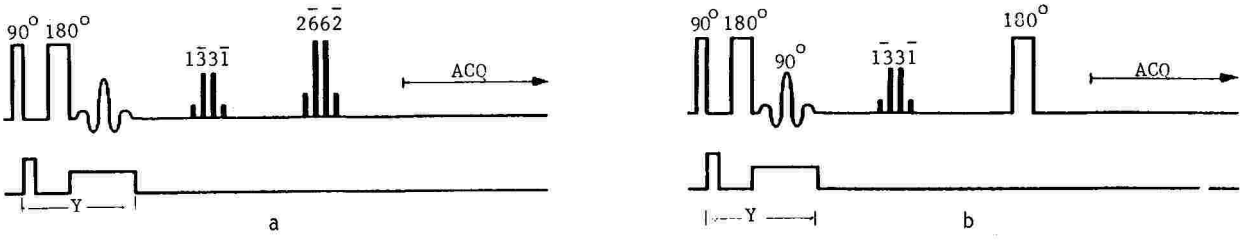

FIGURE 1

REFERENCES

1. H.P. Hetherington, M.J. Avison and R.G. Shulman, Proc. Natl. Acad. Sci. USA 82, 3115 (1985).
2. S.R. Williams, D.G. Gadian and E. Proctor, J. Magn. Reson. 66, 562 (1986).
3. P.A. Narayana, D.J. Jensen, W.W. Brey and M.V. Kulkarni, Mag. Res. Med. (communicated).
4. P.R. Luyten, A.J.H. Marien, B. Sijitsma and J.A. den Hollander, J. Magn. Reson. 67, 148 (1986)

Wam-A8
IN VIVO ^{19}F NMR STUDY OF HALOTHANE ELIMINATION FROM THE RABBIT BRAIN USING THE ISIS SPATIAL LOCALIZATION TECHNIQUE

C.H. Sotak, Ph.D.,[1] W.M. Chew, B.S.,[2] P.A. Mills, Ph.D.,[2] M.E. Moseley, Ph.D.,[2] and L. Litt, M.D.,Ph.D.[2]

General Electric NMR Instruments, Inc., Fremont, California;[1] Department of Radiology, University of California, San Francisco, California[2]

Spatially localized ^{19}F spectroscopy was used to evaluate washout of halothane from the adult rabbit brain to corroborate data previously obtained from a surface coil preparation.[1] Localized spectra were obtained using a modified version of the ISIS technique[2] in which all slice selective gradients remain on and only the amplitude of the associated rf pulses are cycled on and off during the course of the sequence. This results in constant eddy current effects from one scan to the next. The ISIS technique was chosen over spin echo-based localization methods because of the short T_2 value of halothane in the brain (3 msec).

Localized spectra were obtained from the brain of a 3 kg NZW rabbit using a 4 inch, low pass, birdcage design coil that could be tuned to either ^{1}H or ^{19}F. Following 3.5 hours of 1.5% halothane administration, baseline spectra were collected. Halothane was then discontinued and the localized ^{19}F spectra collected as a function of time. A coronal proton image through the brain served to locate the regions of interest for localized ^{19}F spectroscopy. Spectra were obtained from 8 cm^3 (2 cm X 2 cm X 2 cm cube) volumes in the brain and in a region containing primarily subcutaneous fat. Data was alternately collected for 10 minute intervals from each region for a period of 100 minutes. A logarithmic plot of relative halothane peak areas versus time was used to determine the $t_{1/2}$ for the halothane washout in the different compartments.

The ^{19}F signal from the brain decreased rapidly ($t_{1/2}$=1 hour) compared with that obtained from the region containing primarily subcutaneous fat ($t_{1/2}$=3 hours). The relative differences in washout rates between the two regions is similar to that obtained by surface coil methods and suggests that the spectra arise from the desired regions of interest. ISIS appears to be a useful noninvasive method for monitoring halothane washout rates from different areas of the rabbit brain in vivo.

1. W.M. Chew, M.E. Moseley, P.A. Mills, D.I. Sessler, R. Gonzalez-Mendez, T.L. James, and L. Litt, Magnetic Resonance Imaging, in press, 1986.

2. R.J. Ordidge, A. Connelly, and J.A.B. Lohman, Journal of Magnetic Resonance, 66, 283 (1986).

(Wam-B) BODY-CONTRAST AGENTS

Presiding: A. Lupetin & P. Hahn

10:20 am

ROOM C-107

12 MINUTES PER PRESENTATION

Wam-B1
GD-DTPA CONTRAST ENHANCEMENT IN CONVENTIONAL AND FAST MR-IMAGING OF MEDIASTINAL MASSES

D. Hahn, M. Nägele, K. Seelos, J. Lissner

Dept. of Radiology, University of Munich

The diagnostic value of Gadolinium-DTPA as an i.v. contrast medium was tested in 25 patients with mediastinal masses. In all patients conventional spin-echo images were compared with such aquired at reduced echo delay times or by using different flip angles in gradient echoes. Signal intensity measurement was obtained in every sequence before and after application of contrast medium to evaluate the relative enhancement rate in tumor tissue, fat, muscle and bone marrow. The uptake of contrast medium in benign masses was significantly lower than in malignant masses. High enhancement allowed a better differentiation of solid, liquid and necrotic tumor lesions. Due to a high relative enhancement of mediastinal masses there was a loss of contrast in

comparison to the sourrounding fat. The differential diagnosis of an occlusion of mediastinal veins by a thrombus or a mass was possible by using Gd-DTPA. The contrast between lung tissue and pleural effusions seemed to be better with short echo delay. Fast imaging with a TE of 17 msec delivered optimal delineation of mediastinal structures.

Wam-B2

RENAL CORTICAL PERFUSION: CORRELATION OF RADIONUCLIDE MICROSPHERE INJECTION WITH CONTRAST ENHANCED RAPID SEQUENCE MRI

W.A. Erdman, J.C. Weinreb, B. Barker, R.M. Peshock, C. Chaney, and K. Maravilla

Departments of Radiology and Internal Medicine, The University of Texas Health Science Center at Dallas, TX

Although bolus gadolinium DTPA and rapid sequence (FLASH) images have been shown to have physiologic-like signal versus time curves in the renal cortex, these results have not been quantified. We evaluated renal cortical perfusion by both MRI (0.35T) and radionuclide microsphere injection in four laboratory dogs before and after unilateral renal artery balloon occlusion. Relative changes in renal cortical perfusion, documented by radionuclide, were reliably correlated with MRI (TR 50/TE 9, 45° flip angle, 6 sec slice) signal intensity only in the images obtained in the first 24 seconds after gadolinium injection (0.1 mg/kg IV bolus) (Fig. 1). Subsequent images were less sensitive to small changes in perfusion owing to increased contribution from glomerular filtration with time. Spin echo (SE) and inversion recovery (IR) sequences showed virtually no change in general appearance (or corticomedullary junction) for up to one hour after renal artery occlusions (Fig. 2). ''Flow sensitive'' FLASH type non-sequential images (TR 50/TE 9, 45° flip angle, 20 acquisitions) without Gd-DTPA, as well as gated end-systolic-end-diastolic images, were also unsuccessful in documenting changes in renal cortical perfusion. We conclude that acute (i.e., less than 60 min) changes in renal cortical perfusion are not reflected in appearance of the corticomedullary junction, but may be evaluated by rapid sequence contrast enhanced MRI.

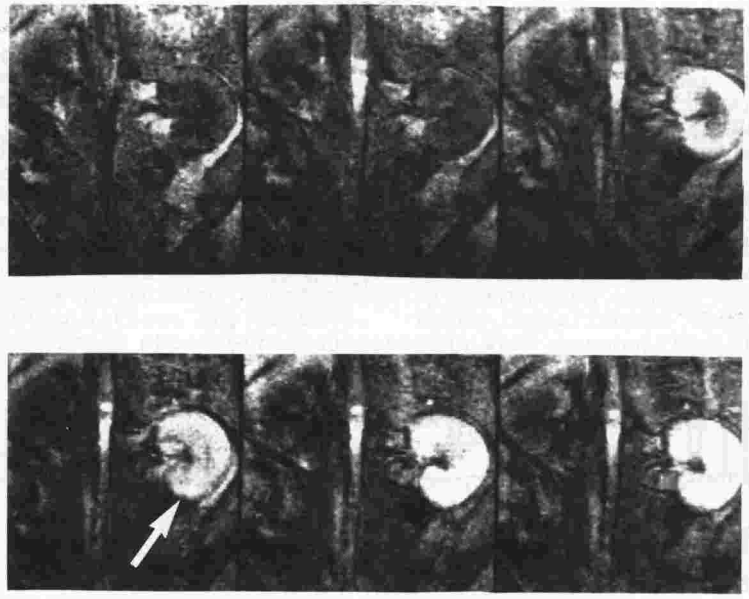

FIGURE 1
Post gadolinium DTPA sequential FLASH (TR 50/TE9, 45° flip angle, 6 sec/slice acquisition time with 6 second interval between acqusitions). Images in laboratory dogs obtained with right renal artery occlusion. Note increased signal in renal medulla indicative of of Gd-DTPA filtration on the left (normal side) 24 seconds after injection (arrow).

FIGURE 2
High resolution (0.9mm X 0.9mm). Thin section (5 mm) SE 0.5/30 coronal image of a laboratory dog 30 min after balloon occlusion of right renal renal artery (arrow). Note normal appearance of cortical medullary junction bilaterally.

Wam-B3

ASSESSMENT OF MYOCARDIAL PERFUSION IN VIVO USING NUCLEAR MAGNETIC RESONANCE IMAGING

S. Schaefer, R.M. Peshock, P.V. Kulkarni, J. Katz, C.R. Malloy, R.W. Parkey, J.T. Willerson

The Departments of Cardiology and Radiology, The University of Texas Health Science Center at Dallas

We examined the use of nuclear magnetic resonance imaging in the assessment of myocardial perfusion. A new paramagnetic contrast agent, manganese-gluconate (Mn-Glu), was prepared and its relaxation properties in solution and in rat myocardium were measured. Using these data, conditions to optimize contrast between normally perfused (NP) and hypoperfused (HP) myocardium were determined. Imaging studies were then performed using Mn-Glu in an in vivo canine model of acute left anterior descending coronary artery (LAD) occlusion.

RESULTS: In solution, the relaxation properties, $\Delta R1/C$ and $\Delta R2/C$, of Mn-Glu were 7.8 and 41.6 sec^{-1} mM^{-1} respectively. The T1 of normal rat myocardium was markedly shortened with administration of low doses of Mn-Glu with relatively small changes in T2, whereas significant T1 and T2 shortening was seen at higher doses (0.1 mM/kg). After true or sham LAD occlusion and injection of 0.1 mM/kg Mn-Glu, 6 dogs were imaged in vivo using a gated, T2-weighted spin-echo sequence. All dogs with occlusion demonstrated a reduction in intensity in the NP myocardium consistent with T2 shortening with no change in the HP myocardium (Fig. 1) resulting in a contrast ratio of 2.1 ± 0.6 ($p < .001$ vs control). A typical sequence of images is shown in Figure 2. Four dogs were then given 0.035 mM/kg Mn-Glu and imaged using a heavily T1-weighted short TR sequence. Under these imaging conditions, NP tissue showed increased intensity consistent with T1 shortening in the normal myocardium, resulting in a contrast ratio of 0.54 ± 0.16 ($p < .01$ vs control). Hence, nuclear magnetic resonance imaging with Mn-Glu can be used to detect myocardial perfusion abnormalities in vivo in a canine model of acute coronary occlusion.

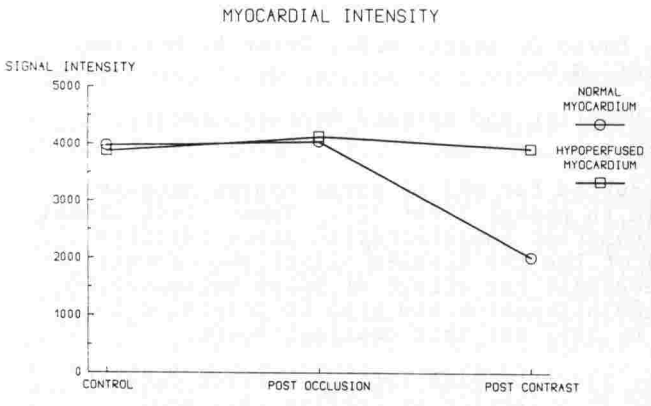

Figure 1. Signal intensity of normal and hypoperfused myocardium during control and post occlusion periods, and then following administration of 0.1 mM/kg Mn-Glu (post contrast). Delivery of the contrast agent to normal myocardium markedly shortened its T2 relaxation time and its signal intensity.

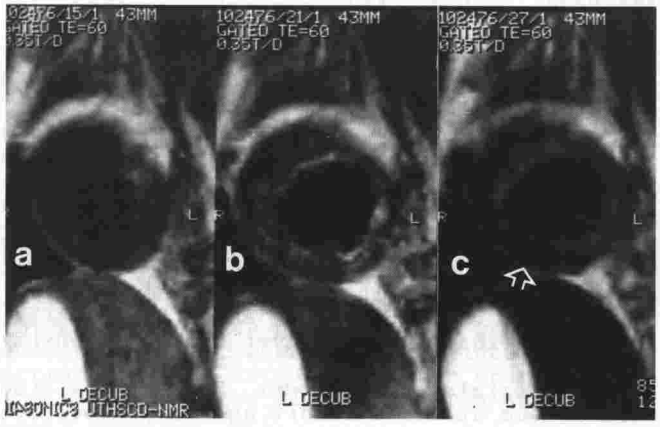

Figure 2. (a) Control, (b) post occlusion, and (c) post contrast short axis images with acute coronary occlusion. The arrow indicates dark, normally perfused myocardium, with hypoperfused myocardium retaining its normal signal intensity.

Wam-B4

CONTRAST ENHANCED GATED IMAGING OF RAT MYOCARDIUM

P. Pflugfelder, M.D.; M. Wendland, Ph.D.; S. Quay, M.D., Ph.D.; W. Holt, M.D., Ph.D.; N. Derugin, M.A.; C.B. Higgins, M.D.

Department of Radiology, University of California, San Francisco, California

Magnetic resonance imaging (MRI) offers significant potential for the assessment of myocardial disease; however, its ability to estimate myocardial perfusion has not been established. Paramagnetic contrast media tested up to now are rapidly removed from the myocardium and are unreliable for defining myocardial perfusion on gated spin echo images. A contrast medium causing prolonged steady state enhancement is needed as a marker of myocardial perfusion for MRI. A new tetraphosphonate chelate of manganese (MnTP) was tested as a paramagnetic agent for myocardial perfusion imaging.

Adult Sprague-Dawley rats (250-350 gm.) were anesthetized with sodium Pentobarbital (50 mg/Kg IP). Following tail vein canulation the animals were positioned within a GE 2-Tesla Imager/Spectrometer. Imaging was performed with coronal sections using a cardiac gated spin-warp imaging sequence. Four minute images were acquired with a slice thickness of 3 mm, TE 20 msec and a 10 msec delay after R wave triggering. TR ranged from approximately 190 msec to 270 msec. Signal intensity was measured for regions of interest over the left ventricular wall, the liver and an oil standard which was used to normalize tissue data. Images were obtained immediately preceding contrast injection (50 micromol./Kg IV) and at subsequent 10 minute intervals for an additional 60 minute period. Subsequently, after sacrifice T-1 values (myocardial and hepatic-following contrast) were measured in excised tissue using an NMR spectrometer.

Preliminary analysis indicates that myocardial signal intensity is enhanced 40 to 88% above the non-contrast baseline, reaching a peak in the initial 20 to 40 minutes after contrast injection and maintaining enhancement at those levels for the remainder of the experiment. The liver was enhanced to an even greater extent reaching a maximum of 133%. In excised myocardial tissue (post-contrast), T-1 value was reduced to approximately half that of normal.

Thus, MnTP significantly enhanced myocardial tissue signal intensity to a plateau level extending over 60 mins. Since enhancement is maintained for a prolonged period, this agent has considerable potential as a myocardial perfusion agent for MR imaging.

Wam-B5

CONTRAST ENHANCED MRI OF LIVER CANCER USING FERRITE PARTICLES: PULSE SEQUENCE AND DOSE ANALYSIS

Sanjay Saini, M.D., Peter F. Hahn, M.D., Ph.D., David D. Stark, M.D., Peter R. Mueller, M.D., Joseph F. Simeone, M.D., Joseph T. Ferrucci, M.D.

Department of Radiology, Massachusetts General Hospital and Harvard Medical School, Boston, MA 02114

Introduction: Ferrite particles are well suited for MRI of liver cancer because they are sequestered exclusively by the RE cells in normal liver (1). Tumor-liver signal differences should therefore be enhanced after contrast administration since ferrites will alter signal intensity only in one (liver) of the two tissues (liver and cancer) being compared. This study was undertaken to evaluate the effect of pulse sequences on tumor-liver contrast before and after ferrite administration and also to determine the ED_{50} (dose that reduces liver signal intensity by 50%) for this contrast agent.

Materials and Methods: Five female Fisher 344 rats with implanted liver cancer were imaged at 1.4 T before and 15 minutes after IV injection of ferrite (0.1 mmol Fe/kg). T1-weighted pulse sequences (SE 250/15/6 and IR 1500/450/15/2), mixed T1-T2-weighted pulse sequence (SE 500/30/3), and T2-weighted pulse sequence (SE 1500/60/2) were utilized. Tumor-liver signal difference/noise ratio was calculated using an operator determined region of interest.

Ten normal rats were imaged at 0.6 T with a SE 500/30/4 pulse sequence before and after administration of varying doses (0-114 micromol Fe/kg) of ferrite. The ED_{50} was thereby calculated.

Results: Pulse sequences with T2-weighting (SE 1500/60 and SE 500/30) showed marked enhancement of tumor-liver signal differences after ferrite injection, whereas T1-weighted pulse sequences (SE 250/15 and IR 1500/450/15) reduced tumor-liver signal differences (Table I). Although the maximal post ferrite tumor-liver signal difference was seen on SE 1500/60, considerable contrast was present on SE 500/30. "Greying" of normal liver parenchyma on this pulse sequence allowed precise anatomic definition which was obscured at higher doses and/or with more T2-weighted pulse sequences where liver "blackening" and increased motion artifacts were present. The ED_{50} for the SE 500/30 pulse sequence was 8 micromol Fe/kg (Figure 1).

Conclusion: Although maximal tumor-liver signal differences occur with higher doses of ferrite and with heavily T2-weighted pulse sequences, there is considerable latitude in pulse sequence timing parameter selection for ferrite enhanced MR imaging of liver cancer. Any pulse sequence with T2 dependent contrast will be suited for ferrite enhanced MRI of focal liver disease. A mixed T1-T2-weighted pulse sequence may, in fact, be superior to a more heavily T2-weighted pulse sequence because greater signal averaging is possible with the former which reduces motion artifacts in upper abdominal imaging (2).

Tumor-Liver Signal Differences After Ferrite

	Signal Intensity/Noise				% △ SD
	Pre		Post		
	Liver (L)	Tumor (T)	Liver (L)	Tumor (T)	(T-L)/N
SE 1500/60	9.2	22.8	4.6	25.8	+56
SE 500/30	15.9	17.0	12.0	21.8	+791
SE 250/15	21.6	17.9	15.5	18.6	-16
IR 1500/450/15	9.7	3.7	8.5	4.6	-35

(SD = signal difference)
%△SD = % change in tumor-liver signal after ferrite $\frac{(post-pre)}{pre}$
+ indicates increase in contrast
- indicates loss of contrast

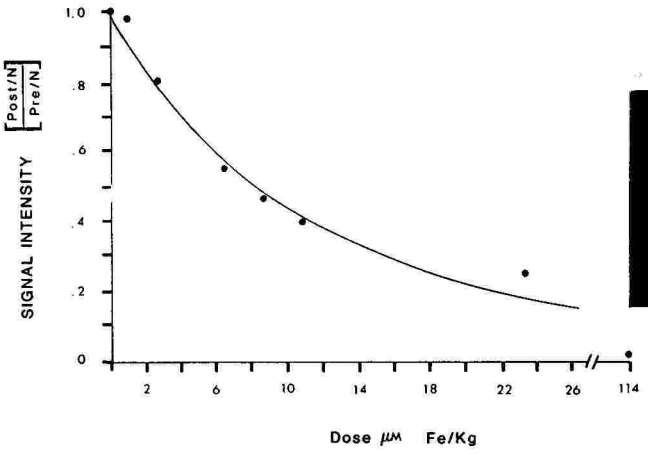

FIG. 1: There is an exponential decrease in liver SI after ferrite. ED_{50} = 8 micromol/kg.

Reference:
1. Saini S, Ferrucci J, Stark DD: Radiology (in press).
2. Stark DD, Wittenberg J, Ferrucci JT, et al: Radiology 159:365-370, 1986.

Wam-B6
DOUBLE CONTRAST MR IMAGING OF LIVER CANCER

Ralph Weissleder, M.D., Sanjay Saini, M.D., David D. Stark, M.D., Peter F. Hahn, M.D., Ph.D., Ernst Rummeny, M.D., Jean-Claude Bousquet, M.D., Joseph T. Ferrucci, Jr., M.D.

Introduction: Early studies indicate that MR contrast agents can improve the detection of liver cancer (1). Paramagnetic gadolinium-DTPA is an extracellular agent which requires imaging early in the post-contrast infusion period using heavily T1-weighted pulse sequences (2). Superparamagnetic ferrites (Fe_3O_4 particles) show specificity for hepatic reticuloendothelial cells and have less rigid timing and pulse sequence requirements (3). Gadolinium-DTPA and ferrites have opposing effects on liver signal intensity. As a T1 agent, gadolinium-DTPA increases signal intensity while ferrite predominantly affects T2 and decreases signal intensity. This study was undertaken to evaluate tumor-liver signal differences when gadolinium-DTPA and ferrites were utilized simultaneously for "double contrast" MRI.

Methods: We used a rat model of liver cancer in which intrahepatic adenocarcinoma tumor nodules developed two weeks following surgical implantation (2). Imaging was performed using a prototype 8 cm bore 1.4 Tesla scanner (Technicare). Five animals were imaged with an SE 250/15 (scan time one minute) pulse sequence immediately (1-2 minutes) following intravenous administration of .2 mmol/kg of Gd-DTPA. Ferrite (50 u mol/kg of Fe) was subsequently administered to these animals in the equilibrium phase of Gd-DTPA (5-15 minutes). In three animals, ferrite was administered first and followed by gadolinium-DTPA. SE 500/30 and 1500/60 pulse sequences were also evaluated. Contrast was calculated as the mean tumor-liver signal difference using an operator-determined region of interest, and this difference was normalized to standard deviation of background noise.

Results: In the model of liver cancer used in this study, tumor-liver contrast in the precontrast phase was greatest on T2-weighted pulse sequence. Gadolinium-DTPA produced the greatest tumor-liver contrast on short TR/short TE sequences, whereas ferrites produced the greatest tumor-liver contrast with the long TR/long TE

sequence. Maximal tumor-liver contrast was achieved when both ferrite and gadolinium-DTPA were given and a mixed T1-T2 weighted pulse sequence (SE 500/30) was utilized (Figure).

Conclusion: Previous studies have shown that in the equilibrium phase after gadolinium-DTPA infusion, tumor enhancement may actually exceed that of liver (2). This reversal of tumor-liver signal intensities from the precontrast infusion level has been attributed to the slower washout of contrast agent from tumor tissue. We exploited this phenomenon by further reducing the signal intensity of normal liver by administering ferrite, which does not affect tumor signal intensity (3). As a result, tumor-liver contrast was greatly enhanced. Combining "T1" and "T2" contrast agents was most effective when a mixed T1/T2 pulse sequence was utilized. While the SE 500/30 technique is a poor choice for noncontrast hepatic MRI, it has the advantage of wide availability and produces images relatively free of artifacts with excellent anatomic resolution. Therefore, our double contrast technique may prove simple, inexpensive, and efficient with respect to patient throughput. Preliminary evidence suggests that the toxicity of intravenous ferrite is low, and even two drugs may be less toxic than iodinated agents now in widespread clinical use.

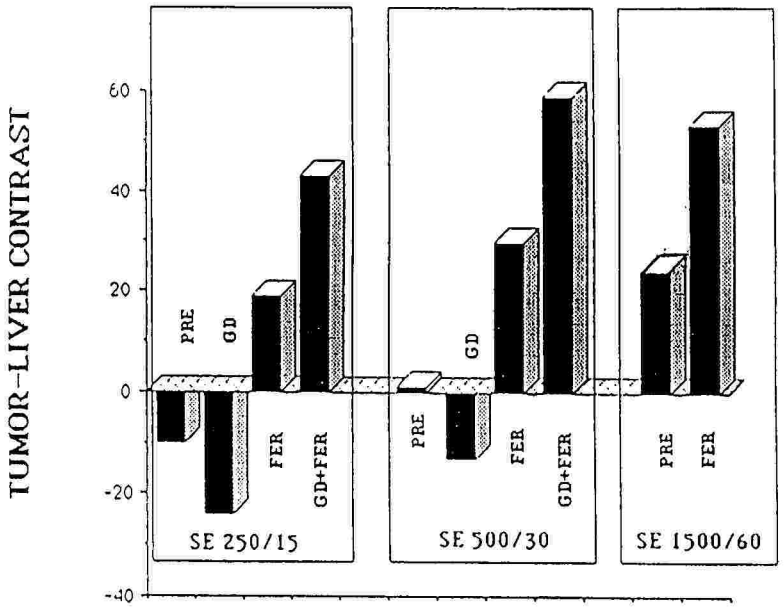

REFERENCES
1. Carr DH: AJR 143:214-224, 1984.
2. Saini S: AJR 147:357-362, 1985.
3. Saini S: Radiology 1987 (in press).

Wam-B7

THE USE OF GD-DTPA FOR GASTROINTESTINAL CONTRAST ENHANCEMENT IN HEALTHY MALE VOLUNTEERS

Wolfgang Kornmesser, Michael Laniado, Bernd Hamm, Wolfram Clauß, Roland Felix

Departments of Radiology,Klinikum Charlottenburg and Klinkum Steglitz,Freie Universität Berlin,Schering AG

The purpose of the present study was to evaluate safety and efficacy of different Gd-DTPA formulations (Schering AG, Berlin, West Germany) for gastrointestinal (GI) contrast enhancement in man.

Subjects and Methods:

Twenty healthy male volunteers (22-46 years, 52-98 kg) were investigated by MRI (Siemens Magnetom, 0.5 T) prior to and after administration of contrast. Spin-echo (SE) sequences with TR intervals of between 200 and 2000 ms and TE intervals of between 20 and 70 ms were employed. Fast imaging was performed with a gradient echo sequence (1)(TR 40 ms, TE 16 ms, 40°). The contrast media employed were clear aqueous formulations of Gd-DTPA/dimeglumine (1.0 mmol/l n=15 and 0.5 mmol/l n=5). The contrast medium was either given with 30 g mannitol/l, 15 g mannitol/l, or without mannitol. After precontrast scans had been obtained each subject drank 10 ml/kg of contrast medium equivalent to a dose of either 0.01 mmol or 0.005 mmol Gd-DTPA/kg. Postcontrast imaging was performed 10 to 150 min after administration of contrast. Baseline and postcontrast (24 and 48 h) blood samples were taken to screen for changes in a variety of hematological and serum parameters.

Results:
The tasteless contrast medium caused only minor signs of discomfort in the GI tract in 6 of the 20 volunteers. These side effects could be attributed to the amount of mannitol (15 g and 30 g/l, respectively). No changes of any parameter measured in blood and serum were observed following administration of either 0.01 or 0.005 mmol Gd-DTPA/kg.

Diagnostically useful contrast enhancement of the GI tract was present in all cases with all sequences employed. The observed contrast enhnacement permitted clear distinction between GI structures and adjacent abdominal viscera. In particular, contrast enhancement within the stomach provided visualization of the gastric lumen and the gastric wall. The head of the pancreas could be well differentiated from the C-loop of the duodenum.

In the lower abdomen results were influenced by the amount of mannitol, the concentration of Gd-DTPA, the time of measurement after administration of contrast, as well as the pulse sequence employed. On postcontrast images obtained about 100 min post applicationem (p.a.) (SE 2000/35,70) homogeneous contrast enhancement in the small bowel was observed in only 2 of 5 cases investigated without mannitol. There was no enhancement in the ascending colon. When contrast medium was given with 15 g mannitol/l homogeneous enhancement occurred in 4 of 5 volunteers and contrast enhancement in the colon was present in 1 case. With 30 g mannitol/l both homogeneous enhancement of the small bowel and high signal intensity (SI) in the ascending colon was observed in 5 of 5 subjects.

Five volunteers were investigated with a dose of 0.005 mmol Gd-DTPA/kg as opposed to a dose of 0.01 mmol/kg. With the lower dose less contrast enhancement was observed in the lower abdomen on short TR (200 and 500 ms), short TE (20 and 35 ms) SE images. Furthermore, a relative increase of SI of the enhanced bowel loops could visually be detected with a TE of 70 ms when compared to a TE of 35 ms (double echo technique)

Excellent delineation of the pancreas was obtained when MRI was performed within the first 10 min after administration of contrast. This applied to all formulations of contrast medium. With time the upper GI tract was cleared from contrast medium and results were poor with regard to the pancreas on images acquired later than 60 min p.a. On the other hand, distal parts of the small bowel showed better enhancement on later postcontrast scans.

In principle, long and short TR SE sequences were found to be suited for Gd-DTPA enhanced abdominal MRI. T1-weighted SE scans (SE 200/20, SE 500/35) showed bright signals from enhanced bowel loops. Fourfold signal averaging could be afforded within a relatively short period of imaging time and respiratory motion artefacts could be reduced. The long TR screening sequence (SE 2000/35,70), however, also highlighted the enhanced GI tract along with 20 slices measured at a time. The double echo technique provided high SI from the GI tract at a TE of 70 ms where the intensity of fat started to decrease. This in turn compensated for the disadvantage of isointensity of enhanced bowel loops with abdominal fat. The same applied to fast images. Contrast enhancement always provided higher SI when compared to the SI of fat. Due to the short data acquisition time per slice (20 sec) individual bowel loops could be identified on fast scans. In the upper abdomen, however, results of fast scans were greatly diminished due to high signal flow artefacts along the y-axis arising from the aorta and the V. cava.

Conclusions:
Gd-DTPA is an effective contrast agent for contrast enhanced abdominal MRI. A dose of 0.01 mmol Gd-DTPA/kg is recommended along with mannitol at least at a dose of 15 g/l. The formulation provides diagnostically useful results with long and short TR SE sequences as well as with fast imaging techniques. It facilitates the identification of normal anatomy and most likely will improve MRI in abdominal pathologies.

Reference:
Matthaei, D, Frahm, J., Haase, A., Hänicke, W.
Lancet, 893, 1985.

Wam-B8

MRI OF THE SPLEEN: CONCEPTS FOR THE USE OF CONTRAST AGENTS FOR TUMOR DETECTION

Ralph Weissleder, M.D., Peter F. Hahn, M.D., Ph.D., David D. Stark, M.D., Sanjay Saini, M.D., Jean-Claude Bousquet, M.D., Joseph T. Ferrucci, Jr., M.D.

Department of Radiology, Massachusetts General Hospital, Harvard Medical School, Boston, MA

MR imaging has been proven insensitive for the detection of neoplasms in the spleen and lymph nodes. Low inherent contrast between normal splenic tissue and tumor is due to the similar proton density, long T1 and T2 relaxation times, and the absence of MR observable fat in both tissues.

Exogenous magnetic contrast agents under development are designed to improve contrast between pathologic and normal tissue. Gadolinium(Gd)-chelates are representative of the paramagnetic agents which preferentially shorten T1 relaxation times. Unfortunately, Gd-chelates show weak relaxation effects in the spleen (Table). Furthermore, biodistribution of Gd-chelates is nonspecific, with significant accumulation in tumor tissue, limiting their ability to improve tumor-spleen contrast.

A new approach to contrast enhancement was suggested by examination of patients with systemic iron overload. MR images in these patients typically show dramatically reduced splenic T2 relaxation times due to the presence of crystalline iron oxyhydroxide within ferritin and hemosiderin (1). As tumors do not accumulate iron, tumor-spleen contrast is improved and focal lesions are readily detected (Figure).

Methods: A rodent model with adenocarcinoma implanted in the liver was used (2). Animals were administered Gd-DTPA and Gd-DOTA (0.2 mmol/kg) and ferrites (0.3 mmol Fe/kg). Determination of tissue relaxation times was made with PC/20 multispec pulse NMR spectrometer(IBM) which operates at a field strength of .47T.

Results: Ferrite particles produced a profound decrease in T2 relaxation time from normal splenic tissue (Table). This effect is not observed in adenocarcinoma which showed no uptake of intravenously administered particles.

Discussion: The proposed mechanism for enhanced detection of focal splenic lesions is analogous to the detection of tumor by sulphur colloid scintigrams; ferrite particles are only phagocytosed by the reticuloendothelial system but not tumor tissue.

We anticipate that ferrite particles will be valuable in the evaluation of focal splenic disease. Discrimination between benign splenomegaly and diffuse neoplastic infiltration may also be possible by quantitating splenic reticuloendothelial activity as our data show ferrite-enhanced MRI to be a sensitive discriminator of reticuloendothelial function.

		Spleen	Adenocarcinoma	Liver
Control	T1	**516** ± 62	**540** ± 82	282 ± 47
	T2	**37.8** ± 13.6	**49.7** ± 8.8	34.5 ± 4.9
Gd-chelate	T1	**379** ± 15.2	**343** ± 26.1	195 ± 25.7
	T2	33.8 ± 1.3	41.2 ± 4.7	26.9 ± 2.1
Ferrite	T1	325 ± 17	580 ± 56	269 ± 370
0.3 mmol Fe/kg	T2	**13.0** ± 2.1	**48.2** ± 7.1	13.8 ± 4.8

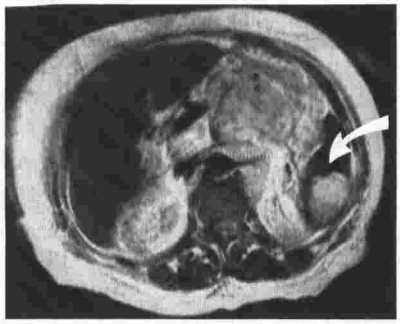

TABLE: Relaxation times measured in vitro at 0.47T using an IBM PC/20 spectrometer. Data condensed from Gd-DOTA, Gd-DTPA, and ferrite time/dose response studies.

FIGURE: Focal lymphoma of the spleen is detected due to its long T2 relaxation time relative to surrounding splenic tissue which has an abnormally short T2 due to transfusional iron overload.

REFERENCES

1. Stark DD: Radiology 154:137-142, 1985.
2. Saini S: Investigative Radiology (in press).

(Wam-C) CARDIOVASCULAR

Presiding: D. Hahn & L. Axel

10:20 am

ROOM C-101

12 MINUTES PER PRESENTATION

Wam-C1

MAGNETIC RESONANCE ANGIOGRAPHY - INITIAL CLINICAL INVESTIGATION

C. L. Dumoulin, S. P. Souza, H. R. Hart Jr, and G. Wood*

General Electric Corporate Research and Development Center, Schenectady, New York and *Albany Medical Center, Albany, New York

Magnetic resonance angiography can be performed in a variety of ways. The work presented here makes use of a modified version of the phase-contrast method (1,2). In this investigation, several vascular pathologies were examined to determine the potential of MR angiography as a clinical tool. Disease states such as carotid artery stenosis and occlusion (Figure 1), arterial venous malformations (AVMs) and aneurysms were investigated by MR angiography. The MR examinations were compared to DSA studies obtained on the patients shortly before or after the MR exam. Initial experience indicates that MR angiography is capable of replacing many, although not all, dye-contrast angiographic procedures.

Figure 1 shows an MR angiogram of a 64 year old male patient with a left internal carotid occlusion. This image was obtained in approximately 3 minutes. The pulse sequence time, TR, was 33 msec. 44 excitations were performed for each increment of the phase encoding gradient to remove artifacts due to the changing blood velocity during the cardiac cycle.

1. C. L. Dumoulin and H. R. Hart, "MR Angiography", Radiology (December, 1986).
2. C. L. Dumoulin, H. R. Hart, S. P. Souza, "Magnetic Resonance Angiography - a new fast scanning technique", presented at this meeting.

Wam-C2
RAPID SMALL FLIP ANGLE (CINE) MAGNETIC RESONANCE IMAGING OF AORTIC INSUFFICIENCY

Schiebler ML, Axel L, Reichek N, Aurigemma G, Cohen E, Kressel HY

Hospital of the University of Pennsylvania, Philadelphia, PA

The introduction of cardiac gated rapid small flip angle (cine) magnetic resonance imaging (C-MRI) provides a new non-invasive technique for the evaluation of aortic valvular insufficiency (AI). On C-MRI the regurgitant jet of AI can be demonstrated as a discrete area of signal void within the left ventricle. The C-MRI characteristics of mild AI are contrasted with those of massive AI in this presentation.

Ten patients with documented AI, either by 2-DPDE or angiography, were imaged in a 1.5 T magnet (Signa, G.E.) with C-MRI. Routine axial imaging planes were employed, and supplemental coronal planes were used in cases where the regurgitant jet was not seen on the axial images. All cases of AI were classified as either mild, moderate, or severe by the size of the regurgitant jet on 2-DPDE. There was complete agreement between the 2-DPDE and the C-MRI for both the size of the regurgitant jet and its position within the ventricle.

Mild aortic regurgitation, seen in two of our cases, is best imaged in the coronal plane by C-MRI. In one case, the regurgitation jet was only demonstrated after supplementary coronal images were obtained.

Severe AI was easily demonstrated in both the axial and coronal planes. In two of our patients, the regurgitant jet demonstrated preferential flow posteriorly and inferiorly along the mitral valve. This jet of regurgitant flow in the axial plane, appears to have two effects on the mitral valve: first it inhibits excursion of the anterior leaflet and secondly it may help to cause premature opening of the valve in early diastole.

Analysis of the defective valve with C-MRI was more difficult. The presence of a bicuspid valve was demonstrated in a single case where a known bicuspid valve was present. Routine identification of the separate leaflets of the defective tricuspid valves and their excursion was difficult, due to angulation of the valve, which is oblique with respect to the axial imaging plane. The small size of the cusps are also at or beyond the resolution of C-MRI.

C-MRI is a promising noninvasive tool with which to study the various hemodynamic components of AI.

Wam-C3
RAPID SMALL FLIP ANGLE MRI (C-MRI) MITRAL VALVE INSUFFICIENCY

M. Schiebler, L. Axel, N. Reichek, G. Aurigemma, E. Cohen, H.Y. Kressel

Hospital of the University of Pennsylvania, Radiology Department

The introduction of cardiac gated rapid small flip angle (cine) magnetic resonance imaging (C-MRI) has provided a new non-invasive technique for the evaluation of mitral valve insufficiency.

Six patients with mitral regurgitation, documented by either two dimensional pulsed doppler examination (2-DPDE) or ventriculography, were examined on a 1.5T MRI system (Signa, GE) using a C-MRI pulse sequence. All mitral valve imaging was performed in the axial plane.

Mitral regurgitation was detected by the presence of a region of decreased signal corresponding to the regurgitant jet. The amount of mitral regurgitation was graded as either mild, moderate or severe based on the size of the visualized jet on C-MRI. In each case both the direction and size of the jet corresponded completely with the 2-DPDE results. In the two cases where a left ventriculogram was performed, there was also total agreement of the data. In one case, clinically occult mitral regurgitation was detected by C-MRI before 2-DPDE was performed.

C-MRI was able to demonstrate thickening of the mitral valve leaflets in one of the patients, who was known clinically to have a myxomatous mitral valve. Excursion of the anterior leaflet of the mitral valve could be easily assessed as well. In two of the six patients this excursion was limited due to the presence of a concommitant jet of aortic regurgitation (AI). AI has two effects on the mitral valve: The predominant one is a limitation of the degree of excursion of the anterior mitral leaflet; it may also help to accelerate the initial opening of the anterior leaflet due to a Venturi effect causing a relative decrease in pressure along the ventricular side.

Evaluation of both left atrial enlargement and left ventricular enlargement is also readily accomplished with C-MRI.

C-MRI is a promising noninvasive imaging modality for the evaluation of mitral valve regurgitation.

Wam-C4

CINE MAGNETIC RESONANCE IMAGING OF INTRACARDIAC FLOW PATTERNS

S R Underwood, D N Firmin, R H Mohaiddin, R H Klipstein, R S O Rees, D B Longmore

The National Heart and Chest Hospitals, London UK

Conventional spin echo sequences usually give no signal from moving blood and this provides excellent contrast in images of the cardiovascular system. It is possible, however, to maintain signal even from rapidly moving blood using a short field echo sequence and even echo rephasing (the FEER sequence (1)). Areas of turbulent flow do not give signal and it is possible to detect and quantify the turbulence of valvular disease and of intracardiac shunting. The sequence can be repeated at up to 50ms intervals using a reduced excitation pulse angle and this provides a cine display which greatly simplifies interpretation. In this study we evaluate the use of this technique in 10 normal subjects and in 4 patients with intracardiac shunts and 4 with valvular heart disease.

The normal subjects were studied in a transverse plane 5cm above the aortic valve. Signal loss never occured at this level implying that flow at this distance from a normal aortic valve is not turbulent. In a coronal plane a small area of signal loss occured within 1cm of the valve during systole, and also within the left ventricle during diastole because of filling through the mitral valve. In 2 patients with severe aortic stenosis there was signal loss in the whole ascending aorta throughout systole, and in 2 with aortic regurgitation the jet of diastolic regurgitant flow within the left ventricle was seen and allowed the regurgitation to be classified as severe and mild respectively. In one patient with severe mitral regurgitation there was a large jet of regurgitant flow in the left atrium during systole. Turbulent flow through a ventricular septal defect and a Gebodie defect in a single patient allowed the relative size of the shunts to be estimated, and shunting through a detached VSD patch in another patient was observed. Flow through an atrial septal defect was nonturbulent but through a failed atrial patch graft it was turbulent.

We conclude that cine magnetic resonance imaging using the FEER sequence allows a noninvasive assessment of abnormal intracardiac flow patterns and should allow a noninvasive assessment of the significance of valvular disease and intracardiac shunting.

1 Nayler GL, Firmin DN, Longmore DB. Cine MR flow imaging. J Comput Assist Tomogr 1986;10:715-22

Wam-C5

NONINVASIVE MEASUREMENT OF REGURGITANT FRACTION IN PATIENTS WITH MITRAL OR AORTIC REGURGITATION BY CINE MRI

P. Pflugfelder, M.D.; U. Sechtem, M.D.; R. White, M.D.; C.B. Higgins, M.D.

Department of Radiology, University of California, San Francisco, California

Cine MRI is a new pulse sequence that uses small flip angles, short TR and TE, and gradient recalled echoes. The heart can be imaged with a temporal resolution of approximately 20 msec and good anatomical detail. Since the severity of left-sided regurgitant valve lesions is related to the difference between left and right ventricular stroke volumes, we determined this difference in 10 normals and 21 patients with mitral (N = 15) or aortic (N = 6) regurgitation. Qualitative grading of the severity by Doppler echocardiography (15) or angiography was used for comparison.

The entire heart was imaged by cine MRI with 12 - 15 transverse sections and a total imaging time of approximately 15 to 30 minutes. End-diastolic and end-systolic right (RV) and left ventricular (LV) volumes were measured using a modified Simpson's method. Ratio of LV and RV stroke volumes (L/R) and regurgitant fraction (RF) were calculated.

	Normal	Mild	Moderate	Severe
	N = 10	N = 8	N = 5	N = 8
L/R	0.97 ± 0.07	1.12 ± 0.16	1.49 ± 0.15*	2.74 ± 0.35**
RF	4 ± 7	10 ± 9	30 ± 9**	63 ± 5**

* $p \leq 0.051$ ** $p \leq 0.001$ vs less severe groups

Cine MRI can distinguish between mitral and aortic regurgitation of different grades of severity and quantify the severity of the lesion by the ratio of ventricular stroke volumes and the left ventricular regurgitant fraction. This 3-dimensional technique is easily reproducible and noninvasive and may be of value in the follow-up of patients with left-sided valvular regurgitation.

Wam-C6

MEASUREMENT OF PULSATILE VOLUME BLOOD FLOW IN THE LOWER EXTREMITY BY CW NMR

R.E. Halbach, Ph.D. (1), J.B. Towne, M.D. (2), David J. Tolan (1)

1. Metriflow Medical Systems Inc., Milwaukee, WI 53226, 2. Medical College of Wisconsin, Milw., WI 53226

Continuous wave (CW) NMR techniques have proved to be useful for the measurement of arterial blood flow. Two modes of operation have been demonstrated through measurements on normal subjects. The first is a whole limb measurement technique where flowmeter output represents a summation of the pulsatile component of arterial flow in all major arteries through a limb cross section. In the second technique, oscillating gradient fields are applied to create a null region, or flow sensitive cylindrical flow detection voxel, which may be rectilinear scanned across a limb to locate arterial flow and enable flow measurement in individual vessels. An AFM-100 blood flow scanner (Metriflow Medical Systems Inc., Milwaukee, WI) incorporating a .1T permanent magnet field source was used to obtain the data presented. The system has a 19 cm. internal diameter detector cylinder bore to accept a limb for measurement.

A study was conducted on five normal subjects to characterize pulsatile arterial flow at three levels in the normal leg. Whole limb cross sectional data was obtained from three sites on both legs, with each measurement repeated on two separate days for a total of 180 measurements. The mean pulsatile arterial flow and peak flow are listed in the following table.

	Mean flow ml/min	**Peak flow ml/min**
Knee	**121.0 ± 30.0**	**418.7 ± 75.1**
Calf	**64.8 ± 24.5**	**236.4 ± 69.3**
Ankle	**22.5 ± 13.0**	**91.2 ± 35.9**

The reproducibility studies of repeated measurements of mean flow done on the same individual revealed a mean coefficient of variance of 8.5% for the knee, 11.8% at the calf, and 22.8% at the ankle. Data obtained at each site was signal averaged to reduce inter-beat variability and enchance the signal. An example of a signal obtained from the popliteal artery is shown in figure 1. The digitized signal is analyzed for area under the curve to determine mean pulsatile volume flows in milliliters per minute and for peak systolic flow. The system was calibrated by pulsatile pumping of paramagnetically doped (copper sulfate) water solution through a flow phantom to simulate blood flow.

Leg scans have been obtained clearly showing the location of and volume flow in the popliteal artery at a point just distal to the knee. Individual artery cross sectional scans from the lower calf have yielded measurement of flow in the anterior tibial, posterior tibial, and the peroneal arteries, all of which summate to approximately the whole limb flow from the same cross section.

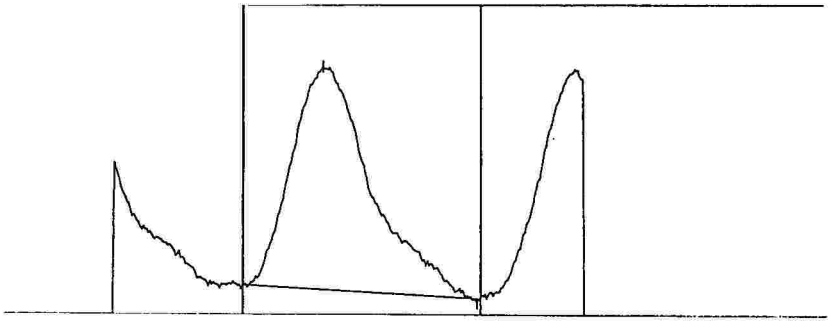

Figure 1. Flow Signal, Popliteal Artery, Normal Subject

Wam-C7

CARDIAC LEFT VENTRICULAR EJECTION FRACTION CALCULATION USING FAST FIELD ECHOES IN MR IMAGING

Fred L. Steinberg, M.D.

Madeleine R. Fisher, M.D., Lee F. Rogers, M.D.

The left ventricular ejection fraction was calculated from transverse MR images acquired with fast field echo pulse sequences through the left ventricle in four normal male volunteers. All subjects were scanned on a Philips Gyroscan 1.5 tesla imaging device operating at 0.5 tesla. Between seven and ten levels were scanned with 1.0 cm slice thickness at contiguous 1.0 cm intervals. The matrix size was 128 by 128. Cardiac gating was performed by a Hewlett Packard telemetry device. Sixteen frames at different times in the cardiac cycle were produced at each level. The time interval between frames was determined by the heart rate. The scan time per level was about four minutes and the total scan time was approximately one hour. For each frame, the cross sectional of the left ventricle was approximated by the area of an ellipse. The volume for each level was calculated by multiplying the area by the slice thickness and adding all the levels. The frame with the largest and smallest cross sectional volumes were selected as the end diastolic and end systolic values respectively. The mean ejection fraction was calculated to be 63.2% + 3.9% s.d. The main advantage of this technique is that the ventricular volumes are actually calculated from the transverse images rather than approximately from a single slice. In conclusion, cardiac MR images can be used to calculate left ventricular ejection fraction.

Wam-C8

THREE DIMENSIONAL RECONSTRUCTION OF THE HEART AND GREAT VESSELS FROM CONTIGUOUS MULTI-SLICE EKG GATED CARDIAC MR IMAGES

Suzanne Gronemeyer, PhD[1]; John Laschinger, MD[2]; Michael Vannier, MD[3]; Robert Knapp, BM, RT[3]; Fernando Gutierrez, MD[3]

[1]Siemens Medical Systems, St. Louis, MO; [2]Division of Cardiothoracic Surgery and [3]Mallinckrodt Institute of Radiology, Washington University School of Medicine, St. Louis, MO

Two dimensional (2D) multi-slice EKG gated cardiac imaging is often useful in the definition of cardiac and great vessel anatomy. Three dimensional (3D) images are desirable in preoperative planning for correction of congenital cardiac anomalies. But 3D high resolution cardiac image data acquisition requires excessive patient scanning time because it necessitates EKG gated phase encoding in two dimensions. We have used existing computer graphics and animation techniques to generate 3D images of the heart and great vessels by reconstruction of 2D serial EKG gated data sets obtained within a clinically feasible scanning time.

Contiguous thin EKG gated 2D images are obtained from the apex of the heart to the aortic arch. Images are obtained at several points in the cardiac cycle for each slice. The axial orientation is chosen to reduce respiratory and aliasing artifacts. For example, for an adult male with a heart rate of 60 and an arch to apex dimension of 14 cm, 28 five mm slices are necessary for a complete transaxial data set. During each scan, 7 (or more) slices are obtained at different delay times (TD) with respect to the R wave. Since for 3D reconstruction one needs to have all slices at the same TD, 28 scans are required, but the result is seven complete data sets, each at a different TD, which permits cine 3D presentation. By using a 25 cm FOV and a 128x512 data acquisition matrix (2 mm x 2 mm pixels, but 512 frequency samples) on a 1.5T Siemens Magnetom, each of the 28 scans require 2.1 minutes, for a total data acquisition time of one hour (excluding setup time). Fewer slices (and therefore shorter imaging times) are required for smaller hearts. Faster heart rate also speeds data acquisition, but reduces the number of delay times (TD) imaged for each slice.

Images from each TD are then edited using selective erasure and region filling to isolate pertinent cardiac and great vessel structures. High resolution 3D surface reconstructions for each TD are obtained by stacking the edited images. To view the endocardial surfaces, a region filling process is used to produce an endocast of the volume contained in the heart and great vessels. Sequential projection of either 3D surface reconstructions or endocast volumes from each TD yields 4D (time) cine images. Both surface and endocast projections can be viewed from any axis or divided by any plane to allow assessment of

cardiac volumes, wall motion and function non-invasively.

We have demonstrated the feasibility of this technique in normal volunteers (see figure) and are extending it to patients with congenital heart disease.

(Wam-D) TECHNICAL DEVELOPMENTS

Presiding: K. Ohtomo & M. L. Wood

10:20 am

ROOM C-102

12 MINUTES PER PRESENTATION

Wam-D1
APPLICATION OF ROTATING FRAME TECHNIQUES TO MAGNETIC RESONANCE IMAGING

G. E. Santyr, R. M. Henkelman, M. J. Bronskill

Dept. of Medical Biophysics, University of Toronto, Toronto, Canada

The desire to improve T_1 contrast while maintaining high signal-to-noise ratio is an important concern in MRI. Development of techniques in the rotating frame may provide a means of exploiting low frequency T_1 contrast in tissue without the loss in signal strength normally associated with low static fields. Such techniques also offer the possibility of performing relaxometry imaging.

In the rotating frame, spins are subject to an effective field:

$$H_{eff} = (H_o - \omega/\gamma)\mathbf{k} + H_1\mathbf{i}$$

where H_o is the magnitude of the static field, γ is the gyromagnetic ratio and ω and H_1 are the frequency and magnitude of the applied rf field respectively.

On resonance ($\omega=\gamma H_o$), the magnetization in the rotating frame is perturbed only by the rf field. A rotating frame experiment employs a hard 90° excitation pulse followed immediately by a pulse of amplitude H_1 which is shifted $\pi/2$ in phase. The magnetization is "spin-locked" along the rf field for the duration of this pulse and relaxes with a time constant, $T_{1\rho}$, characteristic of low frequency ($\omega_1=\gamma H_1$) spin-lattice effects. This relaxation time is measured by observing the magnitude of the FID immediately after the locking pulse as a function of the locking time.

The variation of $T_{1\rho}$ in tissue with the locking field frequency ω_1 has been investigated (1). We have used the spin-locking method to measure $T_{1\rho}$ in several mouse tissues. Fig. 1 shows the dependence of $1/T_{1\rho}$ on the frequency of the locking field ω_1 for liver, muscle and kidney. As $\omega_1 \to 0$ the rotating frame relaxation rate approaches the transverse relaxation rate ($1/T_2$). At higher locking frequencies ($\omega_1 \to \omega_0$), $1/T_{1\rho}$ approaches the longitudinal relaxation rate ($1/T_1$). The shapes of such tissue dispersions ($1/T_{1\rho}$ vs ω_1) indicate the contrast to be expected in a rotating frame image and may also provide dynamic information about the tissue.

Such spin-locking techniques can be used to derive $T_{1\rho}$-weighted images. Spatial localisation is accomplished by utilising a slice selective 180° pulse to refocus the FID following the locking pulse. Frequency compensation and phase encoding are accomplished in the interval between the locking pulse and the refocusing pulse and a readout gradient is applied at the echo (2).

Rotating frame images have been obtained using a 0.15 T imager. These images demonstrate the potential for contrast improvement possible with rotating frame techniques.

Fig.1 :

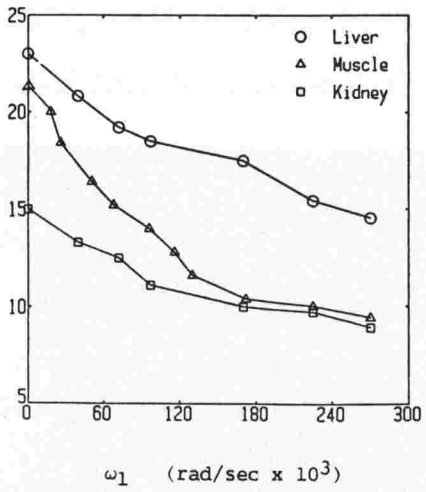

References:

(1) R.R. Knispel, R.T. Thompson, M.M. Pintar. J. Mag. Res. 14 (1974) 44.

(2) R.E. Sepponen, J.A. Pohjonen, J.T. Sipponen, J.I. Tanttu. J. Computer Assisted Tomography 9 (1985) 1007.

Wam-D2

DUAL ECHO IMAGE RECONSTRUCTION FOR TE 26/100 PROTOCOL

RICHARD ONG[a,b], LEE CHIU[a], PRADIP PATTANY[b], and JAMES LIPCAMON[a]

[a]Department of Radiology,Harbor-UCLA Medical Center, Torrance, CA, [b]Picker International, Cleveland, OH

MR dual echo technique consists of two sequential spin echoes such as TE 30/60, 30/90, and 40/80. It has been routinely used in many institutes including ours, and known to be time-saving and to provide optimal information for clinical diagnosis. In the past 3 months, we have developed a dual echo sequence TE 26/100 with the motion artifact suppression technique[1] on our 0.5 T Picker at Harbor-UCLA Medical Center, and applied this protocol to patients and volunteers. The unique features and clinical data of this protocol are presented as follows:

(1) The sequence is composed of two widely separated echoes with a TR 2 sec: at 26 msec for proton density and at 100 msec for T2-weighted images. Within-view motion artifacts are suppressed for TE 100 in order to eliminate any positional deviation from TE 26.

(2) By adding the two images obtained at TE 26 and 100 msec, a 3rd "pseudo echo" corresponding to an intermediate TE (~ 50 msec) can be generated. The fact that most lesions are not obvious in proton density images, and the overall low intensities in TE 100 due to signal dropout make the diagnosis difficult sometimes. The 3rd echo image will enhance the T2-weighted lesions, and in the meantime maintain a good proton image, i.e., 50% proton density + 50% T2-weighted (Fig. 1). This technique has helped us confirm small lesions such as illustrated in Fig. 2a-c, an infarct in the basal ganglia.

Fig. 1

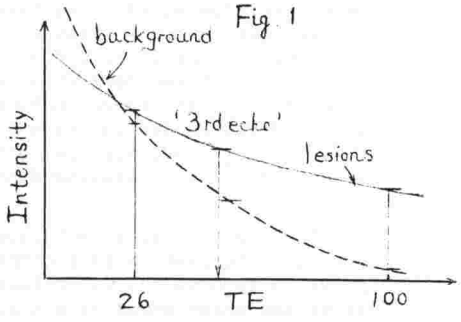

(3) By subtracting the TE 100 image from the TE 26 image, we are able to detect as low intensities the very long T2 (> 180 msec) components. While displaying adequate anatomy, the subtracted image

Fig. 2a

TE 26

2 b

TE 100

2 c

⊕

does best in picking up fluid components. Figure 3a-c shows an intracerebral hematoma. The outmost edematous zone surrounding the lesion turn out low intensity in Fig. 3c, whereas the blood still remains bright. Interestingly, these results are comparable to CT findings (Fig. 3d). Similarly, in addition to CSF, a cyst in the 3rd ventricle can be highlighted using this technique (Fig. 4a-c)

Furthermore, the TE 26/100 sequence has the potential for flow studies, as the motion artifact suppression technique therein refocuses the flow. This protocol has also been applied to abdomen and pelvis areas, and proven useful in routine diagnosis. In summary, TE 26/100 has some advantages over currently most employed protocols in providing additional information.

1. Pradip M. Pattany, et al. manuscript submitted.

3d

CT

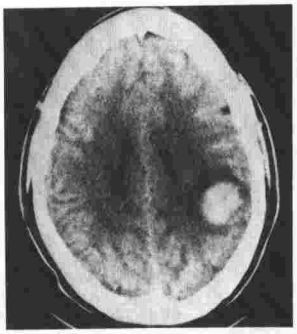

Fig. 3a

TE 26

3 b

TE 100

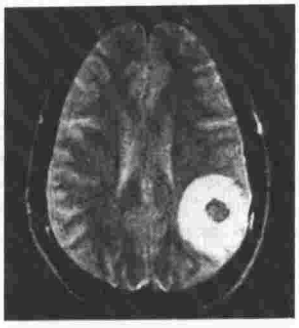

3 c

Fig. 4a

TE 26

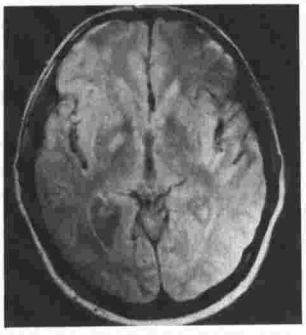

4 b

TE 100

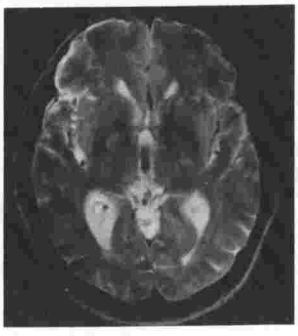

4 c

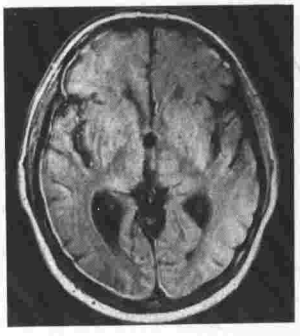

Wam-D3

CLINICAL EVALUATION OF MAGNETIC RESONANCE IMAGING USING THE HYBRID FAST-SCAN TECHNIQUE

Errol M. Bellon, M.D.[1,2,3], Michael A. Morich, B.S.E.E.[3], Linda M. Eastwood, Ph.D.[3], Damon C. Sacco, M.D.[1,2], Jane E. Benson, M.D.[1,2], Raymond E. Gangarosa, M.D., Ph.D.[3]

Departments of Radiology, Case Western Reserve University[1] and Cuyahoga County Hospital[2], Cleveland, Ohio and the Clinical Science Center[3], Picker International, Highland Heights, Ohio

The high lesion-to-normal-tissue contrast of T2-weighted as opposed to T1-weighted images is accompanied by a concommitant increase in diagnostic sensitivity. Several fast-scanning techniques have been proposed to overcome the long scan times usually required for T2-weighted scans. The Hybrid technique has been designed to achieve acceptably short scan times while maintaining T2-weighting as well as good spatial and contrast resolution.

We studied 50 patients with infarct, primary tumor, metastatic tumor, or demyelinating disease of the brain, examining each prospectively with Hybrid as well as the standard 2DFT method. We compared the accuracy of lesion detection for each technique.

Studies were performed on a 0.5T Picker Vista 2055 superconductive imaging system using a 30cm head receiver coil. Imaging parameters for the standard 2DFT spin-echo technique were: TR 2000/TE 80, 1 or 2 excitations, 256 x 256 acquisition matrix, 17 or 8.5 mins. scan time; and for Hybrid: TR 2000/TE 80, 1 or 2 excitations, 256 x 256 acquisition matrix (128 x 256 during initial phase of study), 4.3 or 2.2 mins. scan time.

The study confirms that the two methods have equivalent accuracy, and that Hybrid provides fast data acquisition while maintaining the high T2 contrast necessary for lesion detection. It provides images with adequate T2 weighting in 1/4 normal scan time, with no loss in diagnostic accuracy.

These results will be illustrated by representative clinical examples, providing a comprehensive demonstration of the utility of the Hybrid fast-scan technique in disorders of the brain.

Wam-D4

A NEW HIGH THROUGHPUT MR PULSE SEQUENCE WITH VARIABLE TR, VARIABLE TE, MULTIPLE SLICE ACQUSITION

Raj Shenoy PhD., R. Wolf, T. Morrone, R. Lufkin, W. Hanafee.

Fonar Corporation, New York and UCLA

Multiple slice, multiple echo MR pulse sequence contrast is limited by the fact that the same TR must be used for both echoes in the sequence. Multiple slice acquisitions with varying TR and TE can alternatively be obtained by rescanning the patient but this requires additional time for the extra pulse sequences. We describe a new high throughput, variable TR, variable TE, multiple slice acquisition pulse sequence which overcomes many of the limitations of the two previous approaches.

A special 2D-FT spin echo pulse sequence was written which produced images with two different TR's and TE's for multiple slices using a 0.3 Tesla whole body permanent magnet imager (FONAR B-3000). Scans of phantoms, normal volunteers, and patients with a variety of pathology were obtained. Comparison was made with conventional multiple slice, multiple echo as well as single echo sequences obtained on the same machine. The new sequence produced significantly greater image contrast variation than the standard multiple echo sequences which could only vary the TE. For n= the number of phase encoding levels, the new sequence required only (TR1*n)+(TR2*n) msec compared to up to (TRI*n)+2*(TR2*n)msec using standard single echo sequences and rescanning to produce the same number of slices. Image signal to noise and spatial resolution were identical with the new technique compared to conventional spin echo images with the same parameters.

Wam-D5

COMPOSITE ECHO IMAGING

Perry Sprawls, Inder K. Daftari, Patricia C. Davis, Jacques J. Coumans

Emory University Hospital, Department of Radiology, Atlanta, Georgia 30322

Most conventional MRI techniques (IR, SE, etc.) produce a series of individual spin-echo images, each with a finite but different TE value. In these images the visibility of tissue structures is often limited by the cancellation effect between T1 and T2 contrast and low signal-to-noise in the longer TE, T2 weighted images. Also, acquisitions must be repeated using different pulse parameters if both T1 and T2 weighted images are needed for a specific study.

A set of composite images constructed from one echo series overcomes many of the limitations of individual echo images.

A variety of composite-image construction algorithms have been developed and investigated for clinical usefulness. They are implemented on a conventional clinical image processing unit and used in both interactive and fixed protocol modes.

For many clinical applications one short TR sequence is used to generate a pair of composite images. The "Formula-one" image has enhanced T1 contrast and the "Formula-two" image is a heavily T2 weighted image with improved signal-to-noise characteristics.

Composite echo images are a valuable adjunct to conventional imaging techniques because of their increased contrast sensitivity, reduced noise, and the potential for reducing image acquisition time.

Wam-D6

A NEW METHOD FOR ACQUIRING ACCURATE SPIN-LATTICE RELAXATION TIME IMAGES WITHOUT A SIGNIFICANT SCANNING TIME LOSS.

W.T. Sobol, W.H. Hinson, P.R. Moran, D.A. Saloner

Radiology Department, The Bowman Gray School of Medicine,
Wake Forest University, Winston-Salem, NC 27103

The use of transient effects in the dynamic equilibrium experiments to calculate spin-lattice relaxation time T_1 first proposed in NMR by Look and Locker[1] has recently caught the attention of the MRI community as a possible tool for fast and accurate determination of T_1 images[2-3].

When a train of identical r.f pulses, spaced periodically with time T, is applied to the sample placed in a magnetic field $\mathbf{B}_0$, then the magnetization after each pulse, monitored in the rotating

reference frame, can be written as

$$\mathbf{M}(n) = \{[1 - (1-Z)^{-1}(1-Y)]Z^{n-1} + (1-Z)^{-1}\}\ \mathbf{P}\ \mathbf{M}_0 \qquad (1)$$

where $\mathbf{M}_0=(0,0,M_0)$ represents the equilibrium magnetization at the beginning of the experiment, **P** is the matrix of magnetization rotation induced by an r.f. pulse and **Z=PR**, where **R** is the relaxation matrix (with elements $X=\exp(-T/T_2)$, $Y=\exp(-T/T_1)$ and off-resonance terms)[4]. This general equation can be solved by numerical iteration. However, in a simplified case, when it can be assumed that the perpendicular components of magnetization vector vanish in time between pulses (due to spin-spin relaxation or the loss of coherence, induced by magnetic field gradients), Eq.(1) can be solved analytically. The signal amplitudes after consecutive pulses can be seen as a discrete sampling of a continuous function

$$FID(t,T,T_1,\alpha)=a*\exp(-t/T_{eff}) + b \qquad (2)$$

where $t=(n-1)T$ $(n>0)$, $a=M_0Y\sin\alpha(1-\cos\alpha)/(1-Y\cos\alpha)$, $b=a(1-Y)/(1-\cos\alpha)$, and $0<\alpha<\pi/2$ is the pulse tip angle. The effective transient decay time

$$T_{eff}=TT_1/[T-T_1\ln(\cos\alpha)] \qquad (3)$$

permits the determination of the relaxation time T_1 of the sample.

To test this procedure in MRI we have used a simple modification of the FAST[5] protocol in Picker .5T mobile scanner to collect 6 partial images of doped water phantom with T_1 of 190 ms. A single exponential fit to these data, collected with $\alpha=30^0$ and T=50 ms yields T_{eff}=118 ms and T_1=181 ms, respectively.

The major advantage of this protocol in the clinical practice is based on our discovery that the partial images, obtained in this way, can then be added together to form a final image of good diagnostic quality. Thus, accurate T_1 images can be obtained in clinical protocols without a significant loss of the patient scanning time or loss of the diagnostic image quality. This point is well illustrated in another paper, presented at this meeting.[6]

REFERENCES

[1] D.C. Look, D.R. Locker, Rev.Sci.Instrum. **41**, 250 (1970).

[2] R. Graumann, M. Deimling, T. Heilman, A. Oppelt, Proc. Fifth SMRM Meeting, Montreal 1986, p.922.

[3] W.H. Hinson, P.R. Moran, D.A. Saloner, Relaxation rate discrimination from dynamic equilibrium acquisition in MRI, using limited angle r.f. excitation sequences; Radiology: special edition, RSNA Abstracts 1986, in press.

[4] W.S. Hinshaw, J.Appl.Phys. **47**, 3709 (1976).

[5] M.L. Gyngell, G.L. Nayler, N. Palmer, M. Paley, Magn.Reson.Imag. **4**, 101 (1986).

[6] W.H. Hinson, W.T. Sobol, P.R. Moran, D.A. Saloner, In vivo relaxation time measurements from a single dynamic equilibration acquistion sequence using limited angle r.f. excitation sequences; SMRI Fifth Annual Meeting, 1987.

(Wpm-A) ABDOMEN - PELVIS

Presiding: J. Weinreb & D. Kushner

3:20 pm

RIVER ROOM

12 MINUTES PER PRESENTATION

Wpm-A1

MRI OF ABDOMINAL MASSES IN CHILDREN

Rosalind B. Dietrich, M.D., Hooshang Kangarloo, M.D., M. Ines Boechat, M.D.

UCLA

Purpose. The purposes of our study were: 1) to demonstrate the ability of magnetic resonance (MR) to image, evaluate and define the extent of abdominal masses in children, 2) to assess the scanning planes which give the maximum information for each organ imaged, 3) to evaluate if MR may be more useful than or give additional information to other imaging modalities, and 4) to assess if T2-weighted images give additional information to that provided by T1-weighted images.

Introduction. The radiographic evaluation of a suspected abdominal mass is a frequent pediatric problem (1). Previously, such masses were evaluated with a combination of plain roentograms, excretory urography, ultrasonography or computed tomography. A few authors have recently shown limited numbers of MR images of certain abdominal masses in children, in particular neuroblastoma (2-7). No study has yet been performed, however, to specifically evaluate the usefulness of MRI in a large series of children with suspected abdominal masses.

Methods. Ninety children (aged 1 week to 17 years) with suspected abdominal masses were evaluated by MRI. Several children were scanned more than once in order to evaluate response to therapy or recurrence of disease for a total of 118 scans. Images were obtained using a Fonar B-3000 imager with a 0.3 Tesla permanent magnet. The sections obtained were 6-9mm thick. All images were obtained with spin-echo pulse sequences with scanning times varying from 4-17 minutes. T1-weighted images were obtained in multiple planes in all cases. T2-weighted sequences were also obtained when lesions were suspected of being cystic, inflammatory or neoplastic. At the time of initial evaluation all children also had ultrasound and/or CT scans performed and these were available for comparison in all cases.

Results. MRI was able to demonstrate the organ of origin and the extent of abdominal masses to show displacement and/or involvement of adjacent organs and vessels. Optimal imaging planes depended on the organ of origin. Renal and pararenal lesions were best imaged in the coronal plane. This plane clearly defines the size and origin of masses, their superior-inferior extent and displacement and/or involvement of major vessels. Lesions arising in or involving the liver, pancreas, small bowel or mesentery were best imaged axially. This is the optimal plane for evaluation of the portal vein and common bile and shows fluid-fluid levels well. Sagittal images were useful for evaluation of lesions arising from the pelvis and extending into the abdomen, especially in defining their structure of origin. MR was better able to demonstrate the extent of pathology in multiple planes and the degree of vascular involvement than was CT. It was better able to show an overall image of the abdomen and assess the extent of lesions than ultrasound. T2-weighted images gave additional information in the evaluation of cystic lesions and better tissue differentiation of tumors and inflammatory lesions from normal tissues than T1-weighted images alone.

Conclusions. MRI, due to its high quality images, its ability to image in any plane and its non-invasive, non-irradiating nature, is an extremely useful imaging modality in the evaluation of children with abdominal masses. Its appropriate use will obviate the need for multiple procedures and thus may reduce the time and cost of hospitalization in this group of patients.

References

1. Currarino G. Choice of imaging procedure. In: Silverman FN, ed. Caffey's pediatric x-ray diagnosis: An integrated imaging approach. 8th ed. Chicago:Year Book Medical Publishers, INC., 1608-1610, 1985.
2. Smith FW. The value of NMR imaging in pediatric patients: A preliminary report. Pediatr Radiol 13:141-147, 1983.
3. Moon KL, Hricak H, Crooks LE, et al. Nuclear magnetic resonance imaging of the adrenal gland: A preliminary report. Radiology 147:155-160, 1983.
4. Schultz CL, Haaga JR, Fletcher BD, Alfidi RJ, Schultz MA. Magnetic resonance imaging of the adrenal glands: A comparison with computed tomography. AJR 143:1235-1240, 1984.
5. Cohen MD, Weetman R, Provisor A, et al. Magnetic resonance imaging of neuroblastoma with a 0.15-T magnet. AJR 143:1241-1248, 1984.
6. Fletcher BD, Kopiwoda SY, Strandjord SE, Nelsen AD, Pickering SP. Abdominal neuroblastoma: Magnetic resonance imaging and tissue characterization. Radiology 155:699-703, 1985.
7. Dietrich RB, Kangarloo H. Retroperitoneal mass with intraspinal extension; Role of magnetic resonance imaging in children. Diagnostic Oncology Case. AJR 146:251-254, 1986.

Wpm-A2

1.5 T Magnetic Resonance Imaging of Hepatocellular Carcinoma

B. Gyi MD, A. Wilbur MD, B.G. Langer MD, and D.G. Spigos MD
Departments of Radiology University of Illinois and Cook County Hospital, Chicago, Ill.

Five cases of biopsy proven hepatocellular carcinoma were evaluated using a 1.5 T MRI system. Multiple pulse sequences were used in each case including partial saturation, respiratory compensated spin-echo, and suspended respiration gradient reversal (GRASS) technique. The MR studies were compared to standard bolus dynamic CT. In all cases the hepatomas appeared isointense to slightly hyperintense on relatively T1 weighted images becoming hyperintense relative to uninvolved liver onT2 weighted images. Areas of necrosis within tumors appeared hyperintense on both relative T1 and T2 weighting. Using rapid aquisition GRASS technique the tumors in general displayed decreased signal intensity relative to normal liver. A consistent finding with GRASS technique was excellent visualization of normal vasculature as well as absence of normal vessels in areas of tumor involvement. This ability to demonstrate vascular integrity allowed identification of prtal venous tumor involvement in one case. In general we found MR equal or superior to CT in demonstrating vascular structures and equal to CT in demonstrating extent of intrahepatic tumor.

Wpm-A3

HIGH RESOLUTION MR IMAGING OF THE PROSTATE

Ronald J. Otto, M.D., Barry D. Klein, M.D., William G. Bradley, M.D., Ph.D.

MR Imaging Laboratory, Huntington Medical Research Institutes, Pasadena, CA

Initial studies on prostate imaging were promising. However prostate carcinoma has not been shown to be readily differentiated from benign prostatic hypertrophy and a normal appearing gland does not exclude the presence of neoplasm. The purpose of the study was to evaluate various techniques to provide high resolution images of the prostate and surrounding pelvic structures. Over 20 patients with prostate carcinoma or clinical suspicion of carcinoma were scanned. They were imaged on a 0.35 Tesla (15 MHz) superconducting, Diasonics system utilizing a variety of receiver coils.

A specialized transrectal, receive only, coil was constructed about a Bardex balloon (Barium enema rectal catheter). The Bardex was inserted and the balloon expanded with either air, water, or a short T2 liquid, giving the coil diameter of approximately 5 cm. The balloon was positioned posterior to the prostate. Images were acquired on a 256x256 matrix with 0.95 mm pixels.

A specialized "license plate" 25x12 cm and a circular 13 cm surface coil were placed at the level of the symphysis pubis, and the patients were positioned prone over the coil. Images were acquired on a 256x256 matrix with 0.95 mm pixels. These images were compared with pelvic studies acquired using a standard body coil and one utilizing quadrature detection (QD). Some of the images were obtained with smaller fields-of-view, having pixel sizes of 0.95 and 0.625 mm. Other studies were performed using 1.7 mm pixels.

Results: The best images of the prostate in this series were obtained using a double saddle QD body coil and a small FOV. When the patient is positioned in the center of the coil with the 25 cm FOV, aliasing occurs but is beyond the region of interest. Many difficulties were encountered with the rectal Bardex prostate coil, in particular, motion artifact when the balloon was inflated with air and high near field signal intensity when water or a hydrogen containing agent was used to distend the balloon. Even with a short T2, concentrated ferrous sulfate solution high near field signal from surrounding fat and seminal vesicles created significant artifact on the images. Externally placed surface coil images did not provide adequate visualization of the posterior capsular portion of the prostate in many patients. The best images were obtained with the small, 25 cm FOV QD coil with 256x256 acquisition and 0.95 pixels.

Wpm-A4

HEMORRHAGIC ADNEXAL MASSES: 1.5 TELSA MR IMAGING

D.G. Mitchell[1], M.C. Mintz, H.Y. Kressel

Department of Radiology, The Hospital of the University of Pennsylvania, Philadelphia, Pennsylvania
1: Present address: Department of Radiology, The Thomas Jefferson University Hospital, Philadelphia, Pennsylvania

INTRODUCTION: Distinctive MRI signal features of hemorrhage at 1.5 Telsa have been described[1]. To evaluate the MRI appearance of hemorrhagic adnexal masses, we conducted a retrospective study.

MATERIALS AND METHODS: Sixty-one adnexal masses, including 8 with surgically proven hemorrhage [endometrioma (5), hemorrhagic cyst (2), recurrent ovarian carcinoma (1), benign teratoma (1)] were studied by 1.5T MRI. Images were examined for MRI signal characteristics of hemorrhage with short (TR 400-1000 msec, TE 20-25 msec) and long (TR 2000-2500 msec, TE 60-100 msec) TR/TE.

RESULTS: MRI signal patterns in the 8 surgically proven hemorrhagic masses varied, and in 4 masses more than one pattern was present. In 3 masses, low intensity with short and long TR/TE was noted, consistent with deoxyhemoglobin (acute) or hemosiderin (scar). In 3 masses, signal was higher than fat with short TR/TE and lower than fat with long TR/TE, consistent with intracellular methemoglobin (subacute). In 6 masses, signal intensity at least as high as fat with short and long TR/TE was noted, consistent with extracellular methemoglobin (subacute/chronic). Fluid/fluid levels were noted in 4 masses [hemorrhagic cyst (2), carcinoma (1), teratoma (1)], consisting of dependent low signal intensity with long TR/TE.

Small foci with signal characteristics consistent with extracellular methemoglobin were noted in 9 additional adnexal masses without surgically proven hemorrhage [pelvic inflammatory disease (6), carcinoma (2), serous cystadenoma (1)].

CONCLUSIONS: By demonstrating unique signal patterns, MRI is an effective modality for determining if hemorrhage is present in an adnexal mass. Since hemorrhage may be present with multiple etiologies, the clinical value of this application of MRI remains to be determined.

1. Rubin JI, Gomori JM, Grossman RI, Gefter WB, Kressel HY: High field MR imaging of extracranial hematomas. AJR (in press).

SURGICALLY PROVEN EXTENSIVE ENDOMETRIOSIS
Sagittal MR images. Six separate components can be identified.

Figure 1: Short TR/TE (600/25)

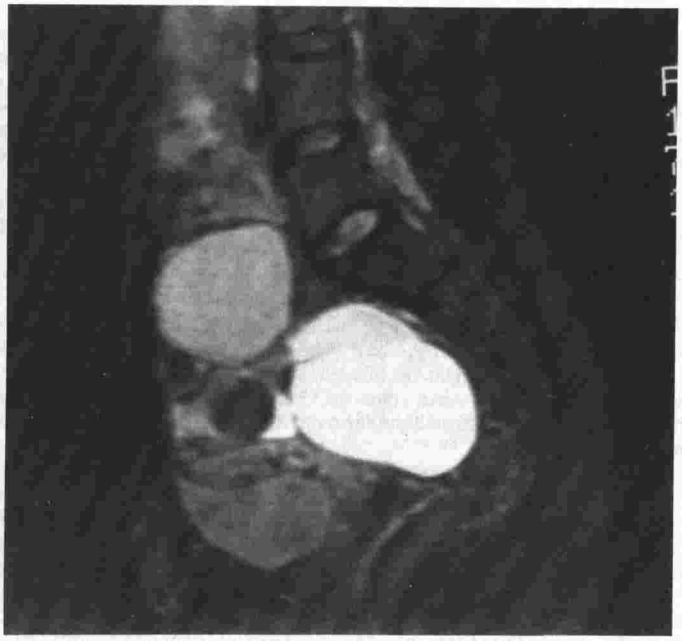

Figure 2: Long TR/TE (2500/80)

Wpm-A5

A COMPARATIVE STUDY OF THE ACCURACY OF ULTRASOUND, X-RAY CT AND MAGNETIC RESONANCE IMAGING FOR THE DIAGNOSIS OF UTERINE MALIGNANCY.

F.W. Smith, A.P. Bayliss, W.T. Fullerton, A.R. Law, E.M. Robertson and J. Weir

Departments of Radiology and Gynaecology, Aberdeen Royal Infirmary, Scotland.

Sixty nine consecutive cases of suspected cervical or uterine malignancy were entered into a study of the diagnostic accuracy of ultrasound, X-ray CT and Magnetic Resonance Imaging. In all cases a final histological diagnosis was made. The mean age of those studied was 66 years with a range of 30-84 years. Four main groups were identified; 18 malignant lesions of the cervix, 24 malignant lesions of the uterus, 24 benign lesions and 3 post hysterectomy follow up examinations. All the patients were studied by ultrasound, X-ray CT and M.R.I. within 24 hours. Each observer completed a questionnaire at the time of reporting his investigation without any knowledge of the findings of any other scan technique and the diagnostic accuracy of each technique compared with the final diagnosis.

Ultrasound diagnosed 63% of all lesions correctly, X-ray CT 67% and M.R.I. 79%. When the techniques were compared with each other to test the significance on the differences found, the comparison of X-ray CT and M.R.I. showed that M.R.I. was more accurate than CT at the 95% significance level. When just malignant lesions of cervix and uterus were compared, M.R.I. was found to be significantly better than both ultrasound and CT at the 95% significance level. When cervical and uterine were compared separately, M.R.I. was found to be significantly better than CT for diagnosing cervical lesions, while in the case of endometrial lesions it was significantly better than ultrasound both at the 95% significance level. It is therefore concluded that M.R.I. is the imaging technique of choice in suspected disease of the cervix and uterus.

Wpm-A6

A COMPARATIVE STUDY OF THE ACCURACY OF ULTRASOUND, X-RAY CT AND MAGNETIC RESONANCE IMAGING IN THE DIAGNOSIS OF OVARIAN MALIGNANCY

F.W. Smith, A.P. Bayliss, W.T. Fullerton, A.R. Law, E.M. Robertson and J. Weir

Departments of Radiology and Gynaecology, Aberdeen Royal Infirmary, Scotland

In an effort to ascertain whether or not any one scan technique or combination of scan techniques was more accurate than any other, 100 consecutive cases with suspected ovarian masses were entered into a trial. All cases were examined by ultrasound, X-ray CT and M.R.I. and all were subjected to laparotomy for histological diagnosis.

The mean age of the patients studied was 55 years, range 18-83. There were 29 cases of primary ovarian malignancy, 38 benign lesions, 7 non-ovarian benign conditions, 1 non-ovarian malignancy and 25 cases of known treated ovarian malignancy studied prior to second look laparotomy.

The diagnostic accuracy of each technique was assessed, both individually and in combination with the other techniques. Ultrasound was 53% accurate, X-ray CT 58% accurate and M.R.I. 60% accurate. When ultrasound and X-ray CT were combined, 46% of all lesions were diagnosed correctly, ultrasound and M.R.I. were 38% accurate and M.R.I. and X-ray CT were 46% accurate. When the combination of all three techniques was analysed there was a consensus agreement in 54% of cases. It was found that all three techniques were of similar ability at detecting and discriminating ovarian lesions. All three have a similar difficulty in differentiating benign and malignant ovarian tumours with approximately half of all benign lesions being diagnosed as malignant by each. As concensus diagnosis showed no improvement over individual techniques by themselves there appears to be no advantage in using multiple diagnostic techniques to detect ovarian malignancy.

This work was supported by the Medical Research Council, Special Project Grant 8121333.

Wpm-A7

THE ROLE OF N.M.R. IN STAGING RETROPERITONEUM IN TESTICULAR CARCINOMA

J.D. Tesoro Tess, L. Balzarini, E. Ceglia, R. Petrillo, R. Musumeci

Section of Urologic Radiology, Lymphangiography and Magnetic Resonance
Istituto Nazionale Tumori - Milano.

Purpose: An high value of accuracy and sensitivity is actually considered mandatory in the staging of non-seminomatous germ-cell testicular tumors, since management is modulated according to clinical stage. The purpose of this study is to evaluate the potential of M.R. in detecting lymphs node metastases in these patients.

Materials and Methods: M.R. evaluation of the retroperitoneal region was performed in 60 patients with histologically proven testicular carcinoma, already assessed by lymphangiography and C.T.. All the studies were performed on a 2 T Magne

tom, operating at 0.5 T during the first part of the study and actually at 1,5 T. At the end of the staging procedures 21/60 patients were considered at Stage I-IIA-B and treated with radical retroperitoneal lymphadenectomy whereas 27 were considered as "advanced" and underwent chemotherapy. Finally 12 patients were re-evaluated after treatment (surgey +/- chemotherapy).

For all patients multiplanar 1 cm thick slices were acquired with 8-10 sections for each plane. Generally two different Spin-Echo pulse sequences were utilized using the multiple-slice with both single (T1 - weighted) and double echo techniques. M.R. findings were correlated with C.T. and pathology in operated patients and with C.T. and other imaging techniques in those cases with advanced disease.

Results: M.R. was able to detect metastases in all advanced cases and in 10/11 operated cases (sensitivity = 90.9%). In 1 case enlarged hyperplastic lymph nodes were misinterpreted as pathologic (1 false positive). Further in 3/8 patients (37.5%) with small (2 cm) adenopathies, M.R. demonstrated to be superior to C.T. that on the contrary provided more useful informations only in one case. In fact, besides the spatial effects to surrounding structures such as compression and/or dislocation, adenopathies demonstrated a remarkable difference in signal intensity, mainly in T2 - weighted images, which permitted to distinguish nodes from muscles, vessels, fat and bowel. In large adenopathic masses a great dishomogeneity in signal occurred, with areas of low signal contiguous to areas of high signal. These features are to be referred to necrosis and emorrhages, commonly present in adenopathies from testicular carcinoma. For the same reason, the calculated T2 values appear to be significantly different from patient to patient and from node to node in the same patient.

Conclusions: M.R. may improve staging accuracy and serve as an effective substitute of C.T. in the evaluation of retroperitoneal adenopathies in testicular carcinoma.

Wpm-A8

MRI OF THE SEMINAL VESICLES: NORMAL ANATOMY AND PATHOLOGY.

Steven Edson, M.D., Yoshi Chang, M.D., Hedvig Hricak, M.D.

Department of Radiology, University of California School of Medicine, San Francisco, CA 94143.

This study was undertaken to determine the normal size and intensity of the seminal vesicles as a function of age. In addition, diseased seminal vesicles were studied.

The normal population included fifty men ranging in age from 31 to 69. All patients were either studied for problems unrelated to the seminal vesicles or the seminal vesicles were proven to be normal at surgery. The abnormal cases included hemospermia (2), seminal vesiculitis (1), bilateral hypoplasia (2), multilocular seminal vesicle cyst (1) and invasion by prostatic carcinoma (4).

All studies were performed with a 0.35T magnet using T1-weighted (TR 500/TE 30) and T2-weighted (TR 2000/TE 60 images).

The size and intensity of the seminal vesicles were measured on T1-weighted images in the axial and coronal planes. The intensity of the seminal vesicles were compared to fat, muscle and urine on spin echo images. For statistical analysis, the intensities of these structures were assigned a number ranging from white (=1) to black (=10).

The average length of the seminal vesicles was 29 mm, and the average width was 15 mm. No significant correlation with age was found, but a tendency toward slightly increased size in the 60 to 69 age group was seen.

On T1-weighted images, the hormonal seminal vesicles were of signal intensity similar to striated muscle, slightly more intense than urine and much less intense than fat. On T2-weighted images, they became heterogeneous with high intensity approximating that of fat. They resembled a cluster of grapes.

Hemorrhage into the seminal vesicle did not alter its size or shape, but caused marked increased signal intensity on the T1-weighted images. Seminal vesiculitis produced a marked decreased intensity on T1-weighted images which was isointense with urine.

The hypoplastic seminal vesicles were not only smaller in size; they had higher signal intensity on T1-weighted images than normal.

The seminal vesicle cyst was multiloculated, measured 5 by 6 cm and was of high signal intensity on both T1- and T2-weighted images. The contents of the cyst were consistent with old blood or proteinaceous fluid.

Prostate carcinoma involving the seminal vesicle usually enlarged the seminal vesicle. Enlargement was caused by obstruction or direct invasion of the seminal vesicle. Obstruction produced a greater than normal intensity, whereas direct invasion produced lower than normal intensity. Tumor did not enlarge the seminal vesicle in one case in which there was direct tumor extension.

In conclusion, MRI offers evaluation of the seminal vesicles which, in addition to demonstration of size and shape, assesses signal intensity which is uniformly low on T1-weighted images and high on T2-weighted images in normal patients and is altered in pathology.

(Wpm-B) MUSCULOSKELETAL

Presiding: E. Kanal & D. Kopp

3:20 pm

ROOM C-107

12 MINUTES PER PRESENTATION

Wpm-B1

MRI OF THE LUMBOSACRAL PLEXUS: AN ANATOMIC RADIOLOGIC CORRELATION

Catherine Chow, M.D. (1), Peter L. Choyke, M.D. (1,2), Joseph Frank, M.D. (2), Andrew Dwyer, M.D. (2), John Doppman, M.D. (2)

Department of Radiology, Georgetown University (1) and National Institutes of Health (2)

Although MRI of the spine and central nervous system has been extensively studied, peripheral nerve roots especially in the pelvis have received less attention. In the abdomen and pelvis these lumbar and sacral nerve roots combine to form the major nerves of the pelvis and lower extremity including the sciatic, femoral and obturator nerves. Injury or compression of these lumbosacral nerve roots can cause a spectrum of pelvic pain syndromes and neurologic deficits. Although CT can occasionally identify the lumbosacral plexus, MRI reliably demonstrates these nerves in coronal, sagittal and axial planes.

This exhibit will review in depth the normal anatomy and neuropathology of pelvic nerves with anatomic drawings in coronal, axial and sagittal planes. Normal MRI anatomy and a comparison of techniques will be demonstrated.

A 0.5T Picker MRI was employed in this study. Special emphasis was placed on a STIR sequence (TR = 1500 ms, TI = 100 ms, TE = 20-26 ms) which results in background suppression of fat signal and excellent delineation of nerve roots as they exit the neural foramina. The MR findings, using this sequence in 9 patients with pelvic and extremity pain syndromes, will be demonstrated. Malignant conditions (lymphoma, rectal carcinoma, ovarian carcinoma, soft-tissue sarcoma) and benign conditions (neurofibromatosis, radiation fibrosis) will be presented.

MR is particularly useful for radiation treatment planning and its role will be discussed in detail. Employing the STIR sequence, MR should be considered the optimal technique to visualize the pelvic peripheral nerves and detect pathology affecting them.

Wpm-B2

MAGNETIC RESONANCE IMAGING (MRI) OF BONE AFTER RADIATION (XRT)

Peter Remedios, MD; Patrick Colletti, MD; Janak Raval, MD; Robert Benson, MD; Linda Chak, MD; William Boswell, MD

Department of Radiology, Los Angeles County-University of Southern California Medical Center, Los Angeles, California 90033

MRI was performed in 18 patients at various times (0-3 years) after they received radiation therapy. T_1 and T_2 weighted images were obtained at 0.5 Tesla. Increased signal was seen after 800-6000 rads (8-60 Gy). Marrow effects corresponded to radiation ports. Recurrent tumor was clearly separated from fatty replacement. This was much better seen on T_1 weighted images. Three patients that had MRI during their course of radiotherapy (dose 2700 rads after 9 days XRT [first patient], 1680 rads after 6 days [second patient], 600 rads after 3 days [third patient]) did not have increased signal on T_1 images of the bone marrow. The earliest fatty marrow change was seen at 12 days following completion of 4000 rads XRT over one month duration. A subsequent MRI in this patient 3 months later showed no further increase in marrow signal on T_1 weighting. One patient who received 800 rads to the upper thoracic spine for eosinophilic granuloma had no radiation effects on MRI when imaged 16 days following completion of XRT given over 5 days. Fatty marrow change was seen in this patient when MRI was performed 6 months later. MRI was particularly useful in defining the extent of prior radiation effects when repeat therapy was needed.

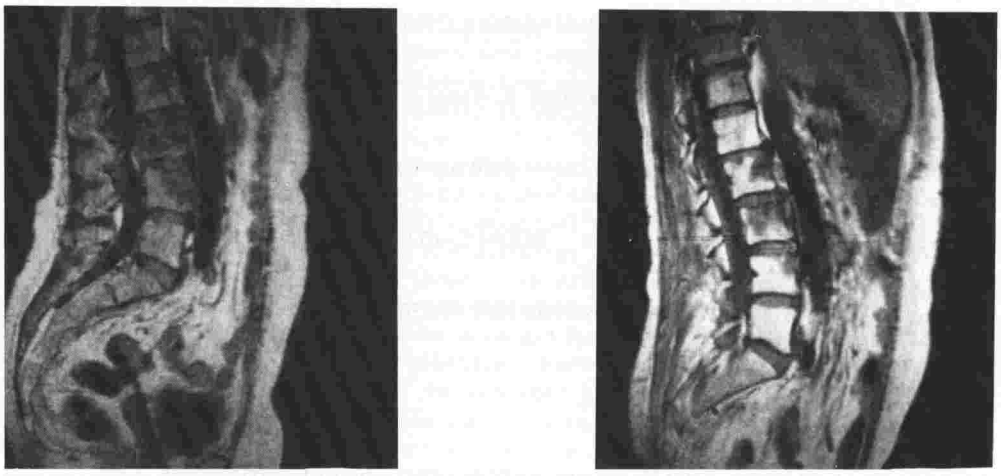

A B

T_1 weighted imaging (TR 550, TE 26 msec) before (A) and two months after (B) 4000 rads radiation therapy to the lumbar spine for metastatic renal cell carcinoma.

Wpm-B3

MRI OF OSTEOMYELITIS

E. Unger, M.D., P. Moldofsky, M.D., R. Gatenby, M.D., G. Broder, M.D. and J. Rosenblum, M.D.

Fox Chase Cancer Center, Philadelphia, PA 19111

We conducted a prospective study on 17 patients clinically suspect of having Osteomyelitis. MRI examinations were conducted on a 1.5 Tesla Siemens Magnetom using spin echo technique. T_1 and T_2 weighted pulse sequences were performed using TR/TE of 450/16, 3000/28/90. All examinations were correlated with bone scintigraphy. Criteria on MRI considered positive for Osteomyelitis were decreased signal intensity within bone marrow on the T_1 weighted image and increased signal intensity on the T_2 weighted image. In all cases in which MRI examinations met these criteria, a clinical diagnosis of Osteomyelitis was confirmed by clinical follow-up, and culture and/or biopsy. In the cases in which MRI was negative for Osteomyelitis, all of these patients were clinically followed and in none of these patients was Osteomyelitis subsequently detected by close clinical follow-up and culture. In the patients in which MRI was negative, bone scintigraphy often could not differentiate Osteomyelitis from adjacent soft tissue inflammation. In such a setting bone scintigraphy was not able to reliably exclude the presence of Osteomyelitis. In cases of cellulitis or soft tissue inflammation unassociated with Osteomyelitis, MRI showed no evidence of abnormal marrow signal intensity.

While other conditions such as tumor and fracture also might cause similar MRI signal characteristics within the marrow (i.e., decreased signal on T_1 weighted image with increased signal on T_2 weighted image), these signal intensity characteristics in a patient clinically suspect for Osteomyelitis should be highly specific for Osteomyelitis. In one case of documented Osteomyelitis, MRI was positive while bone scintigraphy was negative.

The authors conclude that MRI is highly sensitive and specific for the diagnosis of Osteomyelitis.

Wpm-B4

MAGNETIC RESONANCE IMAGING OF MALIGNANT FIBROUS HISTIOCYTOMA.

Bernard F. King, M.D., Gary T. Augustyn, M.D., Tod Abrahams, M.D., Robert Colyer, M.D.

Indiana University School of Medicine, Indianapolis, Indiana.

Malignant Fibrous Histiocytoma (MFH) is a tumor of mesenchymal origin which most commonly arises in the extremities. It may be of primary soft tissue or osseous

origin. It may also occur retroperitoneally and in virtually any organ. Patients are affected primarily in the fifth and sixth decades. The prognosis for patients with this tumor is generally poor. Prognosis may be improved by proper surgical management.

Although the radiographic findings of MFH have been well described, no detailed reports of the Magnetic Resonance (MR) appearance of MFH have been presented. We present the results of MR examinations of 10 patients having MFH of soft tissue origin of the extemities. Correlation and comparison to CT scanning, radionuclide bone imaging, and plain radiographs was made. Pathologic correlation to surgical specimens was available in all cases.

We find that MFH of soft tissue origin has a characteristic MR appearance. This consists of very high signal intensity on T2-weighted images with multiple internal septations in a characteristic pattern. Differentiating features between MFH and aneurysmal bone cyst (ABC) include the absence of internal fluid levels. Differentiating features between MFH and other tumors such as liposarcoma will be presented. Discussion of the use of MRI in planning surgical extirpation of MFH will also be discussed; in particular, the use of the coronal and sagittal imaging planes.

Wpm-B5

NONUNIFORM INTENSITY OF LUMBAR VERTEBRAL BODIES ON MR: AN IN VIVO AND IN VITRO STUDY.

Madeleine R. Fisher, M.D.

Elizabeth Holland, M.D., Sarsfield Dougherty, M.D., Sanford Roth, M.D.,

Ronald W. Hendrix, M.D., Lee F. Rogers, M.D.

An unusual MR appearance of the lumbar vertebral bodies in elderly patients has been observed where the normal high intensity of marrow was replaced by focal inhomogeneities. The purpose of this study was to investigate the etiology of this MR appearance in order to detect signs that may aid in distinguishing between normal variations in the elderly population and other processes affecting the vertebra, particularly, metastases. A retrospective analysis of 99 consecutive patients of all ages who had lumbar spine MR examinations was performed. Comparison was made to plain films and CT when available. These findings were correlated with clinical and laboratory data. Preliminary findings included: increased signal at the vertebral body endplates corresponding to an ill defined increased density on plain films and low intensity regions at the endplates corresponding to dense endplate sclerosis on plain films both associated with degenerative disc disease, arcs of high and low intensity corresponding to some but not all Schmorl's nodes, and regions of high and low intensity within the vertebral bodies not corresponding to any plain film abnormalities. We conclude in the elderly patient it may be difficult to differentiate subtle metastases or inflammation from incidental, intensity variations within the vertebral bodies. In order to further elucidate the etiology of the observed intensity variations, autopsy specimens (10) of elderly patient's vertebral bodies were studied with MR, quantitative CT for bone mineral content, gross and histologic appearance, and bone mineral analysis to correlate in vitro findings with those found in vivo.

Wpm-B6

INFECTIONS OF THE MUSCULOSKELETAL SYSTEM: MRI EVALUATION

Javier Beltran, M.D., Robert B. McGhee, M.D., Angela M. Noto, M.D., R. Marvin Freedy, MS4, Melinda S. McCalla BSRT

Department of Radiology, Ohio State University Hospital, S209 Rhodes Hall, 410 West 10th Avenue, Cols OH 43210

In order to assess the potential value of MRI in the evaluation of musculoskeletal infections, we studied a group of fifteen patients with clinical findings consistent with osteomyelitis, soft tissue infection or both and another group of 23 patients with joint pain but no clinical or laboratory signs of infection. This second group of patients was used as a control group and had in common the presence of hip or knee joint effusions.

A constellation of abnormalities including soft tissue abscesses, osteomyelitis, non-infected joint and tendon sheath effusions and cellulitis were well detected by MRI allowing the correct diagnosis of presence and extension of the infection in all but one of the patients.

Other imaging modalities such as Tc-99m MDP bone scintigraphy and In-111 labeled leukocyte scintigraphy were availabe for comparison in most of the cases. MRI was found to be more specific than other techniques due to its superior spatial resolution which allowed better treatment planning.

Although distinction between non-infected and infected synovial effusions was not possible by MRI in most cases, associated findings such as soft tissue fluid collections or osteomyelitis made this distinction possible in some patients.

It is concluded that when exact delineation of the extension of a musculoskeletal infection is warrented for treatment planning, MRI offers information not available by other techniques.

Wpm-B7

CHARACTERISTICS OF MUSCULOSKELETAL TUMORS BY MRI SIGNAL PATTERNS

Pamela Nurenberg, M.D., Steven E. Harms, M.D.

Department of Medical Imaging, Dallas, Texas 75246, USA
Baylor University Medical Center

INTRODUCTION: Musculoskeletal tumors are characterized by their T1 and T2 relaxation times. MRI has recently gained recognition for its usefulness in the evaluation of musculoskeletal tumors due to the superior contrast provided between muscle, fat, cortical bone, fibrous tissue, blood vessels, and neural tissue (1-3). Its multiplanar capabilities often provide better anatomical definition. Characterization of musculoskeletal tumors by their T1 and T2 relaxation times increases the diagnostic value of the MRI exam.

METHODS: A total of 121 patients are examined with various musculoskeletal tumros which are categorized according to signal characteristics, location, morphology, and age of the patient. All studies are obtained with a Technicare 0.6 T superconductive magnet. A body coil and various surface coils (flat coil, 4in. saddle coil) are used, depending on location and size of the mass. 2D multslice acquisition and 3D selective acquisitions are used. T1 weighting is achieved with a short Te (less than 32 msec) and a TR of 500 or less msec. T2 weighted images utilize a TE of 120 msec and a TR of 2000 msec or greater. Proton density weighting is performed with a short TE and a Tr of 2000 msec.

RESULTS: Tumors tend to fall into groups based on signal intensities with T1, T2, and N(H) weighted scans. Many primary bone tumors, desmoid tumors and fibrosarcomas have low signal relative to surroundings on both T1 and T2 weighted images. Fatty tumors have very high signal on T1 weighted images and moderate signal on T2 weighted images. Round cell tumors, multiple myeloma, plasmacytoma and most metastases have low signal on T1 weighted images and high signal on T2 weighted images. Chondroid matrix has very high signal on T2 weighted images. Subacute hemorrhage has high signal on both T1 and T2 weighted images and can usually be distinguished from other soft tissue masses. Examples of various tumors with pathologic correlation are shown. (Fig. 1)

CONCLISION: Magnetic resonance imaging is a very flexible technique that can provide information from pathologic tissues weighted toward a variety of parameters. This data can be used to improve diagnostic specificity when all of the other clinical factors are considered.

REFERENCES:

1. Zimmer WD, Berquist TH, Mcleod RA, et al: Bone tumors: Magnetic resonance imaging versus computed tomography. Radiology 155:709-18, 1985.

2. Petterson H, Hamlin OJ, Mancuso A, Scott KN: Magnetic resonance imaging of the musculoskeletal system. Acta Radiol [diag] 26:225-34, 1985.

3. Richardson ML, Grant HK, Helms CA, Gillespy T, Heller M, Jergesen HE, Bovill EG: Magnetic resonance imaging of the musculoskeletal system. Orthop Clin North Am 16:569-87, 1985.

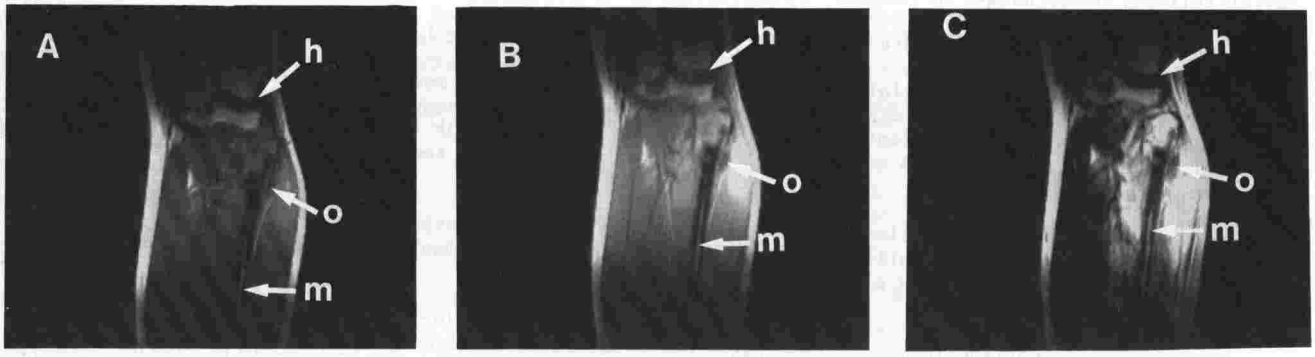

Figure 1: Chondrogenic Osteosarcoma. T1 weighted (A), N(H) weighted (B), and T2 weighted images demonstrate the varying intensities of hyaline cartilage h, osteoid matrix o, and uninvolved marrow m.

(Wpm-C) HEAD & NECK

Presiding: F. W. Smith & J. Clanton

3:20 pm

ROOM C-101

12 MINUTES PER PRESENTATION

Wpm-C1
MRI OF THE OROPHARYNX AND TONGUE: REVIEW OF ONE HUNDRED (100) CASES.

J. Cronin, M.D., R. Lufkin, L. Teresi, F. Vinuela, J. Bentson, G. Wilson, W. Hanafee.

UCLA

A total of 10 healthy and approximately 100 patients with abnormalities of the tongue or oropharynx were studied with magnetic resonance imaging. History and physical examinations were correlated with MR and other imaging studies. Of those patients who went to surgery pathological specimens were obtained for analysis. MR imaging was equal to or better than CT in those patients having both examinations. Direct coronal and sagittal imaging planes on MR allow visualization of intrinsic tongue musculature not possible with CT scanning. T1 weighted images were comparable to CT scanning and delineating nodal enlargement. T2 weighted images were superior to CT in defining subtle tumor extension in the sorrounding fascial planes. Magnetic Resonance is now the imaging study of choice for diseases of the tongue and oropharynx.

Wpm-C2
MR IMAGING OF PARANASAL SINUS INFLAMMATORY DISEASE

Jesse M. Cohen, M.D., Kenneth R. Maravilla, M.D., Dianne Mendelsohn, M.D.

University of Texas Health Science Center at Dallas, Dallas, Texas

Five hundred (500) consecutive magnetic resonance (MR) studies of the head were retrospectively reviewed to determine the incidence and appearance of inflammatory disease of theparanasal sinuses. MR imaging was performed on a superconducting system operating at 0.35 T. Multi-spin echo T2 weighted images were obtained in each case and T1 weighted images were performed in 248 cases. There was an overall incidence of disease of 39.4% (197 cases). The most commonly involved sinuses in decreasing order were maxillary 23.6% (14.8% unilateral, 8.8% bilateral), ethmoid 7.4% (3.4% unilateral, 4.0% bilateral), sphenoid 4.2% (2.8% unilateral, 1.4% bilateral), and frontal 4.0%. Multiple sinus involvement was seen in 8% of the cases with ethmoid and maxillary sinusitis being the most common combination. Post inflammatory septations were seen within the maxillary sinus in 16 cases and sphenoid sinus in one case. There were two cases of hypoplastic maxillary antra.

Three distinct patterns of disease were identified: (1) smooth mucoperiosteal thickening which demonstrated an intermediate T1 and long T2 relaxation time; (2) discrete round/ovoid retention cysts or polyps with intermediate T1 and long T2 characteristics (occasionally areas of high signal were seen on T1 images which may represent hemorrhage); and (3) sinuses completely filled in with material demonstrating intermediate T1 and long T2 relaxation times. One case of an expanded filled in maxillary sinus was felt to represent a mucocele.

A group of 100 subjects were prospectively questioned concerning active or remote sinus disease. The MR findings were correlated with the clinical history to determine the sensitivity of MR in detecting active disease. Eighty-nine percent (25/28) of patients with ongoing symptoms had positive MR findings. Of 72 patients with no known history of sinus disease, 70 (97.2%) had normal MR studies. MR appears to be a sensitive indicator of active inflammatory sinus disease.

Although MR is presently a relatively time consuming and expensive modality for studying paranasal sinus inflammatory disease, the development of rapid imaging techniques may have a significant impact on the use of MR as a screening tool. Examples of two such techniques, i.e., advanced fourier and partial flip angle imaging, will illustrate the future potential of MR in evaluating the paranasal sinuses.

Wpm-C3

TRIGEMINAL NEURALGIA AND HEMIFACIAL SPASM: MR EVALUATION

John D. Reeder, M.D. and Samuel Andelman, M.D.

Magnetic Imaging Associates, Baltimore, Maryland

Vascular compression of the fifth and seventh cranial nerves has been implicated as a major etiologic factor in the development of trigeminal neuralgia and hemifacial spasm. To evaluate the effectiveness of magnetic resonance imaging (MRI) in detecting vascular asymmetry, aneurysms, tumors and other intracranial pathology potentially responsible for facial symptomatology, we reviewed MRI scans on 17 patients with facial pain and 7 patients with hemifacial spasm. Of the trigeminal neuralgia cases, vascular asymmetry or aneurysm formation within or near the cerebellopontine angle cistern was discovered in 8 patients, with the side of relative vascular dilatation coinciding with the side of symptomatic facial involvement in all cases. Scans were normal in 3 of the facial pain patients and lacunar infarcts and/or diffuse atrophic changes were detected in 4 patients. An arachnoid cyst was observed in 2 patients (one of these patients was also in the vascular asymmetry category) and MRI examination in one patient demonstrated a pineal region tumor. Of the 7 patients with hemifacial spasm, unilateral vascular dilatation or aneurysm formation coinciding with the side of facial symptomatology was evident in 5 cases. In one case, atrophy alone was observed and, finally, no intracranial pathology could be discovered in 1 patient. Treatment for hemifacial spasm and trigeminal neuralgia remains controversial and therapeutic options include posterior fossa microvascular decompression, peripheral nerve ablation and various medical regimens. MRI certainly represents an important diagnostic modality in the detection of tumors and demyelinating disease which may result in sensory or motor facial neurologic dysfunction. Additionally, through the identification of cerebellopontine angle vascular asymmetry in patients with trigeminal neuralgia and hemifacial spasm, magnetic resonance imaging may permit more accurate selection of those patients who might specifically benefit from microvascular decompression.

Wpm-C4

M.R.I. OF THE SALIVARY GLANDS IN SARCOIDOSIS

Drs. V. Lopez-Majano, B. Langer, B. Gyi*, R. Rhee, M. Mafee, D. Spigos

Department of Radiology (CCH) and *Department of Radiology
(U. of I.), 1835 W. Harrison Street, Chicago, Illinois
60612.

^{67}Ga The salivary glands of 10 patient with biopsy proven systemic sarcoidosis and positive uptake were studied by MRI. The MRI appearance of the submandibular and parotid glands of these patients was then assessed for size, strength, and homogeneity of MRI signal. These results were then compared to findings in a control group of normal patients. Although in several cases MRI revealed glands that were enlarged or nonhomogenous in MRI signal, the salivary glands of several patients with stongly positive gallium uptake were indistinguishable from normal by MRI. We conclude that while enlarged or nonhmogeneous salivary glands are imaged by MRI may be seen in sarcoidosis, these findings are not universal and no specific MRI findings of salivary gland sarcoidosis could be discerned.

Wpm-C5

SURFACE COIL MR IMAGING OF ORBITAL BLOW-OUT FRACTURES

H. Tonami[1], I. Yamamoto[2], K. Sasaki[3], J.C. Ehrhardt[1]
[1]Department of Radiology, University of Iowa Hospitals and Clinics, Iowa City, Iowa
[2]Department of Radiology and [3]Ophthalmology, Kanazawa Medical University, Ishikawa, Japan

INTRODUCTION: MR imaging of the orbit is being performed with increasing frequency in patients with suspected orbital diseases. Using surface coils as receivers, the S/N ratio can be increased significantly. This permits thinner sections and improves spatial resolution so that it is comparable to CT. We here present surface coil MR findings in patients with blow-out fractures and compare them with CT findings using images in multiple planes.

METHODS: Four patients with orbital blow-out fractures were examined with surface coil MR. The fracture site of the orbit was the medial wall in one case and the inferior wall in the other three cases. CT was performed with 2 mm thick slices in axial or coronal planes. Images were also reconstructed in coronal or oblique sagittal planes from the axial sections. MR imaging was obtained using a Siemens 0.5T superconducting unit. A 10 cm diameter surface coil was used as a receiver. SE pulse sequences with TR = 600 msec and TE = 35 msec or 45 msec were used. Each section was 5 mm thick with 5 mm gap between adjacent slices. Initially, multiple images of coronal plane covering the entire orbit were obtained. Thereafter, additional images of other planes, axial or oblique sagittal, were obtained.

RESULTS: In all four cases, MR demonstrated the fracture and the herniation of the orbital fat more clearly than CT. Although MR has a disadvantage in its inability to image the displaced bony fragments themselves, the fracture could be diagnosed by the presence of the prolapsed orbital fat into the adjacent paranasal sinuses. Two cases of the muscle entrapment by a bone defect were correctly diagnosed on MR, but CT failed to demonstrate one of these lesions.

CONCLUSION: Surface coil MR is found to be superior to CT in the assessment of fracture site, extent of prolapsed orbital fat, and muscle entrapment. Our study indicates that surface coil MR may be more effective than CT for the evaluation of orbital blow-out fractures.

Wpm-C6

DETECTION OF PARATHYROID ABNORMALITIES BY MAGNETIC RESONANCE IMAGING

C.E. Spritzer, M.D., W.B. Gefter, M.D., R. Hamilton, M.D., B. Greenberg, M.D., L. Axel, M.D., H.Y. Kressel, M.D.

Department of Radiology, Duke University Medical Center, Durham, NC 27710
Departments of Radiology and Surgery, Hospital of the University of Pennsylvania, Philadelphia, PA 19104

Neck exploration for hyperparathyroidism is associated with numerous complications including both hypercalcemia and hypocalcemia, hemorrhage and recurrent laryngeal nerve damage. Correct preoperative localization of parathyroid glands may reduce these complications by permitting selective exploration of the neck and mediastinum. Current imaging modalities are limited by the similar appearance of thyroid and parathyroid tissue (CT) or do not provide sufficient anatomical orientation for the surgeon (US and radionuclide studies). We, therefore evaluated 25 patients with hyperparathyroidism to determine the utility of MRI in detecting parathyroid abnormalities. Surgical confirmation was available in all cases.

All studies were performed on a General Electric 1.5 Tesla superconducting magnet. Axial spin echo images utilizing both short (TR = 600 msec, TE = 20/25 msec) and long (TR = 2000/2500 msec, TE = 60/70/80 msec) were acquired in all cases. Coronal and sagittal images were obtained as needed. Surface coils were routinely used. Two studies were nondiagnostic on all pulse sequences due to respiratory motion.

Of the diagnostic studies, MRI accurately localized 15 of 18 parathyroid adenomas, 2 of 2 parathyroid carcinomas, and 5 of 8 hyperplastic glands, the latter from three patients. The lesions ranged in size from 4 mm to 5 cm. In all but one case, abnormal glands had signal greater than or equal to fat on the long TR/TE spin echo images. Parathyroid adenomas, carcinomas, and hyperplasia could not be distinguished from one another. The overall sensitivity and specificity of MRI in the detection of parathyroid abnormalities was 78% and 96%, respectively, resulting in an accuracy of 90%. Magnetic resonance imaging appears to be a sensitive means of evaluating parathyroid abnormalities.

Wpm-C7

MAGNETIC RESONANCE IMAGING OF THE BRACHIAL PLEXUS

Stanley Rapoport, Deborah N. Blair, Terry Desser, Shirley McCarthy, H. Dirk Sostman

Department of Radiology, Yale University School of Medicine

Purpose:
The high soft tissue contrast and multiplanar capabilities of magnetic resonance (MR) give it a distinct advantage over computed tomography (CT) in imaging the brachial plexus. This paper reports the normal and pathologic anatomy of the brachial plexus on MR.

Methods:
Two normal volunteers and seven patients who had brachial plexus symptoms were examined. All imaging was performed on a commercial imaging system (Signa, General Electric 2.0T) operating at 1.5 Tesla. Both body and surface coils were utilized. Both T1- weighted and T2-weighted (TR 800 and 2500 msec, TE 20 and 80 msec) images were obtained in axial, sagittal, and/or coronal planes.

Results:
In each case, the brachial plexus was well visualized throughout its course. The optimum projection in most cases was the sagittal plane. This allowed the brachial plexus to be seen in cross-section and its relationship to adjacent vessels and pathology to be well defined (Figs. 1&2); the spinal cord was also evaluated in this plane. T1-weighted images demonstrated the anatomy to best advantage, while pathology was optimally visualized on T2-weighted images. Five of the seven patients had had prior CT scans. In two of these patients MR revealed more extensive disease than that noted on

CT. In no case was CT superior to MR. In the two patients without CT scans, MR provided sufficient clinical information to obviate the need for CT scanning.

Conclusion:

Our results show that MR is well suited for imaging the brachial plexus. Advantages over CT include superior contrast sensitivity and direct multiplanar image capability. Images obtained in the sagittal plane optimally demonstrated the brachial plexus and surrounding structures.

Figure 1 Sagittal image, SE 20/2,500, through axilla demonstrating normal brachial plexus (open arrow) bordered inferiorly by axillary artery (curved arrow) and axillary vein (straight arrow)

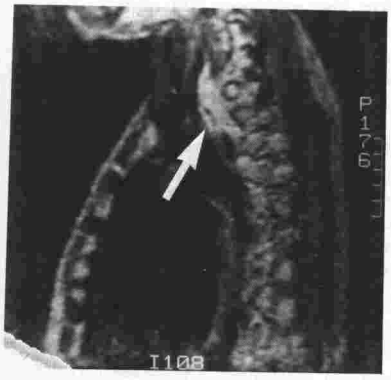

Figure 2 Paramedian sagittal image, SE 80/2,500, in a patient with myeloma. There is a mass (arrow) involving the proximal brachial plexus.

Wpm-C8

MAGNETIC RESONANCE IMAGING OF THE BRACHIAL PLEXUS

Anthony R. Lupetin, M.D.; Nilima Dash, M.D.; Richard H. Daffner, M.D.; William E. Rothfus, M.D.; Ziad L. Deeb, M.D.; Rolf L. Schapiro, M.D.;

Allegheny General Hospital, Pittsburgh, Pennsylvania

PURPOSE: To demonstrate the usefulness of MRI in evaluating the brachial plexus.

METHODS: Thirty patients with a brachial plexus syndrome were evaluated with MRI utilizing T1 and T2-weighted spin echo pulse sequences (TR = 0.5, 2.1 sec; TE = 17, 70 msec) obtained in axial and coronal scan planes utilizing contiguous 1 cm sections.

RESULTS: MRI demonstrated cervical, axillary, or thoracic pathology relating to the brachial plexus in 8 of 30 cases. A neurofibroma arising from the left seventh cervical nerve represented the only primary abnormality of the brachial plexus in our study. In seven cases, brachial plexus symptomatology was related to extrinsic compression by the following etiologies: metastatic adenopathy or mass in the cervical or axillary region, radiation fibrosis, apical chest mass (bronchogenic carcinoma, neurofibroma).

MRI in axial and coronal scan planes was useful in screening the brachial plexus region for pathologic states. It is recommended that scans be obtained from the C3 level to the carina, which is a useful reference point for the lower aspect of the brachial plexus.

CONCLUSION: MRI provides an excellent assessment of the brachial plexus region and is a useful technique in evaluating patients with brachial plexus symptomatology related to intrinsic or extrinsic abnormalities.

(Wpm-D) SAFETY, IMAGE PROCESSING

Presiding: R. Ehman & R. Price

3:20 pm

ROOM C-102

12 MINUTES PER PRESENTATION

Wpm-D1

THERMOGRAPHIC EVALUATION OF SURFACE TEMPERATURE CHANGES ASSOCIATED WITH HIGH-FIELD MAGNETIC RESONANCE IMAGING: NO EVIDENCE OF THERMAL"HOT SPOTS".

Frank G. Shellock, Ph.D.; Daniel J. Schaefer, Ph.D.*; Warren Grundfest, M.D.; and John V. Crues, M.D.

Section of Magnetic Resonance Imaging, Department of Diagnostic Radiology, Cedars-Sinai Medical Center and UCLA School of Medicine, Los Angeles, CA 90048
*Medical Systems Group, General Electric Company, Milwaukee, WI 53201

Increases in skin and body temperatures have been observed in patients undergoing high - field magnetic resonance imaging (MRI) and are believed to be primarily caused by radiofrequency (RF)-induced heating (1,2). Certain parts of the human body are predicted to receive more RF power than normal because of current density concentration due to insulating constrictions (3,4), which may result in unusual heating patterns and/or excessive temperature elevations. Since RF-induced heating occurs predominantly at the surface (4,5), theoretically, thermal "hot spots" related to concentrations of RF power should also be peripherally located (i.e., largest eddy current and largest current density). Therefore, the purpose of this study was to determine the changes and distribution of surface temperatures associated with high - field MRI.

The scanner used in this study has a 1.5 Tesla superconducting magnet and operates at 64 MHz (General Electric Co.). The body coil is driven in quadrature (i.e., circularly polarized). Three normal male volunteers underwent MRI of the spine using conventional RF pulse sequences (multi-slice, multi-echo) for a total imaging time of approximately 45 min. at the following estimated whole body average specific absorption rates (SAR): Subject #1 (wt 82 kg) - 0.9 W/kg, Subject #2 (wt 100 kg) - 1.1 W/kg, Subject #3 (wt 136 kg) - 1.3 W/kg. The study subjects were exposed to a room temperature of 21$\pm$1^{o}C, relative humidity of 45$\pm$5%, and air movement of less than 0.1 m/s for 15 min. to allow for temperature equilibration. Body (sublingual pocket, Mark X Thermometry System, Electromedics, Engelwood, CO) and skin (Medi-Therm Infrared Thermometer, Everest Interscience, Tustin, CA) temperatures were measured immediately before and after MRI. Thermographs of the entire body were obtained with a high-resolution system (Thermovision 782, AGA Infrared Systems, Sweden).

Body temperature changes produced by MRI were as follows: Subject #1 = $^{+}$0.1^{o}C, Subject #2 = +0.2^{o}C, Subject #3 = $^{+}$0.2^{o}C. In general, skin temperatures increased after MRI and the absolute amount was dependent on the anatomical site. The highest skin temperatures measured were: Subject #1 = 34.9^{o}C, Subject #2 = 33.8^{o}C, Subject #3 = 33.1^{o}C. Thermographic imaging revealed normal heating patterns with no discernable "hot spots" (see Figure 1). In conclusion, we did not observe any excessive temperature elevations or abnormal distributions of temperatures in association with high-field MRI at the SARs we studied.

1. Shellock FG, Schaefer DJ, and Crues JV: Thermophysiological alterations associated with magnetic resonance imaging above a specific absorption rate of 0.4 W/kg. Society of Magnetic Resonance in Medicine, Book of Abstracts, pp 351-352, 1986.
2. Shellock FG, Schaefer DJ, Grundfest W, Crues JV: Thermal effects of high-field (1.5 Tesla) magnetic resonance imaging of the spine: Clinical experience above a specific absorption rate of 0.4 W/kg. Acta Radiologica. (in press) 1986.
3. Vollman W: How hot are hot spots? Society of Magnetic Resonance in Medicine, Book of Abstracts, pp 331-332, 1985.
4. Budinger TF: Nuclear magnetic resonance (NMR) In vivo studies: Known thresholds for health effects. Journal of Computer Assisted Tomography. 5: 800-811, 1981.
5. Bottomly PA and Edelstein WA: Power deposition in whole body NMR imaging. Medical Physics. 8:510-512, 1981.

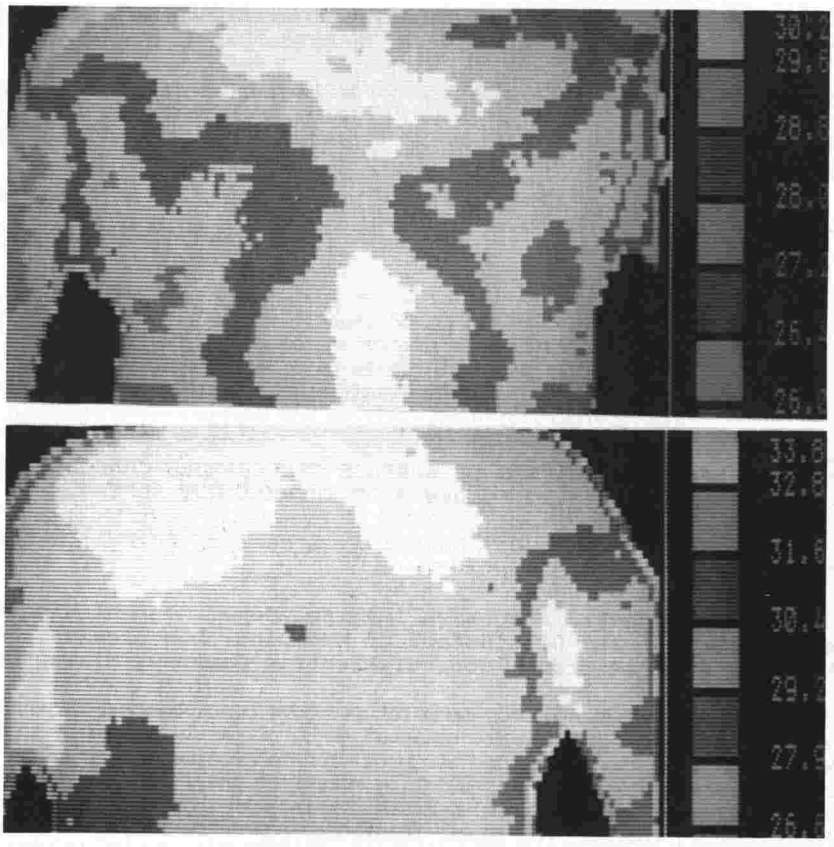

Figure 1. Thermographs obtained from back area of Subject #2 before (A) and after (B) MRI at a whole body average SAR of 1.1 W/kg (highest temperature is indicated in white).

Wpm-D2

PHYSIOLOGICAL MONITORING DURING MAGNETIC RESONANCE IMAGING

Laurence W. Hedlund PhD, Gary P. Cofer MS, G. Allan Johnson PhD

Department of Radiology, Duke University Medical Center, Durham, North Carolina 27710

For clinical and research studies, comprehensive physiological monitoring is often needed, yet most commercially available monitoring systems are not compatible with use in the magnetic and radio-frequency fields typical of high field MR systems. The purpose of this study was to adapt a commercially available recording system to support real time physiologic monitoring (ECG, direct pressure, peripheral pulse, body temperature, respiration) in small and large bore imagers.

We used a modular, physiologic recording system and analog-digital converter (Coulbourn Instruments, Lehigh Valley, PA) interfaced with a personal computer (Model IT, Sperry Corporation, Salt Lake City, UT). Transducers for direct blood and pneumatic pressure were solid state devices. We used thermistor probes for temperature and a photoreflective densitometer for pulse monitoring. ECG used conventional adhesive pad electrodes. Transducers were not effected by magnetic fields up to 2 Tesla. Transducer leads were shielded and rf filtered. Real time display utilized a high resolution color monitor, enhanced graphics, and a waveform scroller board.

Physiologic data were displayed in real time and simultaneously recorded on hard disk with minimal imager noise (rf and gradient). Data acquisition rates of up to 250 Hz for 4 channels of input were achieved. Acquisition of 8 channels of input data can be supported at 100 Hz sampling rate per channel. This is more than adequate to display the fast transients of the ECG potentials. The A/D converter was also interfaced with other equipment (Doppler flow monitor) using available analog output ports. In addition to real time display, a major advantage of this system is the capability for immediate data recall and redisplay and for convenient post-study numerical analysis.

This MRI compatible monitoring system, with its microcomputer interface, provides a valuable tool for performing correlative physiologic-MR imaging studies and real time monitoring of patients and research subjects.

Wpm-D3
AUTOMATED IMAGING PROTOCOLS FOR IMPROVED PATIENT THROUGHPUT IN MRI

Jay Dworkin PhD., R. Lufkin, J. Stutman, J. Cohen, R. Wolf, W. Hanafee.

Fonar Corporation, New York and U.C.L.A.

The toal time spent on each patient in an MR scanner determines patient throughput and ultimately influences MR scan charges. Actual data acquisition often represents only a small portion of this examination time. Other functions such as patient loading and unloading, positioning, coil placement, scan setup, and image reconstruction time also lengthen the examination time.

We describe a technique for creating automated imaging protocols for standard MR examinations which optimize these functions, thereby decreasing operator interventions and shortening the overall examination time. A prototype sequence for examining the larynx and neck was developed which allowed three sequential SE-500/28 multiple slice sequences to be obtained in three orthogonal planes with a single operator setup step. All tuning and scan placement after this first step was done under computer control without operator intervention. The new sequence allowed larynx and neck studies to be performed in less than 30 minutes instead of the 50-60 minutes required by conventional methods. The new technique will be useful for improving patient throughput for a variety of standardized examinations including the temporal bone, head and neck, knees, and other regions.

Wpm-D4
HIGH RESOLUTION 3D RECONSTRUCTION OF MAGNETIC RESONANCE IMAGING

H.E. Cline, C.L. Dumoulin, H.R. Hart Jr., W.E. Lorensen and S. Ludke

General Electric Company, Corporate Research and Development
PO Box 8, Schenectady, New York 12301

Three-dimensional (3D) surface reconstructions provide a means to view complex anatomy contained in a set of CT, MR or SPECT images. The requirements and characteristics of 3D reconstruction methods depends on the imaging modality used to obtain the raw data. We have found that for the above modalities the normalized gradient of the original data points in the raw images provides the best estimate for the surface normal and hence results in higher quality 3D images. Two algorithms that generate 3D surface models will be presented. The methods use polygon and point primitives. In addition, "pixel seeding" techniques for selective surface extraction will be demonstrated.

Extraction of surface features from contiguous multi-slice and 3DFT MR data permits a visualization of soft tissue structures which is not possible with any other non-invasive method. For example, the surface of the brain is easily extracted and presented at any view angle. Surfaces internal to the brain, such as the ventricular system are easily visualized.

An important application of 3D methods is the reconstruction of vascular surfaces. Using a fast scan 3DFT technique it is possible to attenuate the signal from stationary spins and obtain strong signals from the non-saturated blood entering the excited region. The resulting contrast is sufficient for the extraction of the vessel surfaces. For example, the morphology of the carotid arteries in the region of the bifurcation is easily demonstrated and presented with data obtained in a 128x128x256 3DFT examination.

Wpm-D5
MICROWAVE TRANSMISSION OF MR IMAGES

Seibert CE, M.D.*, Smazal ST, M.D.*, Dreisbach JN, M.D.*, Hellyer J**

*Radiology Imaging Associates, Englewood, Colorado, **HSE Communications

MR exams require a high degree of physician-technologist interchange regarding optimization of pulse sequences during exams if non-diagnostic or inadequate studies are to be avoided. This interchange is necessary, but the geography of a free standing MR center makes it difficult to have on site radiologist sub-specialist constant supervision. To meet this challenge, we have installed a microwave transmission system (M/A-COM) for transfer of MR images (real time) from our free standing imaging center at the Denver Technological Center to the joint venture hospital radiology departments six miles away. Since May 1985, we have had uninterrupted function up to seven days a week and have transmitted approximately 4,500 patient images without down time nor maintenance expense. The advantages of this system include: (1) provides on-site supervisory help for technologists by an off-site radiologist, (2) images transferred are of high quality without degradation, (3) transfer is essentially real-time, (4) low maintenance cost, (5) timesaving for radiologists, technologists, (6) potential for improved film logistics, (7) improves medical staff awareness of MR (PR), (8)

tends to discourage early machine duplication by participating hospitals, (9) other image transfer potential.

Limitations and disadvantages: (1) relatively high start-up cost, (2) hard copy production at receiver site currently cumbersome, (3) receiver site image storage required additional peripheral (Digistore by Matrix), (3) no image display control at receiver site, (4) line of sight requirement, (5) existing imaging - vendor incompatibility at sender vs. receiver site increases cost.

The system model will be described and photographic demonstration of day-to-day usage will be detailed.

AUTHOR INDEX

-C-

-D-

-M-

-N-

-S-

-X-

-Y-

-Z-

Acknowledgments

We wish to express special thanks to Diane Taub, Nancy Wysocki and Janice Tully for their help in the preparation of the program and abstracts for this meeting